Synthesis and Characterization of Solid, Hollow, Core-Shell and Worm-Like Carbon Nanostructures for Applications in Organic Photovoltaic Devices and Chemical Sensors

by

Bridget Kanini Mutuma

(M.Sc.)

Student Number: 806599

A Thesis submitted for the faculty of Science at the University of Witwatersrand Johannesburg, in the fulfilment for the degree of

Doctor of Philosophy in Chemistry

Supervisor: Prof. Neil J. Coville

Co-Supervisor: Dr. Daniel Wamwangi

Johannesburg, November 2016

DECLARATION

I declare that this thesis is my own, unaided work under the supervision of Professor Neil J. Coville and Doctor Daniel Wamwangi. It is being submitted for the degree of Doctor of Philosophy in the University of the Witwatersrand, Johannesburg. It has not been submitted before for any degree or examination in any other university.

---------- 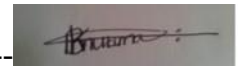 ----------

(Signed) **Bridget Kanini Mutuma**

On this ----04th--- day of-----November----- 2016

ABSTRACT

The synthesis of carbon spheres (solid and hollow) for application in organic photovoltaics and chemical sensors is a means of using inexpensive and readily processable carbons to eliminate global warming and to monitor harmful gases. The synthesis conditions used to make solid carbon spheres can also be used to tailor their structural, paramagnetic and thermal properties. More so, the ability to tailor the morphology, surface, structural and electronic properties of the hollow carbon spheres by a templating method is an added advantage to their applicability in electronic devices.

Solid carbon spheres were synthesized by a vertically oriented chemical vapor deposition (CVD) reactor using acetylene as a carbon source and argon or hydrogen as the carrier gas. The flow rates of the acetylene or carrier gases determined the particle sizes of the carbon spheres. Annealing of carbon spheres in hydrogen resulted in an increase in thermal stability, fewer defects and narrower paramagnetic signals relative to the carbon spheres annealed in argon gas. In contrast, carbon spheres annealed in argon exhibited an increase in the number of defects, a decrease in thermal stability and broader paramagnetic signals. Doped carbon spheres portrayed an increase in I_D/I_G ratios, a decrease in thermal stability and stronger paramagnetic signals due to the presence of defects induced by nitrogen. The N doped carbon spheres synthesized in H_2 comprised of 48% pyridinic-N, 22% pyrrolic-N and 24% quaternary -N while the N doped spheres obtained in the presence of Ar had 17% pyridinic-N, 20% pyrrolic-N and 49% quaternary-N. The presence of a higher percentage of pyridinic-N confirms the presence of more edge defects in carbon spheres synthesized under H_2 gas corroborating with the stronger paramagnetic signal observed from the ESR spectra. Consequently, a higher N/C ratio was exhibited in the N doped CSs obtained in the presence of H_2 (4.96) than in the presence of Ar (3.68). This could be attributed to the presence of edge defects in carbon spheres synthesized in the presence of H_2 gas. The induction of edge defects in carbon spheres in the presence of H_2 gas without the aid of a metal catalyst opens a platform for regulating surface and catalytic reactions using H_2 gas.

Pristine and mesoporous SiO_2 spheres were synthesized using a modified Stober method. Carbonization of the pristine SiO_2, pristine SiO_2@PVP, mesoporous SiO_2 and mesoporous SiO_2@PVP spheres was carried out using a bubbling method with toluene as the carbon

source and argon as the carrier gas in a CVD reactor for 1 h. Upon SiO_2 removal, hollow carbon nanostructures of varying morphologies were obtained. The polyvinylpyrrolidone (PVP) adsorption time, PVP concentration, SiO_2 mesoporosity, SiO_2 particle size dispersion, and carbonization time played a role in the formation of unique hollow carbon nanostructures; complete HCSs, broken HCSs, deformed HCSs, edge connected, open ended, wormlike and bubble-like HCSs. The mesoporous broken HCSs and open ended HCSs portrayed a hierarchical structure with a bimodal pore size distribution. The surface area properties of these materials and the ease of control of the carbon morphology gives an insight into the application of these materials as dye adsorbents. The effect of the size dispersion of Au@SiO_2 sphere templates for the synthesis of hollow carbon structures was evaluated using a CVD nanocasting method. The diameter of the template, the presence of the gold nanoparticles and the amount of PVP determined the size, thickness and shape of the synthesized carbon nanostructures. Carbonization (and SiO_2 removal) of Au@polydispersed silica spheres for 1 h gave a graphene-like HCS layer while longer times (2-4 h) gave nanotube like (or worm like) HCSs. These results highlight the potential use of Au@carbon core shell structures for the generation of few layered graphene-like unusual nanostructures. As a proof of concept, the wormlike carbon structures were incorporated in organic solar cells and found to give a measurable photovoltaic response.

The incorporation of Au nanospheres and nanorods in a hole transport layer (PEDOT:PSS) of a solar cell device increased the current density and the photo-conversion efficiency of the device due to the local surface plasmon resonance and enhanced light scattering effects of gold. However, high series resistance and leakage currents were obtained due to barrier centres created by uneven dispersion of Au nanaorods within the polymer matrix. The performance of bulk heterojunction organic photovoltaic cells based on poly(3-hexyl-thiophene-2,5-diyl) (P3HT) and [6,6]-phenyl-C_{61}-butyric acid methyl ester (PCBM) processed from chlorobenzene solution can be enhanced by solution heat treatment of the blend. The morphology of films spin coated from the heat treated blend solution reveals a more favourable diffusion of PCBM into the P3HT matrix than heating of the individual solutions separately. The films obtained from heat treated P3HT and PCBM solutions had a more homogeneous dispersion and enhanced light absorption than those obtained from solutions heat treated separately. There was a significant improvement in the performance for devices made from a solution heat treated blends relative to the non-treated blend; a

maximum power conversion efficiency of 3.5% and a fill factor up to 43% was achieved under Air Mass 1.5 at 100 mW/cm^2 illumination.

This study also reports on the sensing characteristics of ammonia in humid environment by hollow carbon spheres, hollow carbon spheres-polyvinylpyrrolidone composite and annealed hollow carbon spheres, at 20°C and 40°C. For device fabrication, a surfactant assisted method was used to homogeneously disperse the hollow carbon spheres, allowing their deposition onto an interdigitated electrode by casting. An enhanced response and recovery time of the devices was observed at the higher working temperature. Annealing of the hollow carbon spheres resulted in a tremendous decrease in the humidity dependent ammonia sensing due to a decrease in the number of the oxygenated groups and defects in their structure. The presence of hydroxyl groups on the pristine hollow carbon sphere surface resulted in an enhanced proton conductivity. However, the ammonia sensitivity at high relative humidity in the pristine hollow carbon spheres is negligible due to the inhibition of ammonia adsorption sites by the high concentration of water molecules. The sensor response was investigated by varying both ammonia concentration and relative humidity, determining the topology of the response as a function of these two variables, and applying a tristimulus analysis in an attempt to determine the ammonia concentration independently of the relative humidity. This study demonstrates the critical role played by humidity and surface chemistry in the ammonia sensing properties of hollow carbon spheres. The studies reveal the day to day application of ammonia sensors, with temperature and humidity playing a critical role in the carbon based sensor response and recovery of the materials. These carbon based sensors that simultaneously measure ammonia and relative humidity could be applied in agricultural industries to monitor ammonia concentration in soils, fishponds and in food industries to monitor meat spoilage.

DEDICATION

I would like to dedicate this thesis to;

My parents: Festus Kanake Mutuma and Eunice Ncororo Mutuma for their outmost trust, motivation and inspiration to give my best in everything I do.

My siblings: Lilian, Fanny, Evelyne, Walter, Emily, Ian and Sylvia for their prayers, immense support and encouragement.

My fiancé and love of my life Thommas Mutemi for his encouragement, love and motivation throughout the years.

"And we know that in all things God works for the good of those who love him, who have been called according to his purpose" Romans 8:28

ACKNOWLEDGEMENTS

First and foremost, I would like to thank the Almighty God for giving me the courage, strength and His endless Grace to accomplish this task. I would like to extend my sincere gratitude to my supervisor Professor Neil J. Coville for his outstanding contribution, support and guidance to the success of this research. His prowess and research expertise were of great significance to my skills and am greatly indebted to him as my mentor.

I would like to express my great appreciation to my co-supervisor Dr. Daniel Wamwangi for his guidance and great support in accomplishing this task.

I would like to sincerely thank my mentor Dr. Kamalakannan Ranganathan for his support and fruitful discussions in this work. I am greatly indebted to Boitumelo Matsoso for her contribution, support and positive criticism throughout this research project.

This research would not be complete without the research facilities provided in the School of Physics, University of Witwatersrand. Special thanks to the Thin film laboratory experts (Dr. Daniel Wamwangi, Dr. Kamala Ranganathan, and Mr. Gerrard Peter) for providing solar cell instrument and guidance during this task. Special thanks to Dr. Rudolph Erasmus for providing the ultraviolet-visible (UV-vis) spectroscopy facility and for the Raman and luminescence spectroscopy analysis. I also thank Professor Jonathan Keartland for the assistance with electron spin resonance analysis. I also acknowledge Ms. Joyce Gama for the UV-vis spectroscopy facility in the School of Chemistry.

Sincere gratitude to Ms. Amanda Morgan, Mrs. Colleen Coutts and the late Mrs. Agnes Pointeer for their great assistance in accommodation and travel arrangements during the course of my studies. I never missed a flight; the early check-ins and long waiting hours in the airport were worth it!

I would like to acknowledge the technical support and training by the Microscopy and Microanalysis unit at the University of Witwatersrand. Special thanks to Prof. Alexander Ziegler, Dr. Deran Reddy, Dr. Manoko Maubane, Dr. Zikhona Tetana, Mr. Jacques Gerber and Mrs. Tutuzwa Zuma for their patience and help.

I would like to thank the CATOMAT group members for their positive criticism, valuable suggestions and for providing an encouraging and thrilling working environment. I also thank Baloyi whom I co-supervised in his honour's project. The work done with him contributed a small part of this thesis.

I thank Professor Ivo A. Hummelgen from the Department of Physics in the Federal University of Parana (UFPR), Curitiba, Brazil for hosting me in his laboratory for two and a half months. His guidance and research prowess positively influenced my academic life. Sincere thanks to the group of organic optoelectronic (GOOD) members especially Rafael Rodrigues for the collaborative work in chemical sensors.

This research would not be possible without the financial assistance of National Research Foundation (NRF) grant holder linked funding and funding from the DST-NRF Centre of Excellence in Strong Materials. I also wish to thank the CNPq, ARI-UFPR and IBSA (India-Brazil and South Africa) for the doctoral internship fellowship in Brazil.

Finally, I express gratitude to my family and fiancé for being supportive throughout my studies and wishing me well in my endeavours.

"And we know that in all things God works for the good of those who love him, who have been called according to his purpose" Romans 8:28.

PUBLICATIONS, PRESENTATIONS AND AWARDS

Publications arising from this work

- **Bridget K. Mutuma**, Boitumelo Matsoso, Kamalakannan Ranganathan, Daniel Wamwangi and Neil J. Coville "Generation of open-ended, worm-like and graphene-like structures from layered spherical carbon materials" **RSC. Adv., 2016, 6, 20399.**

- Francis Otieno, **Bridget K. Mutuma**, Kamalakannan Ranganathan, Mildred Airo, Rudolph Erasmus, Neil J. Coville, Daniel Wamwangi "Enhanced Organic Photovoltaic Device Performance by Solution Heat Treatment**", Thin solid films, 2016 (under review).**

- **Bridget K. Mutuma**, Rafael Rodrigues, Boitumelo Matsoso, Kamalakannan Ranganathan, Daniel Wamwangi, Ivo A. Hümmelgen and Neil J. Coville "Hollow carbon spheres and hollow carbon sphere/polyvinylpyrrolidone composites as ammonia sensors", **(submitted).**

- Andrew M. Hank, Hu Li, **Bridget K. Mutuma**, Klaus Leifer, Iakovos Sigalas, Neil J. Coville and Cuthbert Nyamupangedengu "The criticality of filler loading in nanodielectric C/Epoxy. Part 1:AFM and Rheology analysis", **(to be submitted)**

- **Bridget K. Mutuma**, Boitumelo Matsoso, Kamalakannan Ranganathan, Daniel Wamwangi and Neil J. Coville "The incorporation of asymmetric gold nanostructures into the hole transport layer, PEDOT:PSS in Organic Photovoltaic Devices" **(to be submitted).**

- **Bridget K. Mutuma**, Boitumelo Matsoso, Kamalakannan Ranganathan, Daniel Wamwangi and Neil J. Coville "Novel synthesis of broken, deformed and bubble-like Hollow carbon nanostructures from SiO_2@polyvilypyrrolidone sphere templates" **(to be submitted).**

- **Bridget K. Mutuma**, Boitumelo Matsoso, Kamalakannan Ranganathan, Daniel Wamwangi, Jonathan Keartland and Neil J. Coville "Paramagnetic, thermal and surface area properties of annealed solid carbon spheres produced by a vertically oriented CVD reactor" **(to be submitted).**

- **Bridget K. Mutuma,** Boitumelo Matsoso, Kamalakannan Ranganathan, Daniel Wamwangi and Neil J. Coville "Synthesis of open Hollow carbon nanostructures from PVP functionalized mesoporous SiO_2 spheres", **(to be submitted).**

Other publications

- **Bridget K. Mutuma**, Godlisten N. Shao, Won Duck Kim, Hee Taik Kim, "Sol–gel synthesis of mesoporous anatase–brookite and anatase–brookite–rutile TiO_2 nanoparticles and their photocatalytic properties", **Journal of Colloid and Interface Science, Volume 442, 15 March 2015, Pages 1-7.**

- Boitumelo Matsoso, **Bridget K Mutuma**, Kamalakannan Ranganathan, Tsenolo Lerotholi, Glenn Jones and Neil J. Coville "Synthesis of *h*-BN nanodots embedded-graphene hybrid films by atmospheric pressure CVD (APCVD)", **(to be submitted).**

- Kamalakannan Ranganathan, Boitumelo Matsoso, **Bridget K. Mutuma**, Neil J. Coville and Daniel Wamwangi "The study of organic photovoltaics with illumination intensity", **(to be submitted)**.
- Boitumelo Matsoso, Kamalakannan Ranganathan, **Bridget K. Mutuma**, Tsenolo Lerotholi, Glenn Jones and Neil J Coville "Time-dependent evolution of the nitrogen configuration in N-doped graphene films", *RSC Advances, 2016* ***(Accepted manuscript).***

Presentations

- "Comparative investigation of the photocatalytic properties of anatase-brookite and anatase-rutile TiO_2 nanoparticles" Poster presentation. NanoAfrica 2014 International Conference. Vaalberjipark, South Africa. 30th March - 2nd April 2014.

- "Synthesis of Gold nanoparticles and Au@Hollow Carbon Spheres for Applications in Organic Solar Cells" Oral Presentation. Catalysis Society of South Africa (CATSA) Annual conference. Johannesburg, South Africa. 9th - 12th November 2014.

- "Synthesis of Asymmetric Gold Nanostructures for Applications in Organic Photovoltaic Devices" Poster Presentation. Centre of excellence in Strong Materials (CoE-SM) Annual Workshop. Johannesburg, South Africa. 12th May 2015.

- "Synthesis and Characterization of Hollow Carbon Spheres as Electron Acceptors for Applications in Organic Photovoltaic devices" Poster Presentation. SACI Inorganic Conference. Grahamstown, South Africa. 28th June - 02nd July 2015.

- "Synthesis and Characterization of Au nanoparticles and Au@Hollow Carbon Spheres for Application in Organic Solar Cells" Poster Presentation. Carbon 2015 Conference. Dresden, Germany. 12th July - 17th July 2015.

- "Generation of open ended, worm like and graphene like structures from layered spherical carbon materials" Oral Presentation. 3rd International Nanocarbon Workshop. iThemba labs Witwatersrand University, Johannesburg, South Africa. 14th - 15th January 2016.

- "Synthesis of layered graphene like structures from spherical carbon materials" Oral presentation. 7th Wits Cross faculty Symposium. Wits professional hub, Johannesburg, South Africa. 1st - 2nd March 2016.

- "Generation of open ended, worm-like and graphene-like structures from spherical carbon materials" Oral presentation. 6th International Conference in Nanoscience and Nanotechnology (NanoAfrica). University of South Africa (UNISA), Florida Campus, South Africa. 03rd - 6th April 2016.

- "A Novel Synthesis Route of Broken, Deformed and Bubble-like Hollow Carbon Nanostructures from SiO_2@Polyvinylpyrrolidone Spheres as Templates" Poster Presentation. Centre of excellence in Strong Materials (CoE-SM) Annual Workshop. University of Witwatersrand, Johannesburg, South Africa. 26th May 2016.

- "Carbon spheres as photocatalysts for hydrogen generation" Poster presentation. 3rd International Symposium on Catalysis for Clean Energy and Sustainable Chemistry 2016. Madrid, Spain. 7th - 9th September 2016.

Awards

- Postgraduate Merit Award **(February 2014 – December 2015)** University of Witwatersrand.
- Travel Grant Award worth R10, 000 **(June 2015)** University of Witwatersrand.
- Penny Huddle Memorial Award for the Best Undergraduate student teaching assistant **(2015)** University of Witwatersrand.
- Won 3rd Prize Oral Presentation in the Faculty of Science **(1st - 3rd March 2016).** 7th Wits Cross faculty Symposium. Professional Hub, University of Witwatersrand.
- Won 1st Prize Oral presentation PhD category **(3rd – 6th April 2016).** International Conference in Nanoscience and Nanotechnology (NanoAfrica). University of South Africa (UNISA), Florida Campus.

Research Visits

- Visiting student at Federal University of Parana, Curitiba Brazil in Prof Ivo. A. Hummelgen optoelectronics laboratory. **May - July 2016.**

TABLE OF CONTENTS

CHAPTER 3

CHAPTER 4

CHAPTER 5

CHAPTER 8

CHAPTER 9

LIST OF FIGURES

Chapter 2

Chapter 3

Chapter 4

Chapter 5

Chapter 6

Chapter 7

Chapter 8

Chapter 9

LIST OF TABLES

Chapter 3

Chapter 4

Chapter 5

Chapter 6

Chapter 7

Chapter 8

Chapter 9

Appendix A: Supplementary Information

List of Figures

List of Tables

Appendix B: Supplementary Information

List of Figures

ABBREVIATIONS

AFM	Atomic force microscopy
Au@SiO_2	Gold encapsulated inside silica
Au@HCS	Gold encapsulated inside a hollow carbon sphere
BJH	Barett-Joyner- Halenda
BET	Brunner-Emmet-Teller
BHJ	Bulk heterojunction
CNTs	Carbon nanotubes
CTAB	Hexadecyltrimethylammonium bromide
C_{18}TMS	Octadecyltrimethoxysilane
CVD	Chemical vapor deposition
DSSCs	Dye-sensitized solar cells
ESR	Electron spin resonance
FTIR	Fourier transform infrared spectroscopy
FWHM	Full width half maxima
HC	Hollow carbon
HCSs	Hollow carbon spheres
HF	Hydroflouric acid
HOMO	Highest occupied molecular orbital
ICP-OES	Inductively coupled plasma optical emission spectroscopy
ITO	Indium tin oxide
J_{max}	Current density at maximum power
J_{SC}	Current density
LUMO	Lowest unoccupied molecular orbital
OPV	Organic photovoltaic device
PCE	Power conversion efficiency
PCBM	[6,6]-phenyl-C61-butyric acid methyl ester
PEDOT:PSS	Poly(3,4-ethylenedioxylenethiophene):poly(styrenesulfonic acid)
P3HT	Poly(3-hexyl-thiophene-2,5-diyl)
PL	Photoluminescence spectroscopy

P_{max}	Maximum power
PPV	Poly(p-phenylene vinylene)
PVP	Polyvinylpyrrolidone
RH	Relative humidity
R_s	Series resistance
R_{sh}	Shunt resistance
sccm	Standard cubic centimetres per minute
SEM	Scanning electron microscopy
SERS	Surface enhanced Raman spectroscopy
SiO_2@PVP	Silica encapsulated inside polyvinylpyrrolidone
SPR	Surface plasmon resonance
TEM	Transmission electron microscopy
TEOS	Tetraethylorthosilicate
V_{max}	Voltage at maximum power
V_{OC}	Open circuit voltage
WORMs	Write once read many times memory devices

CHAPTER 1

Synopsis

1.1 Motivation of study

Carbon based nanomaterials continue to receive widespread research interest due to their diverse applications in catalysis, fuel cells, solar cells and supercapacitors[1-6]. This results from the ease of availability, the low cost and the wide range of synthesis techniques available for making carbon based nanomaterials. Among the numerous techniques available for synthesis of carbon nanomaterials, the chemical vapor deposition method provides high quality and reproducible carbon nanomaterials using readily available sources[7]. Also, the CVD method offers the advantages of the ability to vary the reaction conditions that affect the morphology, particle size and yield of generated carbon nanomaterials. In addition, the type of carrier gas does affect their thermal and structural properties of carbon based nanomaterials. For instance, hydrogen can etch graphene domains resulting in controlled graphene edges that are applicable in semiconductor industry[8]. Another factor that can affect the electronic properties of carbon based materials is their degree of graphitization. It is well known that diamond and silicon carbide can be graphitized by annealing at higher temperatures[9]. Likewise, carbon spheres can be made more graphitic by annealing at high temperatures. Consequently, their electrical and structural properties can be improved. Thus, studies on the synthesis and annealing of carbon spheres in different carrier gases are quite relevant to their applicability in electronic and magnetic devices. *Then the numerous questions arise: is it possible to simultaneously vary the paramagnetic, thermal and electronic properties of solid carbon spheres by annealing? What is the role of the annealing gas in varying the solid carbon sphere structure? How can the electronic and magnetic properties of these carbon spheres be enhanced?*

Colloidal particles are interesting nanomaterials that have obtained tremendous interest by researchers owing to their electronic, optical and structural properties[10]. These colloidal particles include titania and silica and other metals and metal oxides. The ease of surface modification of SiO_2 with polymers or other metal oxides has led to their vast application in drug delivery systems[11], water treatment[12] and photocatalysis[13]. More recently; the synthesis

of hollow carbon spheres (HCSs) via a templating method using silica spheres has been reported[14]. In addition, SiO_2@PVP (PVP = polyvinylpyrrolidone) composites can be easily modified with fluorophores or other conductive materials suitable for electronic applications[15]. However, the use of SiO_2@PVP materials as templates for the generation of hollow carbon nanostructures has not yet been reported. *Thus, we seek to investigate the possible effects of varying the hollow carbon structural morphology on the surface area, thermal stability and degree of graphitization of the HC nanostructures.*

There is a growing world energy demand for electricity and power consumption. These have led to depletion of fossil fuels and their reserves. Added to these concerns are the deleterious effects that follow the use of fossil fuels on the environment. Solar energy is a renewable energy source that is clean, non-toxic and environmental friendly. At present, most of the solar conversion devices used are made of silicon and other inorganic semiconducting crystals which are expensive to fabricate[16]. Organic photovoltaic devices (OPVs) are solution processable, low cost and can be synthesized at room temperatures[17]. To try and circumvent the high cost of silicon based solar cells, carbon nanomaterials (graphene, reduced graphene oxide and carbon nanotubes) have been applied in OPVs[18]. Also, these carbon nanomaterials due to their electronic properties have been highly employed in chemical sensors[19]. On the other hand, carbon materials such as HCSs have been intensively used as catalysts supports[20] and in supercapacitors[21]. However, the application of the HCSs and Au@HCSs in electronic devices such as solar cells and chemical sensors is still unexplored. *Can these HCSs and Au@HCSs be used for study in solar cells and sensors? What are their limitations and suitability in day to day applications?*

However, their carbon based OPV perfomance and stability are quite low[22] and thus, it is agreeable that silicon cannot be completely replaced by the carbon based materials. In our second approach, colloidal asymmetric gold nanostructures were incorporated into the OPV solar cell. The main intention was to study the challenges faced in device fabrication when using solution processed gold and to report on the enhancement of optical absorption to improve power conversion efficiency (PCE) of the device. Also, in this regard, a strategy of solution heat treatment of the active layer materials was used to optimize nanoscale morphology and subsequently the OPV performance.

1.2 Aim and objectives of this study

1. Synthesis and characterization of pristine, annealed and N-doped carbon spheres in a vertically oriented CVD reactor using acetylene, argon or hydrogen gases as carbon and carrier gases respectively. The effect of varying the carrier gas and flow rate on the carbon spheres will be investigated. The properties of annealed and N-doped carbon spheres will be compared with the pristine carbon spheres.

2. Synthesis and characterization of pristine and mesoporous SiO_2 spheres and their respective hollow carbon nanostructures (HCSs). The effect of varying the SiO_2 precursor, solvent and catalyst molar ratio on the SiO_2 sphere sizes will be determined. The use of pristine SiO_2, mesoporous SiO_2 and mesoporous SiO_2@PVP spheres as templates for the synthesis of hollow carbon nanostructures will be studied.

3. Synthesis and characterization of broken, deformed and bubble-like hollow carbon nanostructures from SiO_2@Polyvinylpyrolidone spheres for use as templates. The role of SiO_2 size dispersity on the properties of hollow carbon nanostructures will be investigated. The effect of polyvinylpyrrolidone surface modified SiO_2 spheres as templates on the morphology of the hollow carbon nanostructures will be determined. The pristine SiO_2 and SiO_2@PVP spheres will be carbonized using varying carbonization times and their effects on obtained hollow carbon nanostructures studied.

4. Synthesis and characterization of open ended, worm-like and graphene-like structures from layered spherical carbon materials. The effect of SiO_2 template size dispersity in Au@SiO_2 spheres for the synthesis of hollow carbon nanostructures will be investigated. The Au@HCSs will be applied in organic photovoltaic devices as a component of the active layer.

5. Synthesis and characterization of gold nanospheres and nanorods for application in organic photovoltaic devices. The effect of incorporating Au nanospheres and Au nanorods into the hole transport layer (PEDOT:PSS) in the organic photovoltaic device on its performance will be investigated.

6. The role of nanoscale morphology modification on the efficiency of OPV through increased donor and acceptor interface and exciton dissociation is established through P3HT:PCBM solution heat treatment. The effect of P3HT pre-heat treatment and P3HT:PCBM blend heat treatment on the current-voltage properties of OPV will be investigated.

7. The application of pristine HCSs and HCSs-polyvinylpyrrolidone composite in relative humidity and ammonia sensors. The effect of annealing the HCSs on their ammonia response and sensitivity will be investigated.

1.3 Organization of the thesis

Chapter 1 gives the motivation of study, aims and objectives of this thesis.

Chapter 2 presents a brief background on solar energy, organic photovoltaic devices, carbon based nanomaterials and their synthesis, hollow carbon nanostructures, yolk shell nanostructures and their application in organic photovoltaic devices and chemical sensors.

Chapter 3 presents the study on the "Synthesis and characterization of pristine, annealed and N-doped carbon spheres by a vertically oriented CVD reactor."

Chapter 4 describes the synthesis, results and discussion on work done on the "Synthesis and characterization of pristine and mesoporous SiO_2 spheres and their respective hollow carbon nanostructures (HCSs)."

Chapter 5 presents an extensive study on "A novel synthesis route of broken, deformed and bubble-like hollow carbon nanostructures from SiO_2@Polyvinylpyrolidone spheres as templates."

Chapter 6 gives the synthesis, results and discussion on the "Generation of open ended, worm-like and graphene-like structures from layered spherical carbon materials." This study has been published in the **RSC Advances, 2016, 6, 20399.**

Chapter 7 reports on the "Synthesis and characterization of gold nanospheres and nanorods for application in organic photovoltaic devices".

Chapter 8 gives a detailed study on the "Improvement of an organic photovoltaic device performance by P3HT:PCBM solution heat treatment." This work is under review in the **Journal of Thin Solid Films**. This work was done as a **50:50** collaboration between the School of Chemistry and School of Physics with equal contribution from the first two authors. I was responsible for introduction section, Raman, FTIR, PL measurements and

discussion. The UV-Vis, AFM and I-V measurements were jointly done and discussed by me and Mr. F. Otieno.

Chapter 9 reports on the "Sensing ammonia vapours in a humid environment using hollow carbon spheres and hollow carbon sphere-polyvinylpyrrolidone composites"

Chapter 10 gives the general conclusions and future prospects that emanated from the study.

References

1. Shao, Y.; Sui, J.; Yin, G.; Gao, Y. *Applied Catalysis B: Environmental* **2008,** 79, (1), 89-99.
2. Hulicova, D.; Kodama, M.; Hatori, H. *Chemistry of Materials* **2006,** 18, (9), 2318-2326.
3. Aitola, K.; Sveinbjornsson, K.; Correa-Baena, J.-P.; Kaskela, A.; Abate, A.; Tian, Y.; Johansson, E. M. J.; Gratzel, M.; Kauppinen, E. I.; Hagfeldt, A.; Boschloo, G. *Energy & Environmental Science* **2016,** 9, (2), 461-466.
4. Wang, F.; Kozawa, D.; Miyauchi, Y.; Hiraoka, K.; Mouri, S.; Ohno, Y.; Matsuda, K. *Nat Commun* **2015,** 6.
5. Yu, X.; Yang, L.; Lv, Q.; Xu, M.; Chen, H.; Yang, D. *Nanoscale* **2015,** 7, (16), 7072-7077.
6. Ravat, V.; Nongwe, I.; Coville, N. J. *ChemCatChem* **2012,** 4, (12), 1930-1934.
7. Creighton, J.; Ho, P. *Chemical Vapor Deposition* **2001,** 2, 1-22.
8. Yang, R.; Zhang, L.; Wang, Y.; Shi, Z.; Shi, D.; Gao, H.; Wang, E.; Zhang, G. *Advanced Materials* **2010,** 22, (36), 4014-4019.
9. Bródka, A.; Zerda, T.; Burian, A. *Diamond and Related Materials* **2006,** 15, (11), 1818-1821.
10. Lohse, S. E.; Murphy, C. J. *Journal of the American Chemical Society* **2012,** 134, (38), 15607-15620.
11. Slowing, I. I.; Trewyn, B. G.; Giri, S.; Lin, V. Y. *Advanced Functional Materials* **2007,** 17, (8), 1225-1236.
12. Sayari, A.; Hamoudi, S.; Yang, Y. *Chemistry of Materials* **2005,** 17, (1), 212-216.
13. Kim, Y. N.; Shao, G. N.; Jeon, S. J.; Imran, S.; Sarawade, P. B.; Kim, H. T. *Chemical Eengineering Journal* **2013,** 231, 502-511.
14. Liu, R.; Mahurin, S. M.; Li, C.; Unocic, R. R.; Idrobo, J. C.; Gao, H.; Pennycook, S. J.; Dai, S. *Angewandte Chemie International Edition* **2011,** 50, (30), 6799-6802.
15. Lu, Y.; Yang, W.; Yin, M. *Industrial & Engineering Chemistry Research* **2014,** 53, (8), 2872-2877.
16. Abdulrazzaq, O. A.; Saini, V.; Bourdo, S.; Dervishi, E.; Biris, A. S. *Particulate Science and Technology* **2013,** 31, (5), 427-442.
17. Günes, S.; Sariciftci, N. S. *Inorganica Chimica Acta* **2008,** 361, (3), 581-588.
18. Ramuz, M. P.; Vosgueritchian, M.; Wei, P.; Wang, C.; Gao, Y.; Wu, Y.; Chen, Y.; Bao, Z. *ACS Nano* **2012,** 6, (11), 10384-10395.
19. Bekyarova, E.; Davis, M.; Burch, T.; Itkis, M.; Zhao, B.; Sunshine, S.; Haddon, R. *The Journal of Physical Chemistry B* **2004,** 108, (51), 19717-19720.
20. Ravat, V.; Nongwe, I.; Coville, N. J. *ChemCatChem* **2012,** 4, (12), 1930-1934.
21. Chen, X.; Kierzek, K.; Wenelska, K.; Cendrowski, K.; Gong, J.; Wen, X.; Tang, T.; Chu, P. K.; Mijowska, E. *Chemistry–An Asian Journal* **2013,** 8, (11), 2627-2633.
22. Bernardi, M.; Giulianini, M.; Grossman, J. C. *ACS Nano* **2010,** 4, (11), 6599-6606.

CHAPTER 2

Literature Review

2.1 Background

Global warming is a major world problem that results from the high usage of fossil fuels. The use of these diminishing energy sources has brought deleterious environment consequences due to increased emission of greenhouse gases. Renewable energy, which contributes to nearly half of the electricity demand, is projected to grow by 77% by 2035 according to the World Energy Outlook 2013[1]. This is against the backdrop of increasing demands. The recent energy report has adduced an increase in energy demand of 26% between 2000 and 2010 and the expected energy demand growth to 2040 is predicted to be 37%[2]. Renewable energy sources; biomass, wind, hydropower and solar are currently the most sustainable energy resources available. However, over recent years, the increase in the production of oil and fossil fuel has stimulated demand for this resource with severe consequences to the environment. Arising from it was the enacted policy to address the concerns of climate change. Some of the environmental measures that have been undertaken include the construction of dam reservoirs for hydropower generation which occupies a vast amount of land thus causing social, economic and environmental cost. In contrast, the wind and solar energy have less direct social, and environmental effects and are deemed as more reliable energy sources for the future. This is due to their lower cost and ease of availability relative to other energy sources. The conversion and storage of the solar energy into useful energy is thus, an alternative source of energy that can mitigate global warming and aid in meriting the deficit in the global energy supply.

2.1.1 Solar energy

The sun delivers on average 120,000 terawatts (TW) of power to earth which is equivalent to 4000 times the projected world energy demand of 26 to 32.9 TW predicted to be required by humankind by 2050[3]. Most of the chemical and physical reactions on earth's surface such as air circulation and photosynthesis result from either direct or indirect solar radiation[4, 5]. More so, solar energy is an exemplary inexhaustible, noise and pollution free fuel source that can mitigate global warming. Solar energy can be generated by a photovoltaic effect or by use of a solar concentrator[6, 7]. Solar conversion devices can be applied either on a small scale level

such as in photovoltaic cells or as solar cells arrayed on an extensive scale such as in solar panels. Various types of solar cells have been developed using different materials[8-14]:

- First generation (monocrystalline silicon)
- Second generation (amorphous silicon, cadmium telluride (CdTe) and cadmium indium gallium (di)selenide (CIGS))
- Third generation (dye-sensitized solar cells (DSSC), nanocrystals, quantum dots, organic polymers, small molecules and perovskites solar cells)
- Fourth generation (inorganic-organic hybrid materials)

At present, the silicon based photovoltaics exhibit high electron mobilities and high power conversion efficiency (PCE). However, their high production costs are prohibitive to their widespread roll out and sustainability. In contrast, organic based solar devices are low-temperature solution processable devices that could be used as alternatives to silicon based devices provided they fulfil the performance benchmarks. Indeed, the materials have been researched on due to low cost per weight. Thus, there is widespread interest in the fabrication of organic based devices for solar energy conversion processes[15, 16].

2.1.2 Photovoltaic devices

2.1.2.1 Characteristics of a photovoltaic device

A photovoltaic device is characterized by the dark and illuminated current-voltage measurements as illustrated in Fig. 2.1.

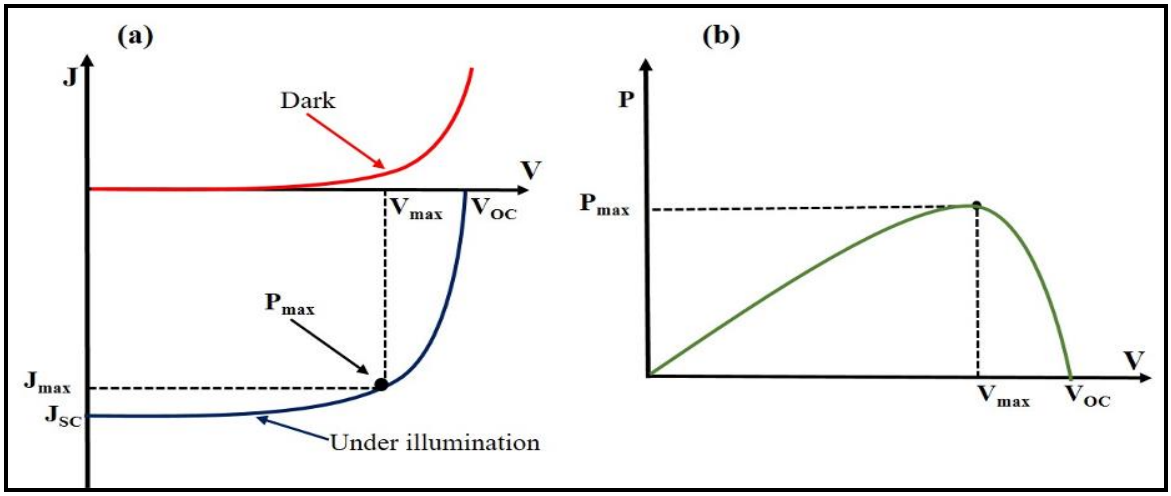

Figure 2.1. The characteristics of a photovoltaic cell (a) current-voltage in the dark and under illumination and (b) the maximum power.

These parameters include;

Short Circuit Current Density (J_{SC}): This is the current density generated by the solar cell under illumination in the absence of a load potential. It is proportional to the effective area of a solar device and increases with the light intensity. Thus, varying the thickness or light absorption properties of the solar cell terminals, builds up a potential difference that accumulates on the terminals. The potential difference produces a current that acts in a reverse direction to the photocurrent leading to a decrease in the short circuit current. This reverse current is referred to as dark current. Considering a solar cell as an ideal diode with an ideality factor of 1, the dark current density is given by;

$$J_{dark}(V) = J_O\left(e^{qV/k_BT} - 1\right) \quad \textbf{(2.1)}$$

where q is the electron charge, V is the voltage across the terminals, J_O is a constant, T is the temperature in degrees Kelvin and k_B is the Boltzmann's constant.

Thus, the overall current of the photovoltaic device is a superposition of the short circuit photocurrent and the dark current as given in equation 2.2.

$$J = J_{SC} - J_O\left(e^{qV/k_BT} - 1\right) \quad \textbf{(2.2)}$$

Open Circuit Voltage (V_{OC}): This is the potential difference between the two terminals of a solar cell under illumination when there is no current flow through the terminal. At V_{OC} the dark current and the short circuit photocurrent cancels out corresponding to a forward bias voltage. Thus the V_{OC} is dependent on the dark current and the generated short circuit current as defined by equation 2.3 below.

$$V_{OC} = \frac{kT}{q}\ln\left(\frac{J_{SC}}{J_O} + 1\right) \quad \textbf{(2.3)}$$

A V_{OC} change is also determined by the energy level difference between the highest occupied molecular orbital (HOMO) of the donor and lowest unoccupied molecular orbital (LUMO) of the acceptor polymer[17, 18]. However, in inorganic semiconductors the V_{OC} is determined by the difference between the valence band (analogous to the HOMO) and conduction band

(analogous to the LUMO) and is highly dependent on the built in equilibrium electrical potential difference required for charge speraration[19].

Fill Factor (FF): This is the proportion of the maximum power delivered to an external load divided by the product of V_{OC} and J_{SC} (Equation 2.1). The maximum power density of a solar cell is obtained between V_O (V = 0) and V_{OC} at a maximum voltage V_{max} and a corresponding maximum current density J_{max}. Hence;

$$FF = \frac{J_{\max} V_{\max}}{J_{SC} V_{OC}} \qquad \textbf{(2.4)}$$

Power Conversion Efficiency (PCE): It is the proportion of the maximum power generated by a solar cell to the power input. This is given by equation 2.5 below;

$$\eta = \frac{JscV_{OC}FF}{P_{in}} \qquad \textbf{(2.5)}$$

where; P_{in} is the power input. The PCE is directly proportional to the J_{SC}, V_{OC} and FF. In real situations, there are limitations for maximum power output through optical losses and interfacial contact related losses. The power losses can result from resistance induced by current or via leakage currents around the sides of the device. The two main parasitic resistances are the series (R_s) and shunt resistance (R_{sh}) as indicated in the equivalent circuit in Fig. 2.2.

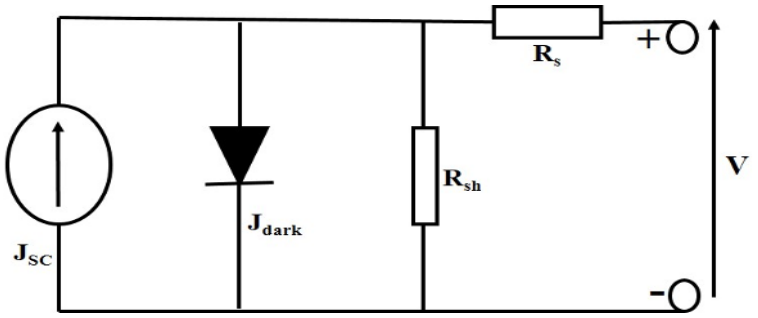

Figure 2.2. The equivalent circuit including the series and shunt resistance.

Series resistance (R_s): This is the resistance that originates from the resistance of the cell material to current flow and the resistive contacts. High series resistance decreases the short circuit current.

Shunt resistance (R_{sh}): This resistance emanates from the leakage of currents between the contacts, around the cell margins and through the device. Low Rsh leads to a decrease in V_{OC}. In the presence of series and shunt resistance, the diode equation becomes;

$$J = J_{SC} - J_O\left(e^{q(V+JAR_s)/kT} - 1\right) - \frac{V + JAR_s}{R_{sh}} \qquad \textbf{(2.6)}$$

Both the series and shunt resistance reduce the fill factor of the OPV device as shown in Fig. 2.3. Thus, a good photovoltaic device should possess a nearly infinite shunt resistance and a low series resistance.

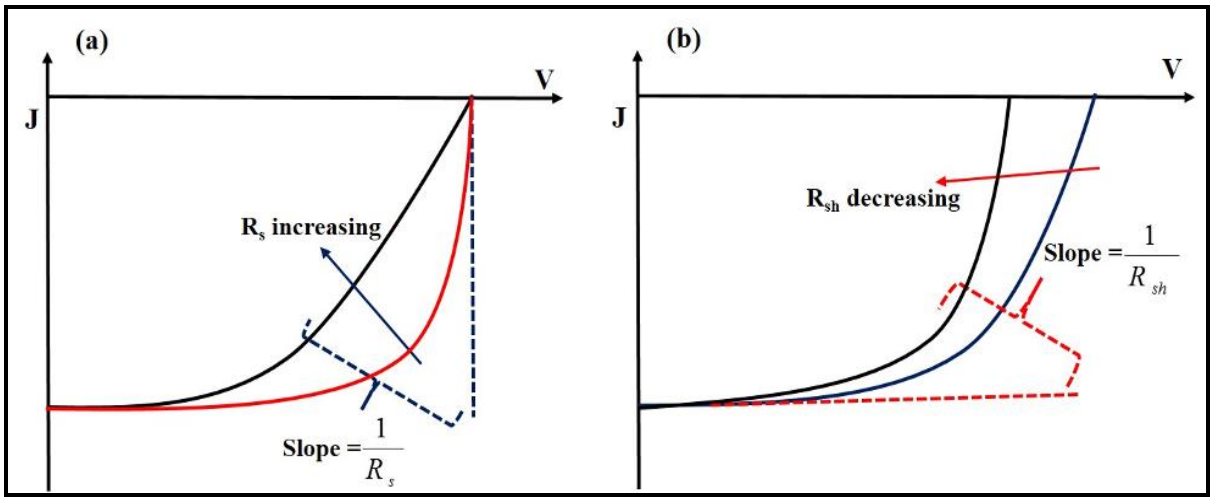

Figure 2.3. The parasitic resistances; (a) series resistance and (b) shunt resistance (modified from ref[20]).

2.1.2.2 Organic photovoltaic devices

Organic photovoltaic devices are solar cells that convert sunlight into electricity using organic semiconductors as active layers[21]. Organic semiconductors are flexible, light weight and have a low sublimation point which makes them easily processable at low temperatures[12]. In addition, the organic semiconductors can comprise of small organic molecules or organic polymers which act as the photon absorption centres referred to as photoactive layer

materials[22]. However, the most widely used device configuration for a bulk heterojunction (BHJ) organic solar cell consists of an active layer (usually a blend of an electron donating and electron accepting polymers) in between a low work function Al cathode and a hole conducting layer PEDOT:PSS (poly(3,4-ethylenedioxylenethiophene):poly(styrenesulfonic acid)) layer coated on an indium tin oxide (ITO) electrode[23].

2.1.2.2.1 The active layer architecture

The active layer produces a strongly bound exciton followed by diffusion and dissociation to give electrons and holes that are transported to the cathode and anode. The nature of the active layer in the device architecture play a significant role in the overall performance of organic photovoltaics. A single layer organic photovoltaic device comprising an organic layer sandwiched between two metallic electrodes with high and low work function was reported in the early 1990's[24, 25]. The short circuit current generated by a photovoltaic device is directly proportional to the active layer area. As a consequence, the larger the active layer thickness, the higher the short circuit current and overall efficiency. However, for optimal absorption of light in organic polymers, a thickness of 100 nm is preferable due to the high absorption coefficient ($>10^{-5}$ cm^{-1}) of the organic compounds. These organic compounds possess a low dielectric constant that results in the production of excitons (electron-hole Coulomb bound pair)[26]. In a single layer architecture, in the absence of an applied voltage, the potential difference is derived by the difference between the metal electrode work functions or the Schottky type potential between one metal and the organic contact[22]. However, this potential difference is not high enough to induce an efficient photogeneration of charges. Hence, charge generation and separation is limited. In addition, the potential depends heavily on the metal electrodes and their contact with the organic layer, making a single layer system highly susceptible to increased series resistance[27]. Consequently, the exciton generated in the organic semiconducting layer after photon absorption can undergo decay through radiative or non-radiative processes limiting the photocurrent efficiency. For instance, Marks and his co-workers' reported a FF of 0.2 and a quantum yield (the ratio of measured short circuit photocurrent to the estimated photon flux incident on a diode) of 0.5% in a 90 nm thick poly(p-phenylene vinylene), PPV, between ITO and Mg as anode and cathode electrodes, respectively[28]. The limiting factors of a single layer OPV are insufficient charge separation, high series resistance, high recombination, causing a low FF and a limited PCE.

To increase the charge carrier separation, Tang *et al.* reported enhanced exciton dissociation by the fabrication of a bilayer heterojunction[29]. He reported on a bilayer OPV cell comprising of copper phthalocyanine (CuPc) a perylene carboxylic derivate (PV) polymer, an ITO anode, Ag cathode with a 0.45 V_{OC}, a 0. 65 FF of and approximately 1% PCE. The heterojunction comprised of a donor and an acceptor material. There are two main types of heterojunctions namely a bilayer and a bulk heterojunction (Fig. 2.4). In a bilayer heterojunction, the donor and acceptor layers are in close contact at the interface to promote the photovoltaic effect. These bilayers are then sandwiched between two electrodes to create an ohmic contact and extract charge carriers. Bilayer heterojunctions are limited by the number of excitons generated which is dependent on the number of photons that can be absorbed and on the type of donor or acceptor materials used. The charge transfer in a bilayer heterojunction is governed by the difference in ionization potential of the two layers. In a bilayer OPV cell, the charge photogeneration is independent of the electric field which subsequently lowers the series resistance resulting in higher FF values compared to a single layer. However, a charge transport in each layer is a diffusion dependent process that makes it poor due to the presence of charge traps and possible recombination thus, limiting the J-V characteristics of these bilayer OPV systems.

In a bulk heterojunction (BHJ) both the donor and acceptor layers are mixed in situ such that there is a phase separation and a percolation pathway formed in the heterojunction allowing faster exciton diffusion and dissociation[30, 31]. In addition, the interpenetrating network of the donor and acceptor polymer increases the active interfacial area which further reduces the series resistance and facilitates faster charge transport. The nanoscale morphology plays a role in enhancing the ultrafast charge carrier separation and charge transport and thus, minimizing possible recombination processes. Photoluminescence quenching can determine the reduction in recombination in the BHJ active layer composite; whereby the dissociation is favored over recombination[32]. In summary, a BHJ offers added advantages such as;

- No electric field dependence of the charge photogeneration
- Faster charge generation and separation resulting to an increased J_{SC}
- Increased active interfacial area
- Reduced series resistance and high shunt resistance
- Increased FF and PCE

Shaheen *et. al.* reported a V_{OC} of 0.82 V, FF of 0.61 and a PCE of 2.5% using BHJ active layer based on a composite of poly(2-methy,5-(3*,7** dimethyl-octyloxy))-p-phenylene vinylene (MDMO-PPV) and (6,6)-phenyl C61-butyric acid methyl ester (PCBM)[33]. Padinger *et al.* showed that varying the donor polymer to poly(3-hexyl-thiophene-2,5-diyl) (P3HT) resulted in a PCE of 3.5%[34]. Recent research shows that the best BHJ consists of an active layer comprising of an interpenetrating network of p-type donor and n-type acceptor molecules represented typically by poly(3-hexyl-thiophene-2,5-diyl) (P3HT) and [6,6]-phenyl-C61-butyric acid methyl ester (PCBM) of 200 nm thickness[35], a hole transporting layer, PEDOT:PSS, Al as a cathode and ITO as an anode. Fig. 2.5 shows the architecture of a typical BHJ organic photovoltaic device.

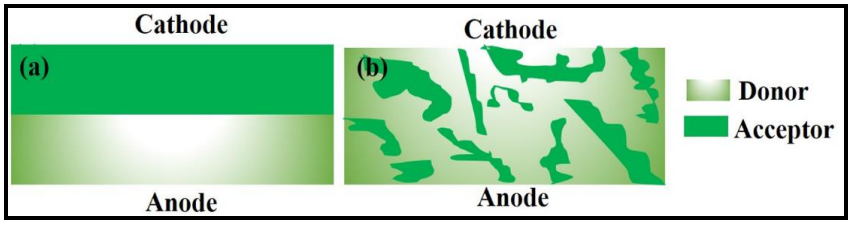

Figure 2.4. A schematic diagram of (a) bilayer heterojunction and (b) bulk heterojunction (modified from ref[36]).

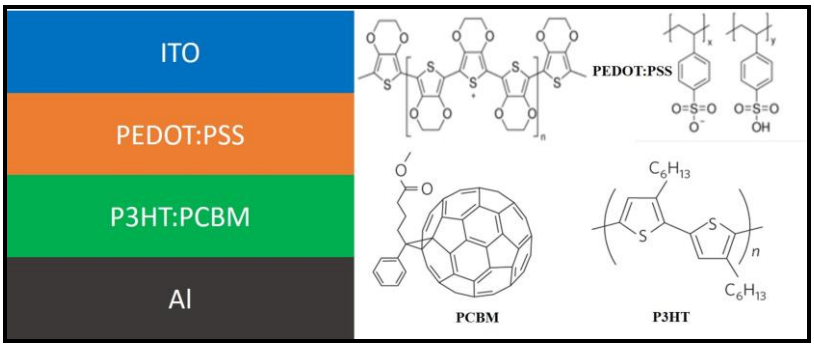

Figure 2.5. A typical organic photovoltaic architecture and the commonly used polymers (summarized from ref[35, 37, 38]).

2.1.2.2.2 Mechanism of operation in an organic photovoltaic cell

The mechanism of charge generation and transport in OPV comprises of four main steps as illustrated in Fig. 2.6. Step **(i)** involves photoabsorption at the donor layer to generate an exciton in the active layer matrix. An exciton is an electrostatically coupled electron-hole pair produced by photon absorption of the delocalized electrons in the HOMO of the donor layer in the organic semiconductors[19]. The absorption coefficient of the active layer should

match the solar irradiation. Thus, light absorption can be enhanced by lowering the optical bandgap of the active layer. Fig. 2.7 illustrates the ionization potential (IP) and the electron affinity, χ difference of the LUMO level of the acceptor and the donor polymer. The interfacial energy bandgap (E_g) of the OPV is calculated as the difference between the HOMO energy level of the donor polymer ($E_{HOMO,donor}$) and the LUMO energy level of the acceptor polymer ($E_{LUMO,acceptor}$) and the exciton binding energy (E_b)[39] as given in equation 2.7. The V_{OC} is determined by the interfacial bandgap and thus, it can be varied by tuning the LUMO energy level of the acceptor polymer.

$$E_g = E_{HOMO,donor} - E_{LUMO,accpetor} - E_b \quad \textbf{(2.7)}$$

In the second step **(ii),** the exciton diffuses to the donor-acceptor interface via a hopping mechanism within the polymer chains. The success of this diffusion is significantly determined by the exciton diffusion length. The diffusion length is dependent on the optical properties and structure of the material. However, excitons exhibit a limited lifetime of a few picoseconds in the organic semiconductor thus, limiting their mobility[40]. Consequently, the distance that the exciton can travel before decaying (known as exciton diffusion length) is less than 20 nm[37, 41]. When the exciton reaches the interface of the active layer, it dissociates into the respective electrons or holes **(step iii).** However, there exist charge carriers recombination processes such as the recombination of two mobile carriers (bimolecular recombination) or the recombination of a mobile carrier with a trapped carrier through a radiative process[42]. Such recombination processes result in insufficient exciton dissociation and transport. Finally, in step **(iv),** the individual charge carriers (electrons and holes) are then transported through the bulk to the electrodes where charge extraction takes place. However, the presence of excitonic losses, radiative and non-radiative recombination, optical losses (resulting from reflection of electrodes) and insufficient charge carrier mobilities suppress the overall J_{SC}, V_{OC} and the PCE of OPVs.

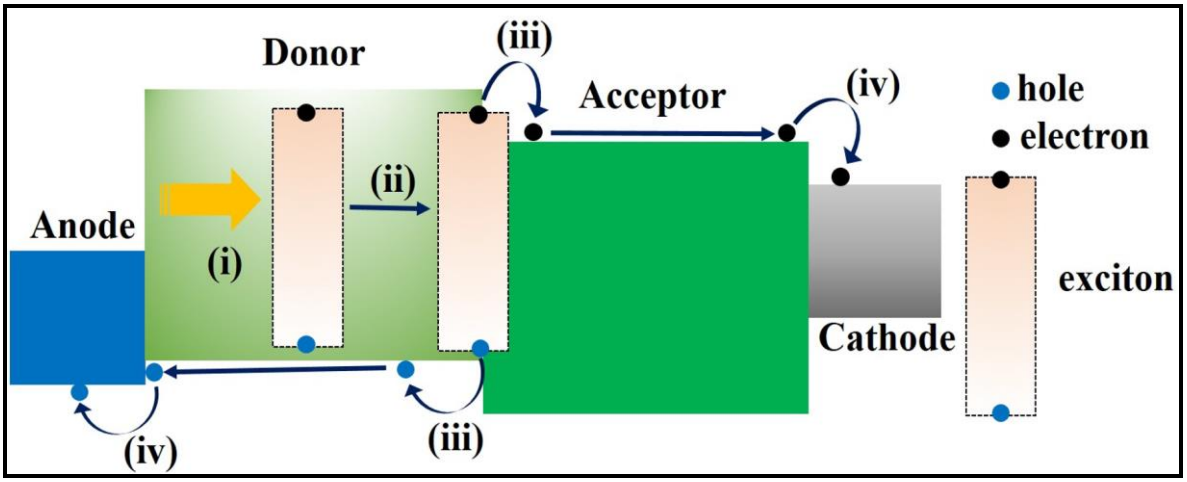

Figure 2.6. A schematic diagram representing the OPV device operation mechanism[43].

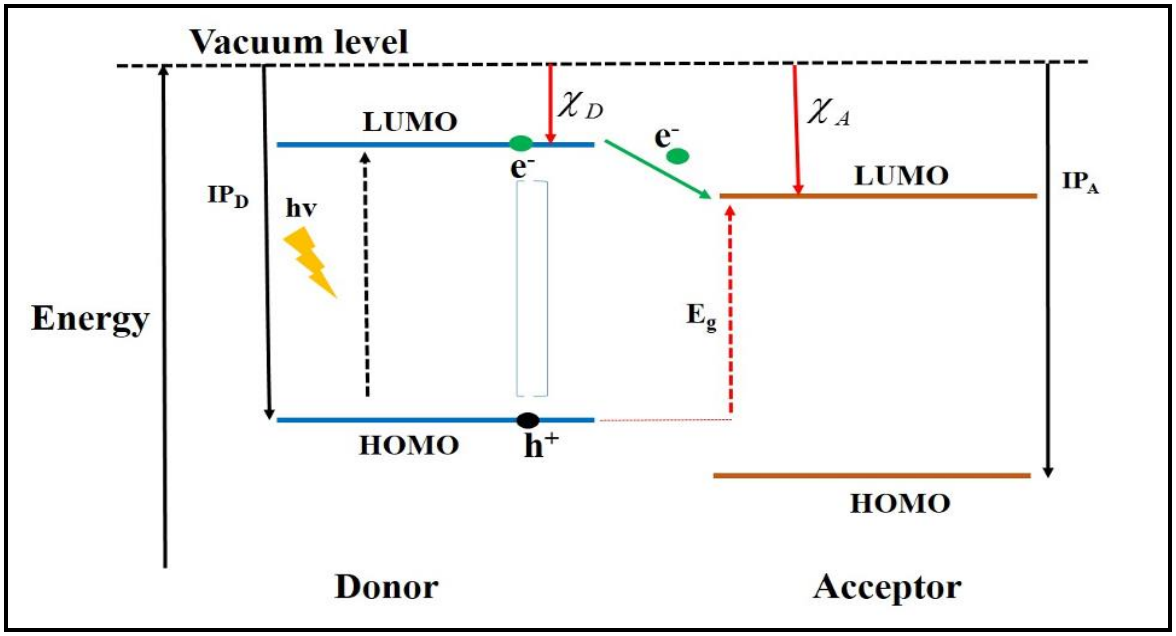

Figure 2.7. Energy level diagram of a typical OPV; with the (IP) as ionization potential and χ as the electron affinity. The subscripts denote the donor and acceptor polymers, respectively. The arrow between the LUMO levels indicates the photoinduced electron transfer after charge carrier generation process (adapted from ref[44]).

2.1.2.3 Improvement of organic photovoltaic device performance

Organic photovoltaic devices portray low electron and hole mobilities that lead to low PCE. Various methods have been used to overcome this problem by incorporating low band gap polymers in the active layer matrix hence increasing the light absorption of the active layer[45]. Also, the use of donor polymers with lower HOMO and acceptor polymers with higher

LUMO has been extensively studied[22, 46-48]. In essence, there has been tremendous interest in the modification of either the anode, the hole transport layer or the active layer to achieve increased photovoltaic performance. Other approaches to achieve charge separation such as heat treatment of P3HT:PCBM to enhance the polymer crystallinity and interchain interactions for an enhanced device performance have been reported[49, 50]. The active layer morphology is crucial in the operation of an organic photovoltaic device. The polymer miscibility and diffusion determine the kinetics of charge dissociation and transport. To this end, BHJ based OPV performance has been enhanced by improving the diffusion and film morphology through thermal annealing and solvent vapor annealing[51-53]. The PCBM diffusion into the P3HT matrix is dependent on the P3HT crystallinity and the prevention of PCBM aggregation can modify the overall charge transport in OPVs (Fig. 2.8). Thus, organic photovoltaic device performance can be improved by correlating the results with the morphological, structural and electrical properties of the different semiconducting materials[54, 55].

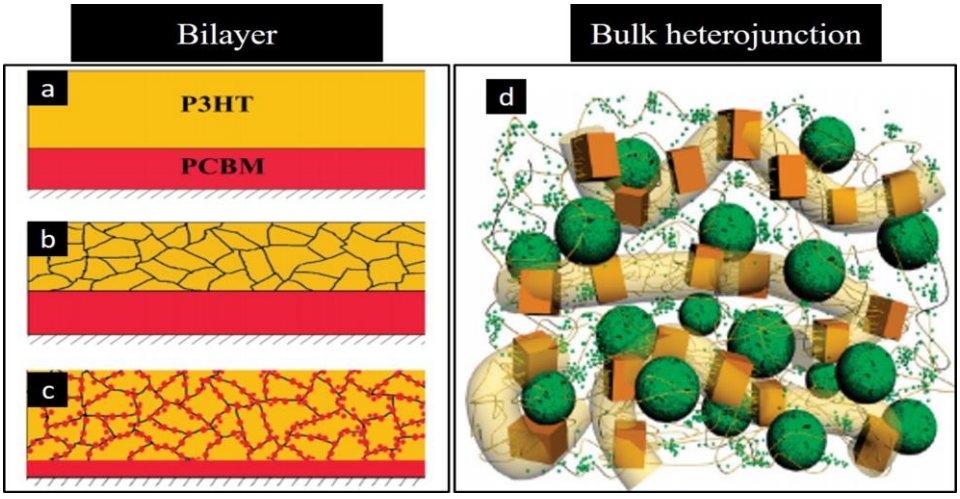

Figure 2.8. A schematic illustration of the diffusion of PCBM into P3HT amorphous domains on thermal annealing; (a) as spun P3HT/PCBM bilayer, (b) P3HT crystallites after thermal annealing and (c) PCBM diffusion into the amorphous domains of P3HT (modified from reference[51]) and (d) shows a thermally annealed bulk heterojunction P3HT:PCBM films; large spheres represents the PCBM aggregates intercalated in the P3HT crystallites (blocks). The thin wire like structures represent amorphous P3HT domains while the small spheres represent the dispersed PCBM molecules (modified from ref[52]).

2.1.3 Carbon based nanomaterials

2.1.3.1 Synthesis of carbon based nanomaterials

Carbon based nanomaterials can be categorized on the basis of their dimensionalities. This includes fullerenes, carbon nanotubes, graphene and graphite as 0-, 1-, 2- and 3-dimensional structures respectively. These materials are prepared mainly by the pyrolysis[56, 57], hydrothermal[58, 59], mechanical or chemical exfoliation[60, 61] and the chemical vapor deposition methods[62, 63]. Among these different synthesis routes, the chemical vapour deposition (CVD) method offers an added advantage of the ability to modulate the carbon morphology and product yield by altering the temperature and gas flow rates.

2.1.3.1.1 Chemical vapour deposition (CVD) method

The CVD method is a chemical process that involves the reaction or decomposition of one or more volatile precursors on a target surface at high temperatures to produce the desired product. The CVD method was reported in the 1890s for the purification and refining of metals such as nickel[64]. The early works of Van Arkel de Boer introduced the use of the high temperature CVD process[65]. The CVD process can be divided into two stages; condensation of the reactant onto the substrate and reaction of the volatile atoms/molecules to form the product. The transport of the gaseous reactant can occur by the application of a pressure change or by use of a carrier gas[66]. For efficient condensation and transport processes, the product should possess a lower vapor pressure and be less volatile than the reactant. The nucleation and growth mechanism of carbon nanomaterials by the CVD method involves the kinetic, thermodynamic and chemical reactions that take place during condensation, transport and evaporation stages[67-69]. Thus, the product properties can be manipulated by controlling the process variables such as temperature, frequency of the plasma source, partial pressures, pressure of the gases used, gas flow rate and reactant composition. As a result, the CVD method can be classified according to pressure (atmospheric, low or ultrahigh vacuum pressure). Often it is classified based on physical characteristics such as the aerosol assisted or direct injection CVD method or according to plasma effects i.e. microwave assisted or plasma enhanced CVD. The great advantages of the CVD method are[70];

- Enhanced versatility in the array of materials that can be obtained
- High quality of the final product
- High reproducibility
- High yield
- Possibility of large scale reaction

It has been used extensively in the semiconductor industry and in the synthesis of carbon and silicon nanostructures such as carbon nanotubes[71, 72], nanofibers[73], diamond[74], graphene[75] and silicon nitride among others[76, 77].

2.1.3.2 Carbon nanotubes

Carbon nanotubes (CNTs) were reported by Ijima[78] in 1991 during a surface study of graphitic electrodes produced using an arc discharge method. Carbon nanotubes exhibit unique strength and other excellent properties such as stiffness, high electron conductivity, high thermal conductivity and high aspect ratio[79, 80]. As a result, the CNTs have been applied in field emission displays[81], nanosensors[82], shipbuilding[83] and in logic circuits among others[84]. However, due to the use of metal catalysts in the preparation of CNTs, they exhibit poor charge transfer and shorting as active layer materials in OPVs due to the difficulty in the removal of the residual catalyst[85]. The CNTs semiconducting or metallic character has led to their application in OPVs in the active layer or as anode or cathode materials[86]. The use of CNTs as electron acceptors with P3HT as donor polymer shows that the OPV device performance due to enhanced charge transport[87, 88]. However, due to the use of metal catalysts in the preparation of CNTs, a high percentage weight of CNTs in the active layer materials exhibit poor charge transfer and shorting in OPVs due to the difficulty in the removal of the residual catalyst[85].

2.1.3.3 Graphene based nanomaterials

Graphene is a transparent and a semi-permeable material with tunable electron transport and work function properties. Due to these properties, graphene was proposed to be a good substitute for the expensive ITO anode in OPVs[89]. More so, the use of graphene as a component of the active layer in OPVs has also been explored. For instance, Gwang *et al.* used N-doped graphene flakes in the active layer of the BHJ organic solar cell (P3HT: PCBM) resulting in a band gap modulation that enhanced the electron transport and led to a higher power conversion efficiency[90]. More recently, graphene quantum dots have been used for the synthesis of ternary graphene-polymer-fullerene blends as bulk heterojunction active layer[91]. The graphene quantum dots enhanced the optical absorption of the active layer and consequently improved the short circuit current and the PCE. However, the performance of an organic photovoltaic device is affected by the film morphology, quality of the device

interface layers and thus, the synthesis of a uniform wrinkle free graphene films are beneficial for OPV applications[92].

2.1.3.4 Hollow carbon nanostructures (HCSs) and yolk shell nanostructures

2.1.3.4.1 Hollow carbon nanostructures

“”These hollow nanostructures can be obtained by two main synthesis routes: a template free route or by a template based strategy[98]. The template free method is a one-step simple synthesis technique that involves ultrasonication and pyrolysis among others[99]. However, it is time consuming to regulate the size, shape and morphology of the obtained hollow nanostructures thus limiting their applications. In contrast, the template based strategy provides advantages such as controlled size, shell diameter, shape, morphology and surface functionalities of the obtained hollow carbon nanostructures[100, 101]. The conversion of a solid core to a hollow core entails surface chemistry, diffusion and growth dynamics which can occur through hard templating, soft templating, self-templating, surface protected etching, Ostwald ripening, a Kirkendall effect and galvanic displacement among others[102-106].

2.1.3.4.1.1 Hard templating approach

Silica and polystyrene spheres are the predominant hard templates employed for fabrication of hollow nanostructures[107]. The hard templates are covered by carbon precursors such as toluene, resorcinol-formaldehyde[108], sucrose[109], glucose[110] and fulfury alcohol[111] to form a carbon precursor/template hybrid material. The carbon precursor is then converted to carbon via high temperature calcination[112]. Lastly, the removal of the hard template by etching using hydrofluoric acid (HF) or sodium hydroxide[113]. Silica sphere template synthesis involves the hydrolysis and condensation reaction pathways that can be controlled to obtain various shaped HCSs. For instance, varying the ammonia catalyst during SiO_2 synthesis in the presence of dopamine can result in HCSs with a single shell, a double shell or a yolk shell structure[114] (Fig. 2.9). These multiple shelled HCSs can further be used to synthesis multiple shelled hollow metal oxides such as TiO_2 and ZnO that enhance light scattering as photoelectrodes in DSSCs[115, 116].

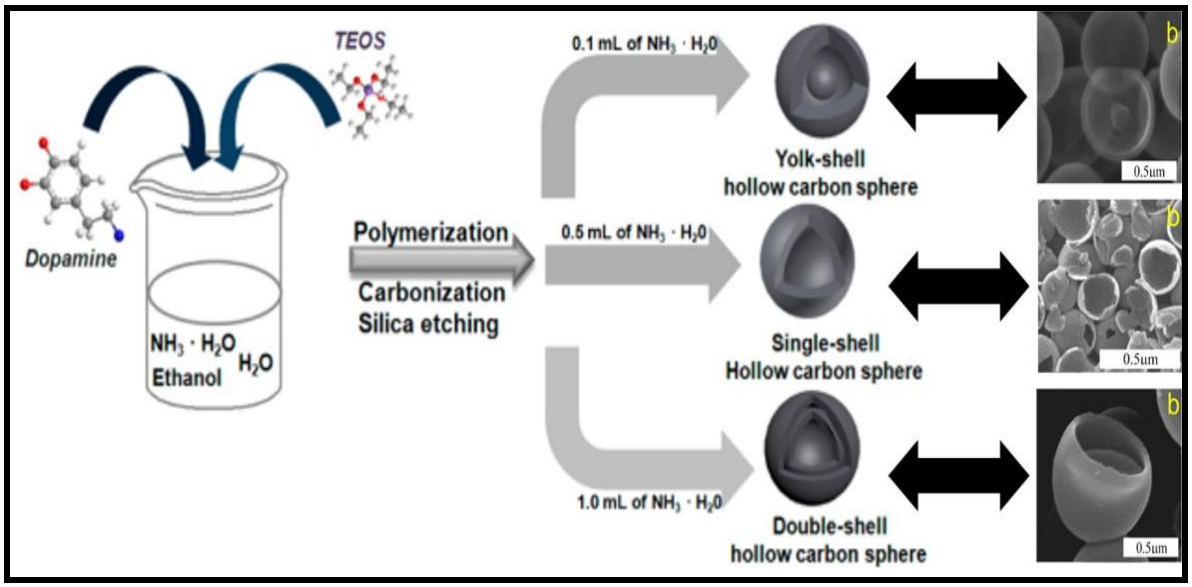

Figure 2.9. Schematic diagram showing the formation of yolk shell, single shell and double shell HCSs and their respective SEM images[114].

Similarly, Zhang *et al.* reported the synthesis of self organized HCSs with an interpenetrating network through a heterogeneous nucleation pathway by varying the SiO_2 and carbon precursors respectively[117]. Thus, the templating process provides a broad range of nanomaterials from zero-dimensional to three-dimensional structures. The synthesis of hierarchically structured functional materials through a templating method has developed as a multidisciplinary novel approach[118, 119]. For instance, by varying the surface and interfacial interactions a three-dimensionally ordered macroporous solid (3DOM) framework can be obtained via the templating route[120]. More recently, Qiao and coworkers synthesized fluorescent HCSs encapsulating carbon dots from fish scale via an in-situ pyrolysis route[121]. The carbon dots were made by crushing the HCSs and this material was applied in sensitized solar cells thus, opening a new platform for HCS studies (Fig. 2.10). An absorption peak was observed at 315 nm from the UV-visible spectra of the carbon dots. In addition, the carbon dots were characterized by an indirect band gap energy of 2.5 eV with a strong quantum confinement effect. The application of the carbon dots as sensitizer in DSSCs resulted in 0.65 mA/cm^2 J_{SC}, 0. 55V V_{OC}, 78.8% FF and 0.28% PCE. These carbon based materials (HCSs and carbon dots) are less toxic, cheap and easily processable; as a result, there is great potential for improvement in their applicability in electronic devices.

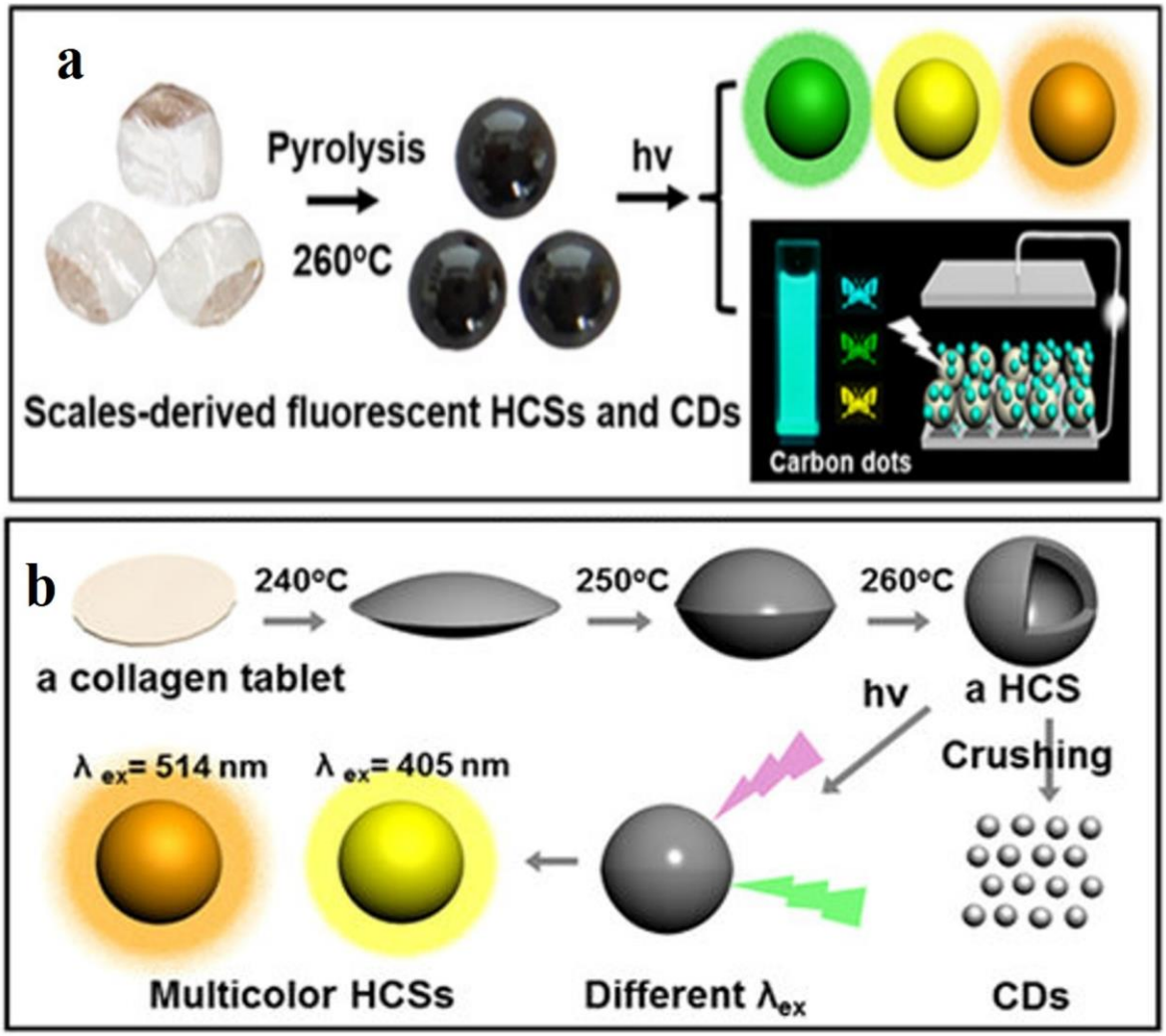

Figure 2.10. A schematic synthesis of multicolor fluorescent HCSs (a) from fish scales via in situ pyrolysis and their use in DSSCs and (b) the formation process from collagen tablet, respectively (modified from ref[121]).

2.1.3.4.2 Yolk shell nanostructures

Yolk shell nanostructures are a new class of materials denoted as A@B with a core@void@shell configuration as shown in Fig. 2.11[122]. Analogous to the yolk shell materials are the core shell nanostructures denoted as A@B with core@shell configuration. The core and shell materials can comprise of metals, metal oxides or polymers among others[123-126]. In 2003, Xia and his coworkers reported for the first time the synthesis of Au@polymer yolk shell nanostructures[127]. More recently, Nongwe and his coworkers synthesized Au@HCS yolk shell materials from Au@SiO_2 core shell templates for application as catalyst supports[128]. To date, there has been tremendous progress in the generation of yolk and core shell nanoparticles for application in drug delivery, sensors,

catalysts and lithium ion batteries[122, 129-131]. The application of core shell nanomaterials in solar cells has been addressed by incorporation of Au@SiO_2 core shell materials into the hole transport layer and the active layer. The enhancement of the overall device efficiency in these materials was attributed to the improved light trapping and optical absorption through the surface plasmon resonance effect[132, 133]. The field of hybrid nanomaterials opens a platform for the synthesis of various functional materials for application in organic photovoltaic devices.

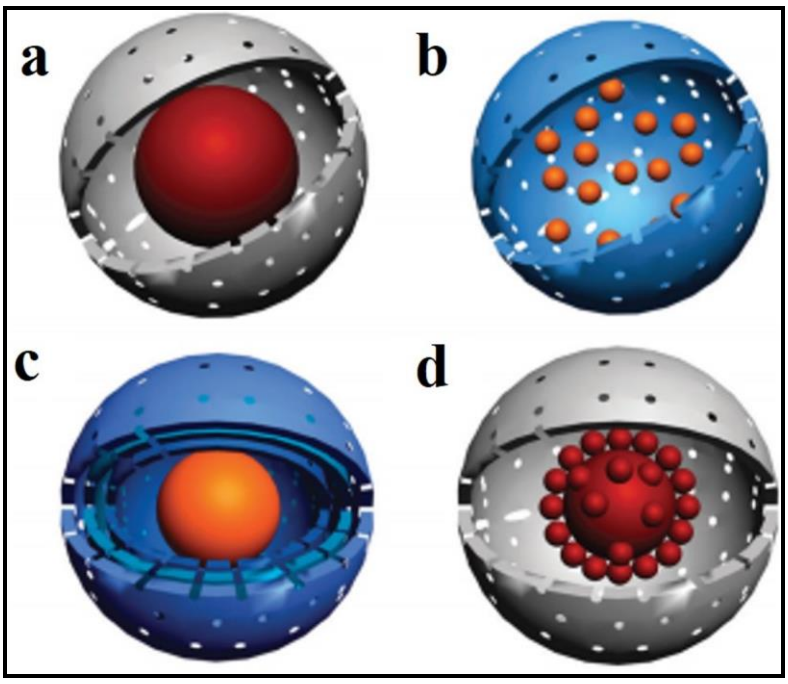

Figure 2.11. Illustration of yolk shell nanoparticles; (A) with a single core, (B) with multiple cores, (C) with multiple shells and (D) with a raspberry like core[122].

2.1.4 Surface plasmon resonance and gold nanoparticles

The early studies of surface plasmon resonance were reported by Mie Gustav[134] and in the late 1950's Ritchie *et al.* observed a characteristic energy loss of fast electrons in metal surfaces due to collective excitations[135]. These collective oscillations were attributed to Coulomb long range interactions of the free valence electrons in metals[136]. Later in the same decade, Powell and Swan confirmed the existence of these collective oscillations on the metal surface as a surface phenomenon that was transmitted through thin films[137]. This energy loss was attributed to quantized surface waves of a degenerate electron gas and was referred to as surface plasmons by Stern and Fercell[138]. When an electromagnetic radiation is incident on a

metal surface, it induces a collective oscillation of free electrons[139]. As a result, it forms an electric dipole that oscillates in the direction of the frequency dependent electric field component of light. The electric force separates the electron from the centre of mass of the charge on the surface. To compensate the forces, a restoring force is generated which is maximum at the resonance frequency. A surface plasmon resonance (SPR) is achieved when the amplitude of the collective oscillation reaches a maximum. The strong absorption caused by SPR can be measured using UV-visible or Infrared absorption spectroscopy. The operation of an OPV is dependent on the amount of light absorption and thus, unveils the importance of SPR absorption.

The light absorption and charge transport properties of OPVs govern the overall device performance[140]. The thickness of the active layer is directly proportional to the light absorption. However, increasing thickness limits charge transport due to increased device series resistance and compromises the exciton dissociation efficiency since the exciton diffusion length is limited to a few tenths of nm. The trade-off between light absorption and charge transport existing in OPVs has led to the development of light trapping, absorption and harvesting techniques[141]. Induction a localized surface plasmon resonance (LSPR) of noble metallic nanoparticles such as Au or Ag incorporated in OPVs is one such route for enhancing the light absorption and scattering. The LSPR extends the optical path length in the active layer and enhances the electromagnetic field near the noble metal surface resulting in enhanced light absorption[142, 143]. For instance, Chen *et al.* incorporated gold nanoparticles into OPVs and observed an enhanced short circuit current density and a significant PCE improvement due to the LSPR of gold[144]. Also, the enhanced electromagnetic field increased the number of excitons generated that could augment the exciton dissociation as illustrated by Wu *et al.* (Fig. 2.12)[145]. The utilization of nanoparticles with plasmonic effects in the active layer or buffer layer to enhance light harvesting has been intensely researched[145-148]. The extensive studies of SPR plasmonics show the future applications of plasmons in electronics, photonics and medical industries[149-151].

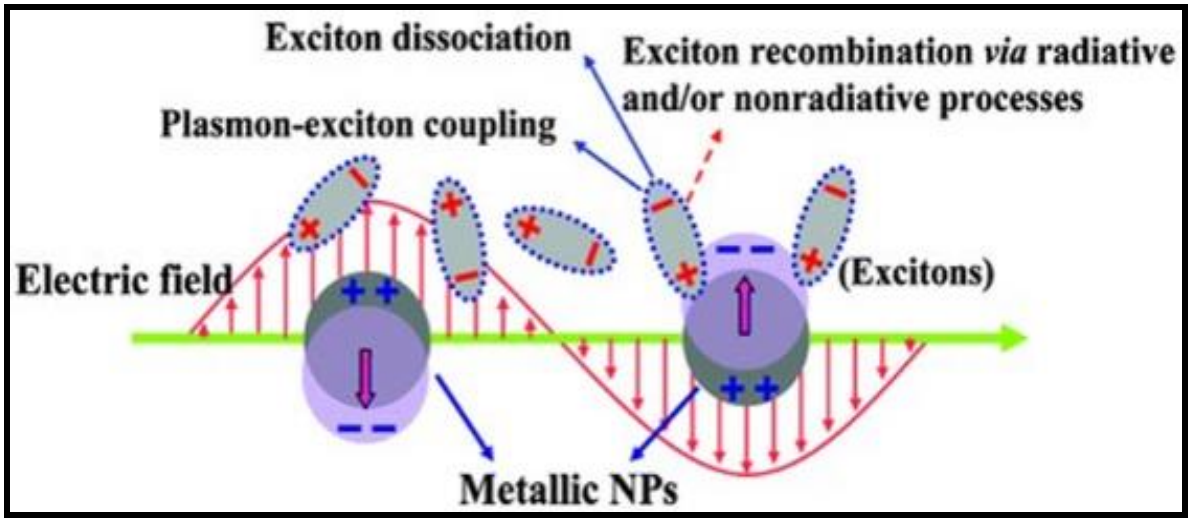

Figure 2.12. A schematic diagram of the interplay between LSPR and excitons resulting in enhanced exciton dissociation and reduced exciton recombination[145].

2.1.5 Use of carbon based nanomaterials in chemical sensors

Chemical sensors are devices that transform chemical information to a useful analytical signal[152]. The chemical information can include an analyte concentration, a chemical reaction or a pressure change. The analytical signal can be a change in conductance or resistance (chemoresistive sensors) or a change in optical properties (optical sensors). The response and sensitivity of chemical sensors are based on the adsorption of molecules that result in a change in resistance or conductance of the sensing element. Carbon based nanomaterials such as carbon nanotubes, graphene oxide and graphene have been used in chemoresistive sensors for detection of toxic and volatile organic compounds such as ammonia[153], nitrogen dioxide[154], acetone and formaldehyde[155] among others. The fabrication of chemoresistive sensors from carbon based materials is readily processable, cheap and offers the added advantage of varying the surface to volume ratio. Carbon based core-shell nanostructures exhibit unique electrical and optical properties that make them applicable in chemical sensors. For instance, Chen and his coworkers reported on the synthesis of a carbon nanotube@SnO_2 core-shell nanostructure and it's use as an ethanol sensor with an improved ethanol sensitivity and response[156]. More recently, Lu and his coworkers reported the application of Ni@porous hollow carbon fibers as nitrogen dioxide sensors[157]. The use of porous carbon fibers opens a platform for application of hollow carbon spheres as chemical sensors.

2.2 Conclusions

Organic photovoltaic devices are cheap and solution processable compared to their silicon counterparts. As a result, there has been tremendous interest in the synthesis of nanomaterials that will enhance the light absorption, the exciton dissociation, the charge separation and transport in OPVs. However, the main material challenge lies in obtaining optimum optical, electrical and structural properties suitable for an improved device performance and stability. Towards achieving an enhanced OPV performance, recent development on the generation of hierarchical and novel structures composed of noble metals, graphenes, carbon dots, HCSs and functional hybrid materials will open a platform for a broad range of application for such materials. In addition, these carbon based nanomaterials can be employed as active materials in chemoresistive sensors.

References

1. IEA, *World Energy Outlook 2013*. IEA.
2. IEA, *World Energy Outlook 2014*. IEA.
3. Kamat, P. V. *The Journal of Physical Chemistry C* **2007,** 111, (7), 2834-2860.
4. Gómez, I.; Pérez-Rodríguez, E.; Viñegla, B.; Figueroa, F. L.; Karsten, U. *Journal of Photochemistry and Photobiology B: Biology* **1998,** 47, (1), 46-57.
5. Lee, J. W.; Jang, E. Y.; Lee, S. H.; Ryou, H. S.; Choi, S.; Kim, Y. *International Journal of Thermal Sciences* **2014,** 75, 36-44.
6. Zhao, Y.; Lunt, R. R. *Advanced Energy Materials* **2013,** 3, (9), 1143-1148.
7. Edmonds, I. R.; Cowling, I. R.; Meara, L. A.; Wheeler, B. *Solar Energy* **1983,** 30, (6), 537-543.
8. Chu, Y. *Global Energy Network Institute (GENI), San Diego, CA* **2011**.
9. Bagnall, D. M.; Boreland, M. *Energy Policy* **2008,** 36, (12), 4390-4396.
10. Bredas, J.-L.; Durrant, J. R. *Accounts of Chemical Research* **2009,** 42, (11), 1689-1690.
11. Grätzel, M. *Journal of Photochemistry and Photobiology C: Photochemistry Reviews* **2003,** 4, (2), 145-153.
12. Günes, S.; Sariciftci, N. S. *Inorganica Chimica Acta* **2008,** 361, (3), 581-588.
13. Green, M. A.; Ho-Baillie, A.; Snaith, H. J. *Nature Photonics* **2014,** 8, (7), 506-514.
14. Noh, J. H.; Im, S. H.; Heo, J. H.; Mandal, T. N.; Seok, S. I. *Nano Letters* **2013,** 13, (4), 1764-1769.
15. Goetzberger, A.; Hebling, C.; Schock, H.-W. *Materials Science and Engineering: R: Reports* **2003,** 40, (1), 1-46.
16. Spanggaard, H.; Krebs, F. C. *Solar Energy Materials and Solar Cells* **2004,** 83, (2), 125-146.
17. Oliveira, E. F.; Lavarda, F. C. *Materials Chemistry and Physics* **2014,** 148, (3), 923-932.
18. Brabec, C. J.; Gowrisanker, S.; Halls, J. J. M.; Laird, D.; Jia, S.; Williams, S. P. *Advanced Materials* **2010,** 22, (34), 3839-3856.
19. Gregg, B. A.; Hanna, M. C. *Journal of Applied Physics* **2003,** 93, (6), 3605-3614.
20. van Dyk, E. E.; Meyer, E. L. *Renewable Energy* **2004,** 29, (3), 333-344.
21. Dennler, G.; Scharber, M. C.; Brabec, C. J. *Advanced Materials* **2009,** 21, (13), 1323-1338.
22. Abdulrazzaq, O. A.; Saini, V.; Bourdo, S.; Dervishi, E.; Biris, A. S. *Particulate Science and Technology* **2013,** 31, (5), 427-442.
23. Brabec, C. J.; Sariciftci, N. S.; Hummelen, J. C. *Advanced Functional Materials* **2001,** 11, (1), 15-26.
24. Wöhrle, D.; Meissner, D. *Advanced Materials* **1991,** 3, (3), 129-138.
25. Chamberlain, G. A. *Solar Cells* **1983,** 8, (1), 47-83.
26. Onsager, L. *Physical Review* **1938,** 54, (8), 554.
27. Tang, C. W.; Albrecht, A. C. *The Journal of Chemical Physics* **1975,** 62, (6), 2139-2149.
28. Marks, R.; Halls, J.; Bradley, D.; Friend, R.; Holmes, A. *Journal of Physics: Condensed Matter* **1994,** 6, (7), 1379.
29. Tang, C. W. *Applied Physics Letters* **1986,** 48, (2), 183-185.
30. Park, S. H.; Roy, A.; Beaupre, S.; Cho, S.; Coates, N.; Moon, J. S.; Moses, D.; Leclerc, M.; Lee, K.; Heeger, A. J. *Nature Photonics* **2009,** 3, (5), 297-302.
31. Scharber, M.; Sariciftci, N. *Progress in Polymer Science* **2013,** 38, (12), 1929-1940.

32. Yu, G.; Gao, J.; Hummelen, J. C.; Wudl, F.; Heeger, A. J. *Science* **1995,** 270, (5243), 1789.
33. Shaheen, S. E.; Brabec, C. J.; Sariciftci, N. S.; Padinger, F.; Fromherz, T.; Hummelen, J. C. *Applied Physics Letters* **2001,** 78, (6), 841-843.
34. Padinger, F.; Rittberger, R. S.; Sariciftci, N. S. *Advanced Functional Materials* **2003,** 13, (1), 85-88.
35. Facchetti, A. *Chemistry of Materials* **2011,** 23, (3), 733-758.
36. Venkataraman, D.; Yurt, S.; Venkatraman, B. H.; Gavvalapalli, N. *The Journal of Physical Chemistry Letters* **2010,** 1, (6), 947-958.
37. Heeger, A. J. *Advanced Materials* **2014,** 26, (1), 10-28.
38. Brabec, C.; Scherf, U.; Dyakonov, V., *Organic Photovoltaics: Materials, Device Physics, and Manufacturing Technologies*. John Wiley & Sons: 2011.
39. Alvarado, S.; Seidler, P.; Lidzey, D.; Bradley, D. *Physical Review Letters* **1998,** 81, (5), 1082.
40. Mayer, A. C.; Scully, S. R.; Hardin, B. E.; Rowell, M. W.; McGehee, M. D. *Materials Today* **2007,** 10, (11), 28-33.
41. Haugeneder, A.; Neges, M.; Kallinger, C.; Spirkl, W.; Lemmer, U.; Feldmann, J.; Scherf, U.; Harth, E.; Gügel, A.; Müllen, K. *Physical Review B* **1999,** 59, (23), 15346-15351.
42. Lakhwani, G.; Rao, A.; Friend, R. H. *Annual Review of Physical Chemistry* **2014,** 65, 557-581.
43. Sun, S.-S.; Sariciftci, N. S., *Organic Photovoltaics: Mechanisms, Materials, and Devices*. CRC press: 2005.
44. Scharber, M. C.; Sariciftci, N. S. *Progress in Polymer Science* **2013,** 38, (12), 1929-1940.
45. Khlyabich, P. P.; Burkhart, B.; Rudenko, A. E.; Thompson, B. C. *Polymer* **2013,** 54, (20), 5267-5298.
46. Li, Y. *Accounts of Chemical Research* **2012,** 45, (5), 723-733.
47. Nakabayashi, K.; Otani, H.; Mori, H. *Polymer Journal* **2015,** 47, (9), 617-623.
48. Ryan, J. W.; Matsuo, Y. *Scientific Reports* **2015,** 5, 8319.
49. Brown, P. J.; Thomas, D. S.; Köhler, A.; Wilson, J. S.; Kim, J.-S.; Ramsdale, C. M.; Sirringhaus, H.; Friend, R. H. *Physical Review B* **2003,** 67, (6), 064203.
50. Nakazono, M.; Kawai, T.; Yoshino, K. *Chemistry of Materials* **1994,** 6, (6), 864-870.
51. Chen, D.; Liu, F.; Wang, C.; Nakahara, A.; Russell, T. P. *Nano Letters* **2011,** 11, (5), 2071-2078.
52. Wu, W.-R.; Jeng, U. S.; Su, C.-J.; Wei, K.-H.; Su, M.-S.; Chiu, M.-Y.; Chen, C.-Y.; Su, W.-B.; Su, C.-H.; Su, A.-C. *ACS Nano* **2011,** 5, (8), 6233-6243.
53. Kohn, P.; Rong, Z.; Scherer, K. H.; Sepe, A.; Sommer, M.; Müller-Buschbaum, P.; Friend, R. H.; Steiner, U.; Hüttner, S. *Macromolecules* **2013,** 46, (10), 4002-4013.
54. Huang, Y.-C.; Tsao, C.-S.; Cha, H.-C.; Chuang, C.-M.; Su, C.-J.; Jeng, U. S.; Chen, C.-Y. *Scientific Reports* **2016,** 6, 20062.
55. Collins, B. A.; Tumbleston, J. R.; Ade, H. *The Journal of Physical Chemistry Letters* **2011,** 2, (24), 3135-3145.
56. Huang, W.-K.; Chung, K.-J.; Liu, Y.-M.; Ger, M.-D.; Pu, N.-W.; Youh, M.-J. *Vacuum* **2015,** 118, 94-99.
57. Aguilar-Elguézabal, A.; Antúnez, W.; Alonso, G.; Delgado, F. P.; Espinosa, F.; Miki-Yoshida, M. *Diamond and Related Materials* **2006,** 15, (9), 1329-1335.
58. Mi, Y.; Hu, W.; Dan, Y.; Liu, Y. *Materials Letters* **2008,** 62, (8–9), 1194-1196.

59. Hu, B.; Wang, K.; Wu, L.; Yu, S. H.; Antonietti, M.; Titirici, M. M. *Advanced Materials* **2010,** 22, (7), 813-828.
60. Stankovich, S.; Dikin, D. A.; Piner, R. D.; Kohlhaas, K. A.; Kleinhammes, A.; Jia, Y.; Wu, Y.; Nguyen, S. T.; Ruoff, R. S. *Carbon* **2007,** 45, (7), 1558-1565.
61. Dreyer, D. R.; Park, S.; Bielawski, C. W.; Ruoff, R. S. *Chemical Society Reviews* **2010,** 39, (1), 228-240.
62. Qian, H.-s.; Han, F.-m.; Zhang, B.; Guo, Y.-c.; Yue, J.; Peng, B.-x. *Carbon* **2004,** 42, (4), 761-766.
63. Koziol, K.; Boskovic, B. O.; Yahya, N., Synthesis of carbon nanostructures by CVD method. In *Carbon and Oxide Nanostructures*, Springer: 2010; pp 23-49.
64. Mond, L., Ludwig mond. Google Patents: 1891.
65. Van Arkel, A.; de Boer, J. H. *Zeitschrift für Anorganische und Allgemeine Chemie* **1925,** 148, (1), 345-350.
66. Bryant, W. *Journal of Materials Science* **1977,** 12, (7), 1285-1306.
67. Gretz, R. D.; Jackson, C. M.; Hirth, J. P. *Surface Science* **1967,** 6, (2), 171-192.
68. Sigsbee, R. A.; Pound, G. M. *Advances in Colloid and Interface Science* **1967,** 1, (3), 335-390.
69. Benzinger, W.; Becker, A.; Hüttinger, K. J. *Carbon* **1996,** 34, (8), 957-966.
70. Creighton, J.; Ho, P. *Chemical Vapor Deposition* **2001,** 2, 1-22.
71. Kong, J.; Cassell, A. M.; Dai, H. *Chemical Physics Letters* **1998,** 292, (4–6), 567-574.
72. Cassell, A. M.; Raymakers, J. A.; Kong, J.; Dai, H. *The Journal of Physical Chemistry B* **1999,** 103, (31), 6484-6492.
73. Che, G.; Lakshmi, B. B.; Martin, C. R.; Fisher, E. R.; Ruoff, R. S. *Chemistry of Materials* **1998,** 10, (1), 260-267.
74. Bartl, A.; Bohr, S.; Haubner, R.; Lux, B. *International Journal of Refractory Metals and Hard Materials* **1996,** 14, (1–3), 145-157.
75. Wang, X.; You, H.; Liu, F.; Li, M.; Wan, L.; Li, S.; Li, Q.; Xu, Y.; Tian, R.; Yu, Z.; Xiang, D.; Cheng, J. *Chemical Vapor Deposition* **2009,** 15, (1-3), 53-56.
76. Hideki, M. *Japanese Journal of Applied Physics* **1998,** 37, (6R), 3175.
77. Kijima, K.; Setaka, N.; Tanaka, H. *Journal of Crystal Growth* **1974,** 24, 183-187.
78. Iijima, S. *Nature* **1991,** 354, (6348), 56-58.
79. Ajayan, P. M.; Ebbesen, T. W. *Reports on Progress in Physics* **1997,** 60, (10), 1025.
80. Guo, J.; Liu, Y.; Prada-Silvy, R.; Tan, Y.; Azad, S.; Krause, B.; Pötschke, P.; Grady, B. P. *Journal of Polymer Science Part B: Polymer Physics* **2014,** 52, (1), 73-83.
81. Lee, N. S.; Chung, D. S.; Han, I. T.; Kang, J. H.; Choi, Y. S.; Kim, H. Y.; Park, S. H.; Jin, Y. W.; Yi, W. K.; Yun, M. J.; Jung, J. E.; Lee, C. J.; You, J. H.; Jo, S. H.; Lee, C. G.; Kim, J. M. *Diamond and Related Materials* **2001,** 10, (2), 265-270.
82. Ting, Z.; Syed, M.; Nosang, V. M.; Marc, A. D. *Nanotechnology* **2008,** 19, (33), 332001.
83. Udupa, G.; Gangadharan, K. In *Future applications of carbon nanotube reinforced functionally graded composite materials*, Advances in Engineering, Science and Management (ICAESM), 2012 International Conference on, 2012; IEEE: pp 399-404.
84. De Volder, M. F.; Tawfick, S. H.; Baughman, R. H.; Hart, A. J. *Science* **2013,** 339, (6119), 535-539.
85. Bernardi, M.; Giulianini, M.; Grossman, J. C. *ACS Nano* **2010,** 4, (11), 6599-6606.
86. Alturaif, H. A.; ALOthman, Z. A.; Shapter, J. G.; Wabaidur, S. M. *Molecules* **2014,** 19, (11), 17329-17344.
87. Wu, M.-C.; Lin, Y.-Y.; Chen, S.; Liao, H.-C.; Wu, Y.-J.; Chen, C.-W.; Chen, Y.-F.; Su, W.-F. *Chemical Physics Letters* **2009,** 468, (1), 64-68.

88. Schuettfort, T.; Snaith, H.; Nish, A.; Nicholas, R. *Nanotechnology* **2009,** 21, (2), 025201.
89. Xu, Y.; Long, G.; Huang, L.; Huang, Y.; Wan, X.; Ma, Y.; Chen, Y. *Carbon* **2010,** 48, (11), 3308-3311.
90. Jun, G. H.; Jin, S. H.; Lee, B.; Kim, B. H.; Chae, W.-S.; Hong, S. H.; Jeon, S. *Energy & Environmental Science* **2013,** 6, (10), 3000-3006.
91. Li, F.; Kou, L.; Chen, W.; Wu, C.; Guo, T. *NPG Asia Materials* **2013,** 5, (8), e60.
92. Park, H.; Brown, P. R.; Bulović, V.; Kong, J. *Nano Letters* **2012,** 12, (1), 133-140.
93. Zhao, W.; Chen, H.; Li, Y.; Li, L.; Lang, M.; Shi, J. *Advanced Functional Materials* **2008,** 18, (18), 2780-2788.
94. Ravat, V.; Nongwe, I.; Meijboom, R.; Bepete, G.; Coville, N. J. *Journal of Catalysis* **2013,** 305, 36-45.
95. Prieto, G.; Tüysüz, H.; Duyckaerts, N.; Knossalla, J.; Wang, G.-H.; Schüth, F. *Chemical Reviews* **2016**.
96. Pan, L.; Chortos, A.; Yu, G.; Wang, Y.; Isaacson, S.; Allen, R.; Shi, Y.; Dauskardt, R.; Bao, Z. *Nature Communications* **2014,** 5, 3002.
97. Chen, Y.; Xu, P.; Wu, M.; Meng, Q.; Chen, H.; Shu, Z.; Wang, J.; Zhang, L.; Li, Y.; Shi, J. *Advanced Materials* **2014,** 26, (25), 4294-4301.
98. Lou, X. W.; Archer, L. A.; Yang, Z. *Advanced Materials* **2008,** 20, (21), 3987-4019.
99. Herring, A. M.; McKinnon, J. T.; McCloskey, B. D.; Filley, J.; Gneshin, K. W.; Pavelka, R. A.; Kleebe, H.-J.; Aldrich, D. J. *Journal of the American Chemical Society* **2003,** 125, (33), 9916-9917.
100. Tsai, C.-K.; Kang, H.; Hong, C.-I.; Huang, C.-H.; Chang, F.-C.; Wang, H. P. *Journal of Nanoparticle Research* **2012,** 14, (12), 1-8.
101. Lai, X.; Halpert, J. E.; Wang, D. *Energy & Environmental Science* **2012,** 5, (2), 5604-5618.
102. Yang, Z.-C.; Zhang, Y.; Kong, J.-H.; Wong, S. Y.; Li, X.; Wang, J. *Chemistry of Materials* **2013,** 25, (5), 704-710.
103. Fan, H. J.; Gösele, U.; Zacharias, M. *Small* **2007,** 3, (10), 1660-1671.
104. Ma, Y.; Qi, L. *Journal of Colloid and Interface Science* **2009,** 335, (1), 1-10.
105. Zhang, T.; Zhang, Q.; Ge, J.; Goebl, J.; Sun, M.; Yan, Y.; Liu, Y.-s.; Chang, C.; Guo, J.; Yin, Y. *The Journal of Physical Chemistry C* **2009,** 113, (8), 3168-3175.
106. Wang, W.; Dahl, M.; Yin, Y. *Chemistry of Materials* **2012,** 25, (8), 1179-1189.
107. Ding, S.-J.; Zhang, C.-L.; Yang, M.; Qu, X.-Z.; Lu, Y.-F.; Yang, Z.-Z. *Polymer* **2006,** 47, (25), 8360-8366.
108. Fuertes, A. B.; Valle-Vigon, P.; Sevilla, M. *Chemical Communications* **2012,** 48, (49), 6124-6126.
109. Oda, Y.; Fukuyama, K.; Nishikawa, K.; Namba, S.; Yoshitake, H.; Tatsumi, T. *Chemistry of Materials* **2004,** 16, (20), 3860-3866.
110. Ikeda, S.; Tachi, K.; Ng, Y. H.; Ikoma, Y.; Sakata, T.; Mori, H.; Harada, T.; Matsumura, M. *Chemistry of Materials* **2007,** 19, (17), 4335-4340.
111. de Almeida Filho, C.; Zarbin, A. J. G. *Carbon* **2006,** 44, (14), 2869-2876.
112. Xia, Y. D.; Mokaya, R. *Advanced Materials* **2004,** 16, (11), 886-891.
113. Yoon, S. B.; Sohn, K.; Kim, J. Y.; Shin, C. H.; Yu, J. S.; Hyeon, T. *Advanced Materials* **2002,** 14, (1), 19-21.
114. Liu, C.; Wang, J.; Li, J.; Luo, R.; Shen, J.; Sun, X.; Han, W.; Wang, L. *ACS Applied Materials & Interfaces* **2015,** 7, (33), 18609-18617.
115. Dong, Z.; Lai, X.; Halpert, J. E.; Yang, N.; Yi, L.; Zhai, J.; Wang, D.; Tang, Z.; Jiang, L. *Advanced Materials* **2012,** 24, (8), 1046-1049.

116. Qi, J.; Lai, X.; Wang, J.; Tang, H.; Ren, H.; Yang, Y.; Jin, Q.; Zhang, L.; Yu, R.; Ma, G. *Chemical Society Reviews* **2015,** 44, (19), 6749-6773.
117. Zhang, H.; Yu, M.; Song, H.; Noonan, O.; Zhang, J.; Yang, Y.; Zhou, L.; Yu, C. *Chemistry of Materials* **2015,** 27, (18), 6297-6304.
118. Shao, Q.; Tang, J.; Lin, Y.; Zhang, F.; Yuan, J.; Zhang, H.; Shinya, N.; Qin, L.-C. *Journal of Materials Chemistry A* **2013,** 1, (48), 15423-15428.
119. Velev, O. D.; Lenhoff, A. M. *Current Opinion in Colloid & Interface Science* **2000,** 5, (1–2), 56-63.
120. Stein, A.; Schroden, R. C. *Current Opinion in Solid State and Materials Science* **2001,** 5, (6), 553-564.
121. Chen, Q.-L.; Ji, W.-Q.; Chen, S. *Scientific Reports* **2016,** 6, 19382.
122. Liu, J.; Qiao, S. Z.; Chen, J. S.; Lou, X. W. D.; Xing, X.; Lu, G. Q. M. *Chemical Communications* **2011,** 47, (47), 12578-12591.
123. Park, J. C.; Song, H. *Nano Research* **2010,** 4, (1), 33-49.
124. Zhang, Q.; Wang, W.; Goebl, J.; Yin, Y. *Nano Today* **2009,** 4, (6), 494-507.
125. Zhao, Y.; Jiang, L. *Advanced Materials* **2009,** 21, (36), 3621-3638.
126. Nongwe, I.; Ravat, V.; Meijboom, R.; Coville, N. J. *Applied Catalysis A: General* **2016,** 517, 30-38.
127. Kamata, K.; Lu, Y.; Xia, Y. *Journal of the American Chemical Society* **2003,** 125, (9), 2384-2385.
128. Nongwe, I.; Bepete, G.; Shaikjee, A.; Ravat, V.; Terfassa, B.; Meijboom, R.; Coville, N. J. *Catalysis Communications* **2014,** 53, 77-82.
129. Ravat, V.; Nongwe, I.; Coville, N. J. *ChemCatChem* **2012,** 4, (12), 1930-1934.
130. Phaahlamohlaka, T. N.; Kumi, D. O.; Dlamini, M. W.; Jewell, L. L.; Coville, N. J. *Catalysis Today* **2016**.
131. Dlamini, M. W.; Coville, N. J.; Scurrell, M. S. *RSC Advances* **2016,** 6, (27), 22222-22231.
132. Janković, V.; Yang, Y.; You, J.; Dou, L.; Liu, Y.; Cheung, P.; Chang, J. P.; Yang, Y. *ACS Nano* **2013,** 7, (5), 3815-3822.
133. Xu, X.; Wong, T. K.; Sun, X. W. In *Enhancement of power conversion efficiency in solution processed organic photovoltaic devices by embedded plasmonic gold-silica core-shell nanorods*, SPIE Photonics Europe, 2014; International Society for Optics and Photonics: pp 91370Z-91370Z-8.
134. Mie, G. *Annalen der Physik* **1908,** 330, (3), 377-445.
135. Ritchie, R. H. *Physical Review* **1957,** 106, (5), 874-881.
136. Pines, D.; Bohm, D. *Physical Review* **1952,** 85, (2), 338-353.
137. Powell, C. J.; Swan, J. B. *Physical Review* **1959,** 115, (4), 869-875.
138. Stern, E. A.; Ferrell, R. A. *Physical Review* **1960,** 120, (1), 130-136.
139. Barnes, W. L.; Dereux, A.; Ebbesen, T. W. *Nature* **2003,** 424, (6950), 824-830.
140. Jo, J.; Na, S. I.; Kim, S. S.; Lee, T. W.; Chung, Y.; Kang, S. J.; Vak, D.; Kim, D. Y. *Advanced Functional Materials* **2009,** 19, (15), 2398-2406.
141. Shrotriya, V.; Wu, E. H.-E.; Li, G.; Yao, Y.; Yang, Y. *Applied Physics Letters* **2006,** 88, (6), 064104.
142. Maier, S. A.; Atwater, H. A. *Journal of Applied Physics* **2005,** 98, (1), 011101.
143. Monestier, F.; Simon, J.-J.; Torchio, P.; Escoubas, L.; Flory, F.; Bailly, S.; de Bettignies, R.; Guillerez, S.; Defranoux, C. *Solar Energy Materials and Solar Cells* **2007,** 91, (5), 405-410.
144. Chen, F.-C.; Wu, J.-L.; Lee, C.-L.; Hong, Y.; Kuo, C.-H.; Huang, M. H. *Applied Physics Letters* **2009,** 95, (1), 013305.

145. Wu, J.-L.; Chen, F.-C.; Hsiao, Y.-S.; Chien, F.-C.; Chen, P.; Kuo, C.-H.; Huang, M. H.; Hsu, C.-S. *ACS Nano* **2011,** 5, (2), 959-967.
146. Stratakis, E.; Kymakis, E. *Materials Today* **2013,** 16, (4), 133-146.
147. Chuang, M.-K.; Chen, F.-C.; Hsu, C.-S. *Journal of Nanomaterials* **2014,** 2014, 12.
148. Liu, S.; Jiang, R.; You, P.; Zhu, X.; Wang, J.; Feng, Y. *Energy & Environmental Science* **2016**.
149. Patching, S. G. *Biochimica et Biophysica Acta (BBA)-Biomembranes* **2014,** 1838, (1), 43-55.
150. Homola, J.; Yee, S. S.; Gauglitz, G. *Sensors and Actuators B: Chemical* **1999,** 54, (1), 3-15.
151. Fang, Y.; Sun, M. *Light: Science & Applications* **2015,** 4, (6), e294.
152. Hulanicki, A.; Glab, S.; Ingman, F. *Pure and Applied Chemistry* **1991,** 63, (9), 1247-1250.
153. Bekyarova, E.; Davis, M.; Burch, T.; Itkis, M.; Zhao, B.; Sunshine, S.; Haddon, R. *The Journal of Physical Chemistry B* **2004,** 108, (51), 19717-19720.
154. Yuan, W.; Liu, A.; Huang, L.; Li, C.; Shi, G. *Advanced Materials* **2013,** 25, (5), 766-771.
155. Alizadeh, T.; Soltani, L. H. *Journal of Hazardous Materials* **2013,** 248, 401-406.
156. Chen, Y.; Zhu, C.; Wang, T. *Nanotechnology* **2006,** 17, (12), 3012.
157. Lü, R.; Shi, K.; Zhou, W.; Wang, L.; Tian, C.; Pan, K.; Sun, L.; Fu, H. *Journal of Materials Chemistry* **2012,** 22, (47), 24814-24820.

CHAPTER 3

Synthesis and Characterization of Pristine, Annealed and N-doped Carbon Spheres by a Vertical CVD Reactor

3.1 Introduction

Interest in carbon based nanomaterials continues to intensify since the discovery of fullerenes[1] and carbon nanotubes[2]. Other forms of carbon based nanomaterials include graphene, graphene oxide and carbon spheres. Graphenes are planar whereas the carbon spheres have a spherical form. These spherical carbon spheres are given names such as carbon spherules[3,4] carbon nanoballs[5] carbon beads[6], carbon pearls[7] and carbon microspheres. Carbon spheres can be categorized in different ways. Inagaki *et al*.[8] classified carbon spheres based on carbon atoms arrangement as either radial, concentric or random depending on the interfacial energy. Serp *et al.*[9] Further classified spheres as either well graphitized (2-20 nm), less graphitized (50-1000 nm) or carbon beads (> 1000 nm). Carbon spheres comprise mainly of hexagonal rings leading to graphene like flakes that incorporate heptagonal and pentagonal rings assembled to give curvature to the graphite flakes[5, 10]. These carbon spheres find application in printer inks[11], in tyres[12] and more recently in write only read many times memory (WORMs) devices[13, 14].

Solid carbon spheres have been synthesized using several methods such as spray pyrolysis, autoclave methods, aerosol deposition and chemical vapor deposition methods. Spray pyrolysis is a process that involves the generation of a spray by an ultrasonic atomizer which transports atoms and molecules into a high temperature furnace where the solid carbon spheres are produced[15-17]. The autoclave method involves the use of autogenous pressure and elevated temperatures to produce carbon spheres using carbon precursors in closed reactor containers. This route allows the use of various carbon precursors in liquid or solid form such as sucrose[18-20] and mesitylene[4] to yield carbon spheres. The chemical vapor deposition synthesis route involves the breaking down of volatile carbon precursors on a target surface at elevated temperatures in a furnace to produce carbon spheres. Thus, it provides high quality and reproducible carbon spheres using readily available carbon sources[21]. The synthesis of carbon spheres unlike that of carbon nanotube does not require metal catalysts and hence a

non-catalytic CVD method can be used[22]. Using this route, different reactor designs for the production of carbon spheres can be employed. The conventional reactor designs that have been used in solid carbon sphere synthesis are; horizontal reactors (Fig. 3.1) and vertical reactors (Fig. 3.2).

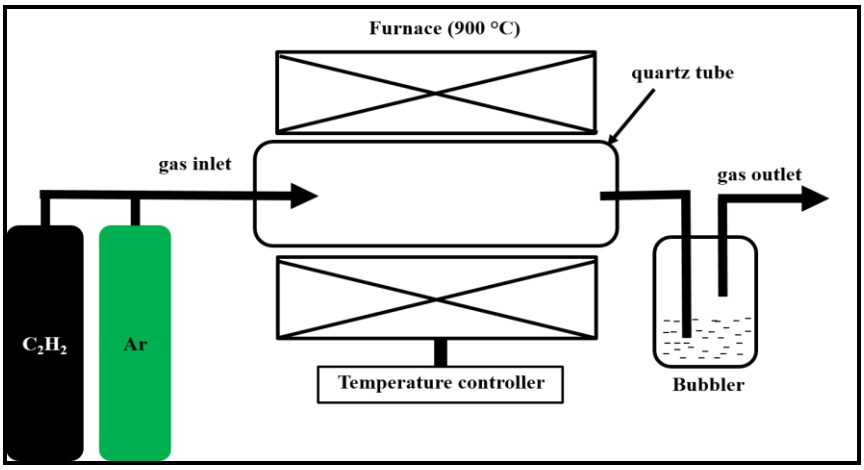

Figure 3.1. A schematic diagram of a horizontal CVD reactor.

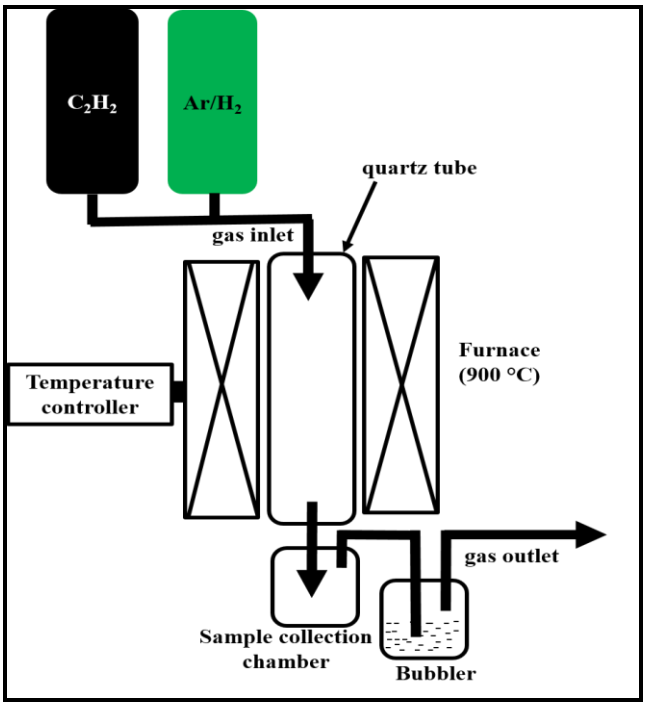

Figure 3.2. A schematic diagram of a vertically oriented CVD reactor.

The vertical reactor CVD method leads to the formation of smaller sized carbon spheres owing to the short dwell time of the carbon precursor in the reactor during the carbon

formation process. Ray *et al.* made 175 nm diameter sized N-doped carbon spheres by pyrolysis of acetylene and acetonitrile as carbon and nitrogen sources and argon as the carrier gas. The experiment was carried out at 900°C for 30 min in a vertical CVD reactor[23]. In contrast, the application of a horizontal reactor results in the production of larger sized carbon nanospheres due to a longer duration time. For instance, Poinern *et al.* managed to synthesize solid carbon spheres in a horizontal furnace using acetylene as a carbon source and nitrogen as a carrier gas with a carbonization time of 5 min at 1000°C[24]. Carbon spheres with a particle size of 100-500 nm were obtained. Xiong *et al.* made carbon spheres by pyrolysis of acetylene with argon as a carrier gas at 900°C in a horizontal CVD reactor and obtained solid carbon spheres of 900 nm particle size[25].

The reaction conditions during carbon sphere synthesis via the CVD method affects the morphology, particle size and yield of the carbon spheres. Unsaturated and saturated hydrocarbons such as ethane, methane, benzene, styrene, acetylene and toluene have been used for the generation of carbon spheres[26]. The carbon source can influence the particle size distribution and yield of the carbon spheres. For instance, acetylene gas favors a narrower particle distribution whereas ethylene gas favors a broad particle size distribution[27]. Other factors such as the type of carrier gas used during carbon sphere synthesis plays a significant role on the morphology and size of obtained carbon spheres. A carrier gas serves the purpose of delivering the reactants into the reactor and maintaining an inert environment. Argon, nitrogen, hydrogen and argon/hydrogen mixtures are the commonly used carrier gases in the CVD method. The use of hydrogen gas produces smaller sized carbon spheres (200 to 400 nm) with a narrower size distribution while pure argon gas favors larger sized carbon spheres (400 to 900 nm) with a broader size distribution[22]. The carrier gases play a critical role in the growth of carbon nanomaterials via the CVD technique. To be specific, Lee *et al.* reported a decreased growth rate of CNTs due to etching of carbon atom by the hydrogen radicals via PECVD using NH_3 as a carrier gas with C_2H_2 carbon source[28]. Similar hydrogen etching effects have been reported in MWCNTs, boron nitride and graphene sheets[29, 30]. More so, hydrogen gas serves a significant role in the growth and kinetics of graphene through dissociative hydrogen chemisorption and methane dehydrogenation chemisorption reactions[31]. However, the hydrogen etching effects in graphene results in trimmed graphene edges of varying sizes and shapes[32-34].

Nitrogen containing carbon materials have attracted intensive research owing to their diverse applications as electrodes in lithium-ion batteries[35], supercapacitors[36] and as catalysts support[37]. The atomic size of N is similar to that of carbon hence it can be incorporated easily into the carbon structure[38]. Carbon spheres without functionalization can have very poor electrical properties. Doping of carbon spheres with nitrogen increases their reactivity and enhances their applications in dye sensitized solar cells[39], oxygen reduction[40] and electronic devices[23]. Nitrogen containing nanomaterials can be obtained by in situ doping or ex situ doping. Some of the chemical precursors used for N-doping are ammonia[41, 42], melamine[43], polyaniline[44], acetonitrile[45, 46], N-containing carbohydrates[47] and amines[48, 49]. Xiong and coworkers synthesized N-doped carbon spheres by pyrolysis of acetylene with ammonia solution as the nitrogen source at 900°C for 1 h in a horizontal furnace and obtained carbon spheres with a diameter of 700 nm[50]. Doping of carbon spheres affects their degree of graphitization, electronic and magnetic characteristics. However, undoped carbon based nanomaterials can also portray magnetic properties resulting from localized edge states and the presence of defects[51, 52].

In this study, solid carbon spheres were produced using a vertically oriented CVD reactor. The effect of carrier gases and flow rates on the particle size, morphology and structural properties of the carbon spheres was investigated. Despite the number of studies carried out on the hydrogen etching effects on carbon nanotubes and graphene, the effect of hydrogen on the growth of carbon spheres using a catalyst free vertically oriented CVD reactor is hardly reported. Thus, the effect of annealing of the carbon spheres in argon and hydrogen gas and post N-doping was studied on the particle size, morphology, structural and magnetic properties.

3.2 Experimental

A vertical chemical vapor deposition (CVD) reactor consisting of a hollow tubular quartz reactor (length: 100 cm × 4 cm i.d) loaded in a furnace was set up as shown in Fig. 3.3. A carbon source (C_2H_2, Afrox) and a carrier gas argon or hydrogen (Afrox) were used in the carbon sphere synthesis. The furnace was heated to 900°C at a rate of 10°C/min under Ar gas (100 sccm). At 900°C, the Ar flow valve was closed and a C_2H_2 flow valve opened at a specific flow rate (100 sccm or 200 sccm). Two flow rates were used to study the role of flow rate on the carbon sphere diameter and size distribution. The C_2H_2 gas was pyrolyzed in the

quartz reactor at 900°C for 15 min. A black soot was generated and collected in a round bottomed flask connected at the outlet of the reactor. The C_2H_2 flow valve was closed and the quartz reactor cooled under a continuous flow of Ar gas to ambient temperature. After cooling, the argon flow was stopped and the quartz reactor removed from the furnace. The same procedure was followed using H_2 as a carrier gas. The black soot that had accumulated on the walls of the quartz reactor was scrapped off using a glass rod and weighed together with the collected sample.

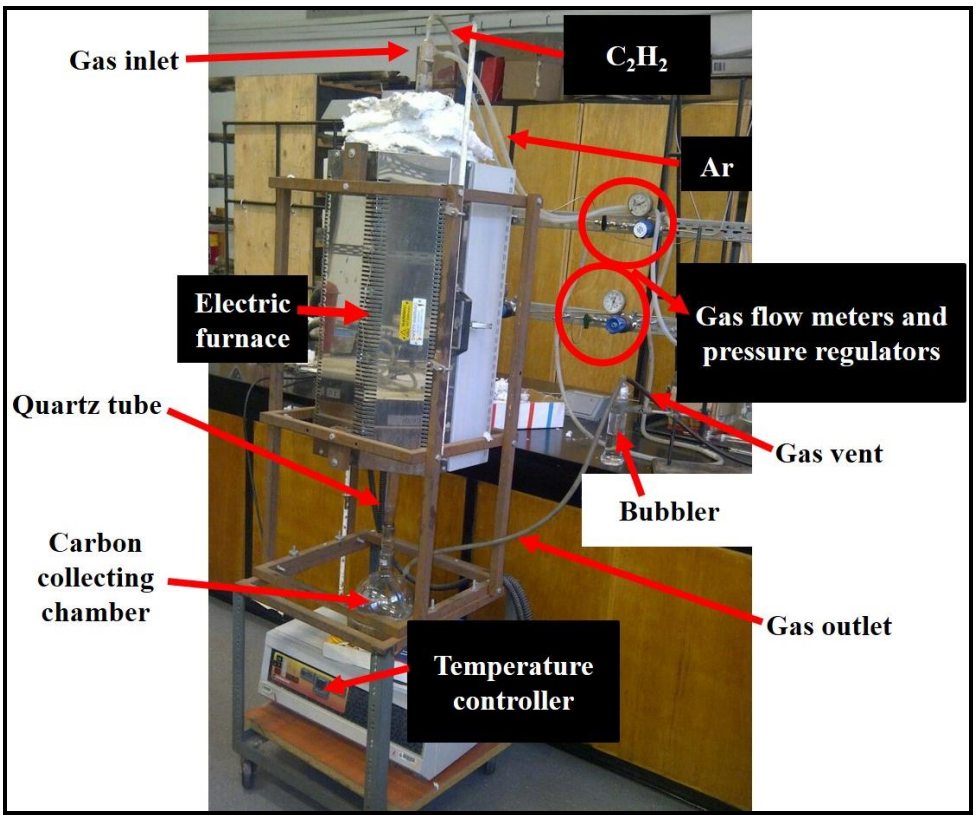

Figure 3.3. A vertically oriented CVD reactor set up.

A soxhlet extraction apparatus (Fig. 3.4) was used to purify the carbon spheres at 150°C for 24 h using toluene solvent (Sigma Aldrich, 99.5%). The toluene changed color from colorless to brown after completion of the purification processing. The brown color was due to the removal of polyaromatic hydrocarbons. The products were dried at 100°C for 12 h and analyzed. To investigate the effect of annealing on the carbon spheres structural, thermal and magnetic properties, the synthesized carbon spheres were then annealed at 800°C under H_2 gas (200 sccm) and also separately under Ar gas (200 sccm) for 1 h in each case. N-doped carbon spheres were obtained by passing acetonitrile (Sigma Aldrich, 99.9%) over the already

prepared and purified products (0.2 g) for 1 h at 800°C with Ar as a carrier gas in a horizontal reactor.

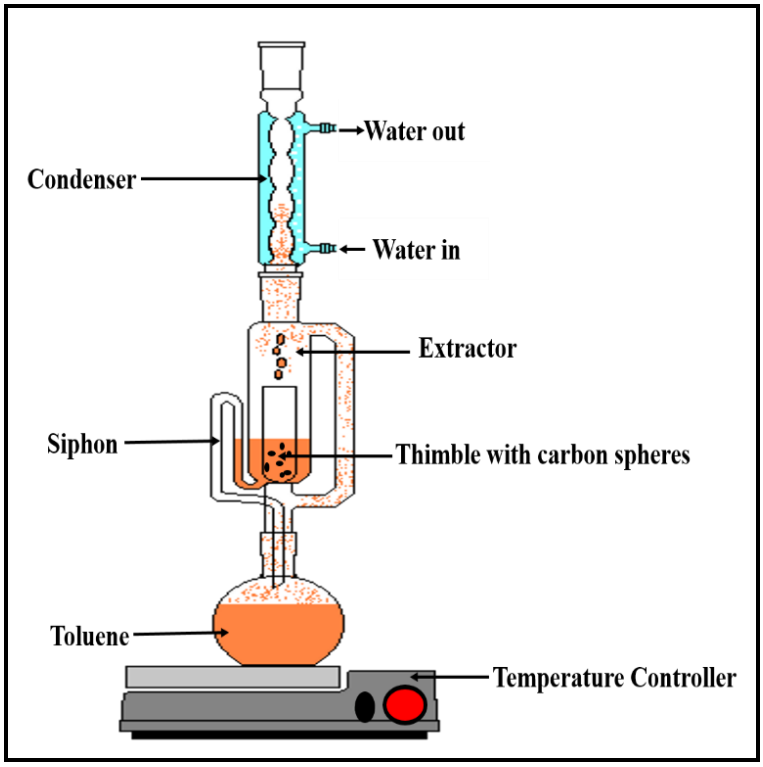

Figure 3.4. A conventional Soxhlet extraction set up for purification of carbon spheres (modified from ref[53]).

3.3 Characterization of the solid carbon spheres

3.3.1 Transmission electron microscopy (TEM)

The morphological features of the synthesized carbon spheres were ascertained by TEM using a FEI Technai G2 spirit electron microscope operating at 120 keV. A sample specimen was prepared by dispersing a small amount (≈2 mg) of purified carbon spheres in ethanol (1 mL) and mixture sonicated to form a homogeneous solution. A few drops of the homogeneous solution were placed onto a carbon coated copper grid and the grid dried in ambient air for 30 min before inserting it in the microscope. The diameters of the carbon sphere images obtained were measured using Image J 1.48v software. The diameters of 100 randomly chosen carbon spheres were measured per sample.

3.3.2 Scanning electron microscopy (SEM)

The morphology of the obtained samples was determined using a FEI Nova Nanolab 600 FIB/SEM. A small amount (($\approx$2 mg) of the carbon sphere sample was evenly spread on a carbon tape placed on a carbon stab. The homogeneously dispersed sample on the carbon tape was coated with a palladium/gold coating for 2 min to make it conductive. The stab was then placed in a SEM and images were taken at 5 keV.

3.3.3 Raman spectroscopy

Raman spectroscopic analysis was done to determine the degree of graphitization and the structure of the synthesized spheres. The measurement was carried out on the carbon spheres using a Jobin-Yvon T6400 micro-Raman spectrometer equipped with a laser excitation wavelength of 514.5 nm and a liquid N_2 cooled charge coupled device detector. The obtained Raman bands were deconvoluted using lorentzian function by using the Origin 8.50 professional package to measure peak areas and intensities.

3.3.4 Thermal gravimetric analysis (TGA)

The thermal stability of the carbon spheres was investigated by TGA instrument conjugated with a weight loss derivative curve (DTG) using a Perkin Elmer Pyris 1 TGA. For each sample a 10 mg was placed in a ceramic pan and put in the instrument furnace. The sample was heated from 35^0C to 900^0C at a rate of 10^0C/min under air (10 mL/min). The weight loss plot (TGA) provided information about the stability, nature and composition of the samples. The derivative curve provided information of the weight loss and temperatures as which it took place.

3.3.5 Brunner Emmet and Teller (BET) Surface area analysis

Before taking the measurements, the samples were degassed at 200ºC for 4 h in N_2. The N_2 adsorption and desorption isotherms of the solid carbon spheres were taken using a Micromeritics Tristar 3000 instrument at 77K. The specific surface area was calculated by the BET method from N_2 adsorption data and the Barett-Joyner-Halenda (BJH) method was used to determine the pore size distributions calculated by analysing the desorption branches of the N_2 isotherms.

3.3.6 Electron spin resonance (ESR)

EPR is a technique that measures the absorption of electromagnetic radiation. It detects the interaction between unpaired electrons localized in a system and an external applied magnetic field. Carbon spheres are comprised of sp^2 and sp^3 hybridized carbon atoms. The sp^2/sp^3 mixed state can be converted to sp^2 hybridized atoms (complete graphitization) by heat

treatment beyond 1300 °C[54, 55]. When heat treatment is done at lower temperatures i.e. 800 °C, the sp^2/sp^3 mixed state cannot be distorted. Heat treatment causes thermally assisted clustering of sp^2 atoms and migration of sp^3 defects resulting to an ordered structure and a decrease in strain energy. Consequently, a transition from Mott variable hopping (VRH) to a weak localization conduction mechanism takes place in disordered carbon[56]. The magnetic properties in carbon nanospheres result from the presence of sp^2 hybridized carbon atoms that act as paramagnetic centers[57]. The non-graphitic carbon nanospheres exhibit Curie type paramagnetic properties arising from non-bonding π electrons at the graphitic carbon edges. Electron spin resonance (ESR) measurements were carried out at room temperature using a Bruker ESP300E X-band spectrometer operating in the frequency range of 9.4 to 9.8 GHz and a g-factor of 2. The samples were placed in NMR tubes and the standard continuous wave technique was used to obtain all the derivative spectra.

3.3.7 X-ray photoelectron spectroscopy (XPS)

The chemical composition of the annealed and N-doped carbon spheres was determined by X-ray photoelectron spectroscopy (XPS). The ex-situ XPS study was carried out on the annealed and post N-doped carbon spheres.

3.3.8 Carbon yield calculation

The carbon spheres yield was deduced by estimating the amount of carbon reactant (C_2H_2) used and the amount of carbon produced. Unpurified products were used for determination of the yield (Equation 3.1).

$$\%yield = \frac{nC}{nC_2H_2} \times 100\% \qquad (\mathbf{3.1})$$

where nC is the number of moles of carbon in the product and nC_2H_2 is the number of moles of carbon in C_2H_2

3.4 Results and discussion

3.4.1 Effect of different carrier gases and their flow rates

The synthesis of pristine carbon spheres was achieved by pyrolysis of C_2H_2 gas at 900°C for 15 min using a vertically oriented CVD reactor without a catalyst. The carbon percentage yields of the obtained spheres were based on the mass of spheres collected and are shown in Table 3.1. Low carbon yield (19 - 24%) was obtained at a low flow rate of the carbon source and carrier gas while more carbon spheres were produced (28 – 40%) at higher flow rates of the carbon source and carrier gas. The results indicate that higher yields of carbon spheres

were obtained with higher flow rates of carbon source and carrier gas as compared to other results in literature[58]. Mhlanga *et al.* obtained 1.4 g of carbon soot via pyrolysis of C_2H_2 (118 sccm) at 900°C for 4 min in a swirled floating vertical CVD reactor[59]. Our reported percentage yields of the carbon spheres by vertical CVD reactor was in close agreement with the yield of carbon spheres reported by Zikhona *et al.*[60]. They obtained carbon spheres yield of 19.8% and 28.0% by pyrolysis of C_2H_2 (100 sccm and 300 sccm) respectively at 900°C for 1 h in a vertical reactor. In our study, the percentage yield of the carbon spheres obtained when Ar was used as a carrier gas was slightly higher than when H_2 was employed. This can be attributed to the etching effects of hydrogen radicals on carbon atoms suppressing the carbon growth rate[28].

Table 3.1. Carbon yields of obtained solid carbon spheres

C_2H_2 (sccm)	H_2 (sccm)	Ar (sccm)	Total weight after reaction (g)	Carbon yield (%)
100	100	0	0.5781	19.5 ± 0.4
200	100	0	0.8463	28.5 ± 0.3
100	200	0	0.6055	20.4 ± 0.5
200	200	0	0.9461	31.9 ± 0.2
100	0	100	0.6459	21.8 ± 0.4
200	0	100	1.0089	34.0 ± 0.2
100	0	200	0.7046	23.7 ± 0.4
200	0	200	1.1568	39.0 ± 0.3

3.4.1.1 Morphology analysis

The effect of using different carrier gases (H_2 and Ar) on the carbon sphere synthesis was investigated using TEM micrographs as shown in Figs. 3.5 and 3.6. The carbon spheres obtained had a spherical morphology and were accreted in agreement with literature[10, 15]. In all the synthesized solid carbon spheres, the particle sizes of the obtained carbon spheres decreased with high C_2H_2 flow rates (Table 3.2 and 3.3). This is attributed to the shorter residence time and low nucleation rate leading to the formation of smaller particle sizes[15]. In contrast, at low flow rates, the C_2H_2 residence time is higher resulting in larger particle sizes (Figs. 3.5a, c and 3.6a, c). At high flow rates of C_2H_2 and low flow rates of either H_2 or Ar gas, solid carbon spheres of smaller sizes and with a narrow particle size distribution were obtained. (Figs. 3.5b, d and 3.6b, d). This could be ascribed to the increased decomposition

rate of C_2H_2 at the higher carrier gas flow rate. Typically, the carbon sphere formation mechanism involves the decomposition of carbon precursors into carbon atoms at high temperatures. The carbon atoms then fuse together to form the carbon spheres. The nucleation rate of carbon atoms can be increased by the presence of catalysts, increase in temperature or increase in the decomposition kinetics[15, 61, 62]. Carrier gases act as transport medium of the carbon precursor, thus increasing the flow rate decreases the overall dwell time of C_2H_2. This varies the carbon decomposition kinetics and growth rate resulting in smaller carbon particles.

Acetylene gas contains sp hybridized carbon atoms and is thermodynamically less stable than other carbon sources such as methane. In the presence of H_2 gas at high flow rates, the acetylene bonds are broken down to form smaller carbon nuclei which then nucleate and form a larger collection of carbon atoms. The carbon formation process involves carbon cluster growth by the coming together of carbon nuclei to minimize interfacial energy. In the presence of a reducing atmosphere such as hydrogen, the edge sites for further carbon growth are eliminated by an etching process resulting in smaller carbon spheres[22, 61]. When argon is used as a carrier gas, larger diameter sized carbon spheres are formed. Qian *et al.* observed a similar behaviour for carbon spheres synthesized in a horizontal CVD reactor whereby carbon spheres synthesized in the presence of argon resulted in larger diameter sizes while growth in hydrogen resulted to smaller sized spheres[22]. Also, in the presence of hydrogen gas, there is more nucleation leading to smaller spheres whereas in argon gas, more growth is favored resulting in larger sized spheres. This further corroborates with the low carbon spheres yield observed when hydrogen gas was used as a carrier gas.

The SEM images of the obtained solid carbon spheres confirmed their accreted nature as shown in Figs. 3.7 and 3.8. The broad particle size distribution of the solid carbon spheres at low carbon source and carrier gas flow rate is evident from the SEM images. However, a few carbon spheres of diameters larger than 500 nm were observed. This can result from the spheres collected from the sides of the quartz tube.

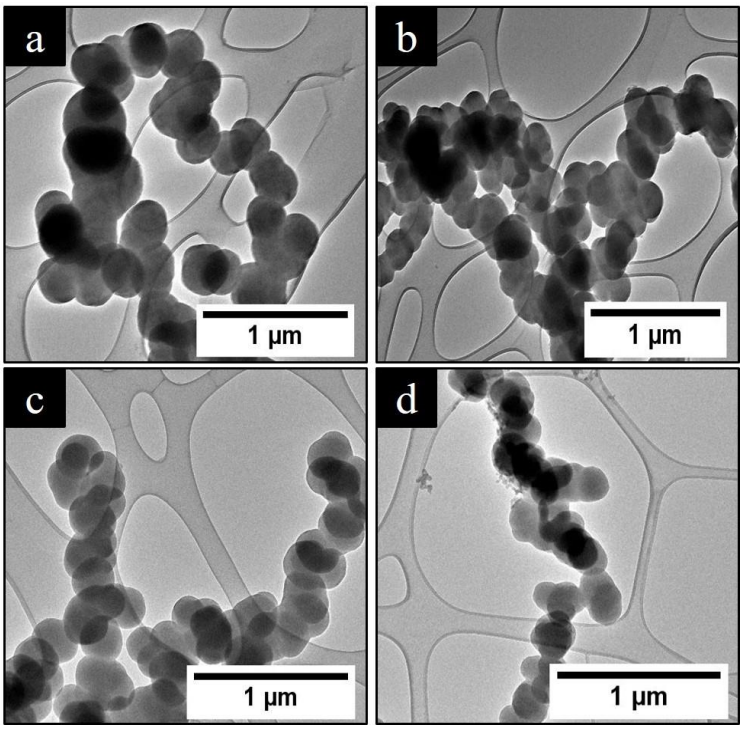

Figure 3.5. TEM images of carbon spheres obtained using different flow rates; (a) 100 sccm, H_2 and 100 sccm, C_2H_2, (b) 100 sccm, H_2 and 200 sccm, C_2H_2, (c) 200 sccm, H_2 and 100 sccm, C_2H_2, (d) 200 sccm, H_2 and 200 sccm, C_2H_2 flow rates, respectively.

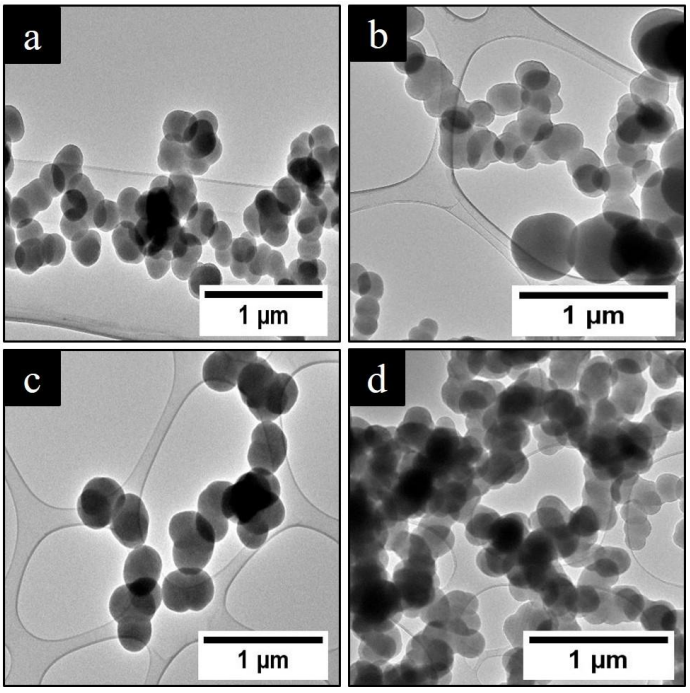

Figure 3.6. TEM images of carbon spheres obtained using different flow rates; (a) 100 sccm, Ar and 100 sccm, C_2H_2, (b) 100 sccm, Ar and 200 sccm, C_2H_2, (c) 200 sccm, Ar and 100 sccm, C_2H_2, (d) 200 sccm, Ar and 200 sccm, C_2H_2 flow rates, respectively.

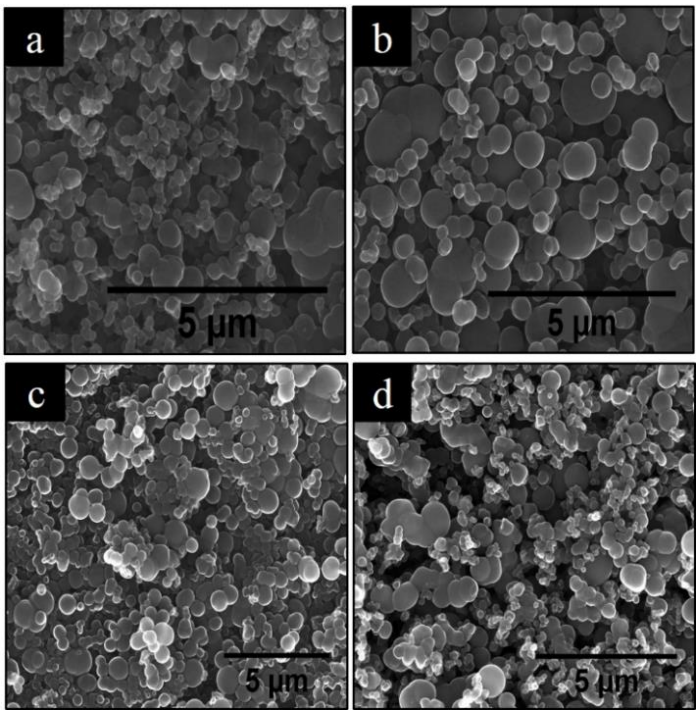

Figure 3.7. SEM images of carbon spheres obtained using different flow rates; (a) 100 sccm, H_2 and 100 sccm, C_2H_2, (b) 100 sccm, H_2 and 200 sccm, C_2H_2, (c) 200 sccm, H_2 and 100 sccm, C_2H_2, (d) 200 sccm, H_2 and 200 sccm, C_2H_2 flow rates, respectively.

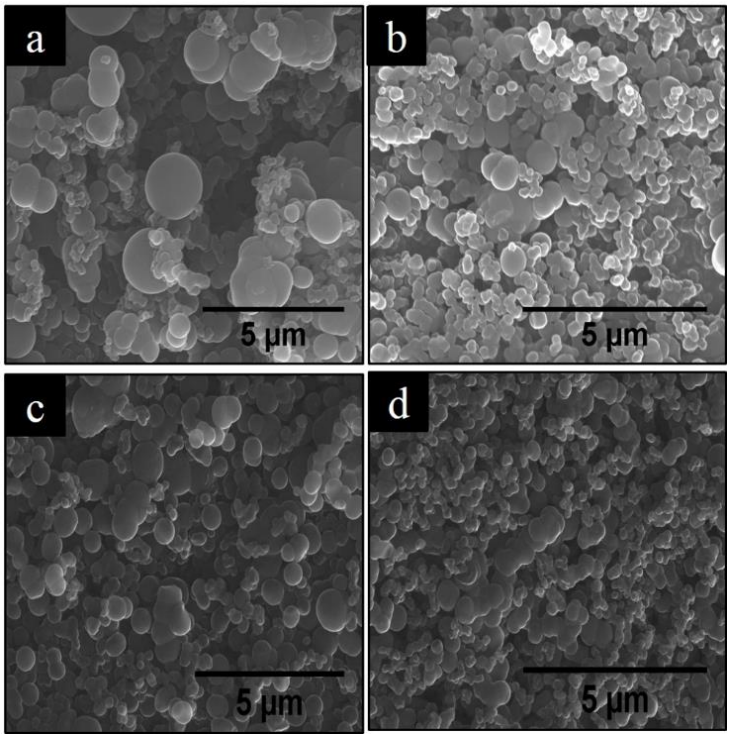

Figure 3.8. SEM images of carbon spheres obtained using different flow rates; (a) 100 sccm, Ar and 100 sccm, C_2H_2, (b) 100 sccm, Ar and 200 sccm, C_2H_2, (c) 200 sccm, Ar and 100 sccm, C_2H_2, (d) 200 sccm, Ar and 200 sccm, C_2H_2 flow rates, respectively.

Table 3.2. Particle sizes of the solid carbon spheres obtained using H_2 as a carrier gas

H_2 flow rate (sccm)	C_2H_2 flow rate (sccm)	Particle size (nm)
100	100	340 ± 106
100	200	186 ± 34
200	100	350 ± 98
200	200	198 ± 57

Table 3.3. Particle sizes of the solid carbon spheres obtained using Ar as a carrier gas

Ar flow rate (sccm)	C_2H_2 flow rate (sccm)	Particle size (nm)
100	100	340 ± 84
100	200	191 ± 34
200	100	327 ± 82
200	200	186 ± 19

3.4.1.2 Raman analysis

Fig. 3.9 shows the D and G Raman bands of the obtained carbon spheres and the band intensities and area agrees with the D/G ratios measured. In all the spheres, a D band was exhibited in between 1328 cm^{-1} and 1343 cm^{-1} due to the breathing mode of sp^2 and sp^3 carbon atoms and defects in the carbon structure[63]. Also, a G peak was observed between 1591 cm^{-1} and 1600 cm^{-1} which is a characteristic of bond stretching of sp^2 atoms[64]. All the synthesized carbon spheres had a low degree of graphitization as shown by their low I_D/I_G ratios (less than 1) as shown in Table 3.4.

Table 3.4. The D and G band positions and I_D/I_G ratio of obtained solid carbon spheres

C_2H_2 (sccm	H_2 (sccm)	Ar (sccm)	D band position (cm^{-1})	G band position (cm^{-1})	I_D/I_G ratio
100	100	0	1336	1591	0.89
200	100	0	1333	1593	0.89
100	200	0	1343	1591	0.88
200	200	0	1329	1598	0.85
100	0	100	1328	1600	0.90
200	0	100	1329	1593	0.92
100	0	200	1338	1595	0.90
200	0	200	1340	1595	0.88

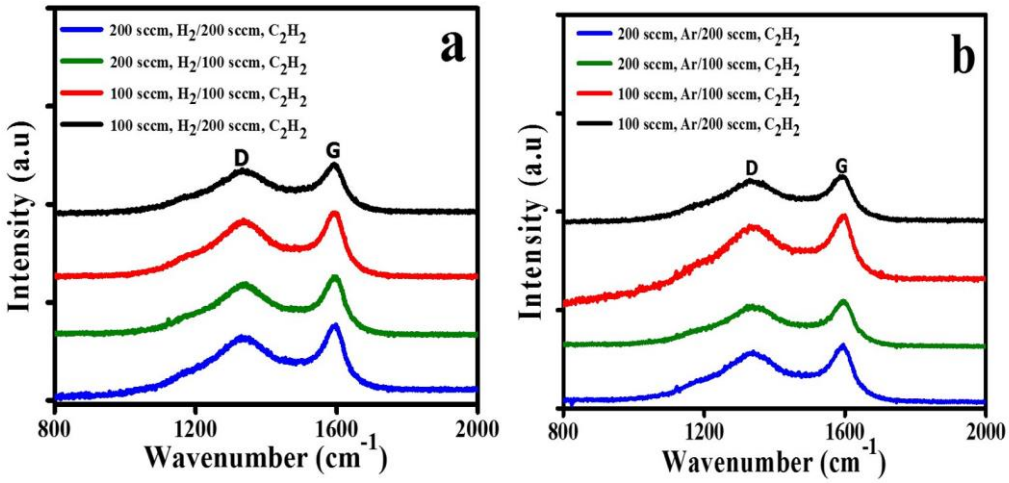

Figure 3.9. Raman spectra of carbon spheres produced using (a) H_2 and (b) Ar as carrier gas at different flow rates.

3.4.2 Effect of annealing carbon spheres on their paramagnetic properties

From the previous study the smallest particle size for the carbon spheres obtained using argon was 186 ± 19 nm at an argon flow rate of 200 sccm and an acetylene flow rate. Similarly sized carbon spheres (186 ± 34 nm) were obtained using H_2 gas at a flow rate of 100 sccm and C_2H_2 gas flow rate of 200 sccm. The effect of annealing on these two samples was investigated by monitoring the change in their paramagnetic properties resulting from the π electrons. The synthesized carbon spheres were annealed at 800°C under H_2 gas (200 sccm) or Ar gas (200 sccm) for 1 h.

3.4.2.1 Morphology

Annealing of the solid carbon spheres (particle size < 190 nm) resulted in accretion (Figs. 3.10 and 3.11). Annealing of the carbon spheres resulted in aggregation yielding a slight increase in the particle sizes (Table 3.5). This is attributed to the tendency of carbon spheres to accrete at higher temperatures due to van der waals forces and collision of adjacent spheres[15].

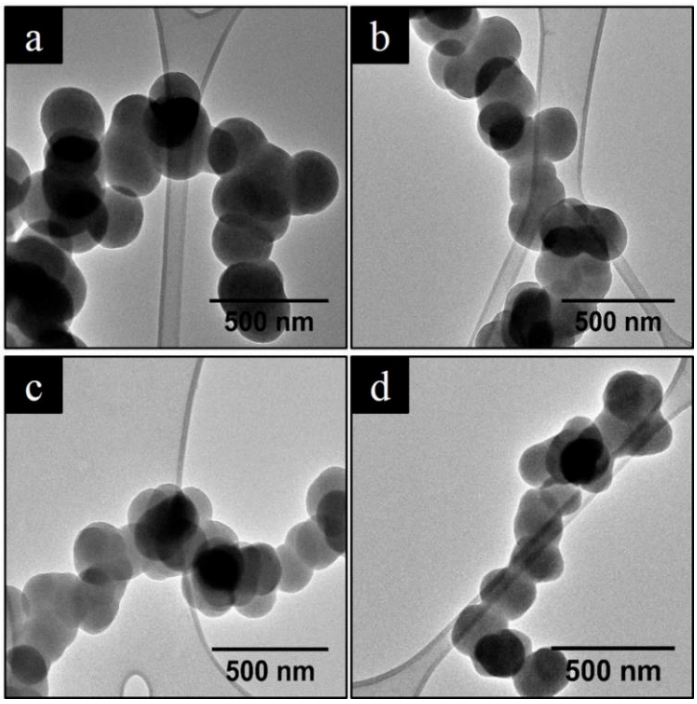

Figure 3.10. TEM images of carbon spheres obtained using 100 sccm, H_2 gas and 200 sccm, C_2H_2; (a) annealed in H_2 and (b) annealed in Ar: while in the case of 200 sccm, Ar gas and 200 sccm, C_2H_2, (c) annealed in H_2 and (d) annealed in Ar, respectively.

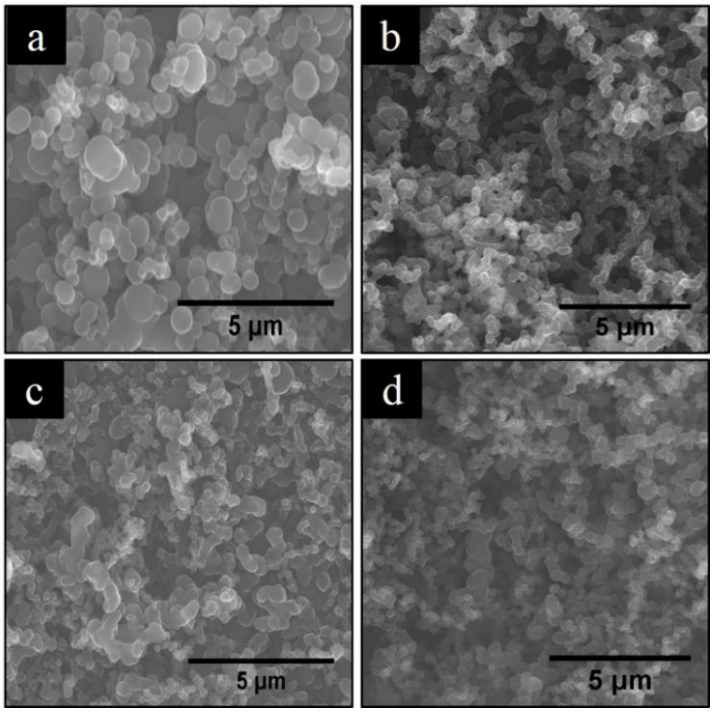

Figure 3.11. SEM images of carbon spheres obtained using 100 sccm, H_2 gas and 200 sccm, C_2H_2; (a) annealed in H_2 and (b) annealed in Ar: while in the case of 200 sccm, Ar gas and 200 sccm, C_2H_2, (c) annealed in H_2 and (d) annealed in Ar, respectively.

Table 3.5. Effect of annealing on the particle size of obtained solid carbon spheres

Synthesis parameters	Pristine (nm)	Annealed in H_2 (nm)	Annealed in Ar (nm)
H_2 100 sccm & C_2H_2 200 sccm	186 ± 34	258 ± 34	199 ± 27
Ar 200 sccm & C_2H_2 200 sccm	186 ± 19	196 ± 31	175 ± 28

3.4.2.2 Raman analysis

The Raman spectra of the solid carbon spheres show an increased D band intensity in all the carbon materials (Fig. 3.12). This is due to vibration of the sp^3 carbon atoms with dangling bonds[63]. A strong G peak with varying FWHM was observed owing to sp^2 hybridized carbon atoms[64]. The intensity ratio of the carbon spheres annealed in argon and hydrogen gas indicated a low degree of graphitization with a $I_D/I_G > 0.6$. Raman analysis of the carbon spheres showed a slight increase in I_D/I_G ratio when annealed under argon gas (Table 3.6). This has also been reported for diamond like carbon films where annealing at T > 300°C increased the D peak intensity[65]. Consequently, the I_D/I_G ratios of the annealed solid carbon spheres are higher (> 0.9) than those of pristine solid carbon spheres (< 0.9). This can be attributed to increase in the number of defects during the annealing process. In contrast, annealing of carbon materials at higher temperatures (T > 2000°C) has been reported to enhance the graphitization of carbon materials[66-69]. This is corroborated by the larger FWHM of the G peak observed in carbon spheres annealed under argon gas than for the carbon spheres annealed under hydrogen (Table 3.6). Thus, annealing under hydrogen gas leads to less structural defects and defect quenching thereby producing more graphitized carbon spheres.

Table 3.6. Effect of annealing on the D/G ratios of the carbon spheres

Synthesis parameters	Annealing	D band position (cm^{-1})	G band position (cm^{-1})	FWHM (cm^{-1})	I_D/I_G ratio
H_2 100 sccm & C_2H_2 200 sccm	H_2	1339	1592	76.77	0.88
H_2 100 sccm & C_2H_2 200 sccm	Ar	1331	1598	99.12	0.91
Ar 200 sccm & C_2H_2 200 sccm	H_2	1337	1592	77.77	0.90
Ar 200 sccm & C_2H_2 200 sccm	Ar	1328	1593	84.06	0.93

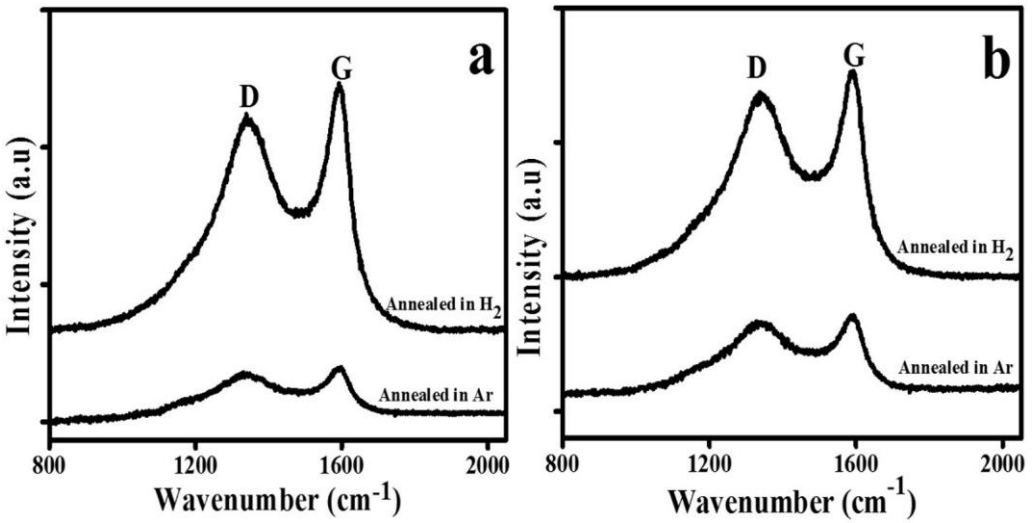

Figure 3.12. Raman spectra of the annealed solid carbon spheres obtained; (a) H_2, 100 sccm and 200 sccm, C_2H_2 and (b) Ar, 200 sccm and 200 sccm, C_2H_2 flow rates, respectively.

3.4.2.3 Thermal gravimetric analysis

The thermal stability of the carbon spheres was determined by the TGA technique. Fig. 3.13 to 3.15 demonstrate the TGA and corresponding derivative profiles of the obtained solid carbon spheres before and after annealing in hydrogen and argon gas, respectively. Table 3.7 shows the decomposition temperatures of the carbon spheres synthesized in argon and hydrogen respectively. The onset decomposition temperature of the carbon spheres synthesized in hydrogen was 530°C whereas in argon gas was 505°C. This shows that the carbon spheres obtained with hydrogen as a carrier gas were more thermally stable than those synthesized in argon[70]. The TGA profile of carbon spheres synthesized or annealed using hydrogen showed broad derivative peaks (Figs. 3.13a, 3.14a and 3.15a). This can be attributed to the H_2 etching of the edges resulting in broader decomposition ranges [24]. In contrast, carbon spheres synthesized or annealed in argon gas exhibited sharp first order derivative peaks (Figs. 3.13b, 3.14b and 3.15b). This suggest presence of more structured spheres; an indication of sample purity. The decomposition temperatures determined by the derivative TGA indicated that the carbon spheres annealed in hydrogen had a slightly higher thermal stability than those annealed in argon.

Table 3.7. Decomposition temperatures of the pristine and annealed carbon spheres

Synthesis parameters	Annealing	Onset decomposition temperature (°C)	Complete decomposition temperature (°C)
H_2 100 sccm & C_2H_2 200 sccm	-	530	789
H_2 100 sccm & C_2H_2 200 sccm	H_2	516	845
H_2 100 sccm & C_2H_2 200 sccm	Ar	470	684
Ar 200 sccm & C_2H_2 200 sccm	-	505	703
Ar 200 sccm & C_2H_2 200 sccm	H_2	510	858
Ar 200 sccm & C_2H_2 200 sccm	Ar	500	700

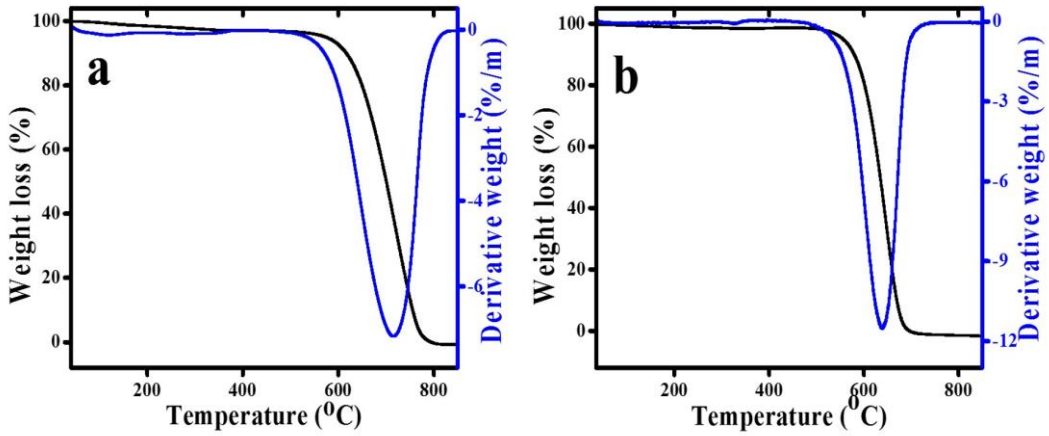

Figure 3.13. Thermal gravimetric curves of obtained pristine solid carbon spheres; (a) H_2, 100 sccm and C_2H_2, 200 sccm, (b) Ar, 200 sccm and C_2H_2, 200 sccm, respectively.

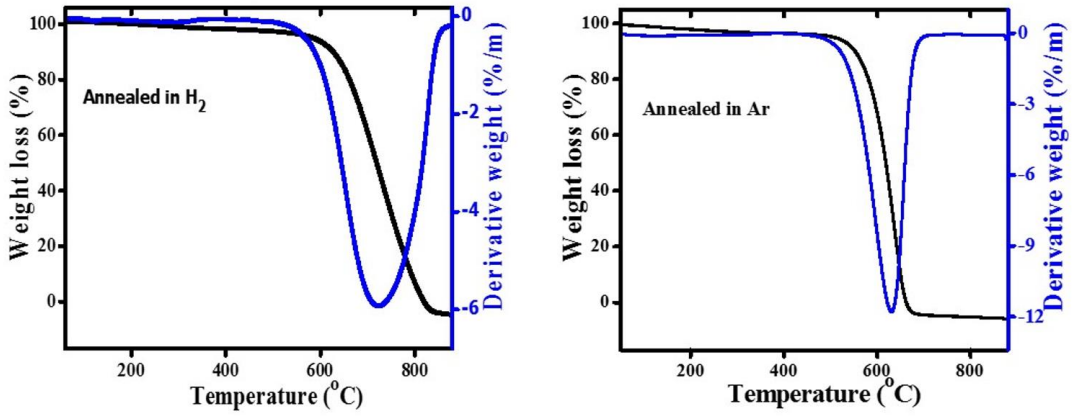

Figure 3.14. Thermal gravimetric curves of annealed solid carbon spheres synthesized at 100 sccm, H_2 and 200 sccm, C_2H_2.

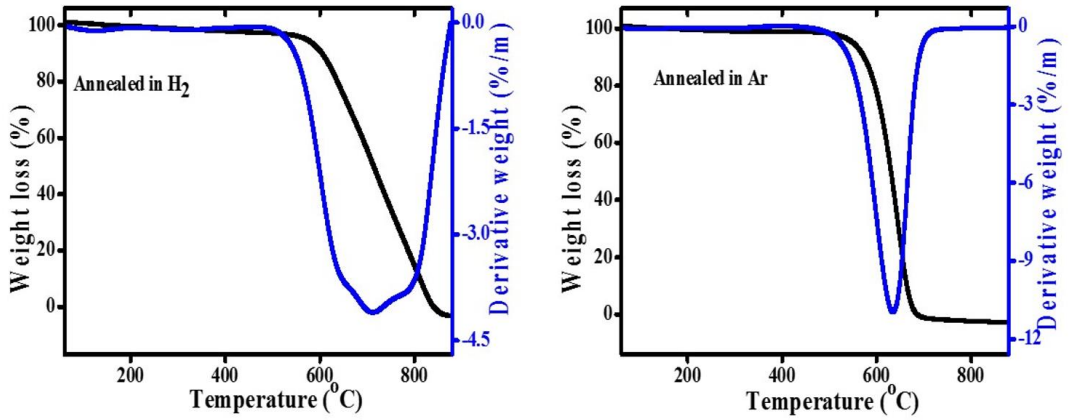

Figure 3.15. Thermal gravimetric curves of annealed solid carbon spheres synthesized at 200 sccm, Ar and 200 sccm, C_2H_2.

3.4.3 Characterization of N-doped carbon spheres

3.4.3.1 Morphology

TEM images (Fig. 3.16) showed that post N-doping of the carbon spheres did not vary their spherical morphology. However, the particle size of the post N-doped carbon spheres was slightly larger than the pristine carbon spheres. (Table 3.8).

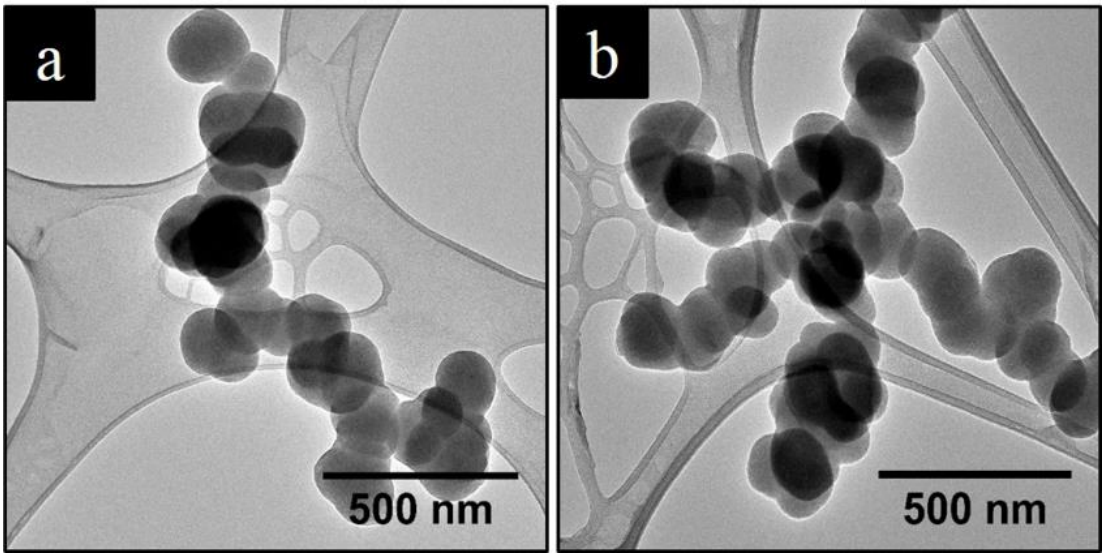

Figure 3.16. TEM images of (a) H_2, 100 sccm and 200 sccm, C_2H_2, post N-doped carbon spheres & (b) Ar, 200 sccm and 200 sccm, C_2H_2, post N-doped carbon spheres, respectively.

3.4.3.2 Raman analysis

Doping of the carbon spheres with nitrogen also led to an increase in the I_D/I_G ratios (Table 3.8). This results from defects induced in the carbon structure after nitrogen doping[71]. This is corroborated by the higher full width half maxima (FWHM) in the N-doped carbon spheres relative to the pristine carbon spheres as characterized by the D and G peaks (Fig. 3.17). Disorder in carbon materials is characterized by an increase in FWHM and an upshift of the D band to higher wavenumbers[72, 73]. The N-doped carbon spheres synthesized in hydrogen resulted in more defects as corroborated by the I_D/I_G ratios (Table 3.8). A detailed explanation on the type of N defects induced in the carbon spheres is given in XPS section 3.4.4.

Table 3.8. Effect of N doping on the particle sizes and I_D/I_G ratios of the carbon spheres

Synthesis parameters		Particle size (nm)	D band position (cm^{-1})	G band position (cm^{-1})	I_D/I_G ratio
Pristine	**H_2 100 sccm & C_2H_2 200 sccm**	186 ± 34	1333	1593	0.89
	Ar 200 sccm & C_2H_2 200 sccm	186 ± 19	1340	1595	0.88
Post N-doped	**H_2 100 sccm & C_2H_2 200 sccm**	200 ± 44	1364	1595	1.02
	Ar 200 sccm & C_2H_2 200 sccm	189 ± 20	1321	1591	0.92

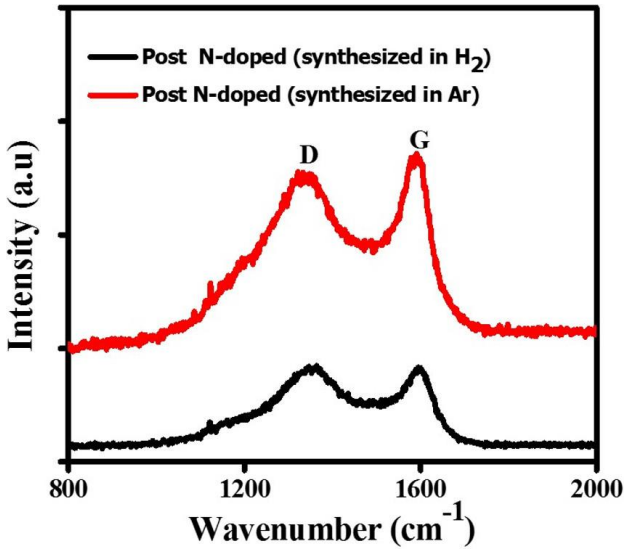

Figure 3.17. Raman spectra post N-doped carbon spheres.

3.4.3.3 Thermal gravimetric analysis

Both the pristine and N-doped carbon spheres gave zero mass residues (0% w/w) after decomposition indicating high level of purity. Post N-doping of the carbon spheres with nitrogen decreased their thermal stability (Fig. 3.18). The increase in defects upon N-doping corroborated with Raman data with a corresponding increase in the I_D/I_G ratios. The decrease in thermal stability with N incorporation is attributed to structural disorder and defects brought about by the presence of N in the carbon lattice[74-76]. In the N-doped carbon spheres synthesized using argon gas, two decomposition peaks were observed at 418°C to 495°C and 520°C to 650°C respectively (Fig. 3.18b). The steepness of the peak slopes suggest the existence of dangling bonds resulting in a rapid oxidative degradation[77]. In contrast, three decomposition peaks were observed at 395°C to 480°C, 529°C to 600°C and 600°C to 610°C in the N-doped carbon spheres synthesized using hydrogen gas (Fig. 3.18a). The decrease in the onset decomposition temperature could be attributed to less thermal stability owing to defects. In this study, the presence of argon as a carrier gas during the post N-doping treatment of the carbon spheres could have resulted in further defects.

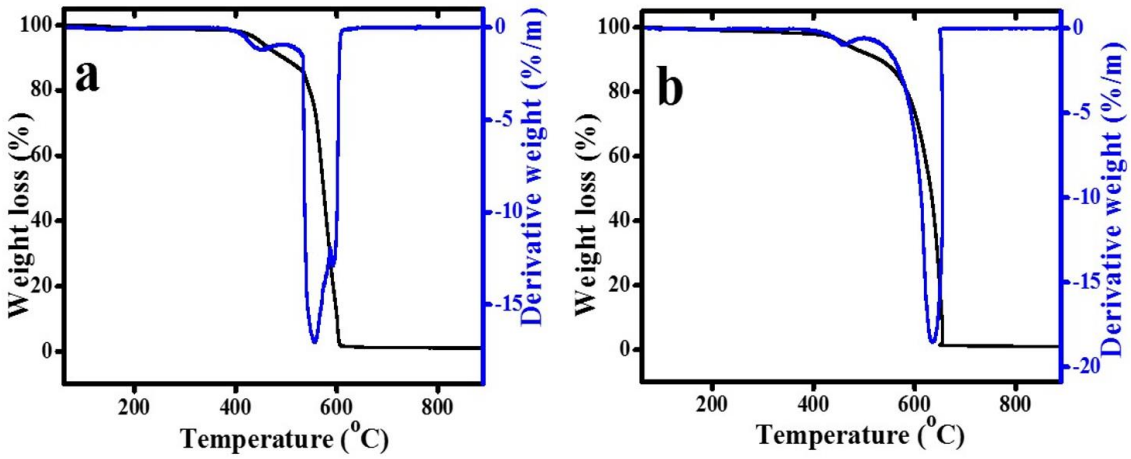

Figure 3.18. Thermal gravimetric curves of obtained pristine solid carbon spheres at different conditions; (a) H_2, 100 sccm and 200 sccm, C_2H_2 post N-doped and (b) Ar, 200 sccm and 200 sccm, C_2H_2 post N-doped carbon spheres, respectively.

3.4.3.4 BET surface area analysis of the pristine, annealed and N-doped carbon spheres

Surface area analysis showed a slight change in the surface areas of the carbon spheres after annealing in both hydrogen and argon gas (Table 3.9). However the surface areas of the carbon spheres are very low (9 and 6 m^2/g) with no change in the pore volume indicating that the surface was non-porous (Fig. 3.19). Annealing of the carbon spheres in either hydrogen or argon gas resulted in an increase in the BET surface areas as shown in Table 3.9. The slightly higher surface area of the CSs synthesized and annealed in H_2 can be attributed to the hydrogen etching of the carbon atoms. A similar increase in BET surface area was reported by Mhlanga *et al.* after heating carbon spheres in N_2 at 800°C[59]. The carbon spheres synthesized in hydrogen portrayed a slight decrease in surface area after N doping while those synthesized in argon gas exhibited an increase in the surface area (Fig 3.20).

Table 3.9. Effect of annealing and N-doping on the surface areas of the carbon spheres

Synthesis parameters	Condition	BET surface area (m^2/g)	Pore volume (cm^3/g)
H_2 100 sccm & C_2H_2 200 sccm	pristine	9	0.03
	annealed in H_2	14	0.04
	annealed in Ar	10	0.02
	post N-doped	7	0.03
Ar 200 sccm & C_2H_2 200 sccm	pristine	6	0.04
	annealed in H_2	11	0.04
	annealed in Ar	12	0.04
	post N-doped	11	0.04

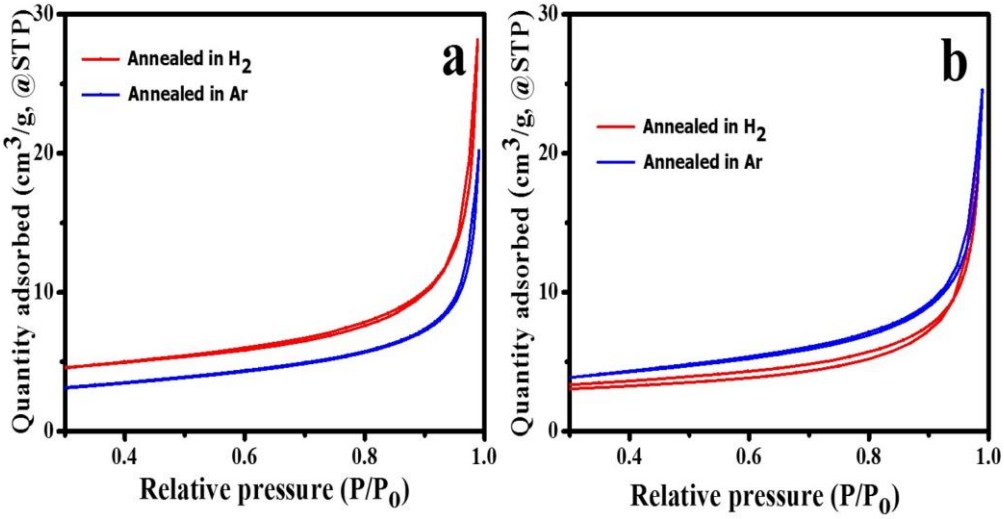

Figure 3.19. The N_2-adsorption and desorption isotherms of annealed carbon spheres synthesized at (a) H_2, 100 sccm and C_2H_2, 200 sccm, (b) Ar, 200 sccm and C_2H_2 200 sccm, respectively.

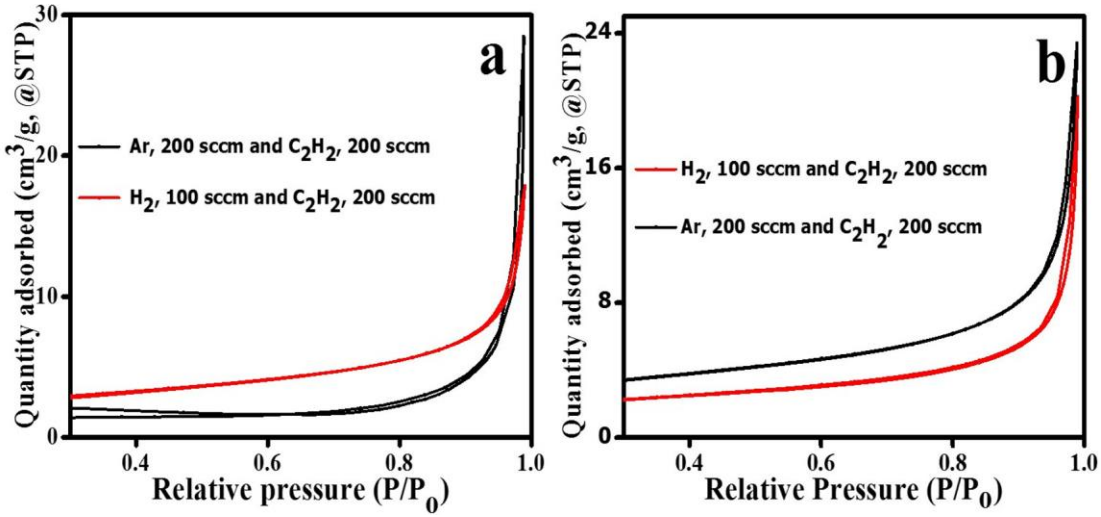

Figure 3.20. The N_2-adsorption and desorption isotherms of (a) pristine carbon spheres and (b) post N-doped carbon spheres, respectively.

3.4.3.5 Continuous wave electron spin resonance (CW ESR) analysis

All samples exhibited ESR response centered at g ≈ 2. ESR spectra of pristine, annealed and N doped carbon spheres showed Dysonian resonance curves implicating the presence of charge carriers[78] (Figs. 3.21-3.24). The spectra were recorded and are comparable to those of doped carbon nanotubes[79], N-doped carbon spheres[80] and pristine carbon spheres[81] reported in the literature. Carbon spheres synthesized using hydrogen as a carrier gas had a narrower paramagnetic resonance characteristic of delocalized spins and the presence of conduction electrons (Fig. 3.21a). In addition, they exhibited a larger peak to signal ratio indicating a more graphitic nature as corroborated by the Raman and TGA data (Table 3.6 and 3.7). In contrast, in the spheres synthesized under argon gas a broad paramagnetic resonance was observed. This can be ascribed to the presence of strongly localized electrons and dangling bonds leading to a weaker ESR signal[61, 82] (Fig. 3.21b). Annealing of the carbon spheres in the presence of hydrogen increased the superparamagnetic properties (Fig. 3.22a and 3.23a). This is confirmed by the larger peak to signal ratio observed after annealing the carbon spheres in H_2. However, annealing of the different carbon spheres in the presence of argon gas resulted in broader and less intense peaks with a low peak to signal ratio (Fig. 3.22b and 3.23b). This is similar to a low peak to signal ratio reported for CNTs synthesized in argon by Zhang *et al.*[83]. The broader line width of the CSs annealed in Ar can be attributed to a more disordered state within the microstructure resulting in a faster oxidation rate as confirmed by the sharp derivative curve in TGA (Figs. 3.14 and 3.15).

Fig. 3.24 shows that N-doping of the carbon spheres led to larger paramagnetic signals due to a stronger paramagnetic signal[84]. In both cases, the N-doped spheres (Fig. 3.24) exhibited a larger linewidth than their pristine counterparts (Fig. 3.21). This can be attributed to the defects created by nitrogen in the carbon spheres. The broad ESR signal in the N-doped spheres synthesized in argon can be ascribed to the substitution of the carbon with nitrogen within the carbon matrix. However, the peak to signal ratio of the N-doped CSs obtained using H_2 was higher than that obtained from Ar. This can be attributed to the additional edge defects induced in the CSs and a broad particle size distribution in the presence of H_2 as confirmed by the particle size data (Table 3.8). Consequently, a stronger ESR signal intensity was exhibited in the N-doped CSs synthesized in H_2 than in argon gas. This indicates the presence of more nitrogen induced defects in the carbon spheres synthesized in H_2 than those synthesized in argon as seen from the Raman I_D/I_G ratios (Table 3.8).

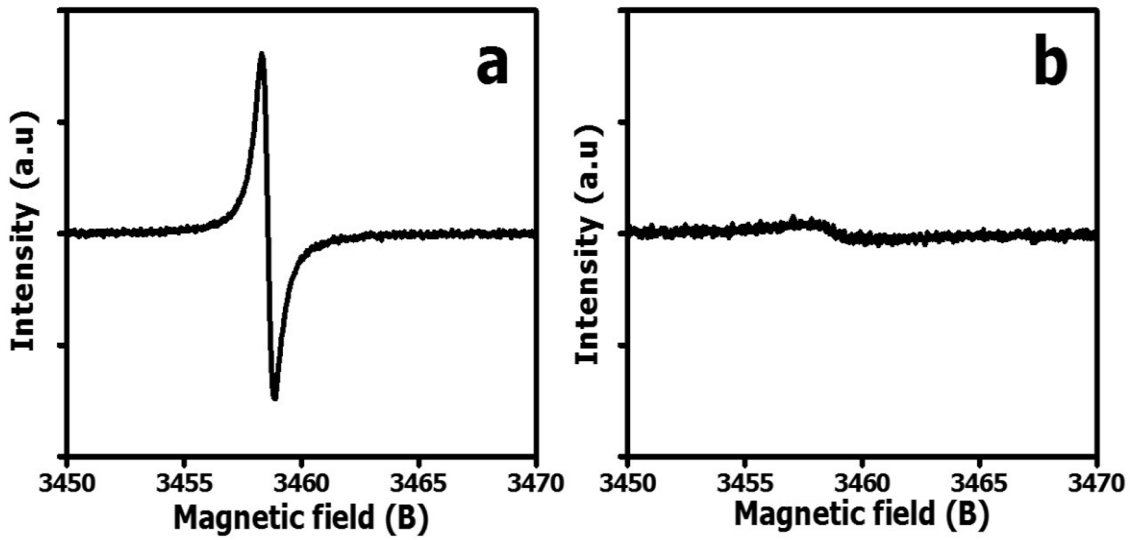

Figure 3.21. Electron spin resonance spectra of the pristine carbon spheres obtained using (a) H_2, 100 sccm & C_2H_2, 200 sccm and (b) Ar, 200 sccm & C_2H_2, 200 sccm, respectively.

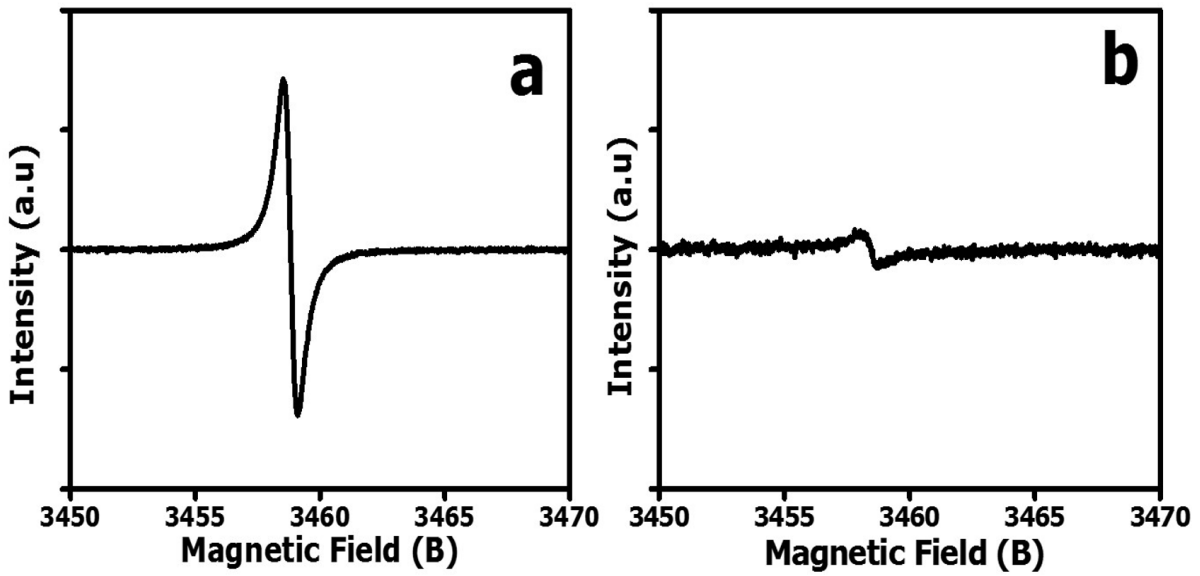

Figure 3.22. Electron spin resonance spectra of obtained with Ar, 200 sccm and C_2H_2, 200 sccm; (a) annealed in H_2 and (b) annealed in Ar, respectively.

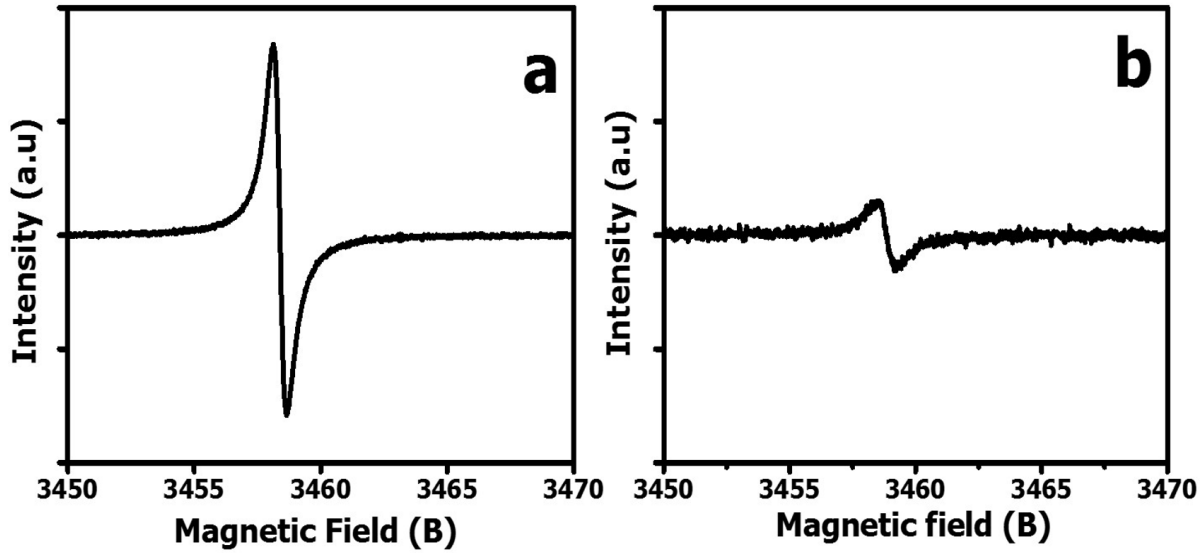

Figure 3.23. Electron spin resonance spectra of obtained with H_2, 100 sccm and C_2H_2, 200 sccm; (a) annealed in H_2 and (b) annealed in Ar, respectively.

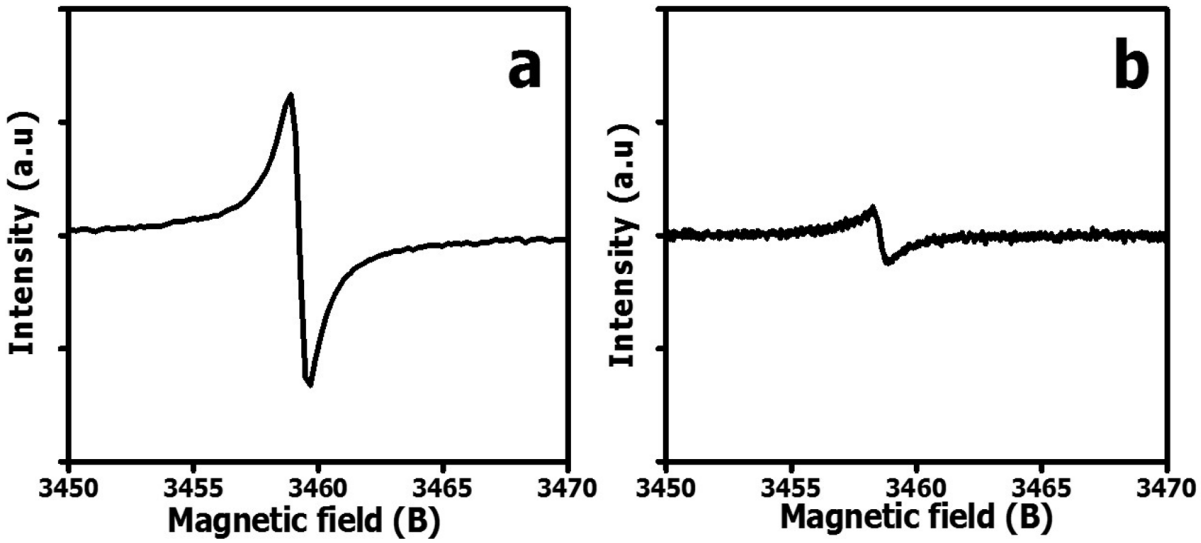

Figure 3.24. Electron spin resonance spectra of N-doped carbon spheres synthesized in (a) H_2 and (b) Ar gas.

3.4.4 XPS analysis of annealed and N-doped solid carbon spheres

The elemental composition (at %) of both annealed and post N-doped carbon spheres were determined from the integral peak areas of the XPS survey spectra (Table 3.10). It can be observed that the carbon content was higher in the carbon spheres synthesized or annealed in the presence of Ar. Consequently, the O content and the O/C ratio was higher in the carbon spheres synthesized or annealed in the presence of H_2. This could indicate the effect of hydrogen etching on the carbon spheres resulting in a lower C content and high O content. The nitrogen content in the carbon spheres synthesized using H_2 as carrier gas was higher (4.96) than in the carbon spheres obtained using Ar (3.68). Consequently, a higher N/C ratio was exhibited in the N-doped CSs obtained in the presence of H_2. This is due to the presence of edge dangling bonds as defects in carbon spheres synthesized in the presence of H_2 gas.

Table 3.10. Atomic compositions of annealed and N-doped carbon spheres

Elements / Samples	C (at %)	N (at %)	O (at %)	N/C (at %)	O/C (at %)
CSs annealed in H_2	95.90	-	4.10	-	4.28
CSs annealed in Ar	97.48	-	2.52	-	2.59
N-doped CSs synthesized in H_2	91.84	4.55	3.61	4.96	3.91
N-doped CSs synthesized in Ar	94.21	3.47	2.33	3.68	2.47

The XPS spectra showing the chemical environment of the C, N and O atoms in the annealed and N-doped carbon spheres are shown in Figs. 3.25 to 3.27, respectively. The bonding states of C 1s spectrum was deconvoluted into two peaks centered at 283.95 eV and 284.85 eV in the carbon spheres annealed in H_2 and at 283.94 eV and 284.95 eV in those annealed in Ar respectively (Fig. 3.23a and c). The lower binding energy region (< 284.50 eV) correspond to the sp^2 C=C bonds and the higher binding energy region correspond to sp^3 C-C bonds close to that of graphite[85, 86]. This indicated that the carbon spheres comprised of sp^2 and sp^3 hybridized carbon. The carbon spheres annealed in H_2 exhibited a higher percentage of sp^2 C=C bonds than those annealed under argon gas. This is in agreement with the higher thermal stability (TGA data) and fewer defects (Raman data) exhibited by the carbon spheres annealed in H_2. Fig. 3.25b shows a narrower peak with a full width at half maxima (FWHM) of 3.46 and an increase in peak intensity of the O1s spectrum of the carbon spheres annealed in H_2 relative to those annealed in Ar with a FWHM of 3.70 (Fig. 3.25d); this corroborates with the high O/C ratio reported in Table 3.10. The presence of higher oxygen content in the carbon spheres annealed under H_2 confirms the hydrogen induced etching of the carbon spheres.

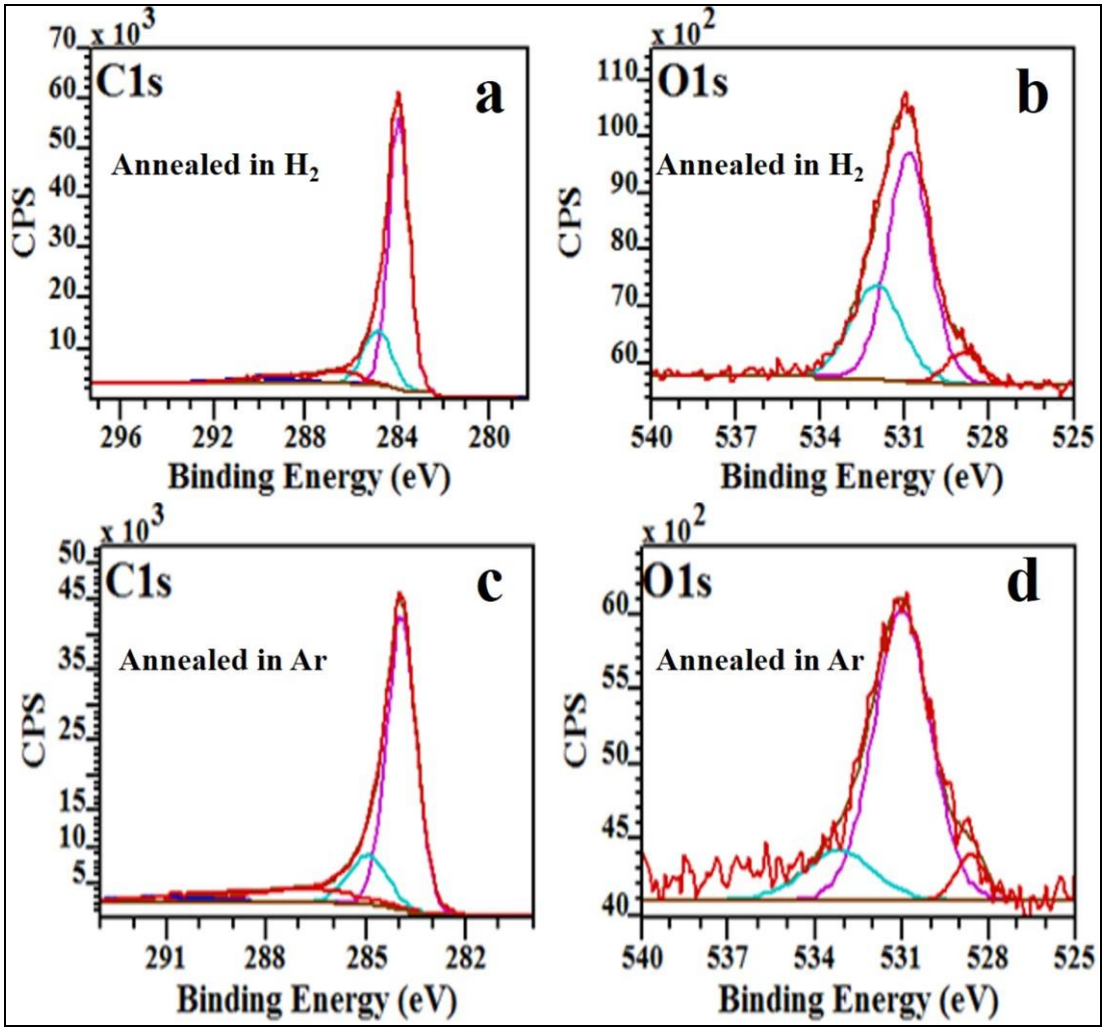

Figure 3.25. The XPS spectra of deconvoluted C 1s and O 1s peaks of carbon spheres; (a and b) annealed in H_2 and (c and d) annealed in Ar, respectively.

In the N-doped carbon spheres, sp^2 C=C bonds were observed at 283.92 eV and 283.93 eV in the carbon spheres synthesized in H_2 and Ar, respectively (Fig. 3.26a and c). Two peaks were convoluted at (284.72 -284.65) eV and (285.47 – 285.18) eV in the N-doped carbon spheres. These peaks can be assigned to carbon bonded to nitrogen atoms which are more electronegative[87] forming sp^3 C-N and sp^2 C=N bonding configurations, respectively[88].

The N 1s spectrum of the N-doped carbon spheres synthesized in the presence of H_2 was deconvoluted into four component peaks centered at 398.30 eV, 399.64 eV, 400.85 eV and 402.60 eV, respectively (Fig. 3.26b). In the N-doped carbon spheres synthesized in Ar, the

four component peaks were centered at 397.78 eV, 398.83 eV, 400.79 eV and 402.74 eV, respectively (Fig 3.26d). The four peaks detected were assigned to; (i) pyridinic-N at 397.78 – 398.30 eV with the N atom contributing one electron to the p-system, (ii) pyrrolic-N at 398.83 – 399.64 eV with the N atom contributing two electrons to the p-system, (iii) quaternary-N (400.79 – 400.85 eV) with the N atom substituting the C atom in the graphitic structure[45, 89] and (iv) pyridinic oxide bonds due to oxygenation of pyridinic-N (> 402 eV)[87, 90, 91]. The N-doped carbon spheres synthesized in H_2 comprised of 48% pyridinic-N, 22% pyrrolic-N and 24% quaternary-N while the N-doped spheres obtained in the presence of Ar had 17% pyridinic-N, 20% pyrrolic-N and 49% quaternary-N (Table 3.11).

The presence of a lower percentage of pyridinic N^+-O^- configuration (7%) in the carbon spheres synthesized under H_2 gas can be attributed to fewer oxygen atoms bonded to the edge defects (Table 3.11). In contrast, a higher percentage of pyridinic-N^+-O^- (14%) in the carbon spheres annealed in argon indicate that most of the oxygen atoms are bonded to the edges. The O1s XPS spectrum (Fig. 3.27a and b) indicates that most of the oxygen atoms are bonded to the carbon and the pyridinic-N in all the N doped carbon spheres. Interestingly, the overall intensity of the oxygen bonds is higher in the carbon spheres synthesized under H_2 than in those synthesized under argon gas (Fig 3.27a versus 3.27b). In addition, the pyridinic-N has fewer oxygen atoms and more pronounced edge defects. *Matter et. al.* reported a higher oxygen reduction reactivity and conductivity in carbon samples with higher pyridinic-N content[92] due to a larger edge plane exposure. The facilitating role of pyridinic-N species in oxygen reduction reaction (ORR) has been reported by other researchers[93, 94]. However, most of ORR activity are carried out in the presence of metal catalysts thus, the role of the metal in the catalytic activity cannot be ignored. Our studies report the presence of edge defects in carbon spheres synthesized without the aid of a metal catalyst and thus, opens a platform towards the use of hydrogen as a carrier gas to induce open edge defects in carbon for enhanced surface and catalytic reactions.

Table 3.11. Summary of % concentration of N-configurations for N-doped solid carbon spheres

Peaks / Samples	% Concentration of configurations			
	Pyridinic-N (eV)	**Pyrrolic-N (eV)**	**Graphitic-N (eV)**	**Pyridinic N^+- O^- (eV)**
N-doped CSs synthesized in H_2	48.11	21.59	23.72	6.59
N-doped CSs synthesized in Ar	17.08	19.80	49.39	13.74

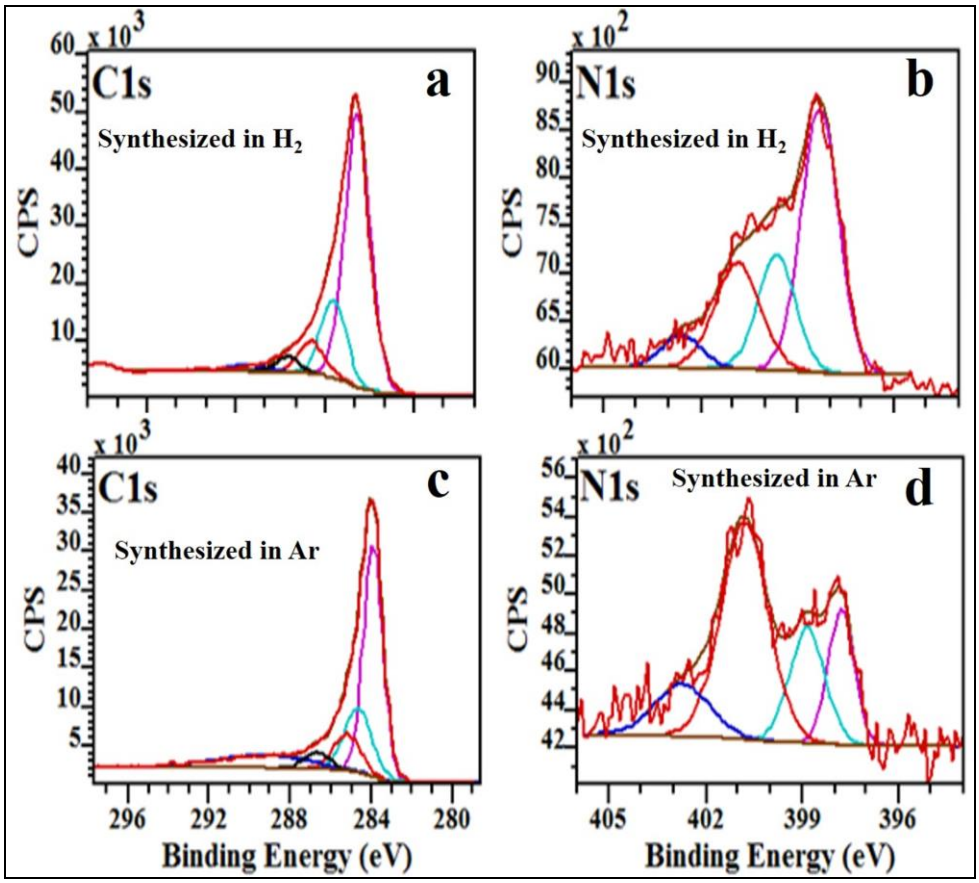

Figure 3.26. The XPS spectra of deconvoluted C 1s and N 1s peaks of post N-doped carbon spheres; (a and b) synthesized in H_2 and (c and d) synthesized in Ar, respectively.

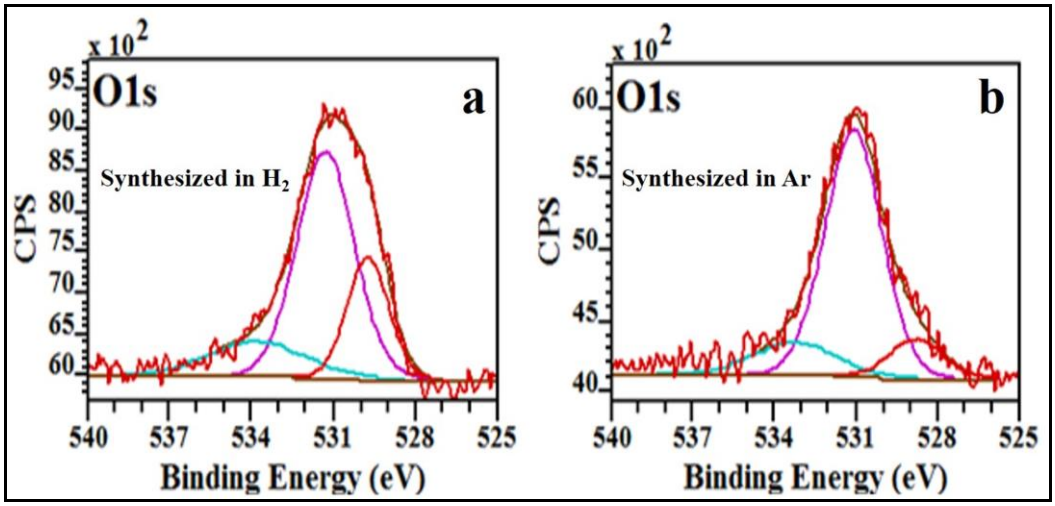

Figure 3.27. The XPS spectra of deconvoluted O 1s peaks of post N-doped carbon spheres; (a) synthesized in H_2 and (b) synthesized in Ar, respectively.

3.5 Conclusions

Carbon spheres of varying particle sizes were synthesized by altering the acetylene and carrier gas flow rates. Use of high flow rates of either the carbon source or carrier gas resulted in the production of smaller carbon spheres. In contrast, at low flow rates of carbon source, larger carbon spheres were obtained. This could be attributed to the longer duration time of carbon source at low flow rates. All the synthesized carbon spheres exhibited a low degree of graphitization as characterized by the low I_D/I_G ratios from Raman data. All the carbon spheres obtained maintained a spherical morphology after annealing and N-doping. Annealing of carbon spheres in hydrogen resulted in a thermal stability of the carbon spheres relative to those annealed in argon gas. Raman data showed the presence of fewer defects, narrower FWHM and lower I_D/I_G ratios in carbon spheres annealed in hydrogen. In contrast, carbon spheres annealed in argon exhibited an increase in the number of defects and a consequent decrease in thermal stability compared to the pristine carbon spheres. Electron spin resonance spectra of carbon spheres annealed in hydrogen indicated a narrower paramagnetic signal and a broad paramagnetic signal in carbon spheres annealed in argon gas. Doping of the carbon spheres with N resulted in an increase in I_D/I_G ratios, lesser thermal stability and stronger paramagnetic signals.

The XPS spectra confirmed the presence of edge defect states in the carbon spheres synthesized or annealed in H_2 gas; characterized by a low C content and a high O/C ratio. All

the N-doped carbon spheres exhibited pyridinic, pyrrolic and quaternary nitrogen configurations. Post N-doping of carbon spheres synthesized in H_2 resulted in higher compositions of pyridinic-N, low content of quaternary-N and higher N% compared to N doped carbon spheres obtained in Ar gas. This study clearly illustrates the effect of annealing carbon spheres in different carrier gases on their magnetic and thermal properties. The ESR and XPS data shows that the synthesis and annealing of carbon spheres in the presence of hydrogen creates a more edge defects and a larger active surface area; opening a plausible application of such carbon materials in electrocatalysis.

References

1. Iijima, S. *Nature* **1991,** 354, (6348), 56-58.
2. Kroto, H. W.; Heath, J. R.; O'Brien, S. C.; Curl, R. F.; Smalley, R. E. *Nature* **1985,** 318, (6042), 162-163.
3. Wang, Q.; Li, H.; Chen, L.; Huang, X. *Carbon* **2001,** 39, (14), 2211-2214.
4. Pol, V. G.; Motiei, M.; Gedanken, A.; Calderon-Moreno, J.; Yoshimura, M. *Carbon* **2004,** 42, (1), 111-116.
5. Deshmukh, A. A.; Mhlanga, S. D.; Coville, N. J. *Materials Science and Engineering: R: Reports* **2010,** 70, (1–2), 1-28.
6. Sharon, M.; Mukhopadhyay, K.; Yase, K.; Iijima, S.; Ando, Y.; Zhao, X. *Carbon* **1998,** 36, (5–6), 507-511.
7. Biró, L. P.; Márk, G. I.; Horváth, Z. E.; Kertész, K.; Gyulai, J.; Nagy, J. B.; Lambin, P. *Carbon* **2004,** 42, (12–13), 2561-2566.
8. Inagaki, M. *Carbon* **1997,** 35, (5), 711-713.
9. Serp, P.; Feurer, R.; Kalck, P.; Kihn, Y.; Faria, J. L.; Figueiredo, J. L. *Carbon* **2001,** 39, (4), 621-626.
10. Kang, Z. C.; Wang, Z. L. *The Journal of Physical Chemistry* **1996,** 100, (13), 5163-5165.
11. Lawes, S.; Riese, A.; Sun, Q.; Cheng, N.; Sun, X. *Carbon* **2015,** 92, 150-176.
12. Alazemi, A. A.; Etacheri, V.; Dysart, A. D.; Stacke, L.-E.; Pol, V. G.; Sadeghi, F. *ACS Applied Materials & Interfaces* **2015,** 7, (9), 5514-5521.
13. Hummelgen, I. A.; Coville, N. J.; Cruz-Cruz, I.; Rodrigues, R. *Journal of Materials Chemistry C* **2014,** 2, (37), 7708-7714.
14. Machado, W. S.; Athayde, P. L.; Mamo, M. A.; van Otterlo, W. A. L.; Coville, N. J.; Hümmelgen, I. A. *Organic Electronics* **2010,** 11, (11), 1736-1739.
15. Jin, Y. Z.; Gao, C.; Hsu, W. K.; Zhu, Y.; Huczko, A.; Bystrzejewski, M.; Roe, M.; Lee, C. Y.; Acquah, S.; Kroto, H.; Walton, D. R. M. *Carbon* **2005,** 43, (9), 1944-1953.
16. Sawant, S. Y.; Senthilkumar, S.; Somani, R. S.; Cho, M. H.; Bajaj, H. C. *RSC Advances* **2015,** 5, (70), 57114-57121.
17. Wang, C.; Wang, Y.; Graser, J.; Zhao, R.; Gao, F.; O'Connell, M. J. *ACS Nano* **2013,** 7, (12), 11156-11165.
18. Krishnamurthy, G.; Namitha, R.; Agarwal, S. *Procedia Materials Science* **2014,** 5, 1056-1065.
19. Chen, C.; Sun, X.; Jiang, X.; Niu, D.; Yu, A.; Liu, Z.; Li, J. *Nanoscale Research Letters* **2009,** 4, (9), 971-976.
20. Dlamini, M. W.; Kumi, D. O.; Phaahlamohlaka, T. N.; Lyadov, A. S.; Billing, D. G.; Jewell, L. L.; Coville, N. J. *ChemCatChem* **2015,** 7, (18), 3000-3011.
21. Creighton, J.; Ho, P. *Chemical Vapor Deposition* **2001,** 2, 1-22.
22. Qian, H.-s.; Han, F.-m.; Zhang, B.; Guo, Y.-c.; Yue, J.; Peng, B.-x. *Carbon* **2004,** 42, (4), 761-766.
23. Ray, S. C.; Tetana, Z. N.; Erasmus, R.; Mathur, A.; Coville, N. J. *International Journal of Energy Research* **2014,** 38, (4), 444-451.
24. Poinern, G. E. J.; Brundavanam, S.; Shah, M.; Laava, I.; Fawcett, D. *Nanotechnology, Science and Applications* **2012,** 5, 49-59.
25. Xiong, H.; Motchelaho, M. A. M.; Moyo, M.; Jewell, L. L.; Coville, N. J. *Journal of Catalysis* **2011,** 278, (1), 26-40.
26. Davies, R. A.; Scully, D. B. *Combustion and Flame* **1966,** 10, (2), 165-170.
27. Mhlanga, S. D.; Mondal, K. C.; Naidoo, N.; Kunjuzwa, N.; Witcomb, M. J.; Coville, N. J. *South African Journal of Science* **2009,** 105, 304-308.

28. Young Lee, T.; Han, J.-H.; Hong Choi, S.; Yoo, J.-B.; Park, C.-Y.; Jung, T.; Yu, S.; Yi, W. K.; Han, I. T.; Kim, J. M. *Diamond and Related Materials* **2003,** 12, (3–7), 851-855.
29. Behr, M. J.; Gaulding, E. A.; Mkhoyan, K. A.; Aydil, E. S. *Journal of Vacuum Science & Technology B* **2010,** 28, (6), 1187-1194.
30. Zhang, R.; Chu, T.; Lee, C. S.; Lee, S. T. *Chemical Vapor Deposition* **2000,** 6, (5), 227-230.
31. Losurdo, M.; Giangregorio, M. M.; Capezzuto, P.; Bruno, G. *Physical Chemistry Chemical Physics* **2011,** 13, (46), 20836-20843.
32. Liang, C.; Wang, W.; Li, T.; Wang, Y. In *Hydrogen etching effect on single-crystal graphene domains*, Nano/Micro Engineered and Molecular Systems (NEMS), 2013 8th IEEE International Conference on, 2013; IEEE: pp 697-700.
33. Zhang, X.; Ning, J.; Li, X.; Wang, B.; Hao, L.; Liang, M.; Jin, M.; Zhi, L. *Nanoscale* **2013,** 5, (18), 8363-8366.
34. Zhang, Y.; Li, Z.; Kim, P.; Zhang, L.; Zhou, C. *ACS Nano* **2012,** 6, (1), 126-132.
35. Bulusheva, L. G.; Okotrub, A. V.; Kurenya, A. G.; Zhang, H.; Zhang, H.; Chen, X.; Song, H. *Carbon* **2011,** 49, (12), 4013-4023.
36. Hulicova, D.; Kodama, M.; Hatori, H. *Chemistry of Materials* **2006,** 18, (9), 2318-2326.
37. Shao, Y.; Sui, J.; Yin, G.; Gao, Y. *Applied Catalysis B: Environmental* **2008,** 79, (1), 89-99.
38. Liu, X. W.; Lin, C. H.; Chao, L. T.; Shih, H. C. *Materials Letters* **2000,** 44, (5), 304-308.
39. Wang, L.; Gao, Z.; Chang, J.; Liu, X.; Wu, D.; Xu, F.; Guo, Y.; Jiang, K. *ACS Applied Materials & Interfaces* **2015,** 7, (36), 20234-20244.
40. Gao, S.; Geng, K.; Liu, H.; Wei, X.; Zhang, M.; Wang, P.; Wang, J. *Energy & Environmental Science* **2015,** 8, (1), 221-229.
41. Wei, D.; Liu, Y.; Wang, Y.; Zhang, H.; Huang, L.; Yu, G. *Nano Letters* **2009,** 9, (5), 1752-1758.
42. García-García, F. R.; Álvarez-Rodríguez, J.; Rodríguez-Ramos, I.; Guerrero-Ruiz, A. *Carbon* **2010,** 48, (1), 267-276.
43. Lee, W.-h.; Moon, J. H. *ACS Applied Materials & Interfaces* **2014,** 6, (16), 13968-13976.
44. Vinu, A.; Anandan, S.; Anand, C.; Srinivasu, P.; Ariga, K.; Mori, T. *Microporous and Mesoporous Materials* **2008,** 109, (1–3), 398-404.
45. Xiong, H.; Moyo, M.; Motchelaho, M. A.; Tetana, Z. N.; Dube, S. M. A.; Jewell, L. L.; Coville, N. J. *Journal of Catalysis* **2014,** 311, 80-87.
46. Yang, Z.; Xia, Y.; Sun, X.; Mokaya, R. *The Journal of Physical Chemistry B* **2006,** 110, (37), 18424-18431.
47. Zhao, L.; Baccile, N.; Gross, S.; Zhang, Y.; Wei, W.; Sun, Y.; Antonietti, M.; Titirici, M.-M. *Carbon* **2010,** 48, (13), 3778-3787.
48. Wickramaratne, N. P.; Xu, J.; Wang, M.; Zhu, L.; Dai, L.; Jaroniec, M. *Chemistry of Materials* **2014,** 26, (9), 2820-2828.
49. Zhou, X.; Yang, Z.; Nie, H.; Yao, Z.; Zhang, L.; Huang, S. *Journal of Power Sources* **2011,** 196, (23), 9970-9974.
50. Xiong, H.; Moyo, M.; Rayner, M. K.; Jewell, L. L.; Billing, D. G.; Coville, N. J. *ChemCatChem* **2010,** 2, (5), 514-518.
51. Santos, E. G.; Ayuela, A.; Sánchez-Portal, D., First-Principles Study of the Electronic and Magnetic Properties of Defects in Carbon Nanostructures. In *Topological Modelling of Nanostructures and Extended Systems*, Springer Netherlands: 2013; Vol. 7, pp 41-76.

52. Rode, A. V.; Gamaly, E. G.; Christy, A. G.; Fitz Gerald, J. G.; Hyde, S. T.; Elliman, R. G.; Luther-Davies, B.; Veinger, A. I.; Androulakis, J.; Giapintzakis, J. *Physical Review B* **2004,** 70, (5), 054407.
53. Soxhlet, F. v. *Polytechnisches J* **1879,** 232, 461-465.
54. Takai, K.; Oga, M.; Enoki, T.; Taomoto, A. *Diamond and Related Materials* **2004,** 13, (4–8), 1469-1473.
55. Emmerich, F. G. *Carbon* **1995,** 33, (12), 1709-1715.
56. Raj, K. G.; Joy, P. A. *Physical Chemistry Chemical Physics* **2015,** 17, (24), 16178-16185.
57. Calderón-Moreno, J. M.; Labarta, A.; Batlle, X.; Pradell, T.; Crespo, D.; Binh, V. T. *Chemical Physics Letters* **2007,** 447, (4–6), 295-299.
58. Wu, H.-C.; Hong, C.-T.; Chiu, H.-T.; Li, Y.-Y. *Diamond and Related Materials* **2009,** 18, (4), 601-605.
59. Mhlanga, S.; Coville, N.; Iyuke, S.; Afolabi, A.; Abdulkareem, A.; Kunjuzwa, N. *Journal of Experimental Nanoscience* **2010,** 5, (1), 40-51.
60. Tetana, Z. N. Boron and Nitrogen Doped Carbons for Photochemical Degradation Reactions. The University of the Witwatersrand, Johannesburg, 2013.
61. Pol, V. G.; Pol, S. V.; Calderon Moreno, J. M.; Gedanken, A. *Carbon* **2006,** 44, (15), 3285-3292.
62. Kang, Z. C.; Wang, Z. L. *Philosophical Magazine Part B* **1996,** 73, (6), 905-929.
63. Ferrari, A. C. *Solid State Communications* **2007,** 143, (1–2), 47-57.
64. Tuinstra, F.; Koenig, J. L. *The Journal of Chemical Physics* **1970,** 53, (3), 1126-1130.
65. Arnal, P. M.; Schüth, F.; Kleitz, F. *Chemical Communications* **2006**, (11), 1203-1205.
66. Andrews, R.; Jacques, D.; Qian, D.; Dickey, E. C. *Carbon* **2001,** 39, (11), 1681-1687.
67. Huang, W.; Wang, Y.; Luo, G.; Wei, F. *Carbon* **2003,** 41, (13), 2585-2590.
68. Jin, Y. Z.; Kim, Y. J.; Gao, C.; Zhu, Y. Q.; Huczko, A.; Endo, M.; Kroto, H. W. *Carbon* **2006,** 44, (4), 724-729.
69. Ci, L.; Zhu, H.; Wei, B.; Xu, C.; Wu, D. *Applied Surface Science* **2003,** 205, (1–4), 39-43.
70. Miao, J.-Y.; Hwang, D. W.; Chang, C.-C.; Lin, S.-H.; Narasimhulu, K. V.; Hwang, L.-P. *Diamond and Related Materials* **2003,** 12, (8), 1368-1372.
71. Ibrahim, E. M. M.; Khavrus, V. O.; Leonhardt, A.; Hampel, S.; Oswald, S.; Rümmeli, M. H.; Büchner, B. *Diamond and Related Materials* **2010,** 19, (10), 1199-1206.
72. Ferrari, A. C. *Solid State Communications* **2007,** 143, (1), 47-57.
73. Jorio, A.; Achete, C. A.; Ferreira, E. H. M.; Cançado, L. G.; Capaz, R. B., *Measuring disorder in graphene with Raman spectroscopy*. INTECH Open Access Publisher: 2011.
74. Ma, X.; Wang, E.; Zhou, W.; Jefferson, D. A.; Chen, J.; Deng, S.; Xu, N.; Yuan, J. *Applied Physics Letters* **1999,** 75, (20), 3105-3107.
75. Kurt, R.; Karimi, A. *ChemPhysChem* **2001,** 2, (6), 388-392.
76. Nxumalo, E. N.; Letsoalo, P. J.; Cele, L. M.; Coville, N. J. *Journal of Organometallic Chemistry* **2010,** 695, (24), 2596-2602.
77. Nikiwe, K. The synthesis of nitrogen doped carbon spheres and polythiophene/carbon sphere composites. Ph. D. thesis, University of the Witwatersrand, Johannesburg, 2009.
78. Joshi, J. P.; Bhat, S. V. *Journal of Magnetic Resonance* **2004,** 168, (2), 284-287.
79. Mondal, K. C.; Strydom, A. M.; Erasmus, R. M.; Keartland, J. M.; Coville, N. J. *Materials Chemistry and Physics* **2008,** 111, (2–3), 386-390.
80. Wright, W. P.; Marsicano, V. D.; Keartland, J. M.; Erasmus, R. M.; Dube, S. M. A.; Coville, N. J. *Materials Chemistry and Physics* **2014,** 147, (3), 908-914.
81. Pol, V. G. *Environmental Science & Technology* **2010,** 44, (12), 4753-4759.

82. Calderon Moreno, J. M.; Swamy, S. S.; Fujino, T.; Yoshimura, M. *Chemical Physics Letters* **2000,** 329, (3–4), 317-322.
83. Zhang, H.; Liu, S.; Wei, A.; He, Y.; Tang, X.; Xue, X.; Liang, L.; Wu, C. *Journal of Physics and Chemistry of Solids* **2000,** 61, (7), 1123-1125.
84. Pol, V. G.; Calderon-Moreno, J. M.; Thiyagarajan, P. *Industrial & Engineering Chemistry Research* **2009,** 48, (12), 5691-5695.
85. Mérel, P.; Tabbal, M.; Chaker, M.; Moisa, S.; Margot, J. *Applied Surface Science* **1998,** 136, (1–2), 105-110.
86. Diaz, J.; Paolicelli, G.; Ferrer, S.; Comin, F. *Physical Review B* **1996,** 54, (11), 8064.
87. Biddinger, E. J.; von Deak, D.; Ozkan, U. S. *Topics in Catalysis* **2009,** 52, (11), 1566-1574.
88. Reddy, A. L. M.; Srivastava, A.; Gowda, S. R.; Gullapalli, H.; Dubey, M.; Ajayan, P. M. *ACS nano* **2010,** 4, (11), 6337-6342.
89. Grant, K. A.; Zhu, Q.; Thomas, K. M. *Carbon* **1994,** 32, (5), 883-895.
90. Zhu, Q.; Money, S. L.; Russell, A. E.; Thomas, K. M. *Langmuir* **1997,** 13, (7), 2149-2157.
91. Jia, Y. F.; Xiao, B.; Thomas, K. M. *Langmuir* **2002,** 18, (2), 470-478.
92. Matter, P. H.; Wang, E.; Arias, M.; Biddinger, E. J.; Ozkan, U. S. *The Journal of Physical Chemistry B* **2006,** 110, (37), 18374-18384.
93. Maldonado, S.; Stevenson, K. J. *The Journal of Physical Chemistry B* **2005,** 109, (10), 4707-4716.
94. Matter, P. H.; Wang, E.; Arias, M.; Biddinger, E. J.; Ozkan, U. S. *Journal of Molecular Catalysis A: Chemical* **2007,** 264, (1–2), 73-81.

CHAPTER 4

Synthesis and Characterization of Pristine and Mesoporous SiO_2 Spheres and their respective Hollow Carbon Nanostructures (HCSs)

4.1 Introduction

Silica can exist in various forms either synthetically or naturally and in both crystalline and amorphous forms. In plants, silica helps in growth and development[1, 2] while in animals silica exists in small quantities in the body to help in bone and brain formation[3, 4]. Silicon dioxide (SiO_2) is made of a SiO_4 tetrahedron with 4 oxygen atoms at its corners and a silicon ion at the centre. The four oxygen atoms of SiO_4 unit are in mutual contact due to the larger ionic radius of oxygen relative to that of the silicon ion. The SiO_4 tetrahedron comprises of Si-O bonds with a bond length 0.162 nm. This short bond length in SiO_2 accounts for the ionic character of the Si-O single bond and its thermodynamic stability[5].

According to the International Union of Pure and Applied Chemistry (IUPAC), a colloid system comprises of particles (sizes:1-1000 nm) dispersed in a continuous phase; solid, liquid or gaseous state of a different state or composition. In nanotechnology, materials comprising of nanometer dimensions are of considerable interest owing to their size tunability and unique size dependent properties. Colloidal SiO_2 nanoparticles are thus, interesting nanomaterials with versatile applications in optical filters[6], as binders[7], in sensors[8] and catalysts[9]. In addition, the properties of these materials can be varied by utilizing commonly known nanomaterial synthesis routes.

Solid SiO_2 particles can be synthesized mainly by the sol-gel[10] and the Stober method[11]. The sol-gel process entails hydrolysis and condensation of metal alkoxysilanes in monomer form to polymeric species[12]. In essence, SiO_2 formation follows a condensation polymerization and aggregation process. The condensation process is affected by the pH, temperature and the presence of small molecules and polymers[13]. Hence, the structure and properties of the SiO_2 can be varied by controlling the precursor molar ratio, the type and nature of catalysts, the

steric and inductive properties and the solvent polarity process parameters[14-17]. In 1968, Stober et al. studied the effect of water and ammonia on the shape of SiO_2 nanoparticles by hydrolyzing alkoxides in alcohols and alcohol mixtures using the Stober method[11]. Similar to the sol-gel method, hydrolysis of a SiO_2 precursor (tetraethyl orthosilicate) followed by condensation are the main reaction mechanism for SiO_2 production using the Stober route. In acidic conditions, a gel (a network of SiO_2 matrix) is obtained whereas under basic conditions a stable suspension is obtained. In the case of Stober SiO_2 spheres, a base catlyst (ammonia) is used to form a stable sol. The commonly explained SiO_2 growth models are the monomer addition model[18] and the controlled aggregation model[19, 20]. The primary factor in SiO_2 synthesis via either the sol-gel or the Stober route is the nucleation and growth that determines the kinetics and dynamics of it's size and shape[21, 22].

On the other hand, mesoporous SiO_2 can be defined as SiO_2 with pore sizes of 1.5 to 30 nm. The commonest synthesis technique to make mesoporous SiO_2 is the template method where a surfactant is used as a template[23]. A surfactant is a large molecule which has a hydrophilic head and a hydrophobic tail. In solution, a surfactant will form a micelle or a liquid crystal phase to maintain its lowest energy. Different surfactants have been used to synthesize mesoporous silica materials[24-26]. The mesoporous structure results from the formation of an inorganic-organic hybrid via self-assembly of the surfactant with the precursor material or the removal of the surfactant by high temperature calcination[27]. The advantage of using a surfactant is the ability to vary the pore diameter, pore morphology and pore size distribution by altering the alkyl length of surfactant or surfactant concentration using the template method[28, 29].

Apart from the use of surfactants, the use of organic compounds such as silane coupling agents to obtain mesoporous SiO_2 materials has also been reported[30]. These organic compounds direct the pore and surface structure to form a mesoporous material. Silane coupling agents such as octadecyltrimethoxysilane (C_{18}TMS) and organic polymers such as polyvinylpyrrolidone (PVP) have been used to obtain mesoporous silica[31-33]. Varying the concentration of the silane coupling agent, the organic polymer and their molar ratios affects the morphology and surface area properties of the mesoporous SiO_2 materials. As a result, these materials have been applied in drug delivery systems[34, 35], separation[36, 37], sensors[38, 39] and catalysis[40].

Solid and mesoporous SiO_2 materials can also be synthesized as core shell structures. Core shell structures are interesting nanomaterials that comprise of a core and shell of the same or different material. The template approach method of generating nanomaterials is one synthesis route for the production of core shell structures[41, 42]. In recent years, the coating of core shell particles with either an organic or inorganic shell with a broad range of chemical composition has been addressed[43, 44]. The ability to vary the chemical composition and surface properties and stability opens a way for the synthesis and subsequent application of these novel core shell particles[45]. Typically, a core shell particle can be converted to a hollow particle by core dissolution or decomposition[46]. Hollow carbon spheres are an example of hollow particles produced by dissolution of core particles such as SiO_2[47-49] or polystyrene[50]. Analogous to hollow particles by a template approach, these hollow carbon spheres have an added advantage in that their size, shape and morphology can be controlled by varying the properties of the template. Due to the tailorability of the surface properties (pore size and surface area to volume ratio), the hollow carbon spheres are applied in supercapacitors[51], fuel cells[52], batteries[53] and as a catalyst support[54].

In this chapter, the parameters for the synthesis of SiO_2 spheres with varying sizes were investigated. The optimal conditions for the growth of silica spheres was used in making of spherical SiO_2 based templates for the formation of hollow carbon spheres. A structure directing agent, C_{18}TMS was used to synthesis mesoporous silica spheres which were carbonized to yield porous hollow carbon nanostructures. Also,the mesoporous SiO_2 spheres were functionalized with PVP and used as templates for the generation of mesoporous hollow carbon nanostructures.

4.1.1 Objectives

i. To study the size and dispersity of SiO_2 spheres using a modified Stober method.
ii. To synthesize hollow carbon nanostructures using pristine, mesoporous and PVP functionalized SiO_2 spheres as templates.
iii. To investigate the role of particle size distribution on the hollow carbon nanostructure morphology.

4.2 Experimental

4.2.1 Starting materials

Tetraethyl orthosilicate, (TEOS, 98%, Aldrich), octadecyltrimethoxysilane, (C_{18}TMS, 90%, Aldrich), polyvinylpyrrolidone, (PVP, 99%, Aldrich), ammonium hydroxide, (NH_4OH, 25% Fluka), ethanol (C_2H_5OH, 96%, Merck) and deionized water were used as reagents for the synthesis of the pristine and mesoporous SiO_2 spheres. Hydrofluoric acid, (HF; 40%, Associated Chemical) was used for SiO_2 removal, and toluene (C_7H_8, 99.5%, Aldrich) was used as a carbon source.

4.2.2 Synthesis of SiO_2 spheres

A modified classical Stober method was used to sysnthesis SiO_2 spheres using ammonia as the catalyst. To control the particle size of the SiO_2 spheres obtained, different concentrations of ethanol, ammonia and silica precursor TEOS were used as shown in Table 4.1. The prepared solutions were centrifuged at 4500 rpm for 20 min and dried at 80°C for 12 h to give the desired products.

Table 4.1. Reaction conditions for the synthesis of solid SiO_2 spheres

Description	Stirring time (h)	H_2O/Ethanol (v/v ratio)	H_2O (mL)	Ethanol (mL)	NH_4OH 28%(mL)	TEOS (mL)	Particle size (nm)
SiO_2A	1	0.35	14	40	1	1	46±7
SiO_2B	1	0.35	14	40	1	2	183±22
SiO_2C	1	0.35	14	40	2	1	170±13
SiO_2D	1	0.35	14	40	2	2	274±18
SiO_2E	1	0.175	14	80	2	2	204±10
SiO_2F	1	0.175	14	80	1	2	110±10

4.2.3 Synthesis of pristine and mesoporous SiO_2 spheres

The synthesis of the pristine, mesoporous monodispersed and polydispersed SiO_2 spheres is summarized in Fig. 4.1. Monodispersed SiO_2 spheres were synthesized by mixing 180 mL of ethanol, 126 mL of distilled water and 10 mL of NH_4OH and the solution was stirred for 10 min. Then 32 mL of TEOS was added *rapidly* and the mixture was stirred for 1 h. In contrast, polydispersed SiO_2 spheres were obtained by adding 32 mL of TEOS *slowly* to an ethanol solution (180 mL), 126 mL of distilled water and 10 mL of NH_4OH and the mixture was

allowed to stir for 1 h. The solutions were centrifuged and dried as described previously (Section 4.2.2). The obtained powders were subsequently calcined at 600°C for 6 h to give the pristine monodispersed and polydispersed SiO_2 spheres, respectively (Fig. 4.1a). Separately, two pristine monodispersed and polydispersed SiO_2 solutions were prepared and 1 mL of TEOS and 5 mL of C_{18}TMS was *rapidly* added and the solutions were stirred for a further 6 h. The solutions were then centrifuged, dried and calcined as described previously to give the mesoporous monodispersed and polydispersed SiO_2 spheres, respectively (Fig. 4.1b).

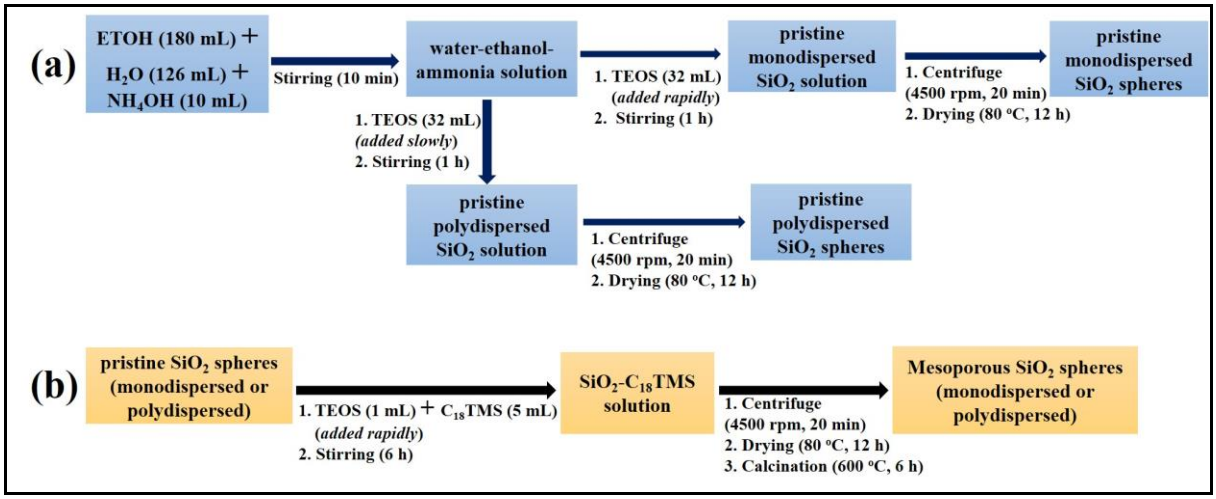

Figure 4.1. A schematic diagram showing the synthesis of; (a) pristine monodispersed and polydispersed SiO_2 spheres and (b) mesoporous monodispersed and polydispersed SiO_2 spheres, respectively.

4.2.4 Synthesis SiO_2@PVP spheres and their respective mesoporous HCSs

The synthesis of the mesoporous monodispersed and polydispersed SiO_2@PVP spheres is summarized in Fig. 4.2a. The mesoporous monodispersed and polydispersed silica spheres (2.0 g) were weighed separately and each was dispersed in 80 mL of ethanol and stirred for 20 min. Two PVP solutions were obtained by dispersing 2.0 g of PVP in 40 mL of distilled water and sonicating for 10 min. The PVP solutions were added to the two silica suspensions separately and stirred for 1 h. The solutions were centrifuged at 4500 rpm for 20 min and the products were dried at 80°C for 12 h to give mesoporous monodispersed SiO_2@PVPspheres and mesoporous polydispersed SiO_2@PVP spheres respectively. The pristine, mesoporous monodispersed and polydispersed SiO_2 spheres and SiO_2@PVP spheres were carbonized by a bubbling method using toluene as the carbon source and argon as the carrier gas in a CVD

reactor for 1 h[47]. The SiO_2 was then removed from the SiO_2@C spheres using 10% HF for 24 h at room temperature and the product dried to give the hollow carbon nanostructures (HCSs) as summarized in Fig. 4.2b.

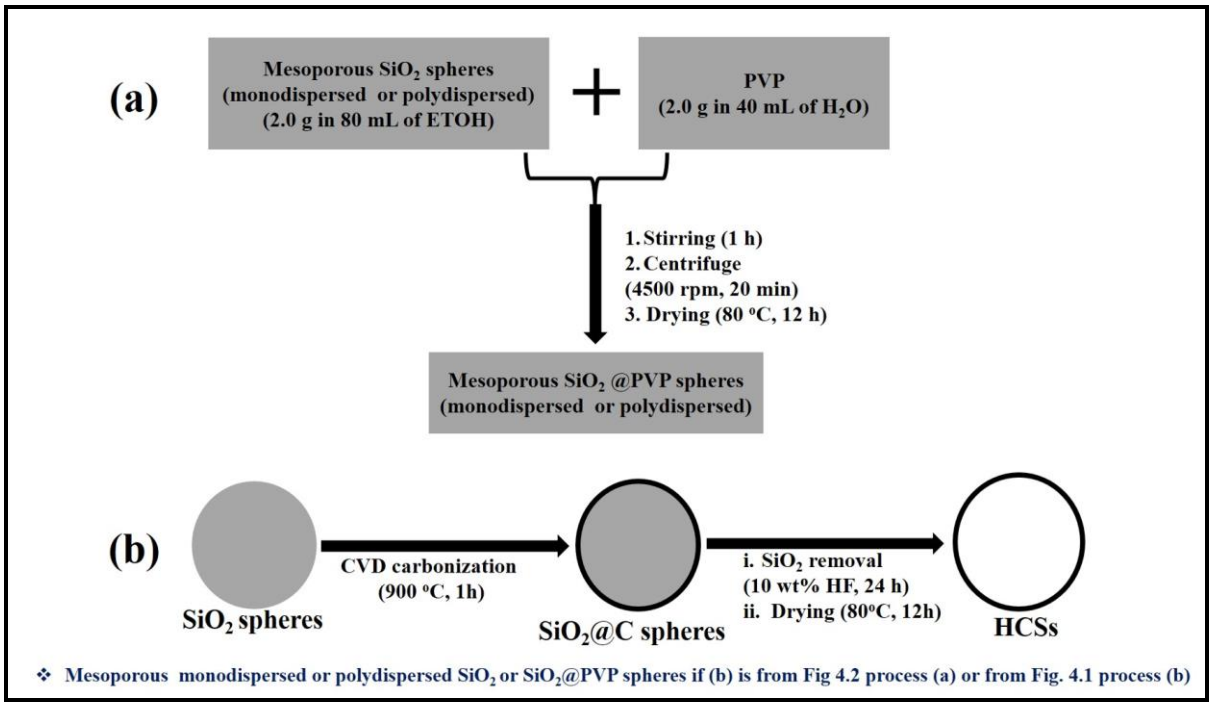

Figure 4.2. A schematic diagram showing the synthesis of; (a) mesoporous monodispersed and polydispersed SiO_2@PVP spheres and (b) hollow carbon nanostructures, respectively.

4.2.5 Characterization of SiO_2, SiO_2@PVP spheres and their respective HCSs

The morphology and the N_2 adsorption and desorption isotherms of the synthesized SiO_2 spheres, SiO_2@PVP spheres and the mesoporous deformed and open hollow carbon nanostructures was determined using TEM and BET as described earlier (Section 3.3). The surface morphology of the samples was also determined using a FEI Nova Nanolab 600 FIB/SEM. A small amount of the hollow carbon nanostructures sample was evenly spread homogeneously on a carbon tape placed on an aluminium stub and coated with a Pd/Au for 2 min to minimize space charge during imaging. The stub was then placed in a SEM and micrographs were taken at 5 keV. The functional groups on SiO_2 and SiO_2@PVP spheres were determined by a Brüker Tensor 27 Fourier transform infrared (FTIR) spectrometer) with measurements between 600 cm^{-1} to 4000 cm^{-1}. The decomposition temperature and thermal stability of the samples was investigated by TGA as decribed previously in section 3.3.4.

Raman spectroscopy analysis was done to determine the nature of carbon allotrope and subsequently the degree of graphitization of synthesized hollow carbon nanostructures.

4.3 Results and discussion

4.3.1 Controlling the parameters for the synthesis of monodispersed SiO_2 spheres

Pristine SiO_2 spheres of various sizes were obtained by varying the reaction time, volume of ammonia, ethanol and TEOS and the ratio of H_2O/TEOS using the Stober method. When small volumes of ammonia, ethanol, TEOS and short stirring times were used, incomplete SiO_2 spheres were obtained (Fig. 4.3a). This is because at a lower ammonia concentration, longer nucleation times are required and the increase in particle density leads to aggregation[20, 22]. Increasing the volume of ammonia or TEOS resulted in SiO_2 spheres of a larger diameter (>170 nm) with a spherical morphology (Fig. 4.3b-c). The larger ammonia, ethanol and TEOS volume ratios and short stirring times yielded larger sized SiO_2 spheres (Fig. 4.3d-e). The SiO_2 particle size increased with increasing ammonia concentration[21, 55, 56]. This is due to an increased polycondensation rate leading to larger particles. Fig. 4.3f shows smaller sized SiO_2 spheres when the larger volumes of ethanol and TEOS and lower volumes of the ammonia solution were used (<150 nm). The amount of solvent used was found to affect the particle size of the synthesized SiO_2 spheres. The particle sizes increased with decreasing ratio of water to ethanol. This is in agreement with literature where a high water concentration leads to increased hydrolysis whereas a low water concentration slows down polycondensation leading to larger particle sizes. The effect of reaction conditions on SiO_2 particle size and shape shows that low concentrations of precursor, catalysts and solvent favor small particle sizes[57, 58]. The respective particle size distribution graphs show the monodispersed nature of the obtained SiO_2 spheres (inset Fig. 4.3). Our studies indicated that high ethanol, ammonia and TEOS volumes were required for the optimal synthesis conditions to obtain SiO_2 spheres of the desired size (200 nm).

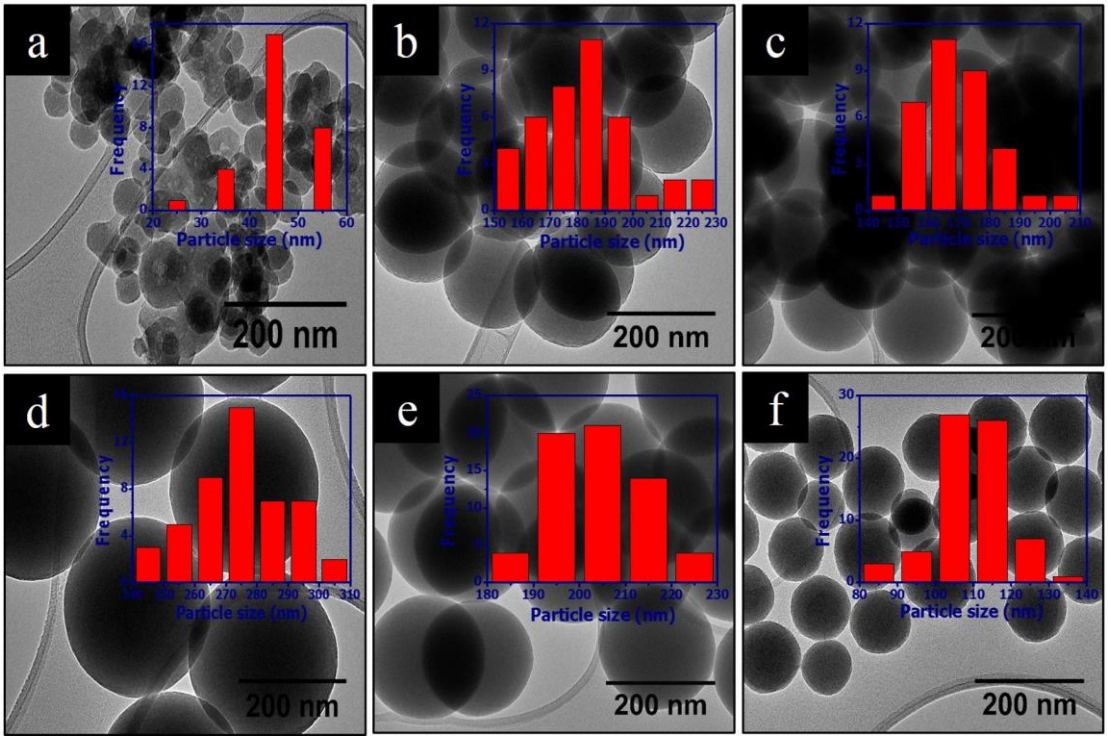

Figure 4.3. TEM images of the SiO_2 spheres: (a-f) represents SiO_2A-SiO_2F and insets; particle size distributions, respectively.

4.3.2 Effect of pristine and mesoporous monodispersed SiO_2 spheres as templates

4.3.2.1 Characterization of monodispersed SiO_2 spheres

4.3.2.1.1 BET surface area analysis

The N_2 adsorption-desorption isotherms of the obtained SiO_2 spheres was a type (II) adsorption isotherm according to the IUPAC nomenclature (Fig. 4.4a). The pristine SiO_2 spheres were macroporous while the mesoporous SiO_2 and mesoporous SiO_2@PVP spheres were macroporous with a H3 hysteresis loop as confirmed by the presence of pore size macropore region (> 60 nm) (Fig. 4.4b). The BET surface area of the pristine SiO_2, mesoporous SiO_2 and mesoporous SiO_2@PVP spheres was 29, 67 and 31 m^2/g, respectively (Table 4.2). The increase in surface area in the mesoporous SiO_2 can be attributed to the mesopores generated by the removal of C_{18}TMS during calcination (seen in Fig. 4.4b broad red curve at < 30nm). There was no change in the pore volume from pristine SiO_2 (0.26) to mesoporous SiO_2 (0.27) while after PVP addition, the pore volume decreased to 0.19 in mesoporous SiO_2@PVP spheres. This can be attributed to the coverage of SiO_2 surface with PVP thus reducing the number of pores.

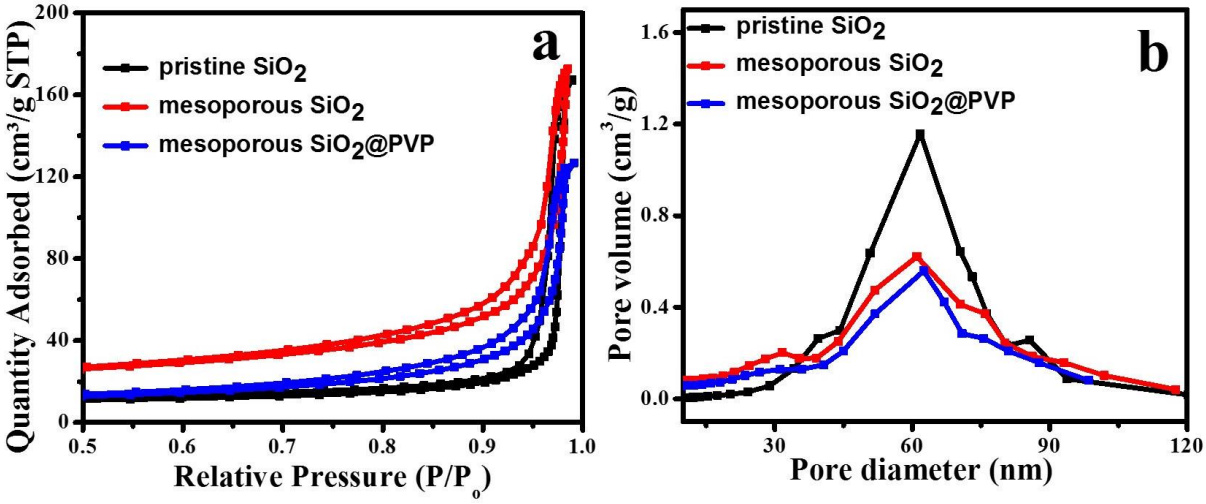

Figure 4.4. The BET surface area analysis spectra of the monodispersed SiO_2 spheres; (a) N_2 adsorption-desorption isotherms and (b) pore volume analysis, respectively.

Table 4.2. The diameters, BET surface area and pore volume of the monodispersed SiO_2 spheres

Description	Particle size (nm)	Surface area (m^2/g)	Pore volume (cm^3/g)
Pristine SiO_2	212 ± 17	29	0.26
Mesoporous SiO_2	195 ± 17	67	0.27
Mesoporous SiO_2@PVP	200 ± 17	31	0.19

4.3.2.1.2 Morphology analysis

The TEM micrographs of the pristine and mesoporous SiO_2 spheres show that the materials maintained a spherical morphology (Fig. 4.5a and 4.5b). The calculated particle sizes were 212 ± 17 nm, 195 ± 17 nm and 200 ± 17 nm for the pristine SiO_2, mesoporous SiO_2 and mesoporous SiO_2@PVP spheres, respectively (Table 4.2). The pristine SiO_2 spheres had a smooth morphology while the mesoporous SiO_2 exhibited a rough surface morphology. This could be attributed to the high volume of ammonia used[59]. Upon addition of PVP onto the mesoporous SiO_2 spheres, an interconnecting layer of PVP on the SiO_2 surface was observed (Fig. 4.5c).

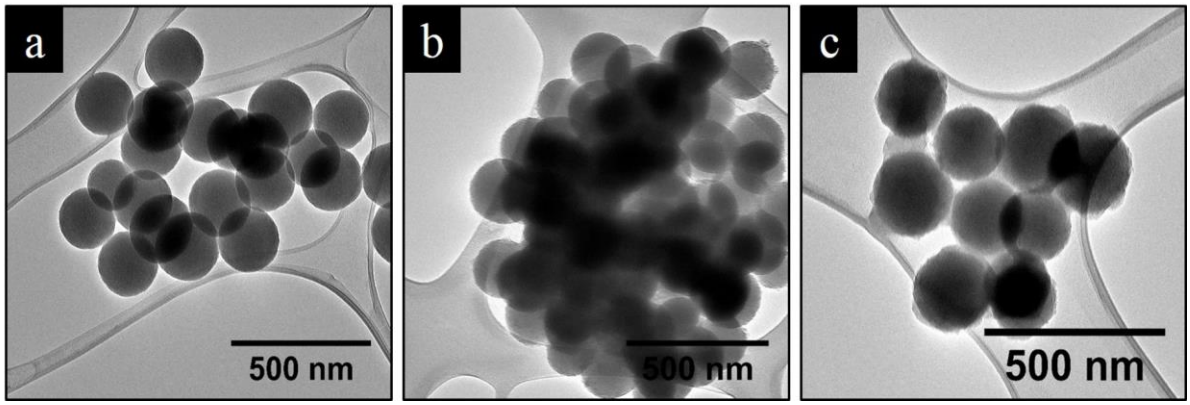

Figure 4.5. TEM images of; (a) pristine SiO_2, (b) mesoporous SiO_2 and (c) mesoporous SiO_2@PVP spheres, respectively.

4.3.2.1.3 FTIR analysis

The infrared spectra of PVP shows bands at 2981 cm^{-1} and 1423 cm^{-1} characteristic of C-H stretching and bending vibrations respectively[60, 61] (Fig. 4.6a). Other bands were observed between 750 cm^{-1} and 820 cm^{-1} (Si-O-Si, symmetric stretch), between 1000 cm^{-1} and 1200 cm^{-1} (Si-O-Si, asymmetric stretch), at 1284 cm^{-1} (C-N band), at 1662 cm^{-1} (carbonyl band and adsorbed H_2O) and at 2368 cm^{-1} (CO_2 band) respectively[60, 62-64]. Fig. 4.6b gives the infrared absorption peaks of the pristine SiO_2 at 798 cm^{-1}, 937 cm^{-1} and 1082 cm^{-1} characteristic of Si-O-Si symmetric stretch and asymmetric stretch respectively[65]. In the mesoporous SiO_2 and mesoporous SiO_2@PVPspheres , bands characteristic of OH stretching with an overlap of the hydrogen bonded H_2O molecules (H-O-H---H) and Si-OH hydrogen bonded to molecular H_2O (SiO-H---H_2O) were observed above 3400 cm^{-1} [66, 67] (Fig. 4.6c-d). Also, bands at 2362 cm^{-1} and 2358 cm^{-1} were observed in the mesoporous and mesoporous SiO_2@PVP spheres. In the mesoporous SiO_2@PVP, a reduction in the intensity of the Si-O-Si band at 1100 cm^{-1} and an increased intensity at 2362 cm^{-1} were observed. This could be attributed to the linking of the polymer to the SiO_2 surface.

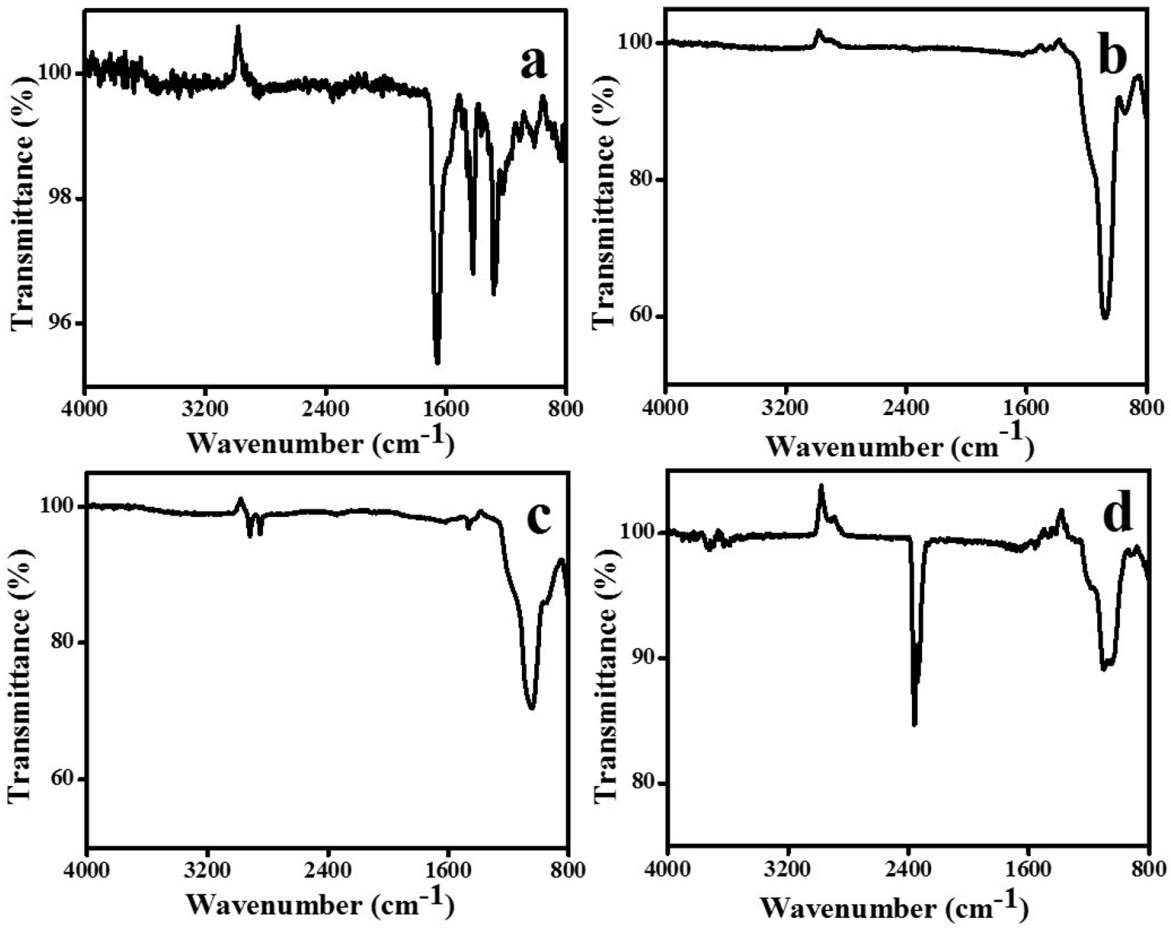

Figure 4.6. The FTIR spectra of; (a) pristine PVP polymer, (b) pristine SiO_2, (c) mesoporous SiO_2 and (d) mesoporous SiO_2@PVP, respectively.

4.3.2.1.4 Thermal gravimetric analysis

Fig. 4.7 shows the TGA and DTG curves of pure PVP, pristine SiO_2, mesoporous SiO_2 and mesoporous SiO_2@PVP spheres taken from 35°C to 900°C in air. The DTG of pure PVP shows a peak at 75°C corresponding to the loss of physically adsorbed H_2O. The decomposition of PVP starts at 380°C and ends at 432°C (Fig. 4.7a). This is in agreement with the decomposition temperature of PVP reported in literature (between 380°C and 420°C)[33]. For the pristine SiO_2, a large peak was observed between 40°C and 200°C, which can be ascribed to the loss of adsorbed H_2O and ethanol molecules (Fig.4.7b). The intensity of this peak gradually decreased in the mesoporous SiO_2 and mesoporous SiO_2@PVP spheres (Fig. 4.7c). This is expected, due to the removal of physically adsorbed H_2O during the formation of mesoporous SiO_2 in the calcination stage. From 250°C to 380°C, a considerable weight loss was observed in pristine SiO_2 spheres due to the removal of organic residues and some OH from Si-OH (Fig. 4.7c). A similar peak was seen in the mesoporous SiO_2 spheres

between 220°C and 360°C but was smaller and broader. In the case of mesoporous SiO_2@PVP spheres, PVP decomposition was observed between 300°C and 440°C (Fig. 4.7c). The maximum PVP decomposition temperature decreased to 346°C relative to that of pure PVP. This could have resulted from non-covalent and hydrogen bond interactions between SiO_2 and PVP polymer leading to a less stable SiO_2-polymer hybrid material[33].

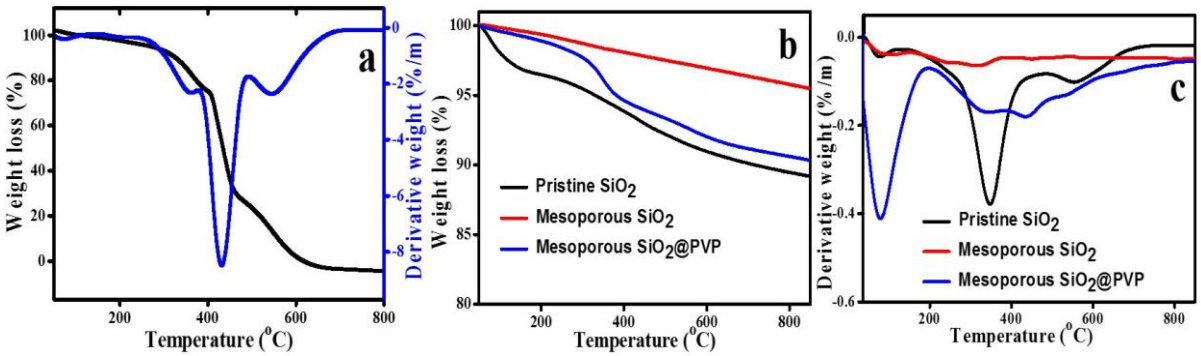

Figure 4.7. TGA curves (a) pristine PVP polymer, (b) Thermogravimetric curves and (c) derivative curves of the obtained monodispersed SiO_2 spheres, respectively.

4.3.2.2 Effect of SiO_2 template on carbon morphology and surface area properties

4.3.2.2.1 BET surface area analysis

Fig. 4.8a shows the N_2 adsorption and desorption isotherms of the obtained HCSs with a type (III) isotherm and a H3 hysteresis loop at a relative pressure of P/Po = 0.7 – 1.0 indicating an assemblage of slit shaped pores or platelike particles[68]. Fig. 4.8b shows a broad pore size distribution in the macroporous region (50 to 100 nm) and sharp peaks observed at 4.7 nm and 3.7 nm in the mesoporous HCSs and mesoporous HCSs (with PVP) respectively. The broad pore size distribution in the macropore region indicates that the structures were open ended with interconnected pores as illustrated in Fig. 4.9. The BET surface areas were 88 m^2/g, 113 m^2/g and 151 m^2/g in the pristine HCSs, mesoporous HCSs and the mesoporous broken HCSs respectively (Table 4.3). This could be attributed to the pores generated after the removal of the PVP polymer covering the mesoporous SiO_2 surface during carbonization and etching. This indicated the coexistence of open interparticle voids derived from the hollow interconnected framework in the sample[69, 70].

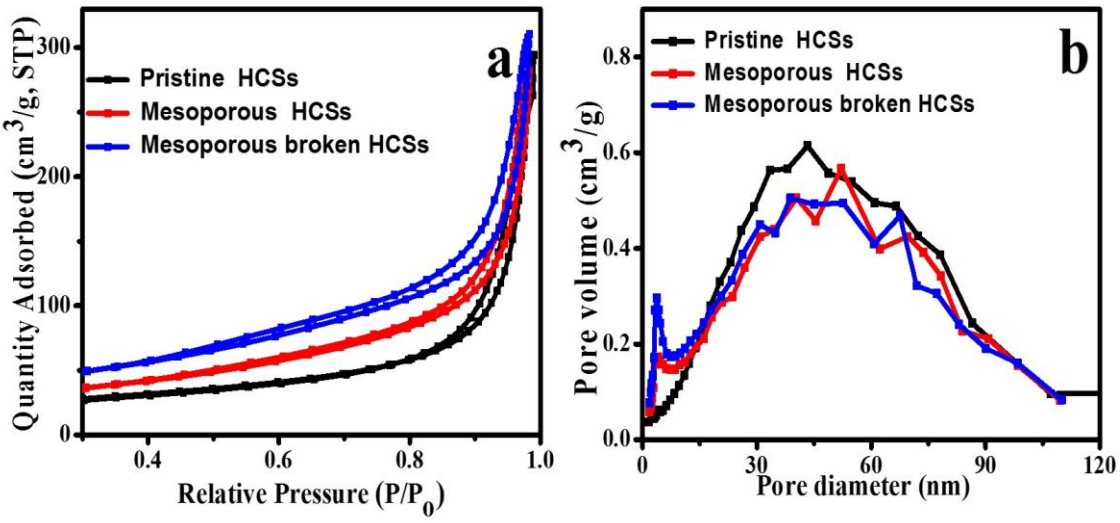

Figure 4.8. The surface area spectra of the obtained HCSs; (a) N_2 adsorption-desorption isotherms and (b) pore volume analysis, respectively.

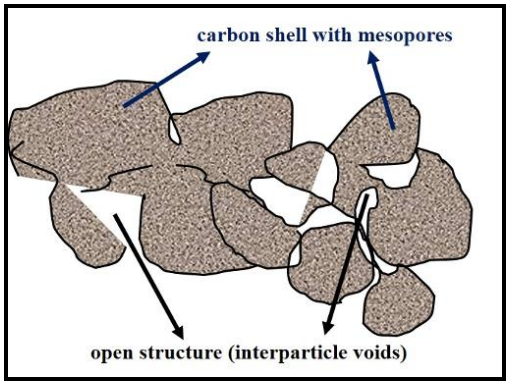

Figure 4.9. A schematic diagram showing the carbon shell and the open structure in the HCSs.

Table 4.3. The particle sizes, BET surface areas and pore volumes of the HCSs

Description	Particle size (nm)	Surface area (m^2/g)	Pore volume (cm^3/g)
Pristine HCSs	211 ± 18	88	0.46
Mesoporous HCSs	190 ± 22	113	0.44
Mesoporous broken HCSs	200 ± 26	151	0.49

4.3.2.2.2 Morphology analysis

After 1 h carbonization time and SiO_2 removal, pristine and mesoporous HCSs of 211 ± 18 nm, 190 ± 22 nm inner diameters and a shell thickness of 18 ± 5 nm were obtained respectively (Table 4.3). The TEM and SEM images show the presence of a few broken spheres in the pristine HCSs (Fig. 4.10a, and 4.10d) and mesoporous HCSs (Fig. 4.10b and 4.10e). This can be ascribed to the short carbonization time and the incomplete coverage of the SiO_2 template. The diameter of the obtained HCSs was smaller than that of the SiO_2 spheres due to shrinkage during carbonization. After 1 h carbonization of the mesoporous SiO_2@PVP spheres and SiO_2 removal, mesoporous broken HCSs of 200 ± 26 nm inner diameter and a 19 ± 6 nm shell thickness were obtained. The TEM and SEM micrographs show that the obtained mesoporous HCSs were broken and interconnected to resemble an open framework array hence they are referred to as mesoporous broken HCSs (Fig 4.10c and 4.10f). This interconnected open structure with the presence of pores is responsible for the increase in the BET surface areas.

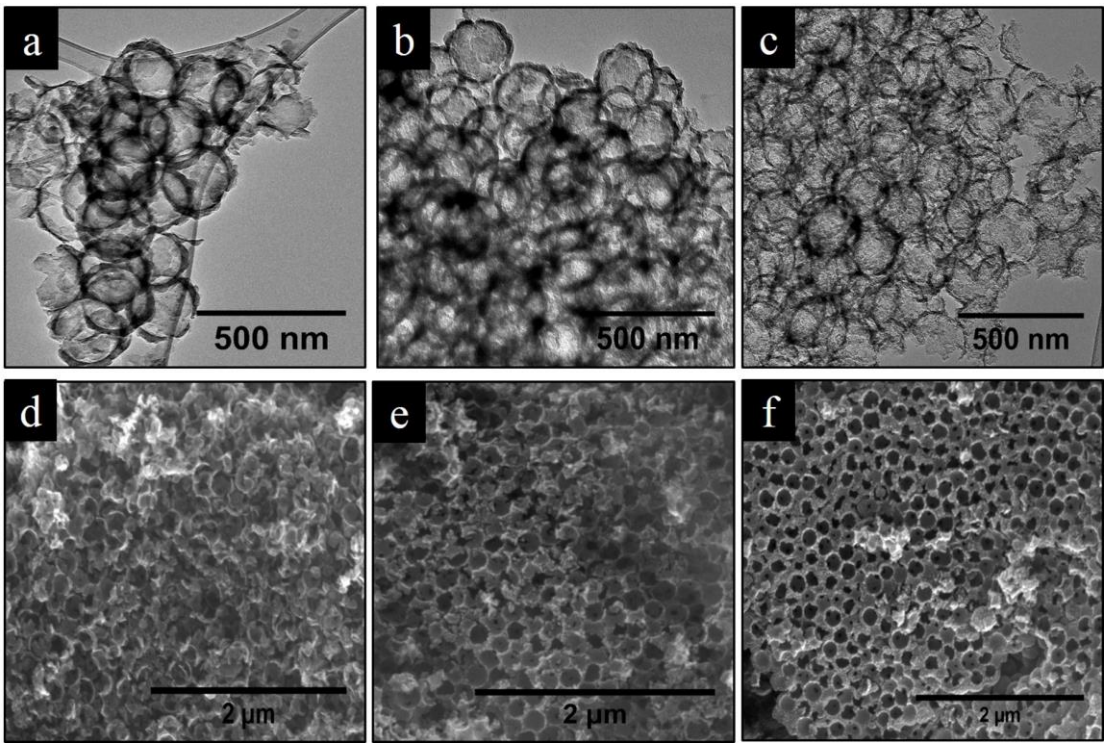

Figure 4.10. TEM and SEM images of; (a and d) pristine HCSs, (b and e) mesoporous HCSs and (c and f) mesoporous broken HCSs, respectively.

4.3.2.2.3 Raman analysis

The Raman spectra of the obtained hollow carbon nanostructures had peaks at 1339-1353 cm^{-1} characteristic of the D band cm^{-1} resulting from the breathing mode of sp^2 and sp^3 carbon atoms and defects in the carbon structure[71, 72]. A G peak was observed between 1579 cm^{-1} and 1596 cm^{-1} due to bond stretching of sp^2 atoms[73]. The shifts in the D and G band positions can be attributed to strain associated defects during the SiO_2 removal. The pristine and mesoporous HCSs exhibited fewer defects (I_D/I_G ratio 0.92 and 0.96) than the mesoporous broken HCSs generated by the PVP modified mesoporous SiO_2 templates (0.99) (Table 4.4). This results from the broken edges that act as defects as observed in the increased D peak intensity of the respective HCSs (Fig. 4.11).

Table 4.4. The I_D/I_G ratios of the HCSs obtained from monodispersed SiO_2 and SiO_2@PVP spheres

Description	D-band position (cm^{-1})	G-band position (cm^{-1})	I_D/I_G ratio
Pristine HCSa	1346	1581	0.92
Mesoporous HCSs	1353	1596	0.96
Mesoporous broken HCSs	1339	1579	0.99

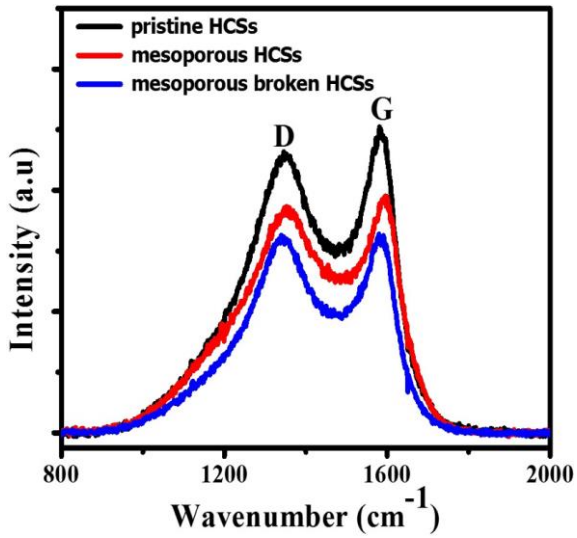

Figure 4.11. Raman spectra of pristine, mesoporous and mesoporous broken HCSs.

4.3.3 Effect of mesoporous polydispersed SiO_2 spheres as templates

In this subsection, the effect of polydispersed SiO_2 spheres and porosity on the carbon morphology is probed.

4.3.3.1 Characterization of the obtained polydispersed SiO_2 spheres

4.3.3.1.1 BET surface area analysis

Nitrogen sorption data of the mesoporous polydispersed SiO_2 spheres gave a BET surface area of 55 m^2/g and a pore volume of 0.25 cm^3/g, which reduced to 27 m^2/g and 0.18 cm^3/g after PVP addition (Table 4.5). This 50% drop in surface area could be due to the polymer infiltration into the different sized SiO_2 spheres. The N_2 isotherms exhibited a type (III) isotherms with the presence of bimodal pore size distribution (Fig. 4.12a-b). This indicates the presence of pores in the mesopores region (< 7 nm) and interparticle voids in the macropore region (> 50 nm) due to intraparticle effects respectively.

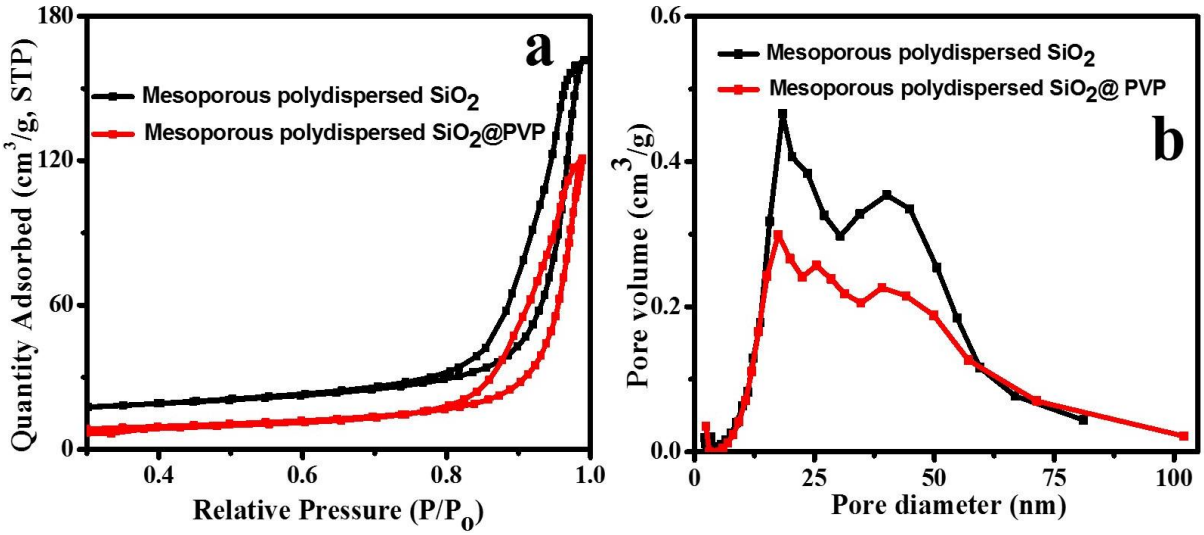

Figure 4.12. The surface area spectra of the obtained SiO_2 spheres; (a) N_2 adsorption-desorption isotherms and (b) pore volume analysis, respectively.

Table 4.5. Surface areas and pore volumes of the polydispersed SiO_2 spheres

Description	Surface area (m^2/g)	Pore volume (cm^3/g)
Mesoporous polydispersed SiO_2	55	0.25
Mesoporous polydispersed SiO_2@PVP	27	0.18

4.3.3.1.2 Morphology analysis

The mesoporous polydispersed SiO_2 spheres were synthesized and their morphology studied using TEM. The obtained SiO_2 spheres were polydispersed with sizes ranging between 60 and 200 nm. The mesoporous polydispersed SiO_2 spheres exhibited a rough morphology while upon addition of PVP an interconnection of the SiO_2 spheres was observed (Fig. 4.13).

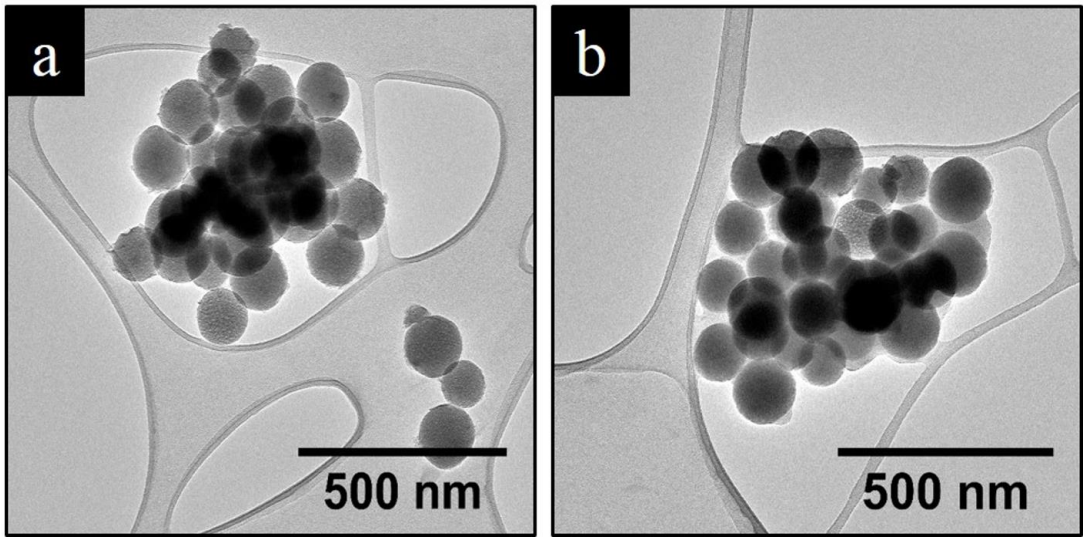

Figure 4.13. TEM images of; (a) mesoporous polydispersed SiO_2 spheres and (b) mesoporous polydispersed SiO_2@PVP spheres, respectively.

4.3.3.1.3 FTIR analysis

The infrared spectra of the mesoporous polydispersed SiO_2 spheres showed low intensity bands between 3600 cm^{-1} and 3800 cm^{-1} (Fig. 4.14) This could be attributed to the vibrations of free surface hydroxyl groups[74]. Upon PVP addition to the mesoporous polydispersed SiO_2 spheres, the peak at 1099 cm^{-1} decreased in intensity while that at 2360 cm^{-1} (CO_2) increased in intensity. Typically, hydrogen bond formation can be identified by a reduction in the wavenumber or a band broadening or peak intensification[75]. A slight blue shift in the OH stretch from 3664 cm^{-1} in mesoporous polydispersed SiO_2 to 3662 cm^{-1} in mesoporous polydispersed SiO_2@PVP spheres was observed. The change in the wavenumber is a confirmation of the formation of hydrogen bonds in the SiO_2@PVP spheres (a silica-polymer matrix)[76].

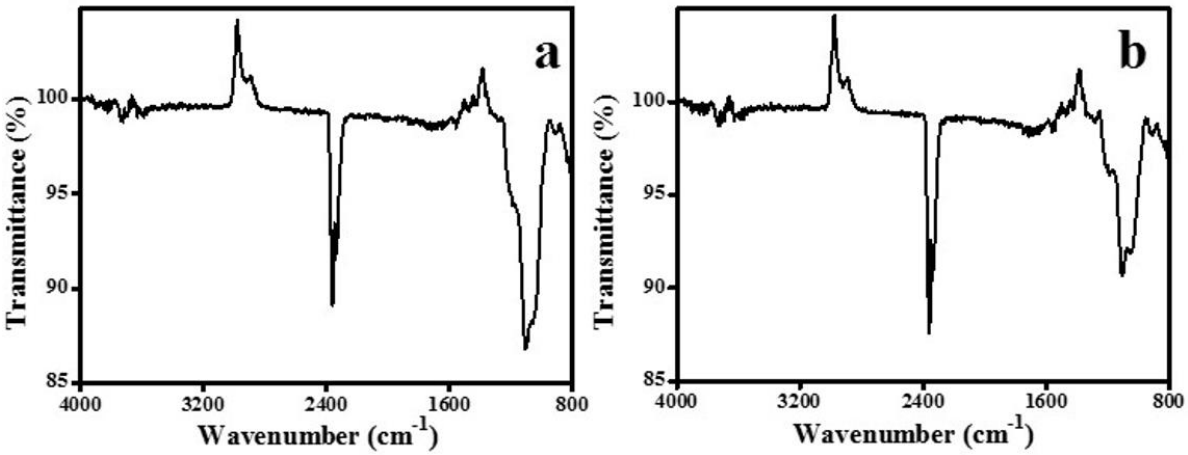

Figure 4.14. The FTIR spectra of; (a) mesoporous polydispersed SiO_2 spheres and (b) mesoporous polydispersed SiO_2@PVP spheres.

4.3.3.1.4 Thermal gravimetric analysis

The thermal gravimetric analysis (TGA) curves and the derivative curves of the mesoporous polydispersed SiO_2 and mesoporous polydispersed SiO_2@PVP spheres were similar to those of the mesoporous monodispersed SiO_2 and SiO_2@PVP spheres with two weight losses observed between 45°C to 170°C and 200°C to 370°C, respectively (Fig. 4.15a-b). The main constituent of the residual sample was SiO_2 as seen from the residual materials at 800°C. The unique property to note in the case of mesoporous polydispersed SiO_2@PVP spheres was the decomposition temperature of PVP that was observed at 350°C with a weight loss of 4.8 wt%. The PVP weight loss was lower than that of pure PVP but slightly higher than that obtained from mesoporous monodispersed SiO_2@PVP spheres. Also, the percentage weight loss was higher than that obtained from mesoporous monodispersed SiO_2@PVP that was 4.4%. This indicates that despite the use of an equal volume of PVP, more PVP was adsorbed on the polydispersed SiO_2 than on the monodispersed SiO_2. This corroborates with the high BET surface areas observed in HCSs when mesoporous polydispersed SiO_2@PVP spheres were used as templates.

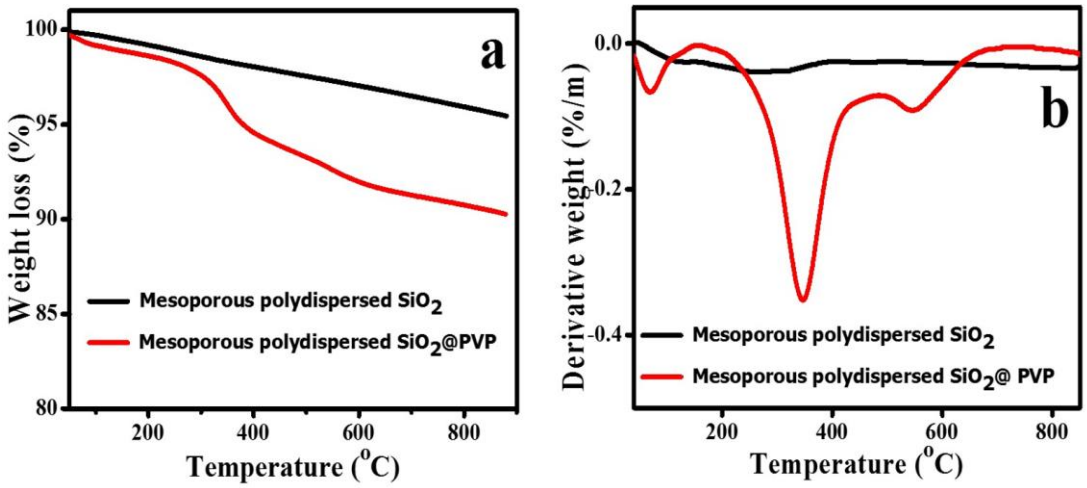

Figure 4.15. TGA curves (a) Thermogravimetric curves and (b) derivative curves of mesoporous polydispersed SiO_2 spheres.

4.3.3.2 Effect of SiO_2 template on carbon morphology and surface area properties

4.3.3.2.1 BET surface area analysis

The N_2 adsorption-desorption isotherms of the mesoporous deformed HCSs and open ended HCSs exhibited a tremendous increase in the BET surface area that revealed a type (III) isotherm characteristic of hierarchical structures (Fig. 4.16a).). Fig. 4.15b shows a broad pore size distribution (60 nm to 100 nm) in both samples characteristic of the presence of macroporous. Also, intraparticle voids were observed at 12 nm and 27.6 nm in the mesoporous open ended HCSs and 35 nm in the mesoporous deformed HCSs respectively. Consequently, an increase in the pore volume from 1.06 cm^3/g to 3.49 cm^3/g was observed (Table 4.6). A fourfold increase in the BET surface area from 210 m^2/g in the mesoporous deformed HCSs to 894 m^2/g in the mesoporous open ended HCSs can be attributed to the role of PVP on enhancing the interconnectivity of the SiO_2 sphere templates. This corroborates with the TEM and SEM micrographs that show the formation of hierarchical structures with interpenetrating open networks from functionalized SiO_2 sphere templates using a CVD appproach. Reports on similar hierarchical structures show their synthesis from biomass carbon sources by hydrothermal carbonization or sol-gel method[77, 78].

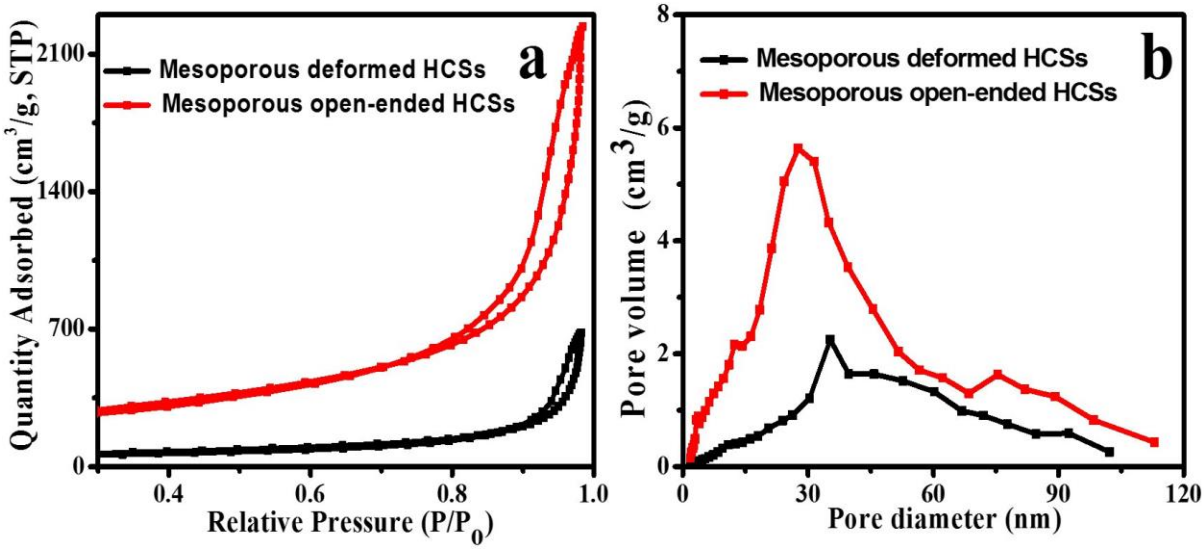

Figure 4.16. The surface area spectra of the mesoporous polydispersed HCSs; (a) N_2 adsorption-desorption isotherms and (b) pore volume analysis, respectively.

Table 4.6. Surface areas and pore volumes of the polydispersed HCSs

Description	Surface area (m^2/g)	Pore volume (cm^3/g)
Mesoporous deformed HCSs	210	1.06
Mesoporous open ended HCSs	894	3.49

4.3.3.2.2 Morphology analysis

TEM images showed that mesoporous deformed HCSs and mesoporous open ended HCSs were obtained after 1 h carbonization and SiO_2 etching of mesoporous polydispersed SiO_2 and mesoporous polydispersed SiO_2@PVP spheres respectively (Fig. 4.17a-b). The mesoporous deformed HCSs were aggregated with an undefined shape while the mesoporous open ended HCSs comprised of a network of broken carbon structures with a porous nature as confirmed by SEM images (Fig. 4.17c-d). This highly interconnected open framework of mesoporous HCSs formed a hierarchical structure which resulted in a high open ended surface area as confirmed by BET surface area.

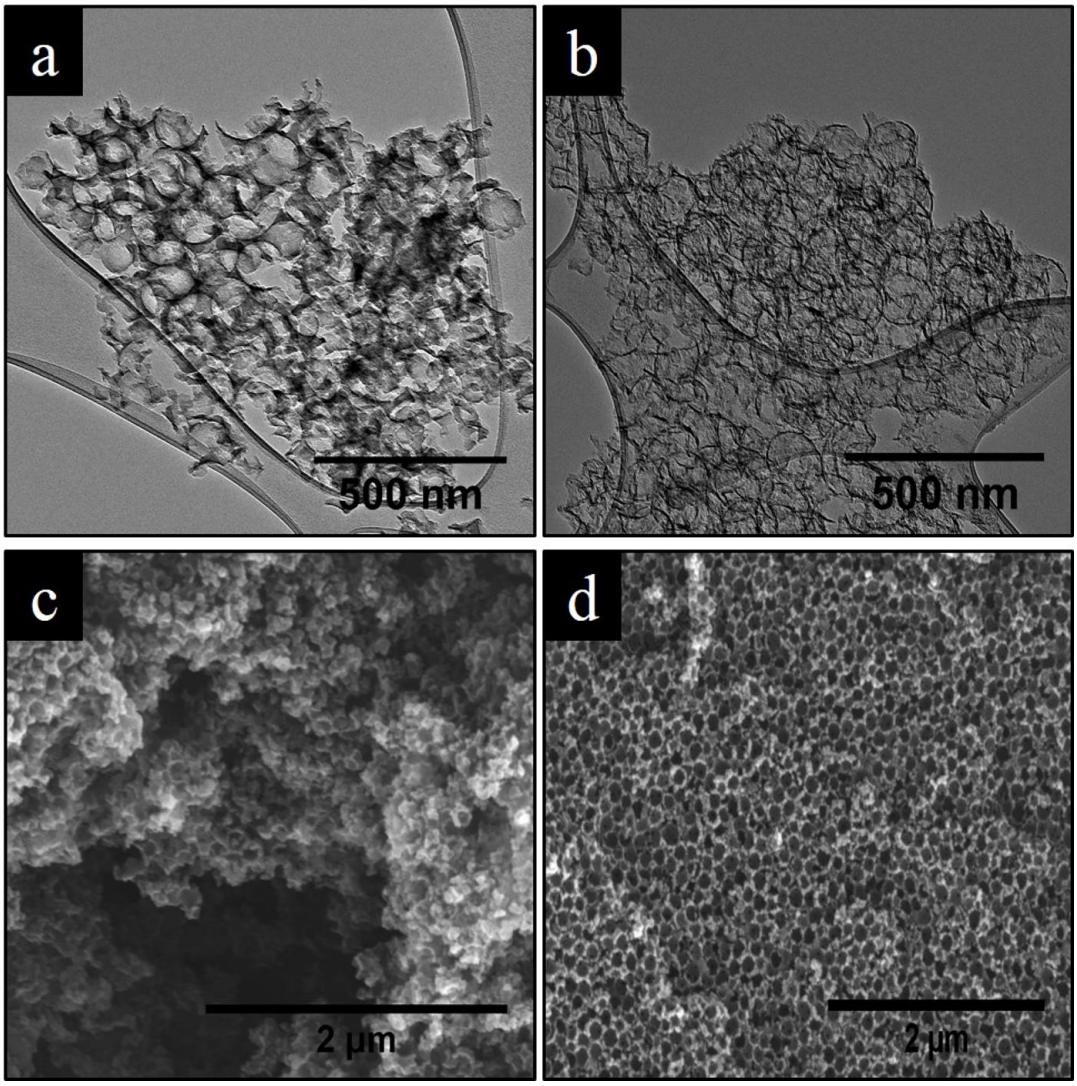

Figure 4.17. TEM and SEM images of; (a and c) mesoporous deformed HCSs and (b and d) mesoporous open ended HCSs, respectively.

4.3.3.2.3 Raman analysis

The Raman spectra of the obtained hollow carbon nanostructures had peaks at 1334-1360 cm^{-1} and 1589 -1598 cm^{-1} characteristic of the D band and the G band respectively (Fig. 4.18). The HCSs comprised of a larger number of defects as seen from the high I_D/I_G ratios 0.94 and 0.99 for the deformed and open ended HCSs, respectively (Table 4.7). The slight increase in I_D/I_G ratio is expected due to defects resulting from the presence of open edges structures of the mesoporous open ended HCSs.

Table 4.7. The I_D/I_G ratios of the deformed and open ended HCSs

Description	D band position (cm^{-1})	G band position (cm^{-1})	I_D/I_G ratio
Mesoporous deformed HCSs	1360	1598	0.94
Mesoporous open ended HCSs	1334	1589	0.97

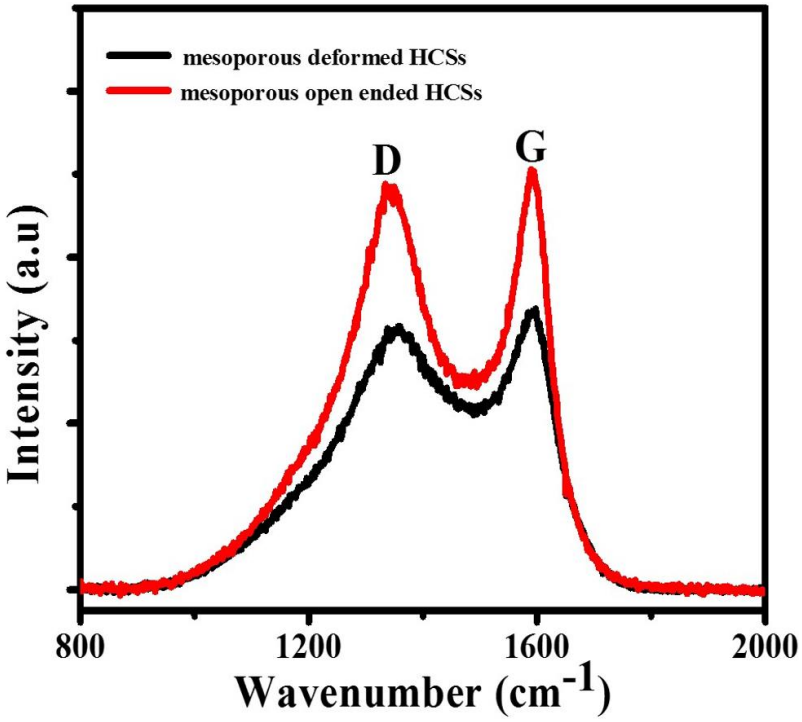

Figure 4.18. The Raman spectra of mesoporous deformed HCSs and open ended HCSs.

To summarize the observations in this study, a schematic diagram that illustrates the formation of various hollow carbon nanostructures as a function of size dispersity, mesoporosity and addition of PVP is shown in Figs. 4.19 and 4.20 respectively. A 1 h carbonization of the pristine and mesoporous monodispersed SiO_2 spheres followed by SiO_2 removal gave complete HCSs and mesoporous HCSs, respectively (Fig. 4.19(i) and (ii)). Addition of PVP to a mesoporous monodispersed SiO_2 followed by 1 h carbonization and SiO_2 removal led to the generation of mesoporous broken HCSs resulting from the infiltration of some of the PVP into the mesopores structure (Fig. 4.19(iii)).

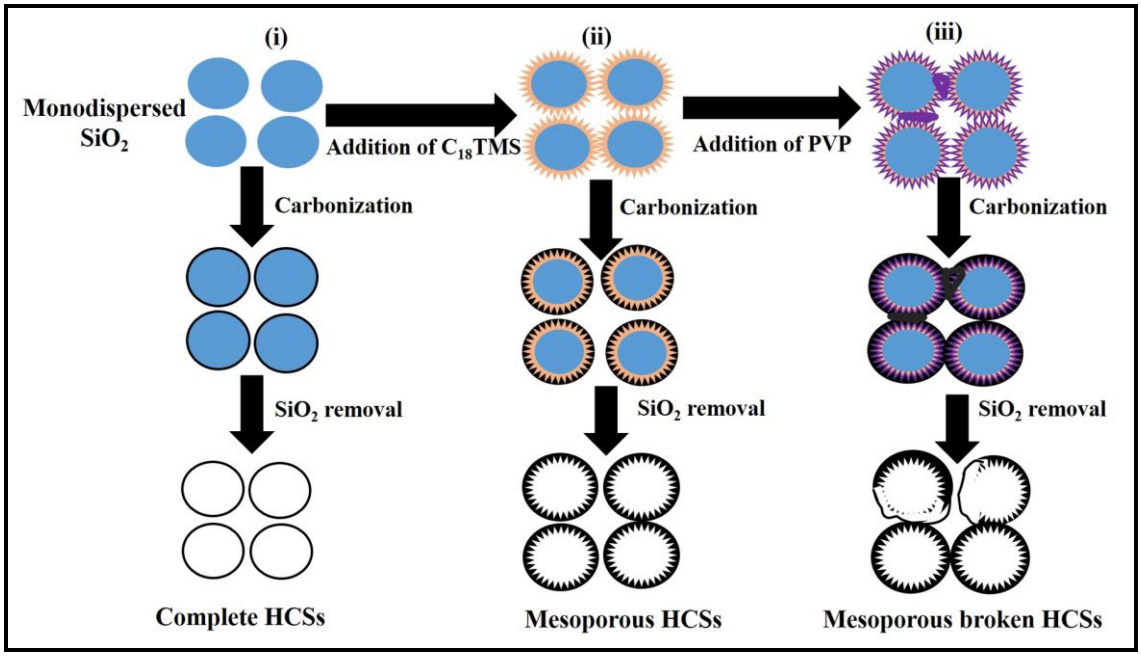

Figure 4.19. A schematic diagram showing the synthesis route of mesoporous monodispersed HCSs.

In contrast, 1 h carbonization of pristine and mesoporous polydispersed SiO_2 spheres followed by SiO_2 removal led to the formation of deformed HCSs and mesoporous deformed HCSs (Fig. 4.20(i) and (ii)). Lastly, the use of the mesoporous polydispersed SiO_2@PVP spheres as templates resulted in the generation of mesoporous open ended HCSs comprising of an interconnected open hierarchical structure (Fig. 4.20(iii)). This could be attributed to the adsorption of more PVP onto the polydispersed SiO_2 spheres and improved SiO_2-SiO_2 surface interactions as confirmed by the FTIR spectroscopy and TGA analysis of the monodispersed and polydispersed SiO_2@PVP spheres.

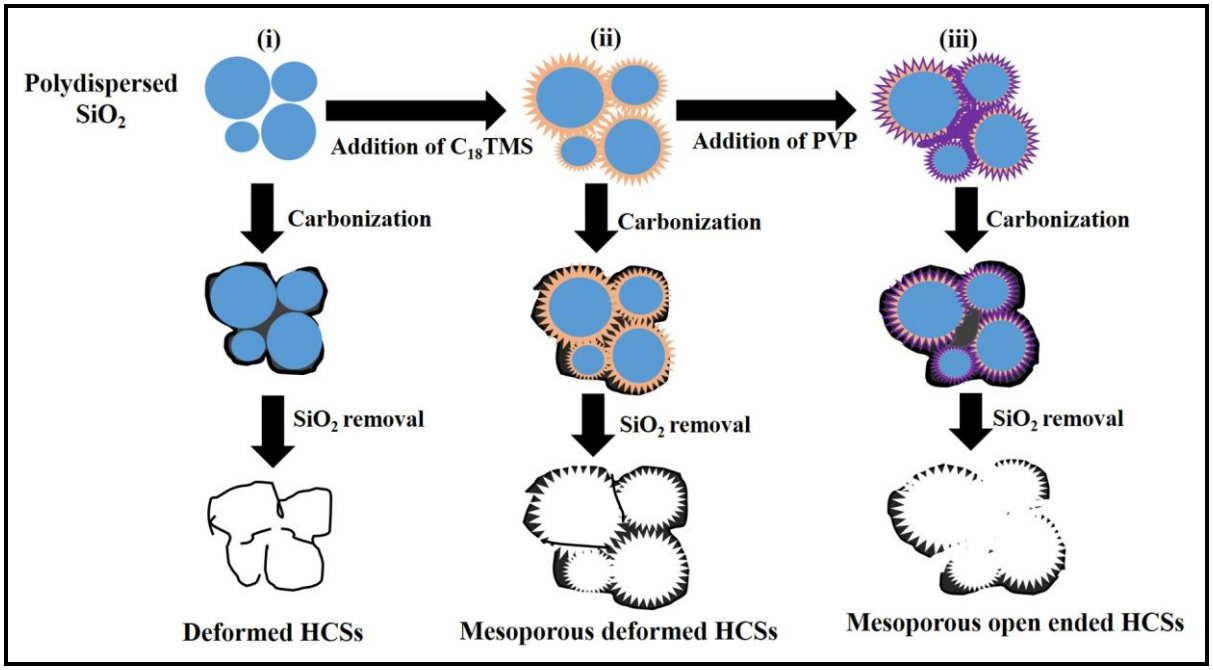

Figure 4.20. A schematic diagram showing the synthesis route of mesoporous polydispersed HCSs.

4.4 Conclusions

The particle size and morphology of SiO_2 spheres was investigated using the Stober method. Varying the volume of the silica precursor (TEOS), the base catalyst (NH_4OH) and the solvent resulted in silica spheres of different sizes. The functionalization of silica with PVP reduced the thermal stability of the PVP and affected the morphology of the produced HCSs (1 h carbonization and SiO_2 removal). FTIR spectroscopy and TGA analysis confirmed hydrogen bonding of the OH silanol group of SiO_2 with the carbonyl group of PVP in the PVP functionalized SiO_2 spheres. Pristine monodispersed SiO_2 sphere templates resulted in the formation of complete HCSs whereas mesoporous monodispersed SiO_2 sphere templates gave mesoporous HCSs. Application of monodispersed mesoporous SiO_2 spheres functionalized with PVP as templates led to the formation of mesoporous broken HCSs after 1 h carbonization time and SiO_2 removal. In contrast, 1 h carbonization of the mesoporous polydispersed SiO_2@PVP spheres, followed by SiO_2 removal, generated mesoporous open ended HCSs that exhibited a high BET surface area of 894 m^2/g. The mesoporous broken HCSs and open ended HCSs portrayed a hierarchical structure with a bimodal pore size distribution. The surface area properties of these materials and in ease of control of the carbon morphology gives an insight on the application of these materials as dye adsorbents.

References

1. Epstein, E. *Proceedings of the National Academy of Sciences* **1994,** 91, (1), 11-17.
2. Currie, H. A.; Perry, C. C. *Annals of Botany* **2007,** 100, (7), 1383-1389.
3. Seaborn, C. D.; Nielsen, F. H. *Biological Trace Element Research* 89, (3), 251-261.
4. Carlisle, E. M., Silicon as an Essential Trace Element in Animal Nutrition. In *Ciba Foundation Symposium 121 - Silicon Biochemistry*, John Wiley & Sons, Ltd.: 2007; pp 123-139.
5. Carlisle, E. M., Silicon. In *Biochemistry of the Essential Ultratrace Elements*, Frieden, E., Ed. Springer US: Boston, MA, 1984; pp 257-291.
6. Kieu, K.; Li, C.; Fang, Y.; Cohoon, G.; Herrera, O. D.; Hildebrand, M.; Sandhage, K. H.; Norwood, R. A. *Opt. Express* **2014,** 22, (13), 15992-15999.
7. Chu, L.; Daniels, M. W.; Francis, L. F. *Chemistry of Materials* **1997,** 9, (11), 2577-2582.
8. Harris, J. M.; Lopez, G. P.; Reichert, W. M. *Sensors and actuators. B, Chemical* **2012,** 174, 373-379.
9. Bergna, H. E.; Roberts, W. O., *Colloidal Silica: Fundamentals and Applications*. CRC Press: 2005; Vol. 131.
10. Scherer, G. W.; Brinker, C. J. *Academic: New York* **1990**.
11. Stöber, W.; Fink, A.; Bohn, E. *Journal of Colloid and Interface Science* **1968,** 26, (1), 62-69.
12. Brinker, C. J. *Journal of Non-Crystalline Solids* **1988,** 100, (1–3), 31-50.
13. Iler, R. K., *The chemistry of Silica: Solubility, Polymerization, Colloid and Surface Pro perties, and Biochemistry*. Wiley: 1979.
14. Pope, E. J. A.; Mackenzie, J. D. *Journal of Non-Crystalline Solids* **1986,** 87, (1–2), 185-198.
15. Sanchez, C.; Livage, J.; Henry, M.; Babonneau, F. *Journal of Non-Crystalline Solids* **1988,** 100, (1), 65-76.
16. Sakka, S.; Kamiya, K. *Journal of Non-Crystalline Solids* **1982,** 48, (1), 31-46.
17. Aelion, R.; Loebel, A.; Eirich, F. *Journal of the American Chemical Society* **1950,** 72, (12), 5705-5712.
18. Matsoukas, T.; Gulari, E. *Journal of Colloid and Interface Science* **1989,** 132, (1), 13-21.
19. Bogush, G. H.; Zukoski Iv, C. F. *Journal of Colloid and Interface Science* **1991,** 142, (1), 1-18.
20. Lee, K.; Sathyagal, A. N.; McCormick, A. V. *Colloids and Surfaces A: Physicochemical and Engineering Aspects* **1998,** 144, (1–3), 115-125.
21. Matsoukas, T.; Gulari, E. *Journal of Colloid and Interface Science* **1988,** 124, (1), 252-261.
22. Green, D. L.; Lin, J. S.; Lam, Y.-F.; Hu, M. Z. C.; Schaefer, D. W.; Harris, M. T. *Journal of Colloid and Interface Science* **2003,** 266, (2), 346-358.
23. Xu, R.; Pang, W.; Yu, J.; Huo, Q.; Chen, J., *Chemistry of Zeolites and Related Porous Materials: Synthesis and Structure*. John Wiley & Sons: 2009.
24. Romero, A. A.; Alba, M. D.; Zhou, W.; Klinowski, J. *The Journal of Physical Chemistry B* **1997,** 101, (27), 5294-5300.
25. Di Renzo, F.; Cambon, H.; Dutartre, R. *Microporous Materials* **1997,** 10, (4–6), 283-286.
26. Katiyar, A.; Yadav, S.; Smirniotis, P. G.; Pinto, N. G. *Journal of Chromatography A* **2006,** 1122, (1–2), 13-20.
27. Burkett, S. L.; Sims, S. D.; Mann, S. *Chemical. Communications.* **1996**, (11), 1367-1368.

28. Shio, S.; Kimura, A.; Yamaguchi, M.; Yoshida, K.; Kuroda, K. *Chemical Communications* **1998**, (22), 2461-2462.
29. Zhang, H.; Li, X. *Journal of Chemistry* **2016,** 2016, 16.
30. Wei, Y.; Jin, D.; Ding, T.; Shih, W.-H.; Liu, X.; Cheng, S. Z. D.; Fu, Q. *Advanced Materials* **1998,** 10, (4), 313-316.
31. Chen, Y.; Chen, H.; Ma, M.; Chen, F.; Guo, L.; Zhang, L.; Shi, J. *Journal of Materials Chemistry* **2011,** 21, (14), 5290-5298.
32. Nongwe, I.; Bepete, G.; Shaikjee, A.; Ravat, V.; Terfassa, B.; Meijboom, R.; Coville, N. J. *Catalysis Communications* **2014,** 53, 77-82.
33. Timin, A.; Rumyantsev, E.; Lanin, S. N.; Rychkova, S. A.; Guseynov, S. S.; Solomonov, A. V.; Antina, E. V. *Materials Chemistry and Physics* **2014,** 147, (3), 673-683.
34. Slowing, I. I.; Vivero-Escoto, J. L.; Wu, C.-W.; Lin, V. S. Y. *Advanced Drug Delivery Reviews* **2008,** 60, (11), 1278-1288.
35. Argyo, C.; Weiss, V.; Bräuchle, C.; Bein, T. *Chemistry of Materials* **2014,** 26, (1), 435-451.
36. Brady, R.; Woonton, B.; Gee, M. L.; O'Connor, A. J. *Innovative Food Science & Emerging Technologies* **2008,** 9, (2), 243-248.
37. Kim, H.-J.; Yang, H.-C.; Chung, D.-Y.; Yang, I.-H.; Choi, Y. J.; Moon, J.-k. *Journal of Chemistry* **2015,** 2015, 9.
38. Sancenón, F.; Pascual, L.; Oroval, M.; Aznar, E.; Martínez-Máñez, R. *ChemistryOpen* **2015,** 4, (4), 418-437.
39. Palaniappan, A.; Su, X.; Tay, F. E. H. *Journal of Electroceramics* 16, (4), 503-505.
40. Joo, S. H.; Park, J. Y.; Tsung, C.-K.; Yamada, Y.; Yang, P.; Somorjai, G. A. *Nature Materials* **2009,** 8, (2), 126-131.
41. Hulteen, J. *Journal of Materials Chemistry* **1997,** 7, (7), 1075-1087.
42. Liu, Y.; Goebl, J.; Yin, Y. *Chemical Society Reviews* **2013,** 42, (7), 2610-2653.
43. Davies, R.; Schurr, G. A.; Meenan, P.; Nelson, R. D.; Bergna, H. E.; Brevett, C. A. S.; Goldbaum, R. H. *Advanced Materials* **1998,** 10, (15), 1264-1270.
44. Caruso, F. *Advanced Materials* **2001,** 13, (1), 11-22.
45. Caruso, F.; Caruso, R. A.; Möhwald, H. *Science* **1998,** 282, (5391), 1111-1114.
46. Caruso, F. *Chemistry – A European Journal* **2000,** 6, (3), 413-419.
47. Xia, Y. D.; Mokaya, R. *Advanced Materials* **2004,** 16, (11), 886-891.
48. Zhu, Y.; Kockrick, E.; Ikoma, T.; Hanagata, N.; Kaskel, S. *Chemistry of Materials* **2009,** 21, (12), 2547-2553.
49. Su, F.; Zhao, X. S.; Wang, Y.; Wang, L.; Lee, J. Y. *Journal of Materials Chemistry* **2006,** 16, (45), 4413-4419.
50. Fu, J.; Xu, Q.; Chen, J.; Chen, Z.; Huang, X.; Tang, X. *Chemical Communications* **2010,** 46, (35), 6563-6565.
51. Wang, Q.; Yan, J.; Wang, Y.; Ning, G.; Fan, Z.; Wei, T.; Cheng, J.; Zhang, M.; Jing, X. *Carbon* **2013,** 52, 209-218.
52. Lai, X.; Halpert, J. E.; Wang, D. *Energy & Environmental Science* **2012,** 5, (2), 5604-5618.
53. Tang, K.; Fu, L.; White, R. J.; Yu, L.; Titirici, M.-M.; Antonietti, M.; Maier, J. *Advanced Energy Materials* **2012,** 2, (7), 873-877.
54. Wen, Z.; Wang, Q.; Zhang, Q.; Li, J. *Electrochemistry Communications* **2007,** 9, (8), 1867-1872.
55. Park, S. K.; Kim, K. D.; Kim, H. T. *Colloids and Surfaces A: Physicochemical and Engineering Aspects* **2002,** 197, (1–3), 7-17.

56. Bogush, G. H.; Tracy, M. A.; Zukoski Iv, C. F. *Journal of Non-Crystalline Solids* **1988,** 104, (1), 95-106.
57. Yoo, J. W.; Yun, D. S.; Kim, H. J. *Journal of Nanoscience and Nanotechnology* **2006,** 6, (11), 3343-3346.
58. Rahman, I. A.; Padavettan, V. *Journal of Nanomaterials* **2012,** 2012, 15.
59. El-Toni, A.; Ibrahim, M.; Labis, J.; Khan, A.; Alhoshan, M. *International Journal of Molecular Sciences* **2013,** 14, (6), 11496.
60. Al-Oweini, R.; El-Rassy, H. *Journal of Molecular Structure* **2009,** 919, (1), 140-145.
61. Du, Y. K.; Yang, P.; Mou, Z. G.; Hua, N. P.; Jiang, L. *Journal of Applied Polymer Science* **2006,** 99, (1), 23-26.
62. Taylor, L. S.; Zografi, G. *Pharmaceutical Research* 14, (12), 1691-1698.
63. Socrates, G., *Infrared and Raman Characteristic Group Frequencies: Tables and Charts*. John Wiley & Sons: 2004.
64. Bartl, A.; Bohr, S.; Haubner, R.; Lux, B. *International Journal of Refractory Metals and Hard Materials* **1996,** 14, (1–3), 145-157.
65. Wood, D. L.; Rabinovich, E. M. *Applied Spectroscopy* **1989,** 43, (2), 263-267.
66. Parida, K. M.; Samantaray, S. K.; Mishra, H. K. *Journal of Colloid and Interface Science* **1999,** 216, (1), 127-133.
67. Brinker, C. J.; Scherer, G. W., *Sol-Gel Science: The Physics and Chemistry of Sol-Gel Processing*. Academic press: 2013.
68. Thommes, M. *Chemie Ingenieur Technik* **2010,** 82, (7), 1059-1073.
69. Tao, H.; Yang, H.; Liu, X.; Ren, J.; Wang, Y.; Lu, G. *Chemical Engineering Journal* **2013,** 225, 686-694.
70. Li, Y.; Xia, W.; Zou, R.; Zhang, J.; Chen, Z.; Xu, Q. *RSC Advances* **2015,** 5, (117), 96580-96586.
71. Ferrari, A. C. *Solid State Communications* **2007,** 143, (1–2), 47-57.
72. Pimenta, M. A.; Dresselhaus, G.; Dresselhaus, M. S.; Cancado, L. G.; Jorio, A.; Saito, R. *Physical Chemistry Chemical Physics* **2007,** 9, (11), 1276-1290.
73. Tuinstra, F.; Koenig, J. L. *The Journal of Chemical Physics* **1970,** 53, (3), 1126-1130.
74. Samantaray, S. K.; Parida, K. *Applied Catalysis A: General* **2001,** 220, (1–2), 9-20.
75. Andrews, G. P.; AbuDiak, O. A.; Jones, D. S. *Journal of Pharmaceutical Sciences* **2010,** 99, (3), 1322-1335.
76. Kaushal, A. M.; Chakraborti, A. K.; Bansal, A. K. *Molecular Pharmaceutics* **2008,** 5, (6), 937-945.
77. Li, Y.; Zhang, Q.; Zhang, J.; Jin, L.; Zhao, X.; Xu, T. *Scientific Reports* **2015,** 5, 14155.
78. Su, B.-L.; Sanchez, C.; Yang, X.-Y., *Hierarchically Structured Porous Materials: From Nanoscience to Catalysis, Separation, Optics, Energy, and Life Science*. John Wiley & Sons: 2012.

CHAPTER 5

A Novel Synthesis Route of Broken, Deformed and Bubble-like Hollow Carbon Nanostructures from SiO_2@Polyvinylpyrolidone Spheres as Templates

5.1 Introduction

The synthesis of nanostructured composites materials of a length scale ranging from nanometres to micrometres has tremendously progressed over the last few decades. To promote the wide variety of applications of these composites materials, the control of size, shape, core structure and morphology is crucial[1, 2]. Silica is a popular inorganic material for mesoporous and composite materials synthesis owing to the well-known hydrolysis and condensation of silicon alkoxides in aqueous solution. Polymer composites such as polymer-SiO_2 have been used in mechanical,[3-5] medical[6] and electrical[7] applications. More recently, Zhang *et al*. obtained raspberry like spheres by PVP functionalization of polystyrene silica spheres[8]. These raspberry particles can be used in superhydrophobic surface owing to their contact angle and wetting properties. Polyvinylpyrrolidone has also been used to stabilize metal nanoparticles such as gold[9, 10] and silver[11, 12].

Polyvinylpyrrolidone is a water soluble polymer that has low toxicity, high polarity and portrays excellent chemical and thermal stability[13, 14]. Polyvinylpyrrolidone (PVP) was discovered by a German Chemist, Walter Reppe in 1939 as a product of acetylene chemistry[15, 16] (Fig. 5.1). The reaction of acetylene with formaldehyde produces 2-butyne-1,4-diol which is hydrogenated to 1,4-butanediol. The butanediol undergoes oxidative cyclization to produce butyrolactone which when reacted with ammonia forms pyrrolidone by the removal of water. The vinyl group is then introduced to form N-vinylpyrrolidone. The vinylpyrrolidone then undergoes polymerization either in aqueous or organic solvents to produce polyvinylpyrrolidone[17-20] (Fig. 5.2). Polyvinylpyrrolidone can also be produced through a radical polymerization[19, 21-23] or a cationic polymerization[24]. Due to its excellent chemical stability and ease of modification properties, it has been used in the cosmetics[25] and pharmaceuticals industries[26, 27] and membrane synthesis[28].

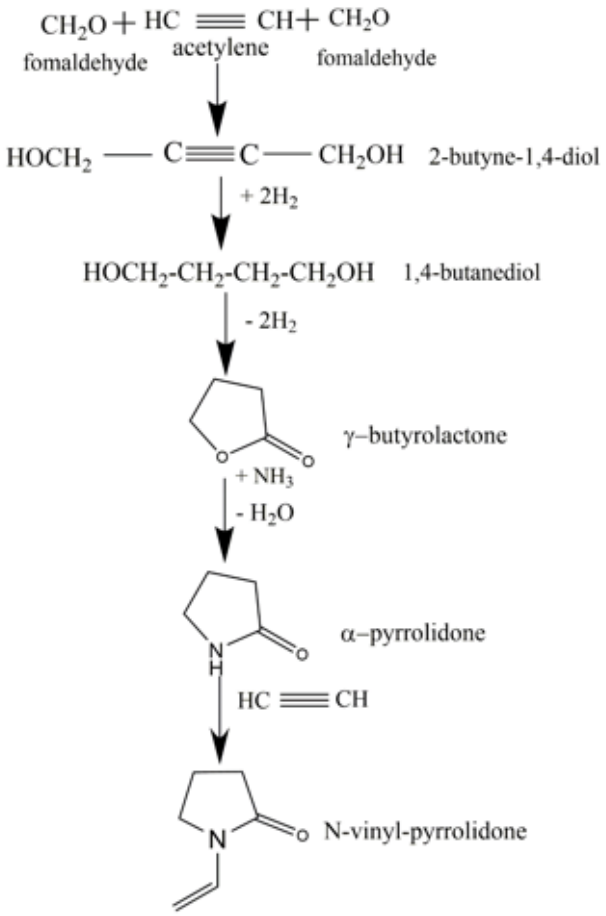

Figure 5.1. Reppe synthesis of N-vinyl-pyrrolidone (obtained from ref[17]).

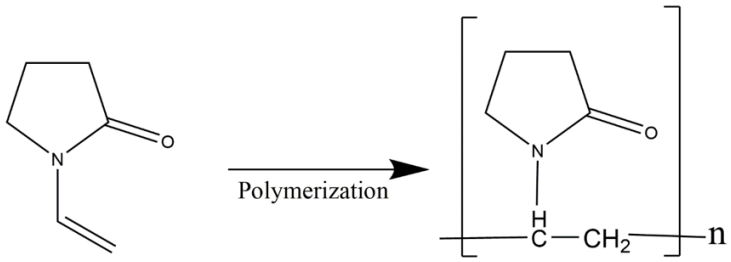

Figure 5.2. Polymerization of vinylpyrrolidone (obtained from ref[17]).

5.1.1 SiO_2@PVP spheres synthesis

Two main routes can be used to synthesize these PVP-silica hybrid materials.

(i) Polymer grafting to SiO_2

Polymer grafting to SiO_2 entails the chemical bonding of the PVP polymer chains to the SiO_2 surface. The adsorption of the PVP on the SiO_2 initiates the process of polymer grafting (Fig 5.3 and 5.4). In the grafting process, the silanol groups on the SiO_2 surface are hydrogen

bonded to the carbonyl group of PVP (Fig. 5.5). The density of silanol groups and that of PVP determines the adsorption energy[29]. The adsorption of PVP on silica is dependent on the PVP dosage, adsorption time and polydispersity.

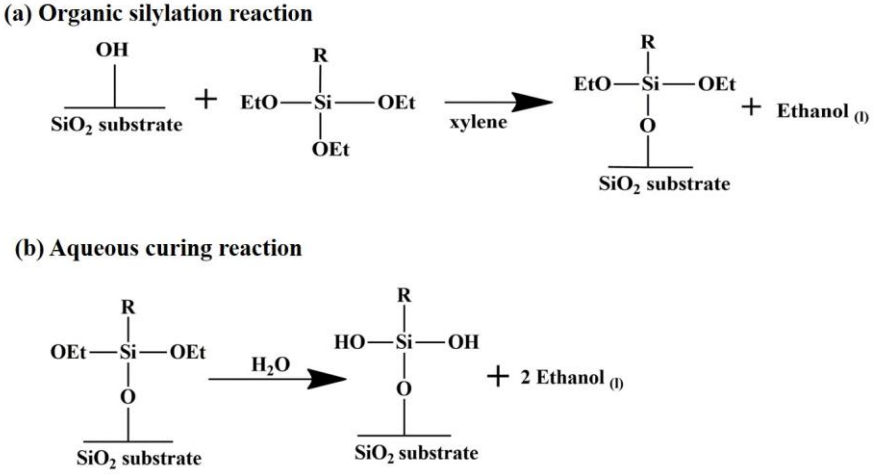

Figure 5.3. Silylation reaction using organic solvents (obtained from ref[30]).

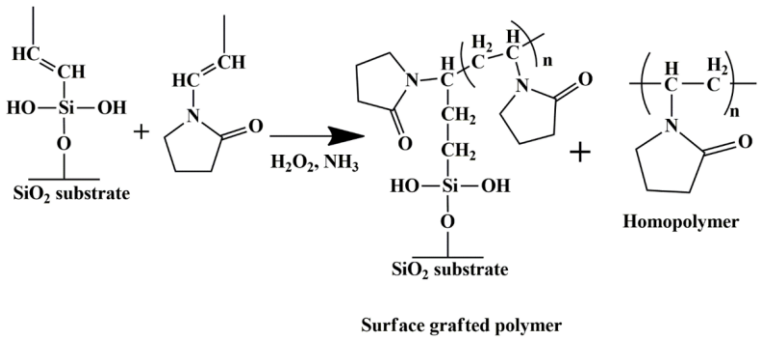

Figure 5.4. Surface grafting reaction of PVP on vinyltri-ethoxy-silylated silica surface (obtained from ref[30]).

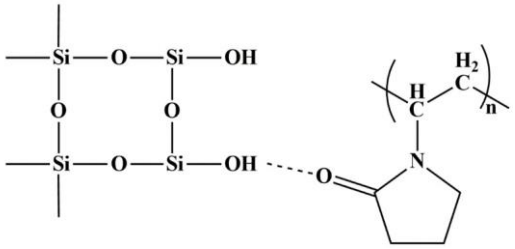

Figure 5.5. Schematic diagram showing hydrogen bonding of SiO_2 to PVP.

(ii) Graft polymerization method

This method entails the activation of silica surface with active sites followed by the growth of polymer chains on the sites using a step or a chain polymerization reaction mechanism. The silanol group of silica is hydrogen bonded to the oxygen atom of the carbonyl group in PVP[31, 32]. Graft polymerization provides a high and uniform surface coverage due to the presence of less steric hindrances[33]. In contrast, the large steric hindrances present during polymer grafting hinder the surface coverage. However, for graft polymerization to occur, a prior chemical modification is required. The silane coupling agents and siloxane bridges are the readily applied for surface modification of silica. However, the major drawback of modification of silica on surface grafted PVP; is the low PVP adsorbed due to the size exclusion mechanism. According to de Gennes *et al*. grafted PVP can be viewed as an entangled network with an interchain spacing that depends on the distance from the surface[34]. The presence of these entangled network excludes PVP molecules in the surrounding solution that are larger than the interchain spacing from the silica surface. Also, the amount of PVP adsorbed onto silica surface is dependent on the organic functionality bound onto the surface[30].

5.1.2 Synthesis of hollow carbon nanostructures

Hollow carbon structures have been produced using the hydrothermal method[35], pyrolysis[36] and templating method[37], [38], among others. The synthesis of the hollow structures provide advantages of tuning their mechanical, chemical and electrical properties. For instance, the refractive index and the active surface area can be modulated in the void space of these hollow structures[39]. Many facile methods such as hydrothermal and CVD nanocasting have been used to synthesize hollow carbon spheres from SiO_2 templates[40, 41]. Use of silica spheres as hard templates is advantageous due to the easy processability of SiO_2 spheres by the Stober method. In our approach, a direct addition of PVP solution into a silica suspension was used to produce SiO_2@PVP spheres; where the SiO_2 surface was modified with PVP. Previous reports have shown that PVP addition during SiO_2 synthesis leads to a broad SiO_2 size distribution and increases SiO_2-SiO_2 surface interactions[42]. Despite the existence of several template materials such as polystyrene and SiO_2, a simple, unique and morphology controllable template is requisite. To this end, a novel material is proposed subject to the following objectives;

i. To determine the effect of PVP concentration and silica size distribution (polydispersity and monodispersity) on the morphology of hollow carbon nanostructures.
ii. To determine the effect of carbonization time of SiO_2@PVP templates on the morphology of hollow carbon nanostructures.

5.2 Experimental procedure

5.2.1 Starting materials

The reagents for SiO_2 and HCSs synthesis were as reported previosuly in Section 4.2.2. Polyvinylpyrrolidone, PVPK30 (Mw 40,000, Aldrich) was used as the surface modifying agent.

5.2.2 Synthesis of SiO_2 spheres and hollow carbon spheres (HCSs)

The synthesis of pristine monodispersed and polydispersed SiO_2 spheres and their respective HCSs is summarized in Fig. 5.6. Pristine silica spheres (406 ± 32 nm) were synthesized by mixing 90 mL of ethanol and 63 mL of distilled water and 5 mL of NH_4OH in a volumetric flask and stirring for 20 min. Then 16 mL of TEOS was added rapidly and the mixture was stirred for another 1 hour. Smaller pristine silica spheres (184 ± 11 nm) were also synthesized by mixing 80 mL of ethanol and 14 mL of distilled water and 2 mL of NH_4OH in a volumetric flask and stirring for 20 min. Then 2 mL of TEOS was added rapidly and the mixture stirred for another 1 h. The obtained pristine SiO_2 spheres (184 ± 11 nm and 406 ± 32 nm) were mixed in a weight ratio of 50:50 to give polydispersed silica spheres. Carbonization of all the pristine SiO_2 spheres was carried out by a bubbling method using toluene as the carbon source and argon as the carrier gas at a flow rate of 200 mL/min in a CVD reactor at 900°C for 1 h. The carbonized silica spheres were then etched with 10 % HF for 24 h at room temperature and dried to give the hollow carbon structures (HCSs). The obtained hollow carbon spheres are referred to as pristine HCSa, HCSb and HCSc representing monodispersed HCS $\approx$ 200 nm, monodispersed HCS $\approx$ 400 nm and polydispersed HCS, respectively.

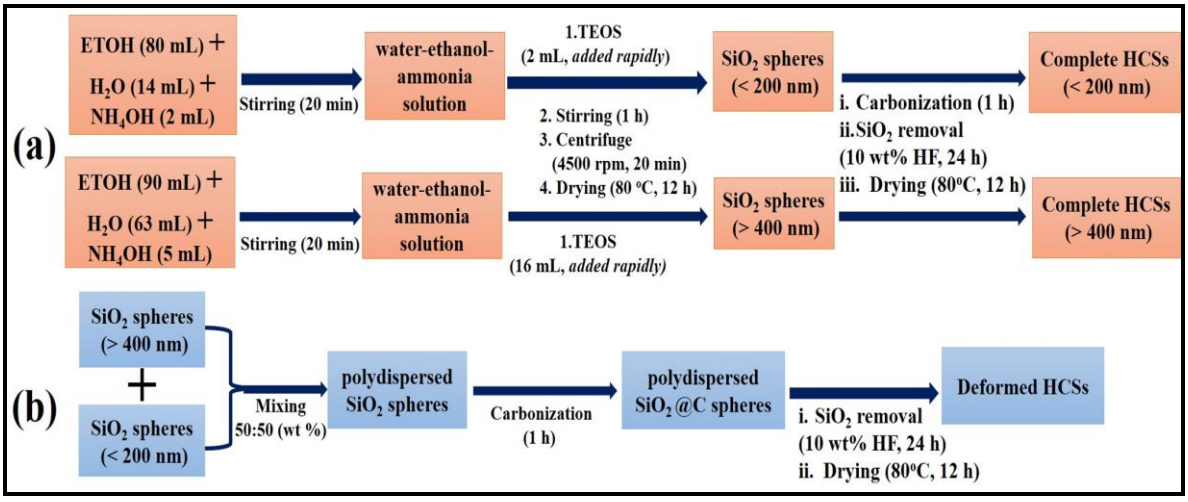

Figure 5.6. A diagram showing the synthesis of; (a) pristine monodispersed SiO_2 spheres and HCSs and (b) pristine polydispersed SiO_2 spheres and HCSs, respectively.

5.2.3 Effect of PVP concentration on the carbon morphology

To study the effect of PVP concentration on the carbon morphology, both monodispersed and polydispersed SiO_2@PVP templates were synthesized using (1:1) and (1:0.1) weight ratios of SiO_2:PVP respectively (Fig. 5.7). Three different samples; the monodispersed $SiO_2 \approx 200$ nm, the monodispersed $SiO_2 \approx 400$ nm and the polydispersed SiO_2 spheres (0.5 g) were dispersed separately in a 40 mL of ethanol for 20 min. A PVP solution was obtained by dispersing 0.5 g in 20 mL of distilled water and sonicating for 10 min. The PVP solution was then added to the respective SiO_2 suspension and stirred for 1 h to give three SiO_2@PVP solutions. The SiO_2@PVP solutions were then centrifuged at 4500 rpm for 20 min and the products dried at 80°C for 12 h. The dried SiO_2@PVP spheres were referred to as SiO_2@PVP-200 nm and SiO_2@PVP-400 nm and polydispersed SiO_2@PVP respectively. Carbonization of all the SiO_2@PVP spheres followed by SiO_2 etching and product drying was carried out as described previously. The obtained HCSs are referred to as HCSa-0.1wt%, HCSb-0.1wt% and HCSc-0.1wt% for the three samples covered with PVP (0.1 wt%) and as HCSa-1wt%, HCSb-1wt% and HCSc-1wt% for the three samples covered with PVP (1 wt%), respectively.

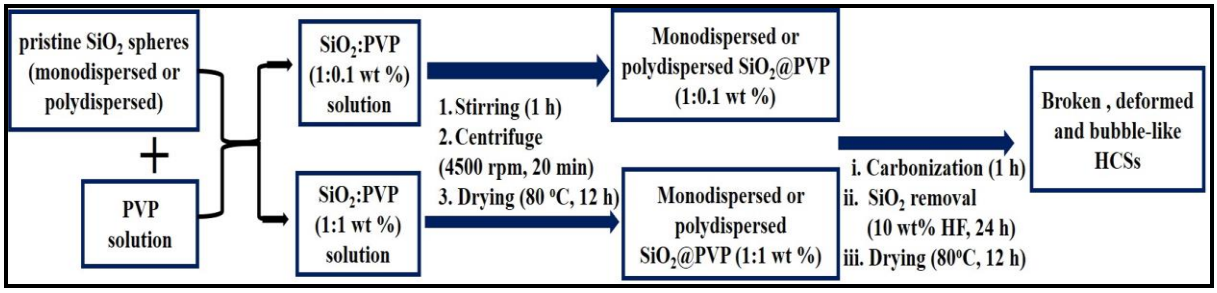

Figure 5.7. A schematic diagram showing the synthesis pristine monodispersed and polydispersed SiO_2@PVP spheres and HCSs, respectively.

5.2.4 Effect of PVP adsorption time on SiO_2 and carbon morphology

To study the effect of PVP adsorption time on SiO_2, solutions consisting of polydispersed SiO_2:PVP (1:1 wt %) were mixed at different stirring times (1, 12 and 24 h) respectively. The obtained polydispersed SiO_2@PVP spheres were referred to as SiO_2@PVP-1h, SiO_2@PVP-12h and SiO_2@PVP-24h respectively. The obtained hollow carbon nanostructures from polydispersed SiO_2@PVP spheres are referred to as HCSc-1wt% (1h) and HCSc-1wt% (12h) and HCSc-1wt% (24h) for the three samples stirred at times 1 h, 12 h, and 24 h respectively.

5.2.5 Effect of varying carbonization time on carbon morphology

The effect of carbonization time was investigated by carbonization of the polydispersed SiO_2 and SiO_2@PVP (SiO_2:PVP, 1:1 wt%) spheres for 1 h, 2 h and 4 h respectively. The obtained hollow carbon nanostructures are referred to as HCSc-1wt% (1h), HCSc-1wt% (2h) and HCSc-1wt% (4h) representing the carbonization times 1 h, 2 h and 4 h respectively.

5.2.6 Characterization

The morphology of the synthesized SiO_2 spheres, SiO_2@PVP spheres and broken, deformed and bubble-like hollow carbon nanostructures was carried out using TEM and SEM. The grahitic nature and thermal stability of the HCSs was investigated using Raman spectroscopy and TGA, respectively.

5.3 Results and discussion

5.3.1. Effect of PVP concentration on carbon morphology obtained from monodispersed SiO_2 spheres

5.3.1.1 Morphology analysis

The pristine SiO_2 spheres were monodispersed and had particle sizes of 184 ± 11 nm and 406 ± 32 nm respectively (Fig. 5.8a, d). To understand the role of PVP concentration in the carbon morphology, two different PVP concentrations were used to functionalize the monodispersed SiO_2 spheres. Fig. 5.8b and 5.8e show that the PVP functionalized monodispersed SiO_2 spheres (1:0.1 wt% of SiO_2:PVP) had less SiO_2-SiO_2 interactions than when a higher concentration (SiO_2:PVP 1:1 wt%) was used (Fig. 5.8c, f). A slight increase in the SiO_2 spheres particle size was observed in all the monodispersed spheres upon addition of PVP (Table 5.1). However, it was noted that the PVP concentration affected the SiO_2-SiO_2 interactions to obtain various arbon nanostructures.

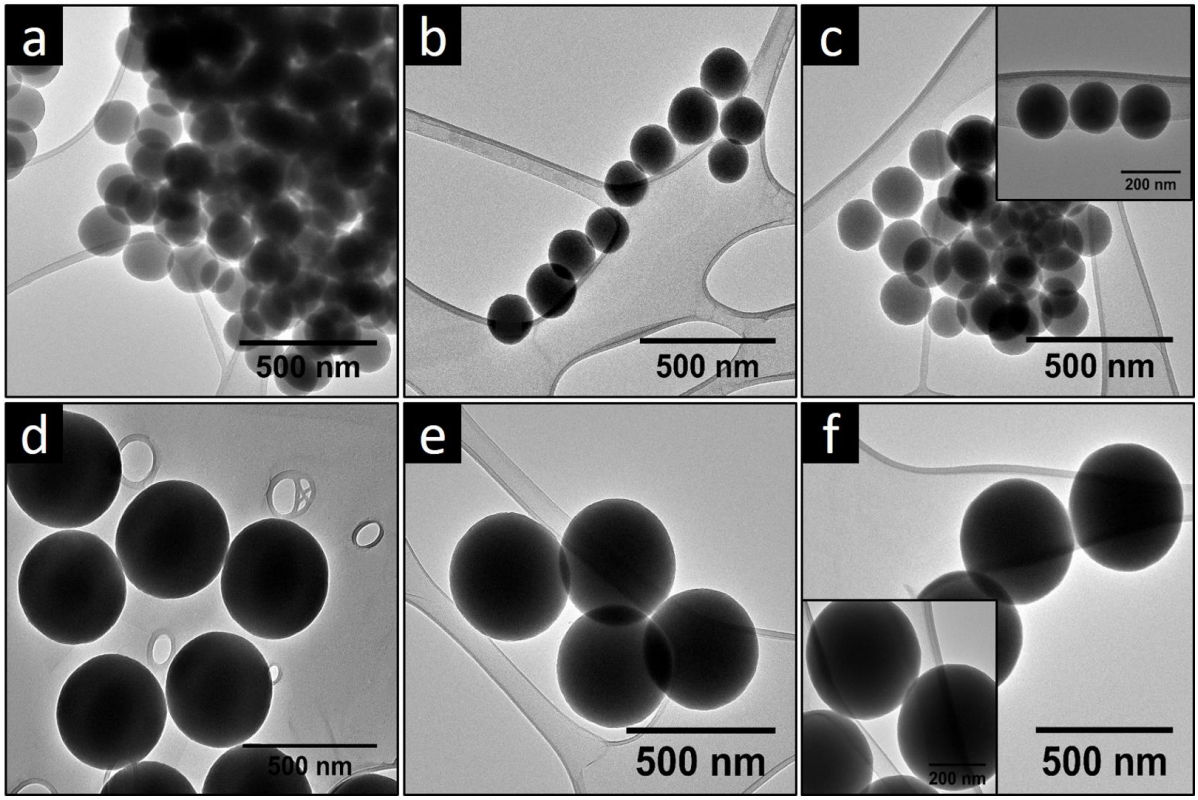

Figure 5.8. TEM images of monodispersed SiO_2 spheres and SiO_2@PVP spheres; (a and d) (pristine SiO_2 200 nm and 400 nm, (b and e) 1:0.1 wt% of SiO_2:PVP 200 nm and 400 nm and (c and f) 1:1 wt% of SiO_2:PVP 200 nm and 400 nm, respectively.

Table 5.1. The effect of PVP concentration on the SiO_2 particle sizes

Description	SiO_2:PVP (wt%)	Particle size (nm)
SiO_2-200 nm	-	184 ± 11
SiO_2@PVP-200 nm	1:0.1	184 ± 22
SiO_2@PVP-200 nm	1:1	185 ± 26
SiO_2-400 nm	-	406 ± 32
SiO_2@PVP-400 nm	1:0.1	407 ± 28
SiO_2@PVP-400 nm	1:1	409 ± 21

Upon carbonization for 1 h and SiO_2 removal, a decrease in the particle size of the HCSs formed from the pristine SiO_2 and PVP functionalized SiO_2 spheres was observed (Table 5.2). This could be attributed to the silica shrinkage during the carbonization process. Another contributing factor is the decomposition of PVP on silica surface during carbonization resulting in a decrease in final particle size of the HCSs. The silica shrinkage and polymer decomposition on the SiO_2 surface have been reported elsewhere in literature[40, 43]. The pristine hollow carbon spheres formed after etching silica had complete carbon shells (Fig. 5.9a, d). Fig. 5.9b and 5.9e show TEM images of HCSs (HCSa-0.1wt% and HCSb-0.1wt%) obtained from SiO_2 functionalized with 1:0.1 wt% of SiO_2:PVP had a mixture of broken and complete carbon shells. In contrast, deformed hollow carbon structures were generated from the 1:1 wt% of SiO_2:PVP spheres as seen in HCSa-1wt% and HCSb-1wt% respectively (Fig. 5.9c, f). Consequently, the inner diameters of the deformed HCSs could not be determined. SEM images of the respective HCSa and HCSb show that indeed the spheres were deformed when 1 wt% PVP concentration was used and comprised of broken carbon shells when a lower PVP concentration 0.1 wt% was used (Fig. 5.10).

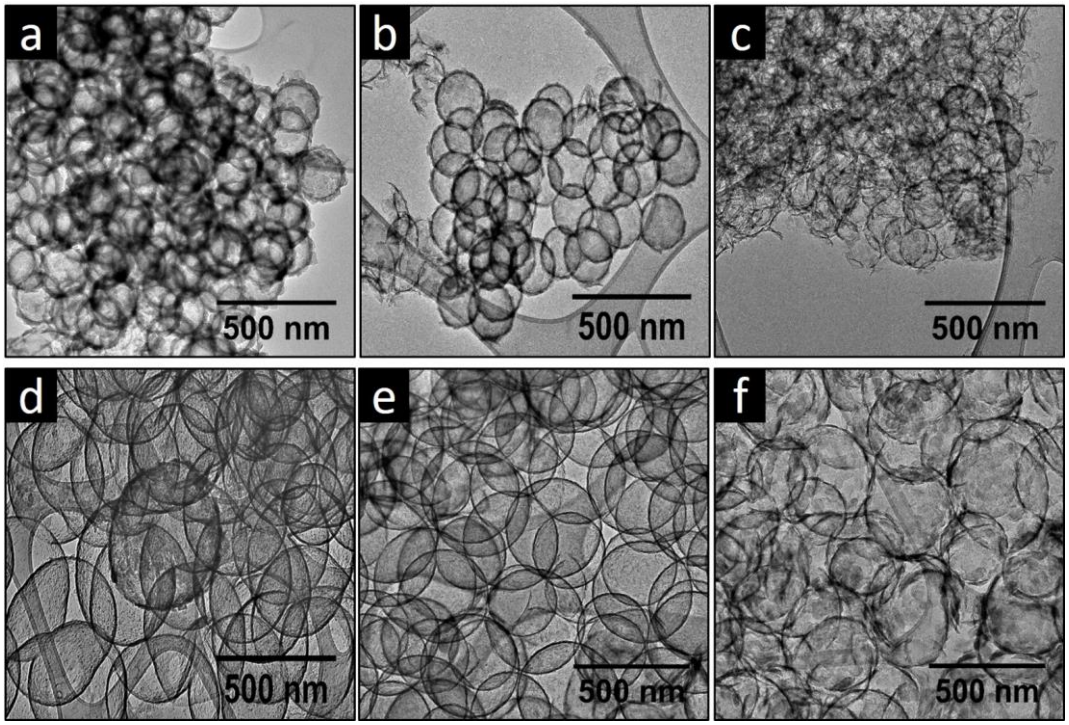

Figure 5.9. TEM images of the obtained HCSs; (a and d) (pristine HCSa and HCSb), (b and e) HCSa-0.1wt% and HCSb-0.1wt% and (c and f) HCSa-1wt% and HCSb-1wt%, respectively.

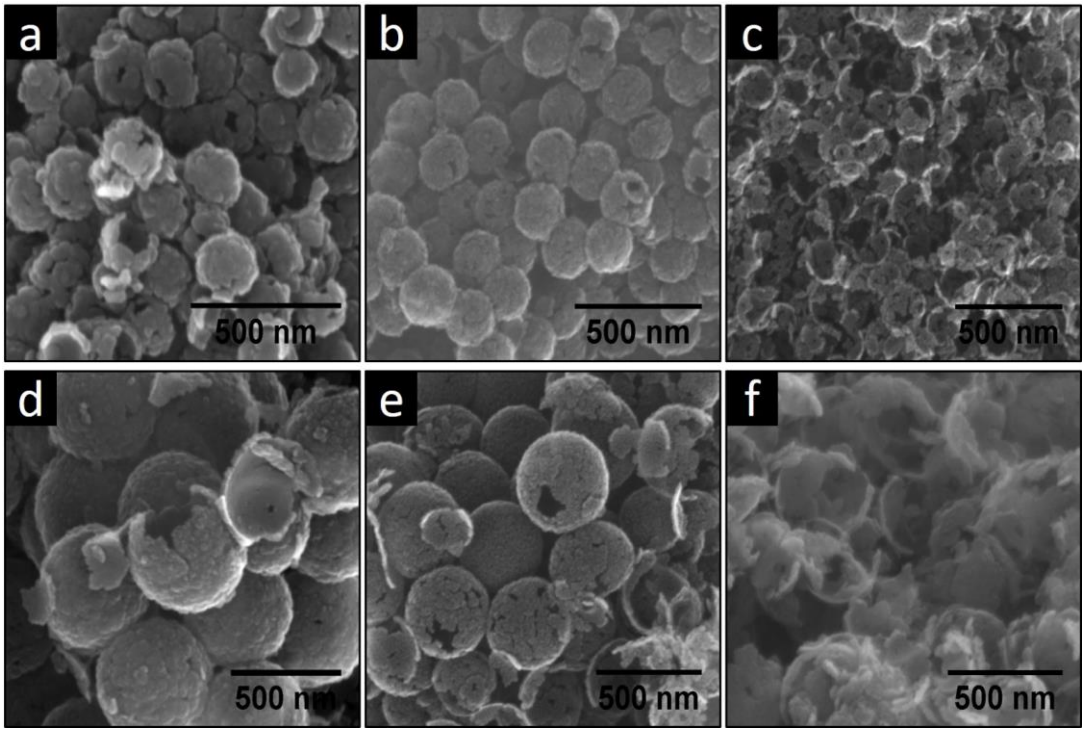

Figure 5.10. SEM images of the obtained HCSs; (a and d) (pristine HCSa and HCSb), (b and e) HCSa-0.1wt% and HCSb-0.1wt% and (c and f) HCSa-1wt% and HCSb-1wt%, respectively.

Table 5.2. Effect of PVP concentration on the carbon shell thickness of hollow carbon nanostructures obtained after 1 h carbonization time and SiO_2 removal

Description	SiO_2:PVP (wt%)	Shell thickness (nm)	Inner diameter (nm)
Pristine HCSa	-	18 ± 4	174 ± 16
HCSa-0.1wt%	1:0.1	15 ± 6	173 ± 17
HCSa-1wt%	1:1	8 ± 3	-
Pristine HCSb	-	12 ± 5	404 ± 20
HCSb-0.1wt%	1:0.1	12 ± 4	405 ± 16
HCSb-1wt%	1:1	15 ± 5	-

5.3.1.2 Thermal analysis

5.3.1.2.1 Thermal analysis of monodispersed SiO_2 spheres and SiO_2@PVP spheres

Fig. 5.11 shows the TGA and DTG curves of monodispersed pristine SiO_2-200 nm, SiO_2@PVP-200 nm spheres with SiO_2:PVP ratio of (1:0.1wt%) and (1:1 wt%) taken from 35°C to 900°C in air respectively. The total weight loss of the pristine SiO_2, SiO_2@PVP (1:0.1wt %) and SiO_2@PVP (1:1 wt%) was 12.6%, 14.72% and 15.30% respectively as shown in Fig. 5.11a. The increase in the total weight loss after PVP adsorption onto SiO_2 (0.1 wt% and 1 wt%) can be attributed to the removal of additional hydrogen bonded silanols and the PVP polymer. The surface of silica spheres is known to consist of silanol groups, adsorbed water and hydrogen bonds[44, 45].

The DTG curves (Fig. 5.11b) shows three derivative weight losses in all the obtained SiO_2 spheres with their respective description indicated in Table 5.3. The first derivative weight loss was observed between 39°C and 200°C owing to the loss of adsorbed H_2O and ethanol molecules[46] (Table 5.3). From 210°C to 386°C, a considerable weight loss (0.11%) was observed in pristine SiO_2 spheres resulting from the decomposition of residual organic molecules and the condensation of the free silanols[47]. A similar peak was seen in the SiO_2@PVP (1:0.1 wt%) and SiO_2@PVP (1:1 wt%) between 210°C and 430°C with a weight loss of 0.25% and 0.34% respectively. The increased weight loss corresponds to the

decomposition temperature of PVP between 360°C and 440°C[48]. The third derivative weight loss was observed between 406°C and 500°C in pristine SiO_2 spheres. This could be attributed to the removal of unreacted organic residues. In the SiO_2@PVP (1:0.1 wt%) and SiO_2@PVP (1:1 wt%) spheres, a weight loss of 0.11% and 0.14% was observed between 440°C and 690°C, respectively. This resulted from the removal of silica networks formed through further polymerization as discussed in the previous chapter (Section 4.3.2.1.4).

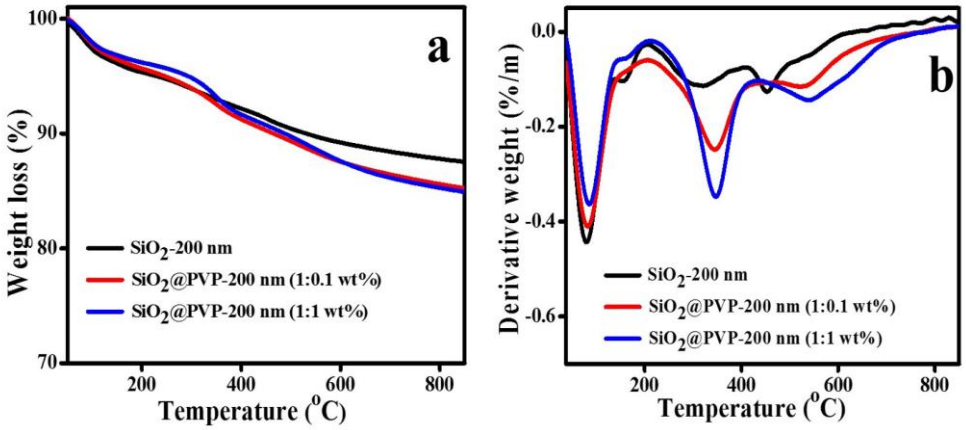

Figure 5.11. TG-DTG curves of pristine monodispersed SiO_2 spheres and SiO_2@PVP spheres; (a) Thermogravimetric curves and (b) the derivative curves, respectively.

Table 5.3. Decomposition temperatures and derivative weight loss of monodispersed SiO_2 and SiO_2@PVP spheres

Sample description	Decomposition temperature (°C)	Weight loss (%)	Description
SiO_2-200 nm	39 to 200	0.45	Loss of adsorbed water
	210 to 387	0.11	Loss of organic residues and condensation of free silanols
	406 to 500	0.12	Removal of organic residues
SiO_2@PVP-200 nm (1:0.1 wt%)	39 to 160	0.41	Loss of adsorbed water
	210 to 426	0.25	Condensation of free silanols and PVP decomposition
	452 to 614	0.11	Removal of organic residues
SiO_2@PVP-200 nm (1:1 wt%)	38 to 200	0.36	Loss of adsorbed water
	220 to 424	0.34	Condensation of free silanols and PVP decomposition
	440 to 690	0.14	Removal of organic residues

5.3.1.2.2 Thermal analysis of monodispersed HCSs obtained from SiO_2-200 nm and SiO_2@PVP templates

Thermal gravimetric curves of the obtained monodispersed HCSs showed the presence of two decomposition curves (Fig. 5.12a). The first derivative weight was observed between 300°C and 400°C with percentage weight loss of 0.65%, 0.80% and 1.20% in the pristine HCSa, HCSa-0.1 wt% and HCSa-1 wt%, respectively (Fig. 5.12b). This can be attributed to organic residues that were not completely removed during the SiO_2 etching process[49]. An increased weight loss in SiO_2@PVP templates was observed due to incomplete removal of PVP and silica related networks. The pristine HCSa and HCSa-0.1 wt% started to decompose in air at 505°C whereas the onset decomposition temperature of HCSa-1 wt% was at 490°C respectively. The slight decrease in thermal stability can be attributed to impurities resulting from PVP used in SiO_2@PVP templates.

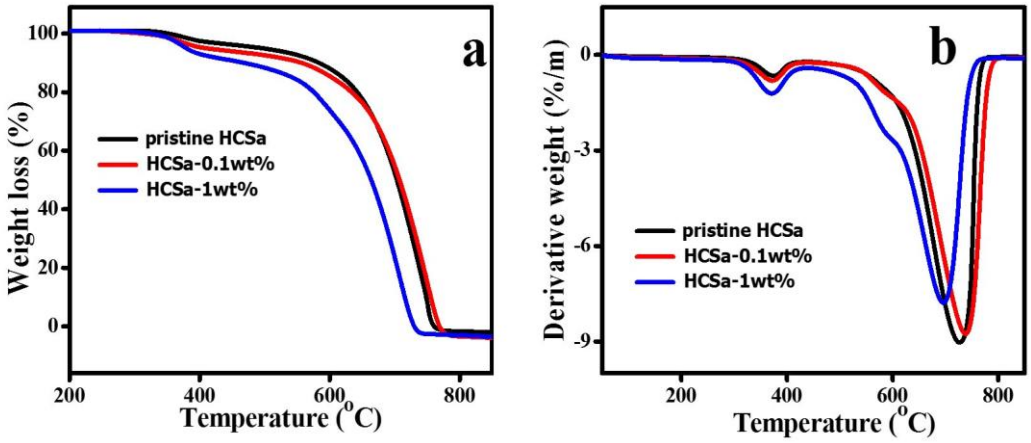

Figure 5.12. TG-DTG curves of pristine HCSa and other obtained HCSs; (a) Thermogravimetric curves and (b) the derivative curves, respectively.

5.3.1.3 Raman analysis of the monodispersed hollow carbon nanostructures

The Raman spectra of the obtained hollow carbon nanostructures had peaks at 1336-1365 cm^{-1} and 1575 -1596 cm^{-1} characteristic of the D band and the G band respectively (Fig. 5.13). Interestingly, the broken and deformed HCSs exhibited fewer defect density (I_D/I_G ratio 0.72 to 0.95) than the pristine HCSs (0.99 to 1.01) (Table 5.4). This can be clearly seen in the

decreased D peak intensity (Fig. 5.13b and 5.13c) of the respective HCSs obtained from SiO_2:PVP templates with 1.0.1wt% and 1:1 wt%, respectively. This can be attributed to the carbonization of both the toluene (our carbon source) and PVP when SiO_2@PVP templates are used resulting in more carbon atoms deposited on the surface. However, when plain SiO_2 is used, toluene is the only carbon source and thus, fewer carbon atoms are coated on the SiO_2 spheres resulting in HCSs of higher I_D/I_G ratios after carbon etching. However, a more detailed study on the effect of PVP on HCS structural properties will be helpful.

Table 5.4. The I_D/I_G ratios of obtained monodispersed HCSs

Description	D-band position (cm^{-1})	G-band position (cm^{-1})	I_D/I_G ratio
Pristine HCSa	1336	1584	0.99
HCSa-0.1 wt%	1346	1596	0.99
HCSa-1 wt%	1358	1594	0.95
Pristine HCSb	1342	1575	1.01
HCSb-0.1 wt%	1360	1579	0.93
HCSb-1 wt%	1365	1584	0.72

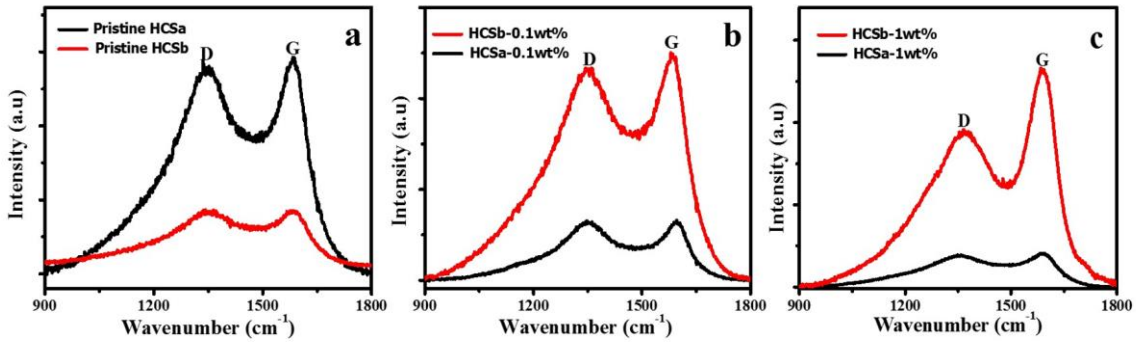

Figure 5.13. Raman spectra of hollow carbon structures obtained from monodispersed SiO_2 spheres; a (pristine HCSs), b (HCSs from 1:0.1 wt% SiO_2:PVP) and c (HCSs from 1:1 wt% SiO_2:PVP), respectively.

5.3.2 Effect of varying PVP concentration and polydispersed SiO_2 and their respective HCSs

5.3.2.1 Morphology analysis of polydispersed SiO_2@PVP spheres and HCSs

To investigate the role of particle size distribution on the carbon morphology, polydispersed spheres were prepared and characterized as previously discussed. Fig. 5.14a shows that indeed the SiO_2 spheres obtained after mixing the 200 nm and 400 nm SiO_2, were polydispersed. To understand the role of PVP in the carbon morphology, two different PVP concentrations were used to functionalize the polydispersed SiO_2 spheres. Fig. 5.14b and 5.14c show that the PVP functionalized polydispersed SiO_2 spheres (1:0.1 wt% of SiO_2:PVP) had less SiO_2-SiO_2 interactions than when a higher concentration (SiO_2:PVP 1:1 wt%) was used. A slight increase in the SiO_2 spheres particle size was observed in the polydispersed spheres upon addition of PVP.

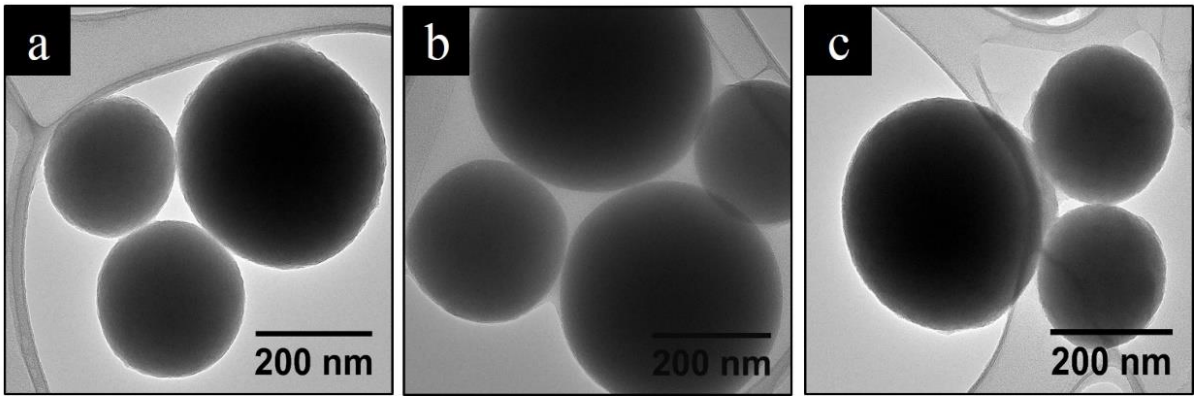

Figure 5.14. TEM images of pristine and PVP functionalized polydispersed SiO_2 spheres; (a) pristine polydispersed SiO_2, (b) 1:0.1 wt% of SiO_2:PVP and (c) 1:1 wt% of SiO_2:PVP, respectively.

The TEM and SEM micrographs of the pristine HCSc show that the spheres were deformed and broken (Fig. 5.15a, d) unlike the monodispersed pristine HCSa and HCSb that were complete. This deformed nature of the spheres can be attributed to the polydispersion of SiO_2 spheres that would hinder infiltration of carbon in between the spheres, but carbonization would occur along the outer edges of the interconnected spheres[42]. In contrast, when a 1:0.1 wt% of the polydispersed SiO_2:PVP spheres were used broken and bubble-like hollow carbon nanostructures were obtained (Fig. 5.15b, e). This is due to the lesser PVP molecules on SiO_2

surface during carbonization compared to the monodispersed spheres (Fig. 5.15b). Fig. 5.15c shows the TEM image of HCSc-1 wt% with a wormlike morphology and SEM image shows that it's open ended (Fig. 5.15f). This indicates that the SiO_2 particle size distribution does affect the carbon coverage and consequently the obtained carbon morphology. Polydispersity of the SiO_2 templates contributes to the breakage of the HCSs due to high strains during SiO_2 removal after carbonization. Table 5.5 shows that there was a decrease in the shell thickness of HCSc from 13 ± 3 nm in pristine HCSc to 7 ± 5 nm in HCSc-1 wt%. The concentration of PVP was found to affect the carbon morphology with the carbon shell thickness increased in HCSc obtained from the 1:0.1 wt% of SiO_2:PVP was added. High PVP concentration (1 wt%) gave deformed wormlike hollow carbon nanostructures whereas low PVP concentration (0.1 wt%) gave bubble-like hollow carbon nanostructures.

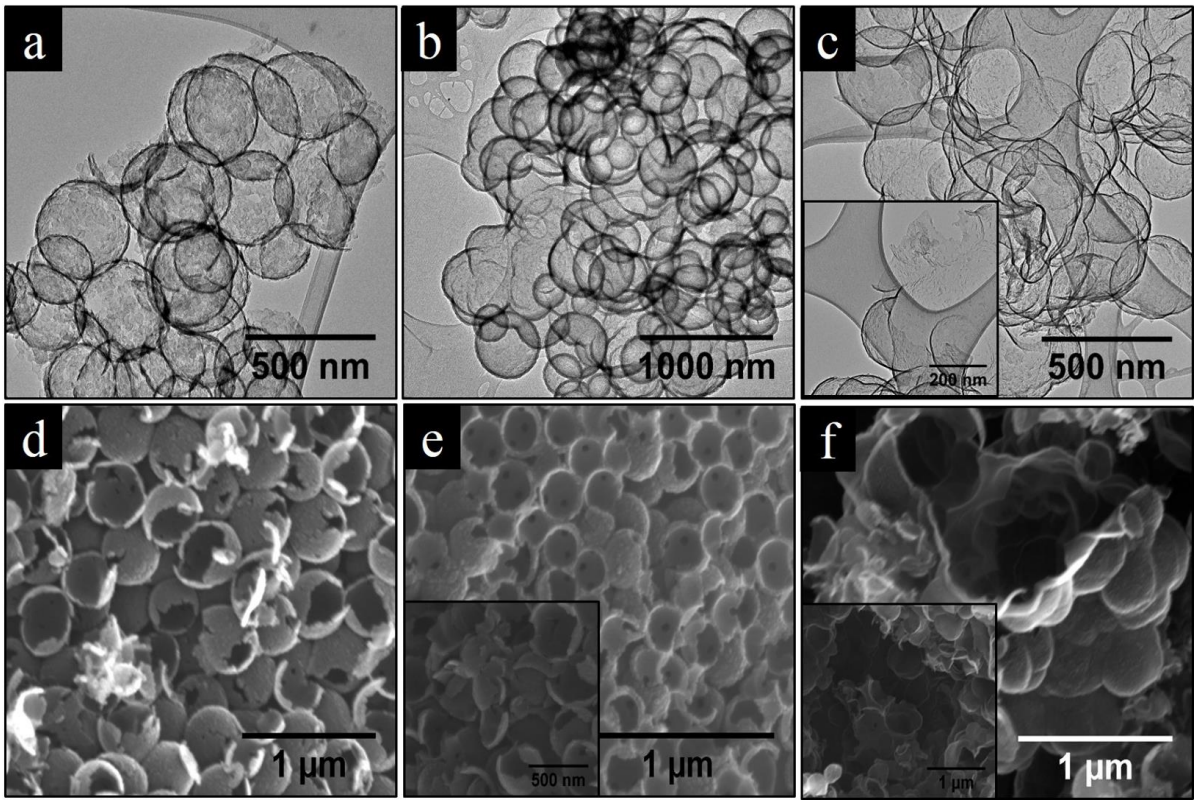

Figure 5.15. TEM and SEM images of obtained HCSs; (a and d) pristine HCSc, (b and e) HCSc-0.1 wt% and (c and f) HCSc-1 wt%, respectively.

Table 5.5. Effect of PVP concentration on the carbon shell thickness of hollow carbon nanostructures

Description	SiO_2:PVP (wt%)	Carbonization time (h)	Shell thickness (nm)
Pristine HCSc	-	1	13 ± 3
HCSc-0.1wt%	1:0.1	1	10 ± 2
HCSc-1wt%	1:1	1	7 ± 5

5.3.2.2 Thermal analysis

5.3.2.2.1 Thermal analysis of polydispersed SiO_2 spheres and SiO_2@PVP spheres

The TGA and DTG curves of polydispersed pristine SiO_2, polydispersed $SiO_{2@}$PVP (1:0.1 wt%) and polydispersed $SiO_{2@}$PVP (1:1 wt%) were recorded from 35°C to 900°C in air respectively (Figs. 5.16a, b). The surface of SiO_2 spheres is known to consist of silanol groups, adsorbed water and hydrogen bonds which are responsible for the weight loss observed in SiO_2 TGA curves[44, 45]. The total weight loss of the pristine polydispersed SiO_2, SiO_2@PVP (1:0.1 wt%) and SiO_2@PVP (1:1 wt%) was 12.10%, 11.14% and 15.16% respectively as shown in Fig. 5.16a. The increase in the total weight loss after PVP adsorption onto SiO_2 (1 wt%) can be attributed to the removal of additional hydrogen bonded silanols and the PVP polymer. The DTG curves (Fig. 5.16b) shows the derivative weight losses in the obtained SiO_2 spheres with their respective description indicated in Table 5.6. The first derivative weight loss was observed between 35°C and 170°C due to the removal of adsorbed H_2O[46]. From 200°C to 415°C, a considerable weight loss (0.20%) was observed in pristine polydispersed SiO_2 spheres resulting from the removal of unreacted organic molecules[47].

In the polydispersed SiO_2@PVP (1:0.1 wt%), a derivative weight loss of 0.22% was observed between 170°C and 424°C and an additional derivative peak between 450°C and 606°C with a 0.13% weight loss respectively; corresponding to the decomposition of PVP and other organic residues[48]. In polydispersed SiO_2@PVP(1:1 wt%), three derivative curves were observed between 470°C and 620°C exhibiting a 1.17% percentage weight loss. This could be attributed to condensation of free silanols, PVP decomposition and the loss of organic residues related to SiO_2 and PVP networks. This increase in weight loss in

polydispersed SiO_2@PVP (1:1 wt%) relative to the monodispersed SiO_2@PVP (1:0.1 wt%) confirms the adsorption of more PVP volume on polydispersed SiO_2 (Table 5.3 versus Table 5.6).

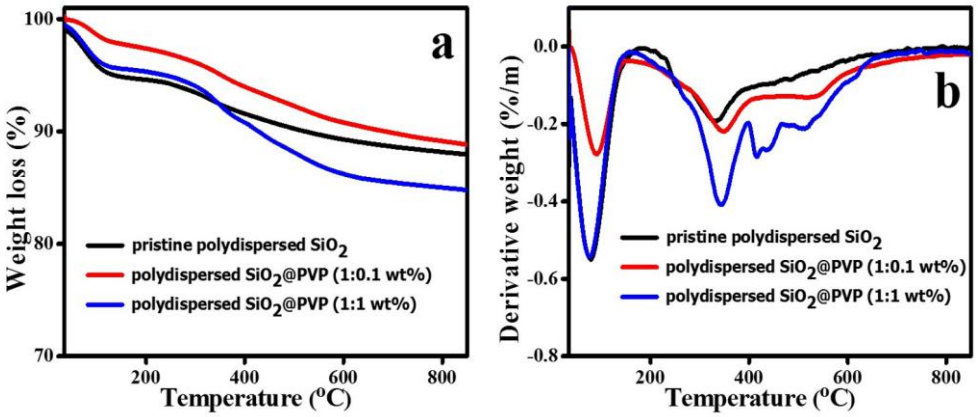

Figure 5.16. TG-DTG curves of pristine polydispersed SiO_2 spheres and SiO_2@PVP spheres; (a) Thermogravimetric curves and (b) the derivative curves, respectively.

Table 5.6. Decomposition temperatures and derivative weight loss of polydispersed SiO_2 and SiO_2@PVP spheres

Sample description	Decomposition temperature (°C)	Weight loss (%)	Description
Polydispersed SiO_2	39 to 170	0.55	Loss of adsorbed water
	200 to 415	0.20	Loss of organic residues and condensation of free silanols
Polydispersed SiO_2@PVP (1:0.1 wt%)	37 to 160	0.27	Loss of adsorbed water
	170 to 424	0.22	Condensation of free silanols and PVP decomposition
	450 to 606	0.13	Removal of organic residues
Polydispersed SiO_2@PVP (1:1 wt%)	35 to 160	0.54	Loss of adsorbed water
	170 to 400	0.41	Condensation of free silanols and PVP decomposition
	401 to 473	0.55	Removal of organic residues
	475 to 620	0.21	Removal of organic residues associated with SiO_2-PVP networks

5.3.2.2.2 Thermal analysis of polydispersed HCSs before and after PVP functionalization

The thermal gravimetric curves show complete burning of the polydispersed HCSs in air at 750°C (Fig. 5.17a). The derivative weight curves of the obtained polydispersed HCSs showed the presence of three decomposition curves (Fig. 5.17b). The first derivative weight was observed between 290°C and 430°C exhibiting a weight loss of 0.71%, 0.29% and 0.26% in the pristine HCSc, HCSc-0.1 wt% and HCSc-1 wt% respectively. This can be attributed to organic residues that were not completely removed during the SiO_2 etching process[49]. In pristine HCSc and HCSc-0.1 wt%, two derivative curves were observed between 480°C and 780°C due to decomposition of organic residues and carbon in air. In contrast, a sharp derivative curve was observed during decomposition of HCSc-1 wt%. This single peak is characteristic of the formation of an interconnected carbon open structure resulting from the use of polydispersed SiO_2@PVP (1:1 wt%) spheres as templates. The TGA curves agree with the different carbon morphologies observed in TEM and SEM images respectively.

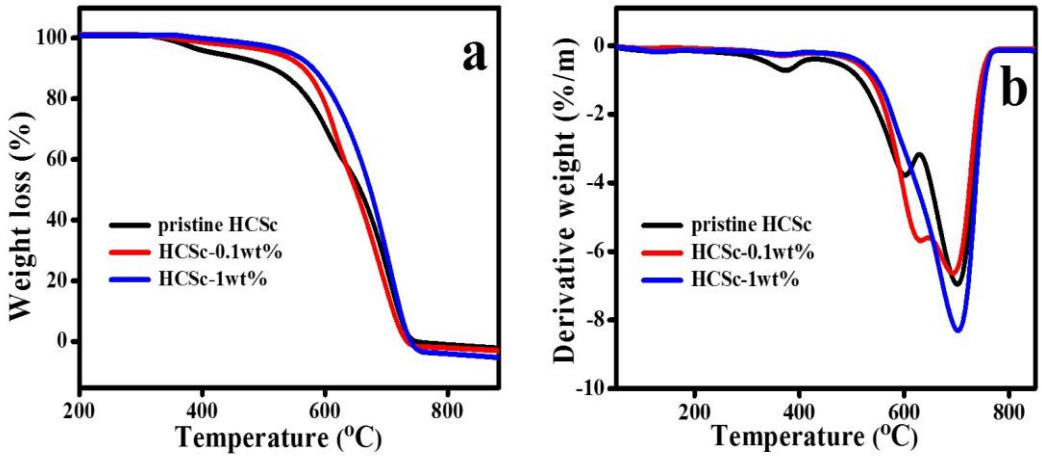

Figure 5.17. TG-DTG curves of pristine HCSc and bubble-like HCSs; (a) Thermogravimetric curves and (b) the derivative curves, respectively.

5.3.2.3 Raman analysis of the hollow carbon nanostructures obtained from polydispersed SiO_2 and SiO_2@PVP spheres

The Raman spectra of the obtained hollow carbon nanostructures show the D and G peaks at 1345-1353 cm^{-1} and 1584 -1597 cm^{-1} respectively (Fig. 5.18). The I_D/I_G ratios of HCSc-0.1 wt% and HCSc-1 wt% was 0.99 and 0.92 while that of the pristine HCSc 0.89 respectively (Table 5.7). This is expected due to defects resulting from the presence of broken open edges and bubble like structures of the HCSc-0.1 wt% and HCSc-1 wt% relative to that of the pristine HCSc.

Table 5.7. The effect of PVP concentration on I_D/I_G ratio of polydispersed HCSs

Description	D-band position (cm^{-1})	G-band position (cm^{-1})	I_D/I_G ratio
Pristine HCSc	1353	1597	0.89
HCSc-0.1 wt%	1345	1584	0.99
HCSc-1 wt%	1351	1592	0.92

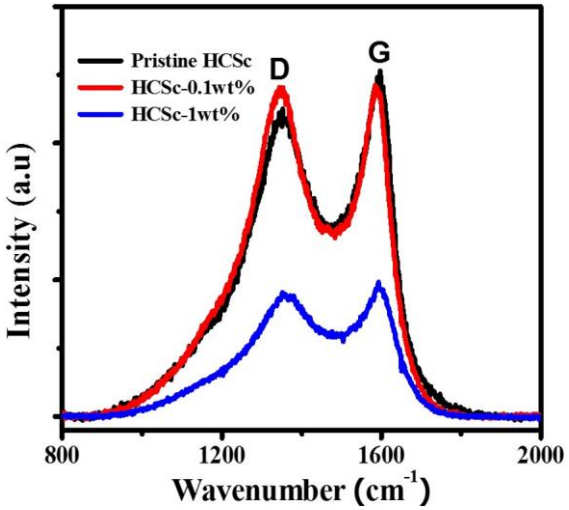

Figure 5.18. Raman spectra of the polydispersed hollow carbon structures obtained from pristine and PVP modified polydispersed SiO_2 spheres.

5.3.3 Effect of PVP adsorption time on the SiO_2 and carbon morphology

5.3.3.1 Morphology analysis of the SiO_2, SiO_2@PVP spheres and their respective HCSs

To investigate the effect of adsorption time on the morphology of the hollow carbon materials 1, 12 and 24 h adsorption times were used respectively. Fig. 5.19 shows the TEM images of the pristine and PVP modified polydispersed SiO_2 spheres before and after carbonization. The addition of PVP enhanced the SiO_2-SiO_2 sphere interactions with PVP adsorption time (Fig. 5.19a-d). This was further confirmed by SEM images (Fig. 5.20a-d). A heterogeneous carbon coverage along the outer silica edges was observed after carbonization of the PVP functionalized SiO_2 spheres as seen in (Figs. 5.19e-h and 5.20e-h) respectively. This change in carbon coverage can be attributed to the increased SiO_2-SiO_2 interactions during carbonization in the presence of PVP. The pristine polydispersed SiO_2 spheres and the SiO_2 spheres with PVP at different adsorption times exhibuited a broad particle size distribution (Table 5.8). However, after 24 h adsorption time, a slight decrease in particle size was observed due to PVP detachment after long adsorption time[50].

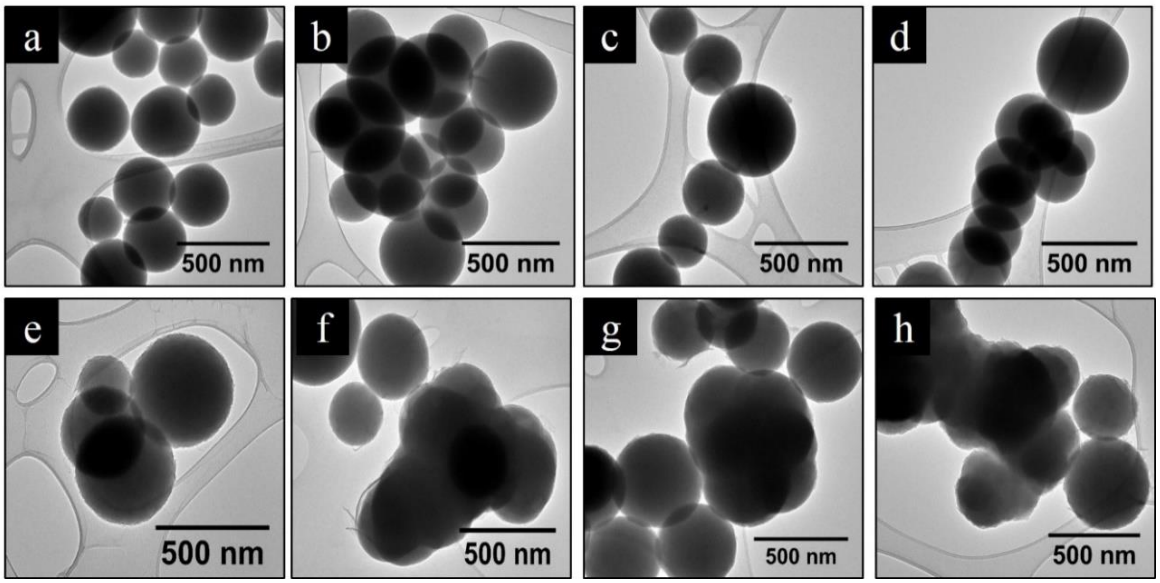

Figure 5.19. TEM images of (a, b, c and d) pristine polydispersed SiO_2, SiO_2@PVP (1 h), SiO_2@PVP (12 h), SiO_2@PVP (24 h) and (e, f, g and h) polydispersed SiO_2C, SiO_2@PVP (1 h)C, SiO_2@PVP (12 h)C and SiO_2@PVP (24 h)C after 1 h carbonization, respectively.

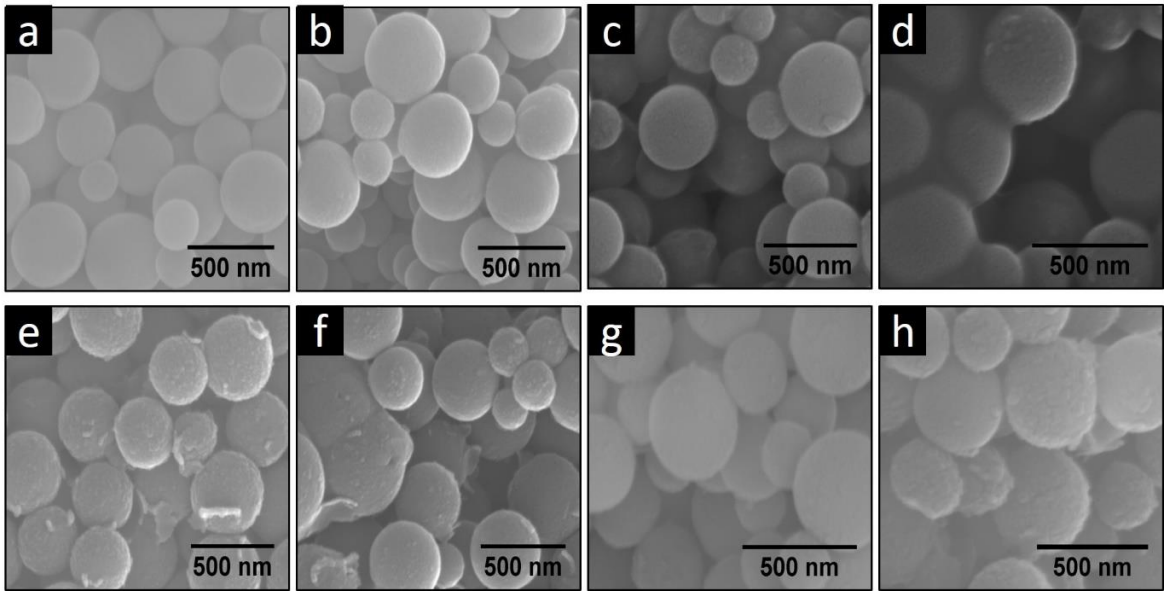

Figure 5.20. SEM images of (a, b, c and d) plain polydispersed SiO_2, SiO_2@PVP (1 h), SiO_2@PVP (12 h), SiO_2@PVP (24 h) and (e, f, g and h) polydispersed SiO_2C, SiO_2@PVP (1 h)C, SiO_2@PVP (12 h)C and SiO_2@PVP (24 h)C after 1 h carbonization, respectively.

Table 5.8. Effect of PVP adsorption time on the particle size of the pristine and modified polydispersed SiO_2 spheres

Description	SiO_2:PVP (wt%)	PVP stirring time (h)	Particle size (nm)
Polydispersed SiO_2	1:1	-	200 - 497
Polydispersed SiO_2@PVP 1h	1:1	1	210 - 488
Polydispersed SiO_2@PVP 12h	1:1	12	209- 496
Polydispersed SiO_2@PVP 24h	1:1	24	200 - 485

Broken and deformed HCSs were obtained after 1 h carbonization of pristine polydispersed SiO_2 followed by SiO_2 removal as seen in the previous section (5.3.2.1). When polydispersed SiO_2@PVP (1 h) spheres were used as templates, worm like hollow structures with a carbon shell thickness of 7 ± 5 nm was produced (Fig. 5.21a, d). On increasing the PVP adsorption time to 12 h and 24 h (polydispersed SiO_2@PVP 12 h and 24 h respectively), bubble-like and deformed hollow carbon nanostructures were obtained (Fig. 5.21b-f). The sublimation of polyvinylpyrrolidone polymer during carbonization process is believed to be the primary

factor affecting the morphology of the carbon nanostructures. Table 5.9 indicates the effect of adsorption time on the carbon shell thickness of the obtained hollow carbon nanostructures. Pristine hollow carbon nanostructures had a deformed morphology with a shell thickness of 13 ± 3 nm. The carbon shell thickness slightly changed to 9 ± 7 nm and 11 ± 4 nm after 12 h and 24 h adsorption times respectively. Short adsorption time of PVP on silica surface led to stronger SiO_2-SiO_2 interactions with a large number of silica spheres tightly packed together.

It is proposed that at longer adsorption times (12 h), the maximum adsorption limit on SiO_2 surface is reached and PVP detaches from the silica surface during the centrifugation time resulting in weaker SiO_2-SiO_2 interaction with a fewer number of silica spheres closely packed together. Consequently, the SiO_2-SiO_2 interaction facilitates the generation of wormlike carbon structures and the weaker SiO_2-SiO_2 interaction leads to bubble-like or deformed hollow carbon nanostructures. The carbonization of the pristine SiO_2 spheres and the SiO_2@PVP spheres was done at 900°C, which is higher than the 300°C (the sublimation temperature of PVP). Thus, carbonization occurred after sublimation of PVP onto the SiO_2 surface resulting in the different carbon morphologies[51].

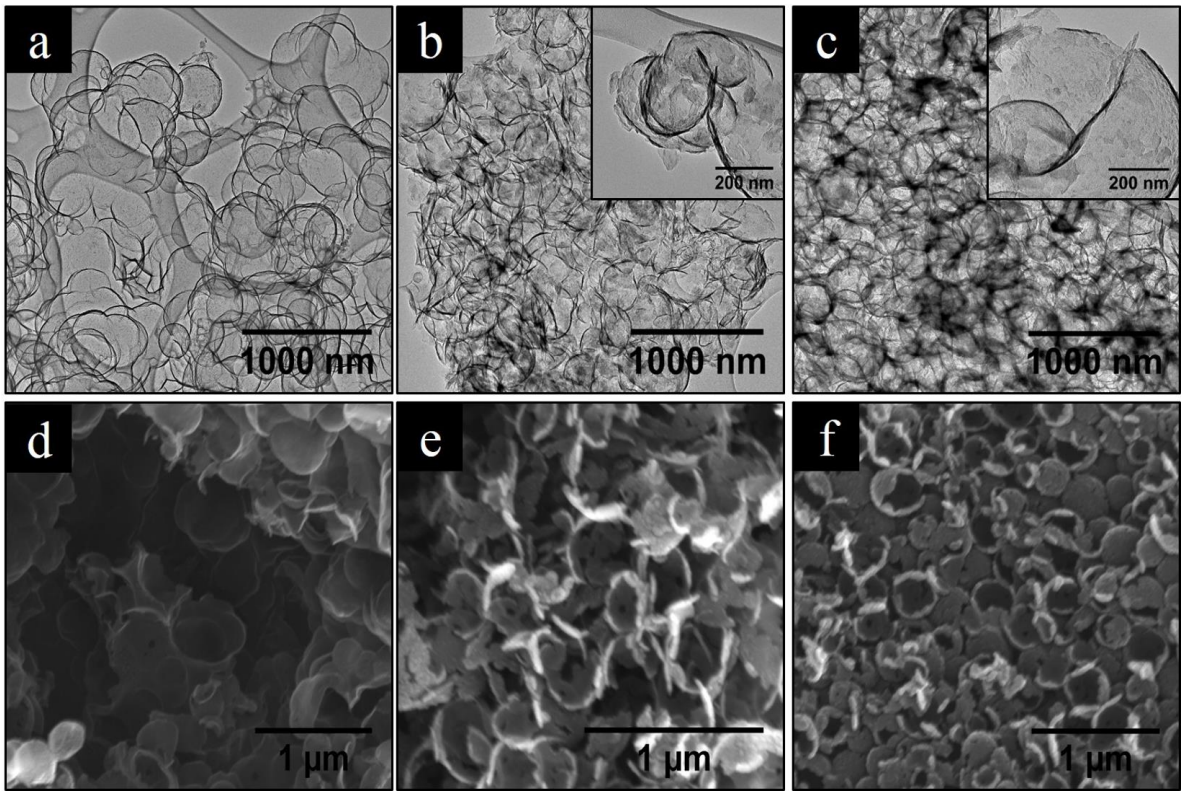

Figure 5.21. TEM and SEM images of the obtained HCSs; (a and d) HCSc-1 wt% (1 h), (b and e) HCSc-1 wt% (12 h) and (c and f) HCSc-1 wt% (24 h), respectively.

Table 5.9. Effect of PVP adsorption time on the carbon shell thickness of hollow carbon nanostructures

Description	PVP stirring time (h)	Carbonization time (h)	Particle size (nm)
HCSc pristine	-	1	13 ± 3
HCSc-1 wt% (1 h)	1	1	7 ± 5
HCSc-1 wt% (12 h)	12	1	9 ± 7
HCSc-1 wt% (24 h)	24	1	11 ± 4

5.3.3.2 Thermal analysis

5.3.3.2.1 Effect of PVP stirring time on thermal stability of polydispersed SiO_2@PVP spheres

The total weight loss of the polydispersed SiO_2, SiO_2@PVP (1:1 wt%) after 12 h and 24 h stirring times 15.37% and 13.04% respectively as shown in Fig. 5.22a. The SiO_2@PVP spheres obtained after a short stirring time (1 h) showed a higher weight loss (16.03%)

indicating maximum adsorption and surface interaction occurrence. The DTG curves (Fig. 5.22b) shows the derivative weight losses in the obtained SiO_2 spheres with their respective description indicated in Table 5.10.

Similar to previous TGA curves, a first derivative weight loss was observed between 38°C and 170°C, resulting from the loss of adsorbed H_2O and ethanol molecules[46]. From 170°C to 415°C, a considerable weight loss of 0.29% and 0.53% was observed in polydispersed SiO_2@PVP (12 h) and polydispersed SiO_2@PVP (24 h) respectively (Table 5.10). This can be attributed to further condensation of silanols, PVP decomposition and the removal of organic residues[47]. Also, a broad derivative curve with a weight loss of 0.18% and 0.10% were observed between 420°C and 620°C respectively; ascribed to the decomposition of organic residues related to SiO_2 and PVP network interactions[48]. The weight losses confirm the adsorption of PVP on SiO_2 at a different stirring time with a 1 h optimal time.

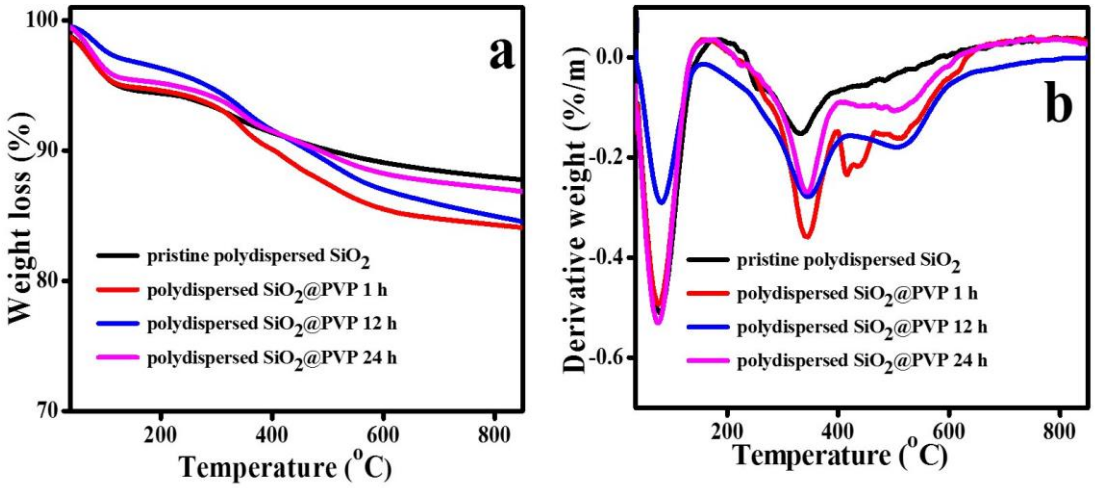

Figure 5.22. TG-DTG curves of pristine polydispersed SiO_2 spheres and SiO_2@PVP spheres; (a) Thermogravimetric curves and (b) the derivative curves, respectively.

Table 5.10. Effect of PVP stirring time on the decomposition temperatures and derivative weight loss of polydispersed SiO_2@PVP spheres

Sample description	Decomposition temperature (°C)	Weight loss (%)	Description
Polydispersed SiO_2@PVP (1 h)	35 to 160	0.49	Loss of adsorbed water
	170 to 400	0.35	Condensation of free silanols and PVP decomposition
	401 to 473	0.44	Removal of organic residues
	475 to 620	0.18	Removal of organic residues associated with SiO_2-PVP networks
Polydispersed SiO_2@PVP (12 h)	38 to 160	0.29	Loss of adsorbed water
	170 to 415	0.28	Condensation of free silanols and PVP decomposition
	430 to 615	0.18	Removal of organic residues associated with SiO_2-PVP networks
Polydispersed SiO_2@PVP (24 h)	39 to 160	0.53	Loss of adsorbed water
	170 to 410	0.26	Condensation of free silanols and PVP decomposition
	420 to 608	0.10	Removal of organic residues associated with SiO_2-PVP networks

5.3.3.2.2 Effect of PVP stirring time on thermal stability of the polydispersed HCSs

The thermal gravimetric curves shows complete burning of the pristine HCSc, HCSc-1 wt% (1 h) and HCSc-1 wt% (24 h) at 770°C and HCSc-1wt% (12 h) at 670°C respectively (Fig. 5.23a). The HCSc-1 wt% (12 h) were less thermally stable due to the presence of several broken edges as seen in the TEM images. The derivative weight curves of the obtained polydispersed HCSc (1 h) and HCSc (24 h) showed the presence of a sharp derivative curve between 490°C and 760°C with a weight loss of 8.28% and 10.74% respectively. This single peak shows the presence of interconnected bubble-like carbon open structures. In contrast, a broad derivative curve with a weight loss of 7.83% was observed between 430°C and 670°C in HCS-1 wt% (12 h). This is attributed to defects resulting from the deformed and broken edges of HCSs as corroborated by TEM and SEM images.

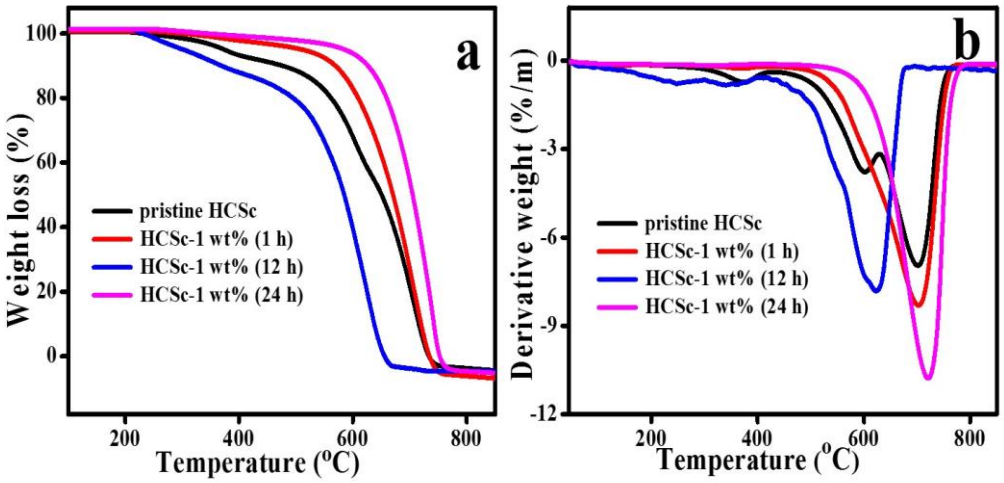

Figure 5.23. TG-DTG curves of pristine HCSc and other obtained HCSs; (a) Thermogravimetric curves and (b) the derivative curves, respectively.

5.3.3.3 Raman spectra analysis

Fig. 5.24 shows the Raman spectra of the obtained hollow carbon nanostructures with first order peak (D) observed at 1346 -1363 cm^{-1} and the graphitization peak (G) seen at 1590 - 1600 $cm^{-1.}$ A comparison of D-band and G-band shows that the ratio is independent of the adsorption times (Table 5.11). The I_D/I_G ratios are nearly constant on increasing the PVP adsorption time. The pristine HCSc was more graphitic than the HCSc-1 wt% (1 h, 12 h and 24 h) obtained after PVP modification of the SiO_2 spheres as indicated by the I_D/I_G ratios. The wormlike carbon nanostructures (HCSc-1 wt%) had more defects than the pristine HCSc. This can be attributed to PVP that creates more defects during carbonization process.

Table 5.11. The effect of PVP adsorption time on the I_D/I_G ratios of obtained polydispersed hollow carbon nanostructures

Description	PVP stirring time (h)	D-band position (cm^{-1})	G-band position (cm^{-1})	I_D/I_G ratio
HCSc plain	-	1353	1597	0.89
HCSc-1 wt% (1 h)	1	1363	1590	0.95
HCSc-1 wt% (12 h)	12	1354	1594	0.93
HCSc-1 wt% (24 h)	24	1346	1600	0.94

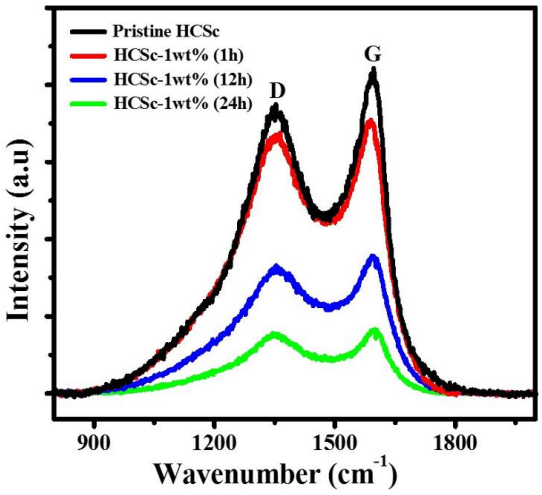

Figure 5.24. Raman spectra of hollow carbon structures obtained from pristine and PVP modified polydispersed SiO_2 spheres.

5.3.4 Effect of varying carbonization time on the HCSs obtained from polydispersed SiO_2@PVP sphere templates

5.3.4.1 Morphology analysis

Effect of carbonization time on monodispersed HCSs have shown that the carbon spherical morphology is maintained with the shell thickness increasing with carbonization time. Also, varying carbonization time on polydispersed SiO_2 spheres shows the formation of deformed HCSs with the time dependent carbon shell thickness. Carbonization of polydispersed SiO_2@PVP (1 h) for 1 h gave wormlike structures as was observed in Fig. 5.21a and 5.21d. It was noted that the presence of PVP on the silica surface favored the formation of the unique hollow carbon nanostructures. *However, could the carbon morphology vary with carbonization time when polydispersed SiO_2@PVP spheres are used as templates?* To address this question, we investigated the effect of carbonization time on HCSs obtained from polydispersed SiO_2@PVP spheres. Carbonization of the polydispersed SiO_2@PVP (1h) spheres for 2 h and 4 h led to edge connected, deformed bubble-like hollow carbon structures (Fig. 5.25a, b, d and e). Indeed, a change in the carbon morphology was observed with carbonization time as confirmed by the SEM images (Fig. 5.25c, f). Table 5.12 shows that an increase in carbon shell thickness of HCSs occurs with an increase in carbonization time. This is expected because an increase in carbonization time implies that there is more amount of carbon that nucleates onto the silica surface leading to more surface coverage.

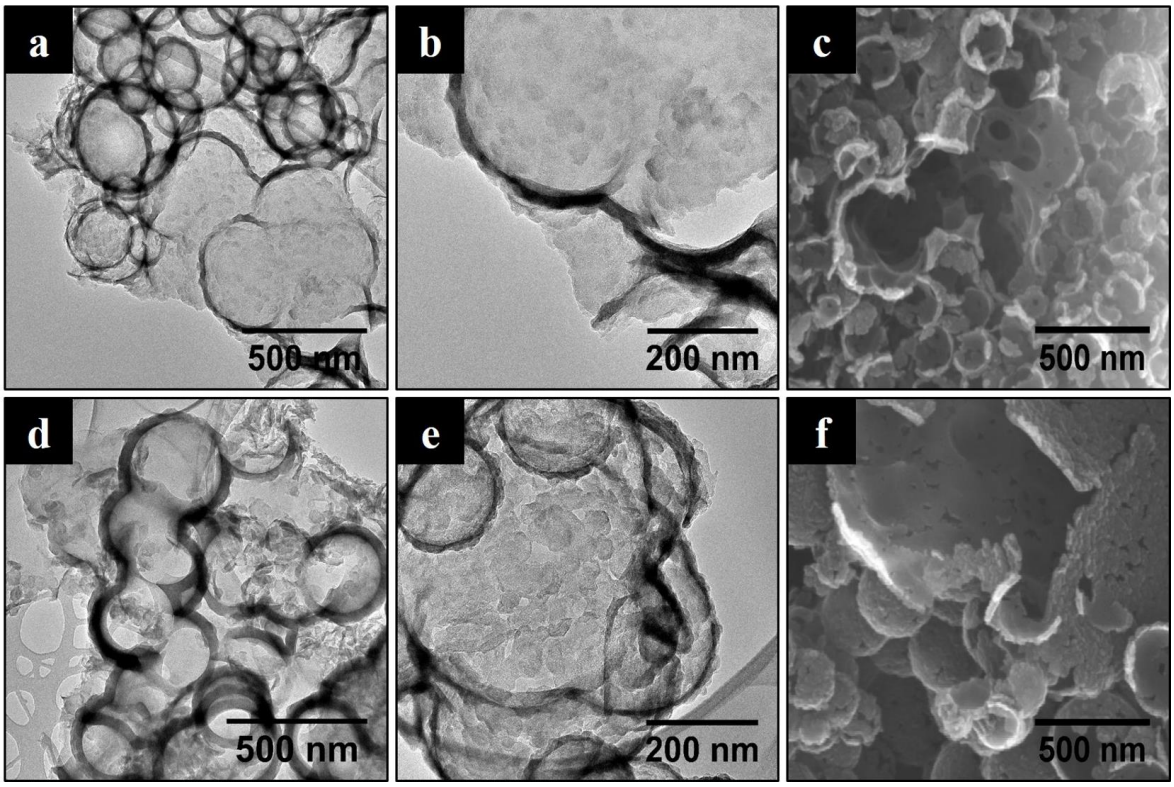

Figure 5.25. TEM and SEM images of obtained HCSs; (a-c) HCSc-1 wt% (2 h) and (d-f) HCSc-1 wt% (4 h), respectively.

Table 5.12. Effect of carbonization time on the deformed bubble-like HCSs carbon shell thickness

Description	Carbonization time (h)	Shell thickness (nm)
HCSc-1 wt% (1 h)	1	7 ± 5
HCSc-1 wt% (2 h)	2	18 ± 6
HCSc-1 wt% (4 h)	4	22 ± 11

5.3.4.2 Effect of carbonization time on the thermal stability of polydispersed HCSs

Thermal gravimetric curves of the deformed and bubble-like HCSs showed that complete burning of carbon in air occurred between 749°C and 754°C (Fig. 5.26a). This is attributed to an increase in the thermal stability with increasing carbonization time. A derivative curve was

observed between 480°C and 750°C with a weight loss of 8.26% and 9.54% in the HCSc-1 wt% (2 h) and HCSc-1 wt% (4 h) respectively (Fig. 5.26b). The increase in weight loss shows the presence of more carbon atoms after 4 h carbonization time. This collaborates with the increased shell thickness with carbonization time as seen in the TEM images.

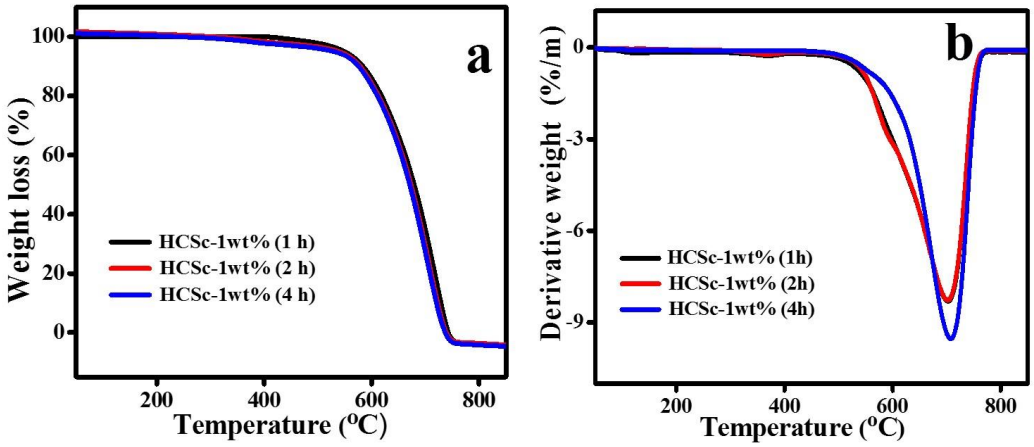

Figure 5.26. Effect of carbonization on thermal stability of deformed and bubble-like HCSs; (a) Thermogravimetric curves and (b) the derivative curves, respectively.

5.3.4.3 Raman analysis

The Raman spectra of the obtained hollow carbon nanostructures had peaks at 1346-1354 cm^{-1} and 1579 -1594 cm^{-1} characteristic of the D and G bands, respectively (Fig. 5.27). All the samples were obtained from carbonization of a 1:1 wt% of SiO_2:PVP sphere templates. Table 5.13 shows the I_D/I_G ratios of HCSs obtained after 1, 2 and 4 h carbonization times respectively. The I_D/I_G ratio was higher in HCSc obtained after longer (4 h) carbonization times than at shorter carbonization times (1 to 2 h). This indicated the presence of defects or adatoms that act as nucleation sites for the growth of the carbon shell.

Table 5.13. The I_D/I_G ratios of the deformed and bubble-like HCSs

Description	D-band position (cm^{-1})	G-band position (cm^{-1})	I_D/I_G ratio
HCSc-1 wt% (1 h)	1351	1592	0.91
HCSc-1 wt% (2 h)	1354	1579	0.92
HCSc-1 wt% (4 h)	1346	1594	0.96

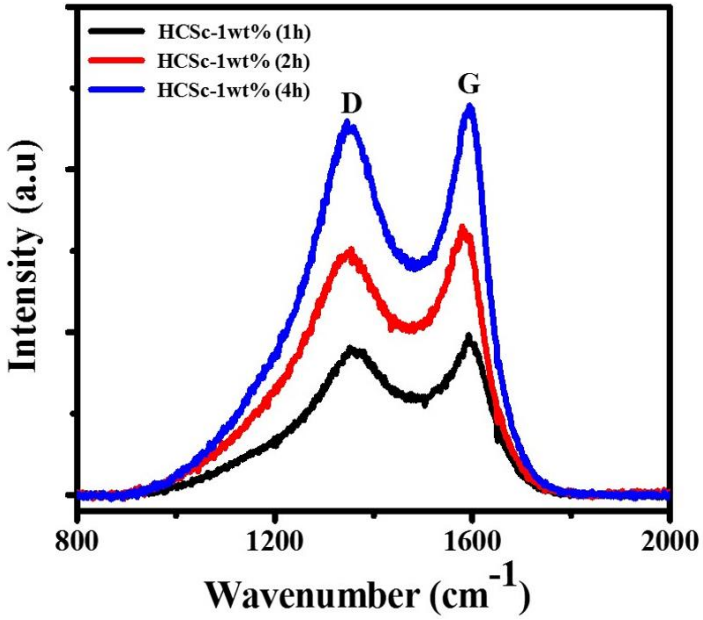

Figure 5.27. Raman spectra of HCSc-1 wt% (1 h), HCSc-1 wt% (2 h) and HCSc-1 wt% (4 h), respectively.

5.4 Conclusions

The effect of PVP adsorption time, PVP concentration, SiO_2 particle size distribution, and carbonization time on carbon morphology was studied. Short PVP adsorption time favoured synthesis of wormlike structures and deformed structures when polydispersed SiO_2 and monodispersed $SiO_{2@}$PVP templates were used respectively. A long PVP adsorption time resulted in deformed hollow carbon nanostructures. High PVP concentration led to stronger

SiO_2-SiO_2 interactions whereas a low PVP concentration gave weak SiO_2-SiO_2 interactions which led to varying carbon morphologies after carbonization and SiO_2 removal. In monodispersed SiO_2 systems both small (< 200 nm) and large (> 400 nm), particle sizes gave the same properties in their carbon morphology. The polydispersity of SiO_2 particle sizes played a role in the formation of unique hollow carbon nanostructures. A 1:1 wt% of SiO_2:PVP system was found to be the optimal condition for the generation of different types of hollow carbon nanostructures. This study opens a new method of synthesizing hollow carbon nanostructures with different morphologies; broken HCSs, deformed HCSs, edge connected, open ended, wormlike and bubble-like HCSs respectively. These materials can find vast applications in electrochemical sensors and separation membranes.

References

1. Caruso, F. *Advanced Materials* **2001,** 13, (1), 11-22.
2. Caruso, R. A.; Antonietti, M. *Chemistry of Materials* **2001,** 13, (10), 3272-3282.
3. Lin, L.-Y.; Kim, D.-E. *Tribology International* **2011,** 44, (12), 1926-1931.
4. Bondioli, F.; Cannillo, V.; Fabbri, E.; Messori, M. *Journal of Applied Polymer Science* **2005,** 97, (6), 2382-2386.
5. Ahmad, Z.; Al-Sagheer, F. *Progress in Organic Coatings* **2015,** 80, 65-70.
6. Ahmad, H. *Journal of Chemistry* **2015,** 2015, 19.
7. Bahari, A.; Shahbazi, M. *Journal of Electronic Materials* **2015,** 45, (2), 1201-1209.
8. Zhang, F.; Xiao, Z.-Y.; Zhai, S.-R.; Zhai, B.; Yang, P.-F.; An, Q.-D. *Journal of Sol-Gel Science and Technology* **2015,** 78, (1), 228-238.
9. Chili, M. M.; Pullabhotla, V. S. R. R.; Revaprasadu, N. *Materials Letters* **2011,** 65, (17–18), 2844-2847.
10. Tang, X.-L.; Jiang, P.; Ge, G.-L.; Tsuji, M.; Xie, S.-S.; Guo, Y.-J. *Langmuir* **2008,** 24, (5), 1763-1768.
11. Yan, J.; Tao, H.; Zeng, M.; Tao, J.; Zhang, S.; Yan, Z.; Wang, W.; Wang, J. *Chinese Journal of Catalysis* **2009,** 30, (9), 856-858.
12. Wei, Q.; Li, B.; Li, C.; Wang, J.; Wang, W.; Yang, X. *Journal of Materials Chemistry* **2006,** 16, (36), 3606-3608.
13. Vijaykumar, S.; Prasannkumar, S.; Sherigara, B. S.; Shelke, N. B.; Aminabhavi, T.; Reddy, B. S. R. *Macromolecular Research* **2009,** 17, (12), 1003-1009.
14. Molyneux, P. *Polymer International* **1999,** 48, (5), 426-426.
15. Delfs, D. *Angewandte Chemie* **1950,** 62, (3), 82-83.
16. Hanford, W. E.; Fuller, D. L. *Industrial & Engineering Chemistry* **1948,** 40, (7), 1171-1177.
17. Haaf, F.; Sanner, A.; Straub, F. *Polymer Journal* **1985,** 17, (1), 143-152.
18. Uhelská, L.; Chorvát, D.; Hutchinson, R. A.; Santanakrishnan, S.; Buback, M.; Lacík, I. *Macromolecular Chemistry and Physics* **2014,** 215, (23), 2327-2336.
19. Stach, M.; Lacík, I.; Chorvát, D.; Buback, M.; Hesse, P.; Hutchinson, R. A.; Tang, L. *Macromolecules* **2008,** 41, (14), 5174-5185.
20. Fried, M.; Moeller, R.; Zuern, L.; Stahnecker, E., Process for aqueous polymerization of N-vinylpyrrolidone utilizing finely divided suspension of water insoluble catalyst. Google Patents: 1975.
21. Karaputadze, T. M.; Shumskii, V. I.; Kirsh, Y. E. *Polymer Science U.S.S.R.* **1978,** 20, (8), 2084-2091.
22. Lu, X.; Gong, S.; Meng, L.; Li, C.; Yang, S.; Zhang, L. *Polymer* **2007,** 48, (10), 2835-2842.
23. Kudyshkin, V. O.; Rashidova, S. S.; Surdina, A. V.; Zaremski, M. Y.; Golubev, V. B. *Polymer Science Series B* **2007,** 49, (11-12), 297-300.
24. Belbachir, M.; Harrane, A.; Megharbi, R. *Macromolecular Symposia* **2006,** 245-246, (1), 1-4.
25. Robinson, B. V., *PVP : A critical Review of the Kinetics and Toxicology of Polyvinylpyrrolidone (povidone)*. Chelsea, MI : Lewis Publishers, c1990.: 1990.
26. Teodorescu, M.; Bercea, M. *Polymer-Plastics Technology and Engineering* **2015,** 54, (9), 923-943.
27. Liu, X.; Xu, Y.; Wu, Z.; Chen, H. *Macromolecular Bioscience* **2013,** 13, (2), 147-154.
28. Borneman, Z.; Gökmen, V.; Nijhuis, H. H. *Separation and Purification Technology* **2001,** 22–23, 53-61.

29. Spruijt, E.; Biesheuvel, P. M.; de Vos, W. M. *Physical Review E* **2015,** 91, (1), 012601.
30. Parnas, R. S.; Chaimberg, M.; Taepaisitphongse, V.; Cohen, Y. *Journal of Colloid and Interface Science* **1989,** 129, (2), 441-450.
31. Feldstein, M. M.; Roos, A.; Chevallier, C.; Creton, C.; Dormidontova, E. E. *Polymer* **2003,** 44, (6), 1819-1834.
32. Guzenko, N. V.; Pakhlov, E. M.; Lipkovskaya, N. A.; Voronin, E. F. *Russian Journal of Applied Chemistry* **2001,** 74, (12), 2017-2020.
33. Chaimberg, M.; Parnas, R.; Cohen, Y. *Journal of Applied Polymer Science* **1989,** 37, (10), 2921-2931.
34. de Gennes, P. G. *Macromolecules* **1980,** 13, (5), 1069-1075.
35. Li, M.; Wu, Q.; Wen, M.; Shi, J. *Nanoscale Research Letters* **2009,** 4, (11), 1365-1370.
36. Jang, B.; Yang, K.; Quan, B.; Piao, Y. *Materials Letters* **2013,** 104, 68-71.
37. Joo, J. B.; Kim, P.; Kim, W.; Kim, J.; Kim, N. D.; Yi, J. *Current Applied Physics* **2008,** 8, (6), 814-817.
38. Cai, P.-j.; Feng, L. *Materials Chemistry and Physics* **2008,** 108, (1), 1-3.
39. Sasidharan, M.; Liu, D.; Gunawardhana, N.; Yoshio, M.; Nakashima, K. *Journal of Materials Chemistry* **2011,** 21, (36), 13881-13888.
40. Lu, A. H.; Schüth, F. *Advanced Materials* **2006,** 18, (14), 1793-1805.
41. Chen, Q.-L.; Ji, W.-Q.; Chen, S. *Scientific Reports* **2016,** 6, 19382.
42. Mutuma, B. K.; Matsoso, B.; Ranganathan, K.; Wamwangi, D.; Coville, N. J. *RSC Advances* **2016,** 6, (24), 20399-20408.
43. Jiang, T.; Budarin, V. L.; Shuttleworth, P. S.; Ellis, G.; Parlett, C. M.; Wilson, K.; Macquarrie, D. J.; Hunt, A. J. *Journal of Materials Chemistry A* **2015,** 3, (27), 14148-14156.
44. Maciel, G. E. *Journal of the American Chemical Society* **1996,** 118, (2), 401-406.
45. Tsuchiya, I. *The Journal of Physical Chemistry* **1982,** 86, (21), 4107-4112.
46. Ramesh, S.; Cohen, Y.; Prozorov, R.; Shafi, K. V. P. M.; Aurbach, D.; Gedanken, A. *The Journal of Physical Chemistry B* **1998,** 102, (50), 10234-10242.
47. Pol, V.; Gedanken, A.; Calderon-Moreno, J. *Chemistry of materials* **2003,** 15, (5), 1111-1118.
48. Timin, A.; Rumyantsev, E.; Lanin, S. N.; Rychkova, S. A.; Guseynov, S. S.; Solomonov, A. V.; Antina, E. V. *Materials Chemistry and Physics* **2014,** 147, (3), 673-683.
49. Wilgosz, K.; Chen, X.; Kierzek, K.; Machnikowski, J.; Kalenczuk, R. J.; Mijowska, E. *Nanoscale Research Letters* **2012,** 7, (1), 1-5.
50. Cohen Stuart, M. A.; Fleer, G. J.; Bijsterbosch, B. H. *Journal of Colloid and Interface Science* **1982,** 90, (2), 310-320.
51. Bogatyrev, V. M.; Borisenko, N. V.; Pokrovskii, V. A. *Russian Journal of Applied Chemistry* **2001,** 74, (5), 839-844.

CHAPTER 6

Generation of Open Ended, Worm Like and Graphene Like Structures from Layered Spherical Carbon Materials

6.1 Introduction

Layered graphene structures can in principle be made by two approaches–by a bottom up approach from carbon building blocks or by top down approaches from layered carbon materials. The bottom-up approach entails the synthesis of graphene structures by epitaxial growth of graphene sheets through Diels-Alder polymerization[1, 2], layer by layer assembly[3], solvothermal[4] and chemical vapor deposition methods. The chemical vapor deposition (CVD) methodology, can entail depositing carbon on a metal template with some or limited carbon solubility such as Cu[5-7], Ni[8, 9], and Co[10] among others. The metal template thus acts as a catalyst for graphene layer formation and growth. In some cases, a catalyst free plasma enhanced chemical vapor deposition method, has been used to produce carbon nanosheets and vertically oriented graphene sheets[11-15]. The top-down approach involves the exfoliation of graphite by mechanical, electrochemical or chemical means to give graphene[16, 17]. Indeed, the classical methodology to make graphene is from graphite[18]. In principle any carbon source (planar, non-planar geometries) that contain layers of carbon atoms could be converted to an open layered carbon material. For instance, unzipping multiwalled carbon nanotubes can result in the formation of graphene oxide nanoribbons[19] and graphene nanoribbons[20]. A recent report has indicated that C_{60} can be converted into graphene quantum dots showing the possibility of creating graphene like structures from spherical carbon materials[21].

Typically, carbon nanomaterials are classified based on their dimensionalities such as zero-dimensional fullerenes (0D), one-dimensional carbon nanotubes (1D), two-dimensional graphenes (2D) and various three-dimensional structures (3D) respectively[22-25]. The 3D carbon based nanostructures such as 3D graphene based composites and 3D porous carbons of high

B.K. Mutuma, B. Matsoso, K. Ranganathan, D. Wamwangi, N.J. Coville, RSC Advances, 6 (2016) 20399-20408.

mechanical and structural stability, high electrical conductivity and large pore volume have been extensively studied[26-31]. The hard template route has been used to synthesize various 3D carbon frameworks for energy applications[32-34]. In addition, these nanostructures could be used as electron acceptors in polymer based solar cells due to their high interfacial area and ballistic type electron transport.

Hollow carbon spheres (HCSs) contain graphite like structures in their carbon shells. Because of these features they have been used extensively in fuel cells[35, 36], as catalysts support[37, 38] and in supercapacitors[39, 40]. This is due to their large pore volume, high surface area and the ability to tailor the diameters of the carbon shells. These nanostructured materials have been synthesized by hydrothermal carbonization[41], templating[42, 43], Kirkendall effect, Ostwald ripening and the galvanic replacement methods among others[44]. A hard templating method offers the ability to modify surface properties of templates, to manipulate the morphology and structure of the final product and to use readily available precursors[45]. The carbon shell thickness can be controlled by varying the surfactant to precursor ratio[46, 47], the amount of the carbon source[48] and the carbonization time[49]. To date, the carbon shell of a HCS is generally retained in the synthesis strategies employed. However, studies have indicated that structural collapse of a HCS can occur to produce broken shell structures[49-51].

Organic solar cell (OSC), devices that convert solar energy into electrical energy often use semiconducting polymers made from carbon. Carbon is cheap, readily available, easily processable and is hydrophobic. This latter property ensures its compatibility with organic polymers used in the active layer when common organic solvents are used to make solar cell devices. In a bulk heterojunction (BHJ), the active layer comprises of an interpenetrating network of the p-type donor (poly(3-hexyl-thiophene-2,5-diyl), P3HT) and an n-type acceptor ([6,6]-phenyl- C_{61}-butyric acid methyl ester, PCBM) respectively. The key component here is the fullerene that is a single layered spherical carbon material. Other hollow carbon nanostructures can also act as the electron accepting materials and be used to form a ternary blend of the active layer. In this approach metallic impurities in the carbon material are not present as HCS

synthesis, unlike carbon nanotube synthesis, requires no catalyst[52-58]. These early studies indicated that a key feature was the graphitic carbon network. To further explore the role of graphitic carbon structures in solar cell devices the use of "collapsed" HCSs has been explored. This is overcomes the issue associated with large HCSs that can conform to the size of the typical active layer dimensions of the OSC device and can lead to shorting. Graphene based nanostructures have been mainly used as electrode materials in organic and dye sensitized solar cells[59-61]. In contrast, carbon nanotubes have been employed in the active layer to improve the efficiency of photovoltaic devices but their metallic character favor charge carrier recombination leading to low photogenerated charge carriers[62-65]. To our knowledge, the use of open ended worm like carbon nanostructures to form an active layer composite in organic solar cells has to date not been reported.

In this study, carbon has been deposited on monodispersed and polydispersed silica templates in the presence of Au nanoparticles embedded in the silica to produce graphene-like layered structures (Au@HCS). Hollow carbon spheres with broken spherical shells were produced from small and monodispersed SiO_2 spheres and unusual open ended worm like layered structures were made from polydispersed silica sphere templates. In essence, the conversion of spherical core shell materials to an open ended worm like carbon nanostructures (3D) with unique morphologies was carried out using a CVD nanocasting method (a hard template route). The effect of Stober sphere diameter, polydispersion and carbonization time on the morphology of the carbon spheres produced as well as the role of the Au nanoparticles and the polyvinylpyrrolidone (PVP) used to cap the Au particles were studied. The obtained wormlike carbon nanostructures and the broken hollow/deformed carbon structures were employed in a ternary blend active layer to fabricate an organic solar cell.

6.2 Experimental

6.2.1 Starting materials

The material used for SiO_2 spheres are as described in Chapter 5. Chloroauric acid, $HAuCl_4.3H_2O$ (99.99%, Aldrich), polyvinylpyrrolidone, PVPK30 (Mw 40,000, Aldrich), and trisodium citrate dihydrate were used as reagents for the synthesis of gold nanoparticles.

6.2.2 Synthesis of silica spheres and hollow carbon spheres (HCSs)

Monodispersed SiO_2 spheres were synthesized by mixing 90 mL of ethanol, 63 mL of distilled water and 5 mL of NH_4OH and the solution stirred for 10 min. Then 16 mL of TEOS was added *rapidly* and the mixture stirred for 1 hour. In contrast, polydispersed SiO_2 spheres were obtained by adding 2 mL of TEOS *slowly* to ethanol (40 mL) and 2 mL of NH_4OH and the mixture allowed to stir for 1 h. The solutions were centrifuged at 4500 rpm for 20 minutes and the product dried at 80°C for 12 h. Carbonization of both the monodispersed and polydispersed SiO_2 spheres was carried out by a bubbling method using toluene as the carbon source and argon as the carrier gas in a chemical vapor deposition reactor for 1 h, 2 h and 4 h respectively[66] (Table 6.1). The carbonized silica was then etched with 10% HF for 24 h at room temperature and dried to give the hollow carbon spheres.

6.2.3 Addition of PVP to polydispersed SiO_2 spheres and synthesis of hollow carbon nanostructures

The polydispersed silica spheres (0.5 g) were weighed and dispersed in 40 mL of ethanol and stirred for twenty minutes. Polyvinylpyrrolidone (PVP) solution was prepared by dispersing 0.5 g of PVP in 20 mL of distilled water and sonicating for 10 min. The PVP solution was added to the silica suspension and stirred for 1 h and 12 h respectively. The solutions were centrifuged at 4500 rpm for 20 min and the products dried at 80°C for 12 h to give SiO_2@PVP 1 h and SiO_2@PVP 12 h respectively. In separate reactors, the two SiO_2@PVP samples (0.06 g) were uniformly spread onto a quartz boat which was placed in the center of a quartz tube. The furnace was heated to 900°C at 10 $^{\circ}$C min^{-1} under an Ar atmosphere (Ar, 200 sccm). Once the desired temperature was reached, Ar (200 sccm) was bubbled through toluene for 1 h. After this, the gas flow was stopped and the system was left to cool down to room temperature under an inert atmosphere (Ar, 200 sccm). The quartz boat was then removed from the reactor and the silica was removed with a 10% HF solution (24 h) and after thorough washing with distilled water the product was dried at 80°C for 12 h to give the two desired hollow carbon nanostructures.

B.K. Mutuma, B. Matsoso, K. Ranganathan, D. Wamwangi, N.J. Coville, RSC Advances, 6 (2016) 20399-20408.

6.2.4 Synthesis of Au nanoparticles

$HAuCl_4.3H_2O$ (0.01 M, 5 mL) was stirred at reflux for 30 min and trisodium citrate dihydrate (50 mL of 0.01 M) was added to the Au solution and the mixture stirred for 30 min. A 0.5 g of PVP was dissolved in 20 mL of distilled H_2O and added dropwise to the Au solution and stirred at room temperature for 12 h. Centrifugation at 12,000 rpm for 15 min gave a suspension of gold nanoparticles (d = 14 ± 4 nm) in solution (Appendix A:Fig. S6.1).

6.2.5 Synthesis of Au@SiO_2 spheres

Gold@silica spheres were synthesized using the conditions shown in Table 6.2. Gold nanoparticles (2 mL, 0.00016 M) were mixed with 20 mL of ethanol and 0.5 mL of ammonia solution (25 wt%). The solutions were stirred for 20 min and then 1 mL of TEOS was added *rapidly* and the solutions stirred separately for 30 min and 1 h respectively. The two solutions were then centrifuged for 20 min at 3500 rpm and the collected solids dried at 80ºC for 12 h to give monodispersed Au@SiO_2A and Au@SiO_2B spheres respectively. Polydispersed Au@SiO_2 particles were made by adding gold nanoparticles (20 mL) to 40 mL of ethanol and 2 mL of ammonia solution (25 wt%). The solution was stirred for 20 min and 2 mL of TEOS was added *slowly* and the solution stirred for 1 h, centrifuged for 20 min at 3500 rpm and the collected solid dried at 80°C for 12 h to give Au@SiO_2C.

6.2.6 Synthesis of Au@hollow carbon structures (Au@HCSs)

Au@hollow carbon spheres (Au@HCSs) were synthesized by carbonization of the synthesized Au@SiO_2 spheres in a horizontal chemical vapor deposition reactor**.** In separate reactors, the three Au@SiO_2 samples (0.06 g) were uniformly spread onto a quartz boat which was placed in the center of a quartz tube. The furnace was heated to 900 $^{\circ}$C at 10 $^{\circ}$C min^{-1} under an Ar atmosphere (Ar, 200 sccm). Once the desired temperature was reached, Ar (200 sccm) was bubbled through toluene for 1 h for Au@SiO_2A and Au@SiO_2B and for 1 h, 2 h and 4 h for Au@SiO_2C (to give Au@SiO_2C1, Au@SiO_2C2 and Au@SiO_2C4) respectively. After this, the gas flow was stopped and the system was left to cool down to room temperature under an inert atmosphere (Ar, 200 sccm). The quartz boat was then removed from the reactor and the silica

was removed with a 10% HF solution (24 h) and after thorough washing with distilled water the product was dried at 80°C for 12 h to give the five Au@HCS samples (Table 6.3).

The characterization of the $Au@SiO_2$ and AU@HCSs was studied using techniques described in earlier chapters. The morphology and graphitic domains in Au@HCS were determined using a JEOL JEM 2100 High Resolution TEM (JEOL, Japan) fitted with a LaB6 gun. A energy dispersive X-ray spectroscopy (EDS) analysis was done to check the elemental composition of the synthesized carbon nanostructures.

6.2.7 Fabrication of a ternary blend active layer based organic solar cell

The devices were fabricated on top of ITO-coated substrates. The ITO coated glass was cleaned in an ultrasonic bath by treatment with deionized H_2O, acetone, ethanol and a mixture of an deionized H_2O and ethanol sequentially for 30 min before solvent removal by a stream of N_2 gas. A hole transport layer, PEDOT:PSS (poly(3,4-ethylenedioxylenethiophene):poly(styrenesulfonic acid)) was spin coated onto the ITO coated substrate at 2000 rpm for 30 s. The resulting film was dried on a hot plate at 70 º C for 15 min. Two sets of P3HT and PCBM samples (10 mg each) were separately dissolved in 0.5 mL of chlorobenzene and stirred in air for 3 h at room temperature. The hollow carbon nanostructure solutions were prepared by dissolving 1 mg of wormlike hollow carbon structures and broken hollow carbon structures separately in 0.5 mL of chlorobenzene. The active layer was prepared by mixing the solutions of P3HT:PCBM:hollow carbon nanostructures in (1:1:0.1) weight ratio to form two different blend solutions and stirred for 2 h. The active layer was then spin coated at 2000 rpm for 30 s on top of the PEDOT:PSS thin film and the cathode was deposited by thermal evaporation of aluminium under 8.0×10^{-6} mbar. Optical absorption measurements of the films made from the blends were carried out using a Cary 500 UV–visible Spectrometer. The surface roughness and topographic images of the films were studied using a Veeco Di3100 AFM in tapping mode installed with a Si_3N_4 tip. The current density–voltage (J–V) characteristics of the films were obtained using a HP 4141B source measure unit under 100 mW/cm^2 illumination

B.K. Mutuma, B. Matsoso, K. Ranganathan, D. Wamwangi, N.J. Coville, RSC Advances, 6 (2016) 20399-20408.

(AM 1.5G). All the measurements were carried out at room temperature under standard conditions.

6.3 Results and discussion

6.3.1 Silica spheres and hollow carbon spheres (HCSs)

Stober silica spheres were synthesized by classical routes[67]. The silica spheres were made using two different reactant concentrations and reaction times to give monodispersed and polydispersed SiO_2 with different sizes as shown in Fig. S6.2. Monodispersed SiO_2 spheres (400-500 nm) were obtained when TEOS was added quickly while polydispersed SiO_2 spheres (90-310 nm) were obtained when TEOS was added slowly. A quick addition of TEOS results in the creation of nucleation sites at the same rate and time whereas a slow addition creates new nucleation site with each TEOS portion added, analogous to an interrupted particle growth mechanism[68, 69]. These spheres were carbonized with toluene for 1 h, 2 h and 4 h and the SiO_2 was removed with HF to give HCSs (Table 6.1). The TEM images of the six different HCSs are shown in Fig. 6.1. It is noted that the HCSs were smaller in diameter than the SiO_2 spheres due to the shrinkage of the silica spheres[37, 70]. For all types of silica spheres used, carbon coverage on SiO_2 was observed prior to etching. The carbon shell thickness increased with increasing carbonization time as shown in Table 6.1. After treatment of the SiO_2@C materials with HF, it is seen that the carbon shells in monodispersed HCSs retained their spherical shape (Fig. 6.1a, b and c). In contrast, HCSs with deformed and interconnected carbon shells were obtained after treatment of the polydispersed SiO_2@C materials with HF (Fig. 6.1d and e). However, HCSs with complete carbon shells were obtained after 4 h carbonization of polydispersed SiO_2 materials and SiO_2 removal (Fig. 6.1f). Also to note: the carbon shell thickness of the polydispersed HCSs was thinner than that of the monodispersed HCSs. Though both mono and polydispersed SiO_2 are chemically the same, SiO_2 polydispersity was found to reduce the number of carbonization layers. This could be attributed to the packing of polydispersed particles which restricts toluene infiltration between SiO_2 spheres during carbon shell growth on SiO_2.

B.K. Mutuma, B. Matsoso, K. Ranganathan, D. Wamwangi, N.J. Coville, RSC Advances, 6 (2016) 20399-20408.

Table 6.1. Effect of carbonization time on the carbon shell thickness

Starting SiO_2 material	SiO_2 (nm)	CVD carbonization time (h)	Carbon shell thickness (nm)
Monodispersed SiO_2	400 - 500	1	12 ± 5
		2	38 ± 8
		4	47 ± 10
Polydispersed SiO_2	90 - 310	1	8 ± 2
		2	10 ± 3
		4	32 ± 8

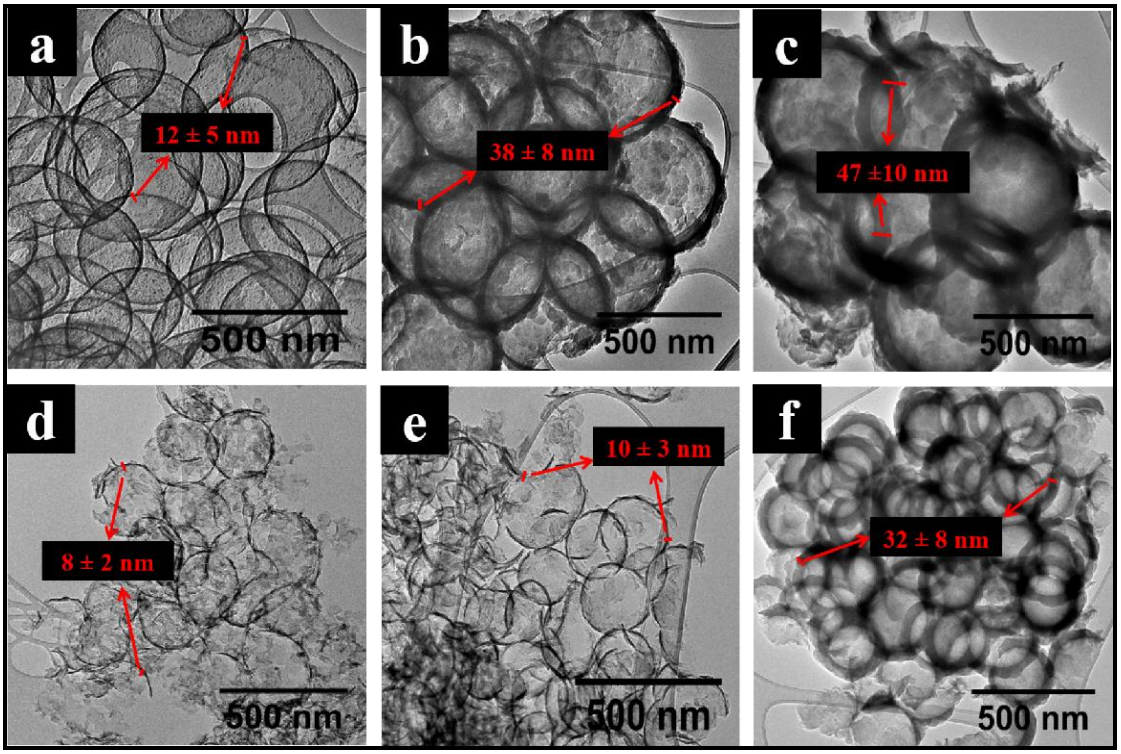

Figure 6.1. TEM images of hollow carbon spheres; (a, b, c) from monodispersed SiO_2 spheres and (d, e, f) from polydispersed SiO_2 spheres after (1 h, 2 h, 4 h) carbonization times and SiO_2 removal, respectively.

6.3.2 Au@SiO_2 and Au@HCSs

Au@SiO_2 was made by classical procedures by dispersing Au particles in a solution containing TEOS (Table 6.2). The sizes of encapsulated gold nanoparticles were almost the same in all the Au@SiO_2 spheres with a slight increase in size observed in Au@HCSs obtained after carbonization and SiO_2 removal (Table 6.3). Fig. 6.2 show the TEM images of Au@SiO_2A and Au@SiO_2B templates with their respective HCS morphologies obtained after 1 h carbonization. The longer reaction time (1 h versus 0.5 h) used in the formation of the template gave a larger HCS as expected[71, 72]. Carbonization of the smaller sized silica spheres (Au@SiO_2A) produced broken hollow carbon spheres after etching away the SiO_2 (Fig. 6.2c) while the large sized silica sphere (Au@SiO_2B; 110-150 nm) gave more unbroken spherical carbon shells after HF etching (Fig. 6.2d). Though, the thickness of the carbon shells was similar after 1 h carbonization time; the smaller HCSs were more prone to break during the etching procedures, due to the large strains induced by the larger curvature which weaken upon SiO_2 removal. Carbon shell thickness dependent collapse of Au@SiO_2A is thus unavoidable due to the smaller diameter size[50, 51].

Table 6.2. Reaction conditions for the synthesis of Au@SiO_2 spheres

Description	Stirring time (h)	Gold nanoparticle solution (mL)	Ethanol (mL)	Ammonia solution 25 wt% (mL)	TEOS (mL)
Au@SiO_2A	0.5	2	20	0.5	1
Au@SiO_2B	1	2	20	0.5	1
Au@SiO_2C	1	20	40	2	2

B.K. Mutuma, B. Matsoso, K. Ranganathan, D. Wamwangi, N.J. Coville, RSC Advances, 6 (2016) 20399-20408.

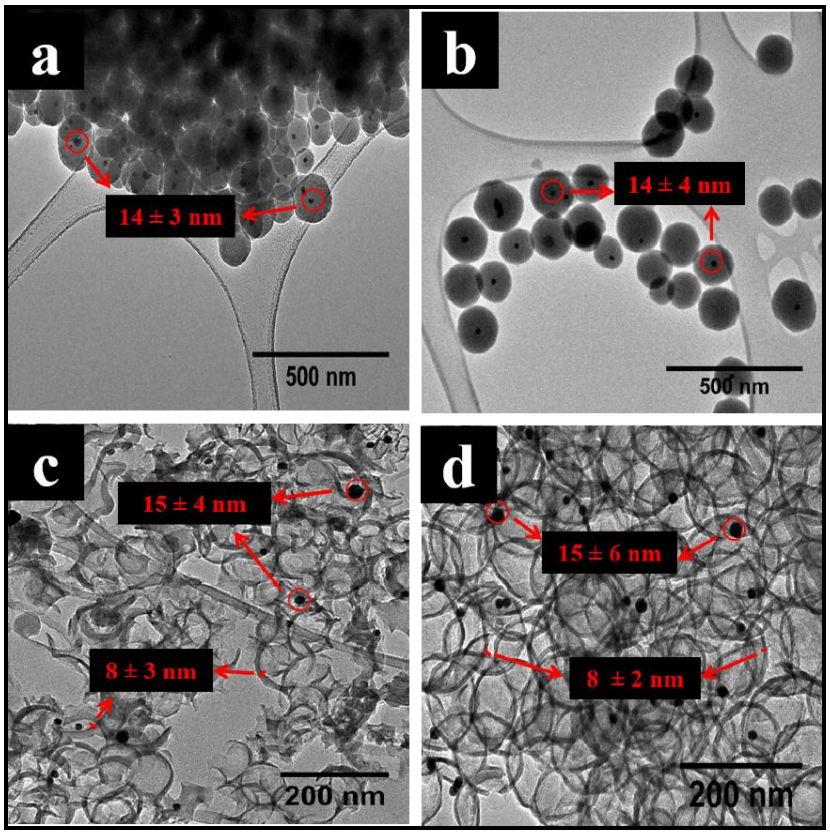

Figure 6.2. TEM images of (a) Au@SiO_2A, (b) Au @SiO_2B spheres before carbonization: (c) Au@HCSA and (d) Au@HCSB after 1 h carbonization time and SiO_2 removal.

Fig. 6.3a shows TEM images of polydispersed Au@SiO_2C spheres after synthesis. After 1 h carbonization a thin carbon shell (11 ± 2 nm) covering the silica (Fig. S6.3) is formed which led to a layered carbon nanostructure (Fig. 6.3b) after HF etching. This contrasts with the morphologies found for Au@HCSA and Au@HCSB as the collapse led to large sheets of carbon shells instead of a hemispherical curved surface. The carbonization of silica spheres to give thin carbon shells occurred where the silica cores interconnected and breaching presumably occurred where the silica spheres intersected. A short carbonization time (1 h) produced a layered carbon nanosheet like morphology due to limited nucleation densities and surface coverage. Carbonization for longer times (2 and 4 h) led to the formation of long nanotube/worm like morphology (length > 500 nm) (Fig. 6.3c, d).

Table 6.3 shows that an increase in carbon shell thickness of Au@HCSC occurs with an increase in carbonization time. Comparison of polydispersed Au@HCSC (Fig. 6.3) and polydispersed HCSs (Fig. 6.1) showed that in the absence of gold, HCSs with deformed and interconnected carbon shells were observed and no carbon nanosheet like morphology was noted. This implicates the presence of Au in the formation of the peculiar carbon structures. A more detailed analysis of Au@HCSC1 was obtained from HRTEM studies (Fig. 6.4). HRTEM images of the Au@HCSC1 revealed that the sample could be viewed as a carbon sheet (Fig. 6.4a) made of overlapping carbon layers formed from the extended array of hollow carbon structures (Fig. 6.4b). The extended array was in the form of discontinuous curved features portraying the wavy nature of the carbon sphere edge[73]. The carbon structure appears to follow the curvature of the unzipped spheres (Fig. 6.4c). Further analysis of the 'film' indicates that the carbon 'shell' shows the presence of graphitic domains (Fig. 6.4d; d interlayer spacing = 0.344 nm) with short range ordering (Fig. 6.4e) over large parts of the carbon structure. The structure also indicates regions of amorphous carbon as confirmed by selected area electron diffraction (SAED) data (Fig. S6.4).

Table 6.3. Effect of SiO_2 sphere diameter in $Au@SiO_2$ template on the carbon morphology

Description	Starting SiO_2 material	SiO_2 (nm)	Au (nm)	CVD carbonization time (h)	Morphology	Carbon shell thickness (nm)	Au (nm)
Au@HCSA	$Au@SiO_2A$	80 - 110	14 ± 3	1	HCSs with broken shells	8 ± 3	15 ± 4
Au@HCSB	$Au@SiO_2B$	110 - 150	14 ± 4	1	HCSs with complete shells	8 ± 2	15 ± 6
Au@HCSC1	$Au@SiO_2C$	90 - 300	16 ± 4	1	Layered graphene-like nanostructures	13 ± 2	15 ± 4
Au@HCSC2	$Au@SiO_2C$	90 - 300	16 ± 4	2	Open ended tube like nanostructures	25 ± 5	16 ± 4
Au@HCSC4	$Au@SiO_2C$	90 - 300	16 ± 4	4	Open ended tube like nanostructures	38 ± 10	21 ± 6

B.K. Mutuma, B. Matsoso, K. Ranganathan, D. Wamwangi, N.J. Coville, RSC Advances, 6 (2016) 20399-20408.

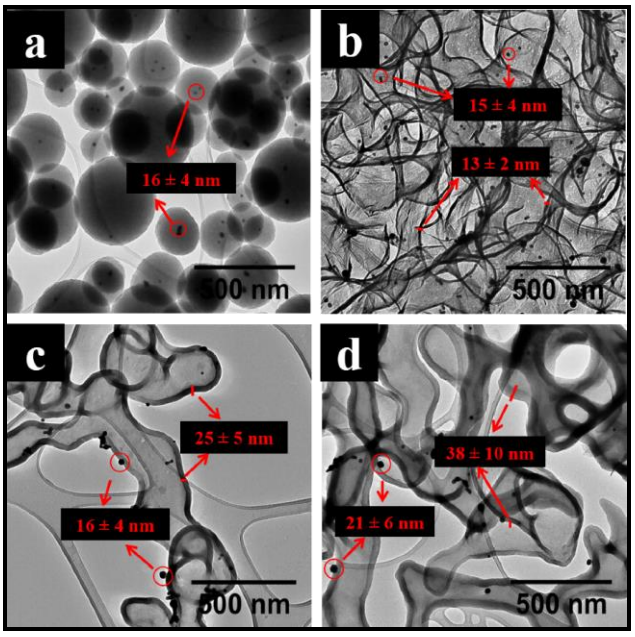

Figure. 6.3. TEM images of **(a)** Au@SiO_2C, **(b)**, **(c)** and **(d)** Au@HCSC obtained after (1 h , 2 h , 4 h) carbonization times and SiO_2 removal, respectively.

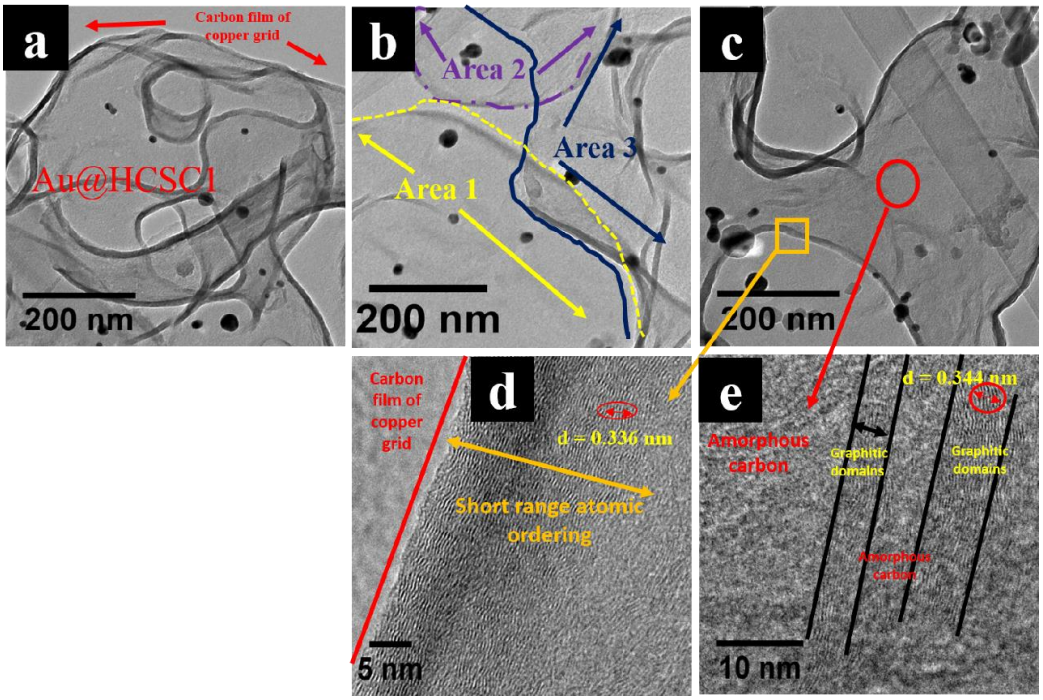

Figure 6.4. HRTEM images of Au@HCSC1; (a) shows the carbon film of Au@HCSC1 and that of the copper grid, (b) shows three overlapping areas of the carbon sheet (black spots are Au

particles), (c) shows a folded region and a sheet like region with magnified images of (d) folded region and (e) sheet like region.

The factors responsible for the formation of the wormlike carbon structures are described below.

(i) Polydispersity

A possible cause of the growth of the wormlike and open ended graphene like structures is related to the SiO_2 polydispersity[74-77]. This is presumably due to the closer contact between the SiO_2 spheres made possible when small and large SiO_2 spheres are mixed. The carbon infiltrates less effectively between the mixed size spheres and this leads to the formation of thinner and hence weaker carbon structures. These are then more easily ruptured.

(ii) Carbonization time

The carbonization time determines the layer structure and wormlike structures after silica etching. The carbon shell thickness has an effect on the completeness of the HCS shell and a thin carbon wall is subject to high stresses which lead to fracture during HF etching. A long carbonization time results in higher nucleation density and diffusivity along the edges leading to a near uniform thickness of the wormlike structures. Continued carbonization results in further coverage and hence formation of thicker open ended and breached nanotube like structures.

(iii) Role of polyvinylpyrrolidone on carbon morphology

The presence of PVP (with a high molecular weight) on SiO_2 synthesis has been reported to cause a broad silica size distribution[78]. In this study, the volume of PVP used to make Au@SiO_2A and Au@SiO_2B (2 mL PVP) was less than that used to make Au@SiO_2C (20 mL PVP) hence leading to modified SiO_2-SiO_2 surface interactions during carbonization leading to different carbon deposits along the external SiO_2 surfaces.

To confirm the influence of PVP on the morphology of the obtained worm like and open ended carbon nanostructures, polydispersed SiO_2 spheres (Fig. S6.2b) and PVP (20 mL) were mixed together and stirred for 1 hour and 12 h respectively. The concentration of PVP was similar to that used in the synthesis of Au@SiO_2C (for comparison purposes). Fig. S6.5a and S6.5b shows the silica spheres mixed with PVP before carbonization confirming the PVP surface coverage on

silica. The polydispersed silica spheres mixed with PVP after 1 h stirring time, followed by carbonization and SiO_2 removal produced worm like hollow carbon nanostructures (Fig. S6.5c). In contrast, a 12 h stirring time, followed by carbonization and SiO_2 removal gave broken hollow carbon spheres with a spherical morphology (Fig. S6.5d). The carbon shell thickness was 7 ± 5 nm in the wormlike hollow structures and 9 ± 7 nm for the broken/deformed hollow carbon spheres. The wormlike carbon nanostructures had a unique hierarchical structure with the coexistence of mesopores and macropores within the non-spherical cavity as shown by the nitrogen adsorption-desorption isotherm (Fig. S6.9). Fig S6.9 indicates the Nitrogen adsorption-desorption isotherm of the open ended wormlike hollow carbon nanostructures that can be classified as a type (III) adsorption isotherm according to the IUPAC nomenclature. The measured isotherm exhibited a H3 hysteresis loop at a relative pressure of P/Po = 0.8 – 1.0 indicating assemblage of slit shaped pores or platelike particles[79]. Consequently, the material exhibited a BET surface area of 98 m^2/g and a pore volume of 0.64 cm^3/g. Fig. S6.9 inset shows the pore size distribution calculated by the BJH method with a sharp peak observed at 23.4 nm; characteristic of mesopores and a broad pore size distribution in the macroporous region (50 to 100 nm). This indicated the coexistence of hierarchical mesopores and macropores derived from the hollow interconnected open network and interparticle voids in the sample[80, 81]. Indeed, the presence of non-spherical hollow cavities in carbon nanomaterials have been reported to reduce the charge transport pathway in electrochemical devices[82].

In the study, 900°C was used for carbonization of the silica. Mixing of silica with PVP results in the presence of hydrogen bonded PVP polymer chains on SiO_2 that carbonizes on the silica surface[83-85]. Some of the PVP was lost due to sublimation at the reaction temperature. The surface morphology is dependent on the amount of PVP bound on the silica surface. When a high concentration of PVP was used on Au@SiO_2 and polydispersed SiO_2 spheres, a thin carbon nanosheet and wormlike hollow structures were obtained.

(iv) Presence of Au

The HRTEM images of the Au@HCS indicate the HCSs have been broken and show folded edges of the carbon sheet on the planar structure (Fig. S6.6a). The folded edges have a higher

interlayer spacing (0.371 ± 0.002 nm) compared to the d spacing of pure graphite (0.335 nm) [86]. (Fig. S6.6b). This indicates an 11% strain in the carbon material around the Au and folding along the edges due to the carbon grown on the interconnected spheres. A difference in the curvature energies of thin carbon walls is thus expected for carbon in the presence/absence of Au particles. On removal of the silica, the carbon atoms can now relax and this leads to collapse/unzipping of the walls, leading to the formation of worm like carbon structures. The unzipping effect is not only related to the thinness of the carbon structure. If this was the case, the polydispersed HCSC1 (Fig. 6.1d) with a shell thickness of 8 ± 2 nm would also be expected to form the worm like graphitic carbon structures. This is not seen. There is clearly less surface strain on the carbon wall after silica removal and hence HCSs with deformed and interconnected carbon shells are formed despite the presence of a thin carbon shell.

Fig. 6.5 shows a schematic diagram that summarizes the formation of the different carbon nanostructures for the Au@monodispersed and Au@polydispersed silica sphere templates. A small sized Au@monodispersed SiO_2 sphere template results in Au@HCSs with breached shells while a large sized Au@SiO_2 monodispersed sphere template gives Au@HCSs with complete shells. In contrast, the Au@polydispersed SiO_2 sphere template gives graphene-like, wormlike and open ended tube like structures.

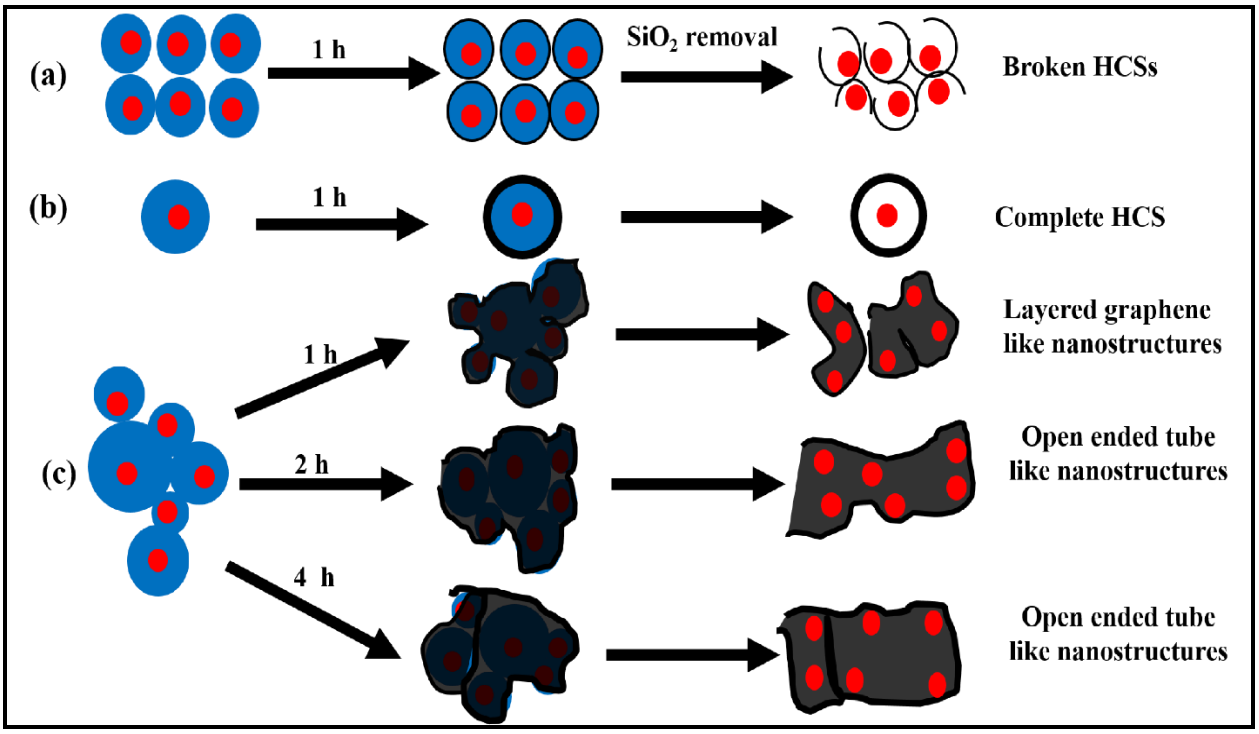

Figure 6.5. Possible carbon nanostructure formation mechanism in (a) Au@SiO_2A, (b) Au@SiO_2B and (c) Au @SiO_2C, respectively.

6.3.3 Raman spectra of hollow carbon spheres and Au@hollow carbon spheres

Table S9.1 shows the I_D/I_G ratios of monodispersed and polydispersed HCSs. The corresponding Raman spectra for HCSs and Au@HCSs are shown in Fig. S6.7 and S6.8. In all cases, a strong D band was exhibited between 1342 cm^{-1} and 1381 cm^{-1} due to the breathing mode of sp^2 and sp^3 carbon atoms[87, 88]. In addition, a G peak was observed between 1575 cm^{-1} and 1597 cm^{-1} which is a characteristic of bond stretching of sp^2 atoms. An increase in structural defects with increasing carbonization time was observed as seen from I_D/I_G ratios. This is expected as an increase in carbonization time increases the number of carbon atoms nucleating on the silica template leading to thicker carbon shells and thus more structural defects. Au@HCSA and Au@HCSC1 had fewer defects than Au@HCSB resulting in lower I_D/I_G ratios (Table S9.2). A comparison of the Raman spectra of polydispersed Au@HCSs and HCSs shows a broad band between 2700 cm^{-1} and 2900 cm^{-1} characteristic of a 2D band. The broadness of the peak indicates the presence of large defects with small graphitic domains[89, 90]. In Au@HCSC1, D and

G bands were observed at 1370 cm^{-1} and 1590 cm^{-1} respectively with a I_D/I_G ratio of 0.91, indicating less graphitic character. A broad 2D band was observed in Au@HCSC1 showing the presence of both graphitic and non-graphitic domains in agreement with the HRTEM results.

6.3.4 Application of worm like hollow carbon nanostructures and broken HCSs in organic solar cells

The hollow carbon nanostructures (wormlike and broken HCSs) were mixed with P3HT and PCBM to form a ternary blend active layer (section 6.2.7). The pristine active layer (PCBM:P3HT blend) had a thickness of 190 ± 10 nm. Fig. S9.11 shows the AFM images of P3HT: PCBM:wormlike carbon nanostructures and P3HT:PCBM:broken HCSs with a surface roughness of 81.5 nm and 91.8 nm respectively. A PCBM absorption peak was observed at 336 nm and 338 nm for P3HT:PCBM with broken HCSs and wormlike HCSs respectively (Fig. 6.6)[91]. The absorption intensity of P3HT peaks were observed at 517 nm and at 553 nm/555 nm, with a shoulder (#) at 604 nm/605 nm in the films containing broken HCSs /wormlike HCSs respectively due to P3HT interchain π-π* interactions[92, 93]. The absorption intensity of the film comprising of P3HT:PCBM:wormlike HCSs was higher than that made of P3HT: PCBM: broken HCSs due to enhanced scattering of light. An increase in absorption intensity in the wormlike HCSs led to an increased short circuit current density (Jsc). The device performance is determined by the structural organization of the interpenetrating network, interface energy and self-assembly of active layer composites[94, 95]. Theoretical studies and experimental results of organic photovoltaic devices have shown that P3HT chains can self-assemble to wrap around the carbon based nanostructures and change the conjugation length of the P3HT to modify the device charge transfer properties[95, 96]. It is proposed that the large interface area provided in the open ended worm like structure could increase the interconnectivity to the P3HT chains and thus, alter the charge transfer properties in the active layer composite.

B.K. Mutuma, B. Matsoso, K. Ranganathan, D. Wamwangi, N.J. Coville, RSC Advances, 6 (2016) 20399-20408.

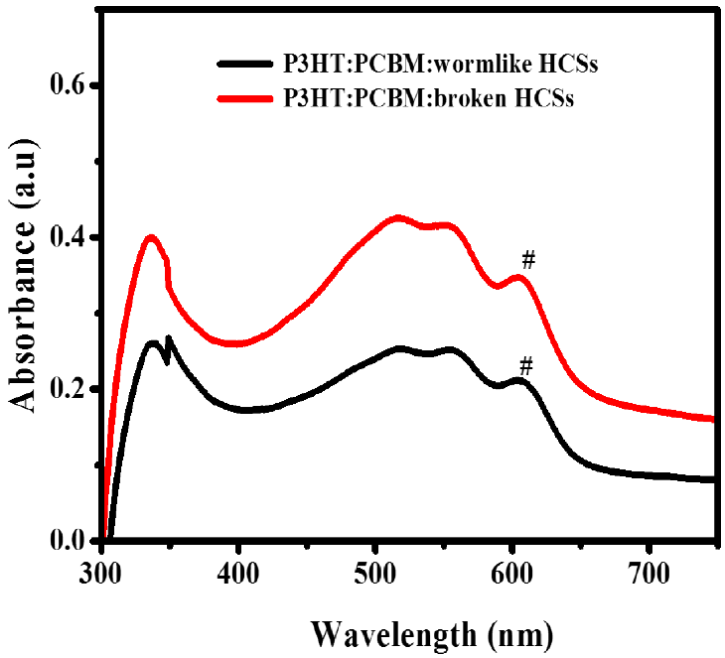

Figure 6.6. UV-visible absorbance spectra of P3HT:PCBM:hollow carbon nanostructures films.

Table 6.4 shows the current-voltage characteristics of the ternary blend active layer based organic solar cell under illumination and in the dark. An attempt to use hollow carbon spheres with a complete shell led to shorting of the photovoltaic devices due to their large diameter size. Hence, wormlike and broken HCSs were used. The current density of the device with wormlike HCSs is slightly higher than in the device with broken HCSs. This can be attributed to a reduced charge-transport distance, a slight increase in absorption intensity and less surface roughness in comparison to that of a device with broken HCSs. There was a slight increase in open circuit voltage (Voc) in the device with wormlike hollow carbon nanostructures which could be attributed to a change in the HOMO and LUMO energies of the active layer components[97-99]. In addition, a possible charge carrier recombination is further corroborated by an S curve kink (see arrow in Fig. 6.7a) and by a high leakage current (Fig. 6.7b). The power conversion efficiency of the ternary solar cell fabricated using worm like structures was 0.11% while with broken hollow carbon spheres it was 0.14%. While these values are low they show an improvement with reference to the unbroken HCSs (see Fig. 6.7). The increase in shunt resistance, open circuit

voltage and fill factor (FF) in P3HT:PCBM:broken HCSs relative to that of the device with wormlike HCSs were responsible for the slight improvement in photovoltaic efficiency.

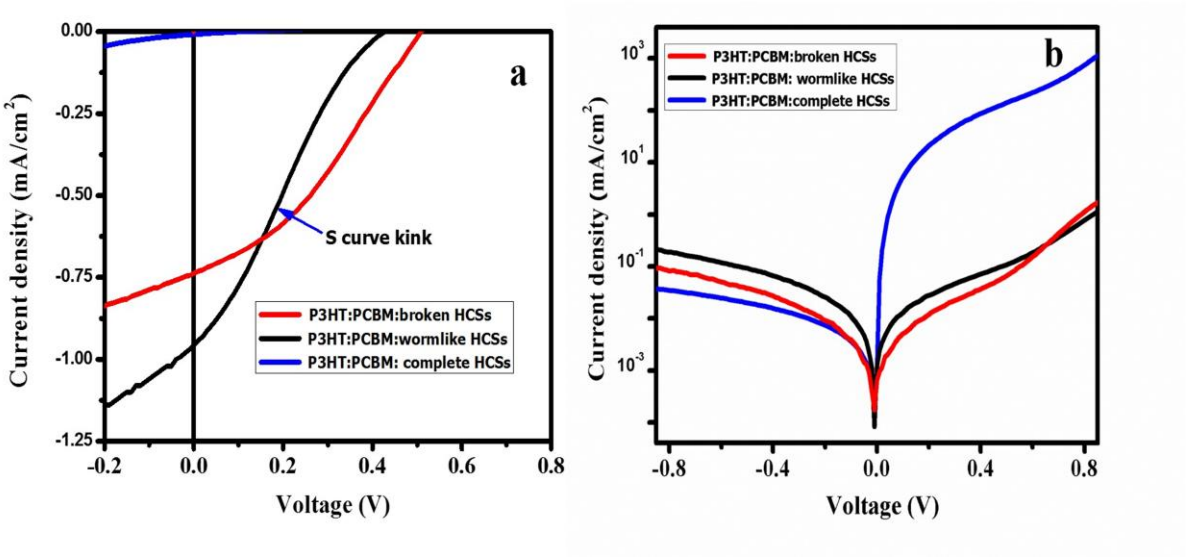

Figure 6.7. P3HT:PCBM:hollow carbon nanostructures current-voltage (J-V) curves **(a)** under illumination and **(b)** Semi log J-V curves in the dark.

Table 6.4. Current -Voltage characteristics of devices with P3HT:PCBM:wormlike HCSs and P3HT:PCBM:broken HCSs

Description	Jsc (mA/cm^2)	Voc (V)	Series resistance (ohms)	Shunt resistance (ohms)	FF (%)	Power conversion efficiency (%)
P3HT:PCBM:wormlike HCSs	0.96	0.42	1.41×10^4	6.07×10^3	26.04	0.11
P3HT:PCBM:broken HCSs	0.73	0.50	5.95×10^3	2.14×10^4	37.26	0.14

B.K. Mutuma, B. Matsoso, K. Ranganathan, D. Wamwangi, N.J. Coville, RSC Advances, 6 (2016) 20399-20408.

6.4 Conclusions

This study provides insight into the effect of Au@polydispersed silica sphere templates and polydispersed SiO_2 sphere templates towards the formation of hollow carbon nanostructures by a CVD nanocasting method, a study rarely performed. Au@HCSs and HCSs were successfully synthesized using a CVD nanocasting method with $Au@SiO_2$ and SiO_2 spheres as templates. The size of the $Au@SiO_2$ and SiO_2 templates used were found to play a key role in the synthesis of the hollow carbon spheres and nanostructures. Monodispersed and large sized $Au@SiO_2$ spheres gave unbroken HCSs, whereas polydispersed $Au@SiO_2$ spheres led to the formation of a range of hollow carbon nanostructures (thin carbon nanosheets and open ended nanotube like carbon). Modification of the surface chemistry of the polydispersed SiO_2 using PVP was found to contribute to the worm like carbon nanostructures. Raman analysis confirmed the presence of the graphitized carbon in all the samples synthesized.

The Au@HCS core shell layered materials have been used for the generation of graphene like open structures. The polydispersed SiO_2 sphere functionalized with PVP generated worm like hollow carbon structures. The application of the wormlike nanostructures in organic solar cells opens new studies into the electronic properties of these materials. However, overcompensation of the number of electron accepting materials limited domain formation of the donor/acceptor thus increasing recombination; substitutional replacemnet would be encouraged.

B.K. Mutuma, B. Matsoso, K. Ranganathan, D. Wamwangi, N.J. Coville, RSC Advances, 6 (2016) 20399-20408.

References

1. Byun, Y.; Coskun, A. *Chemistry of Materials* **2015,** 27, (7), 2576-2583.
2. Narita, A.; Verzhbitskiy, I. A.; Frederickx, W.; Mali, K. S.; Jensen, S. A.; Hansen, M. R.; Bonn, M.; De Feyter, S.; Casiraghi, C.; Feng, X.; Müllen, K. *ACS Nano* **2014,** 8, (11), 11622-11630.
3. Kouloumpis, A.; Spyrou, K.; Dimos, K.; Georgakilas, V.; Rudolf, P.; Gournis, D. *Frontiers in Materials* **2015,** 2, 10.
4. Kuang, Q.; Xie, S.-Y.; Jiang, Z.-Y.; Zhang, X.-H.; Xie, Z.-X.; Huang, R.-B.; Zheng, L.-S. *Carbon* **2004,** 42, (8–9), 1737-1741.
5. Hu, B.; Ago, H.; Ito, Y.; Kawahara, K.; Tsuji, M.; Magome, E.; Sumitani, K.; Mizuta, N.; Ikeda, K.-i.; Mizuno, S. *Carbon* **2012,** 50, (1), 57-65.
6. Kim, H.; Song, I.; Park, C.; Son, M.; Hong, M.; Kim, Y.; Kim, J. S.; Shin, H.-J.; Baik, J.; Choi, H. C. *ACS Nano* **2013,** 7, (8), 6575-6582.
7. Wu, Q.; Jung, S. J.; Jang, S. K.; Lee, J.; Jeon, I.; Suh, H.; Kim, Y. H.; Lee, Y. H.; Lee, S.; Song, Y. J. *Nanoscale* **2015,** 7, (23), 10357-10361.
8. Kim, K. S.; Zhao, Y.; Jang, H.; Lee, S. Y.; Kim, J. M.; Kim, K. S.; Ahn, J.-H.; Kim, P.; Choi, J.-Y.; Hong, B. H. *Nature* **2009,** 457, (7230), 706-710.
9. Liu, W.; Kraemer, S.; Sarkar, D.; Li, H.; Ajayan, P. M.; Banerjee, K. *Chemistry of Materials* **2014,** 26, (2), 907-915.
10. Ago, H.; Ito, Y.; Mizuta, N.; Yoshida, K.; Hu, B.; Orofeo, C. M.; Tsuji, M.; Ikeda, K.-i.; Mizuno, S. *ACS Nano* **2010,** 4, (12), 7407-7414.
11. Wang, J.; Zhu, M.; Outlaw, R. A.; Zhao, X.; Manos, D. M.; Holloway, B. C. *Carbon* **2004,** 42, (14), 2867-2872.
12. Zhu, M.; Wang, J.; Holloway, B. C.; Outlaw, R. A.; Zhao, X.; Hou, K.; Shutthanandan, V.; Manos, D. M. *Carbon* **2007,** 45, (11), 2229-2234.
13. Zhu, M.; Wang, J.; Outlaw, R. A.; Hou, K.; Manos, D. M.; Holloway, B. C. *Diamond and Related Materials* **2007,** 16, (2), 196-201.
14. Zeng, L.; Lei, D.; Wang, W.; Liang, J.; Wang, Z.; Yao, N.; Zhang, B. *Applied Surface Science* **2008,** 254, (6), 1700-1704.
15. Wang, Z.; Shoji, M.; Ogata, H. *Applied Surface Science* **2011,** 257, (21), 9082-9085.
16. Eswaraiah, V.; Jyothirmayee Aravind, S. S.; Ramaprabhu, S. *Journal of Materials Chemistry* **2011,** 21, (19), 6800-6803.
17. Hummers, W. S.; Offeman, R. E. *Journal of the American Chemical Society* **1958,** 80, (6), 1339-1339.
18. Geim, A. K.; Novoselov, K. S. *Nature Materials* **2007,** 6, (3), 183-191.
19. Higginbotham, A. L.; Kosynkin, D. V.; Sinitskii, A.; Sun, Z.; Tour, J. M. *ACS Nano* **2010,** 4, (4), 2059-2069.
20. Li, J.; Ye, S.; Li, T.; Li, X.; Yang, X.; Ding, S. *Procedia Engineering* **2015,** 102, 492-498.
21. Chua, C. K.; Sofer, Z.; Šimek, P.; Jankovský, O.; Klímová, K.; Bakardjieva, S.; Hrdličková Kučková, Š.; Pumera, M. *ACS Nano* **2015,** 9, (3), 2548-2555.
22. Gleiter, H. *Acta Materialia* **2000,** 48, (1), 1-29.
23. Pokropivny, V. V.; Skorokhod, V. V. *Materials Science and Engineering: C* **2007,** 27, (5–8), 990-993.

24. Terrones, M.; Botello-Méndez, A. R.; Campos-Delgado, J.; López-Urías, F.; Vega-Cantú, Y. I.; Rodríguez-Macías, F. J.; Elías, A. L.; Muñoz-Sandoval, E.; Cano-Márquez, A. G.; Charlier, J.-C.; Terrones, H. *Nano Today* **2010,** 5, (4), 351-372.
25. Tiwari, J. N.; Tiwari, R. N.; Kim, K. S. *Progress in Materials Science* **2012,** 57, (4), 724-803.
26. Wu, X.-L.; Xu, A.-W. *Journal of Materials Chemistry A* **2014,** 2, (14), 4852-4864.
27. Jiang, H.; Lee, P. S.; Li, C. *Energy & Environmental Science* **2013,** 6, (1), 41-53.
28. Mao, S.; Lu, G.; Chen, J. *Nanoscale* **2015,** 7, (16), 6924-6943.
29. Yang, Z.; Chabi, S.; Xia, Y.; Zhu, Y. *Progress in Natural Science: Materials International* **2015,** 25, (6), 554-562.
30. Zhang, L.; Shi, G. *The Journal of Physical Chemistry C* **2011,** 115, (34), 17206-17212.
31. Yang, Z.; Yan, C.; Liu, J.; Chabi, S.; Xia, Y.; Zhu, Y. *RSC Advances* **2015,** 5, (37), 29397-29400.
32. Wu, C.; Deng, S.; Wang, H.; Sun, Y.; Liu, J.; Yan, H. *ACS Applied Materials & Interfaces* **2014,** 6, (2), 1106-1112.
33. Lu, A. H.; Schüth, F. *Advanced Materials* **2006,** 18, (14), 1793-1805.
34. Peng, H.-J.; Liang, J.; Zhu, L.; Huang, J.-Q.; Cheng, X.-B.; Guo, X.; Ding, W.; Zhu, W.; Zhang, Q. *ACS Nano* **2014,** 8, (11), 11280-11289.
35. Galeano, C.; Meier, J. C.; Soorholtz, M.; Bongard, H.; Baldizzone, C.; Mayrhofer, K. J. J.; Schüth, F. *ACS Catalysis* **2014,** 4, (11), 3856-3868.
36. Wen, Z.; Wang, Q.; Zhang, Q.; Li, J. *Electrochemistry Communications* **2007,** 9, (8), 1867-1872.
37. Nongwe, I.; Ravat, V.; Meijboom, R.; Coville, N. J. *Applied Catalysis A: General* **2013,** 466, (0), 1-8.
38. Ravat, V.; Nongwe, I.; Coville, N. J. *ChemCatChem* **2012,** 4, (12), 1930-1934.
39. Wilgosz, K.; Chen, X.; Kierzek, K.; Machnikowski, J.; Kalenczuk, R.; Mijowska, E. *Nanoscale Research Letters* **2012,** 7, (1), 1-5.
40. Chen, X.; Kierzek, K.; Cendrowski, K.; Pelech, I.; Zhao, X.; Feng, J.; Kalenczuk, R. J.; Tang, T.; Mijowska, E. *Colloids and Surfaces A: Physicochemical and Engineering Aspects* **2012,** 396, (0), 246-250.
41. Li, M.; Wu, Q.; Wen, M.; Shi, J. *Nanoscale Res Lett* **2009,** 4, (11), 1365-1370.
42. Joo, J. B.; Kim, P.; Kim, W.; Kim, J.; Kim, N. D.; Yi, J. *Current Applied Physics* **2008,** 8, (6), 814-817.
43. Cai, P.-j.; Feng, L. *Materials Chemistry and Physics* **2008,** 108, (1), 1-3.
44. Zeng, H. C. *Journal of Materials Chemistry* **2011,** 21, (21), 7511-7526.
45. Lu, A.-H.; Hao, G.-P.; Sun, Q.; Zhang, X.-Q.; Li, W.-C. *Macromolecular Chemistry and Physics* **2012,** 213, (10-11), 1107-1131.
46. Fang, B.; Kim, J. H.; Kim, M.-S.; Bonakdarpour, A.; Lam, A.; Wilkinson, D. P.; Yu, J.-S. *Journal of Materials Chemistry* **2012,** 22, (36), 19031-19038.
47. Chen, X.; Kierzek, K.; Jiang, Z.; Chen, H.; Tang, T.; Wojtoniszak, M.; Kalenczuk, R. J.; Chu, P. K.; Borowiak-Palen, E. *The Journal of Physical Chemistry C* **2011,** 115, (36), 17717-17724.

48. Dai, Y.; Jiang, H.; Hu, Y.; Fu, Y.; Li, C. *Industrial & Engineering Chemistry Research* **2014,** 53, (8), 3125-3130.
49. Su, F.; Zhao, X. S.; Wang, Y.; Wang, L.; Lee, J. Y. *Journal of Materials Chemistry* **2006,** 16, (45), 4413-4419.
50. Xu, X.; Asher, S. A. *Journal of the American Chemical Society* **2004,** 126, (25), 7940-7945.
51. Arnal, P. M.; Schüth, F.; Kleitz, F. *Chemical Communications* **2006**, (11), 1203-1205.
52. Xia, Y.; Yang, Z.; Mokaya, R. *The Journal of Physical Chemistry B* **2004,** 108, (50), 19293-19298.
53. Laurent, C.; Flahaut, E.; Peigney, A.; Rousset, A. *New Journal of Chemistry* **1998,** 22, (11), 1229-1237.
54. Kim, M.; Yoon, S. B.; Sohn, K.; Kim, J. Y.; Shin, C.-H.; Hyeon, T.; Yu, J.-S. *Microporous and Mesoporous Materials* **2003,** 63, (1–3), 1-9.
55. Wilgosz, K.; Chen, X.; Kierzek, K.; Machnikowski, J.; Kalenczuk, R. J.; Mijowska, E. *Nanoscale Research Letters* **2012,** 7, (1), 269-269.
56. Kanai, Y.; Grossman, J. C. *Nano Letters* **2008,** 8, (3), 908-912.
57. Sun, Q.; He, B.; Zhang, X.-Q.; Lu, A.-H. *ACS Nano* **2015,** 9, (8), 8504-8513.
58. Yang, M.; Yang, Y.; Wang, L.; Hong, B.; Huang, H.; Hu, X.; Zhao, Y.; Dong, Y.; Li, X.; Lu, Y. *Progress in Natural Science: Materials International* **2015,** 25, (5), 386-391.
59. Park, H.; Chang, S.; Smith, M.; Gradečak, S.; Kong, J. *Scientific Reports* **2013,** 3, 1581.
60. Liu, Z.; You, P.; Liu, S.; Yan, F. *ACS Nano* **2015,** 9, (12), 12026-12034.
61. Zhu, Y.; Meng, X.; Cui, H.; Jia, S.; Dong, J.; Zheng, J.; Zhao, J.; Wang, Z.; Li, L.; Zhang, L.; Zhu, Z. *ACS Applied Materials & Interfaces* **2014,** 6, (16), 13833-13840.
62. Khatri, I.; Adhikari, S.; Aryal, H. R.; Soga, T.; Jimbo, T.; Umeno, M. *Applied Physics Letters* **2009,** 94, (9), 093509.
63. Derbal-Habak, H.; Bergeret, C.; Cousseau, J.; Nunzi, J. *Solar Energy Materials and Solar Cells* **2011,** 95, S53-S56.
64. Stylianakis, M. M.; Kymakis, E. *Applied Physics Letters* **2012,** 100, (9), 093301.
65. Keru, G.; Ndungu, P. G.; Mola, G. T.; Nogueira, A. F.; Nyamori, V. O. *Journal of Nanomaterials* **2016,** 2016, 11.
66. Xia, Y. D.; Mokaya, R. *Advanced Materials* **2004,** 16, (11), 886-891.
67. Stöber, W.; Fink, A.; Bohn, E. *Journal of Colloid and Interface Science* **1968,** 26, (1), 62-69.
68. Masalov, V.; Sukhinina, N.; Kudrenko, E.; Emelchenko, G. *Nanotechnology* **2011,** 22, (27), 275718.
69. Nozawa, K.; Gailhanou, H.; Raison, L.; Panizza, P.; Ushiki, H.; Sellier, E.; Delville, J. P.; Delville, M. H. *Langmuir* **2005,** 21, (4), 1516-1523.
70. Kim, J. H.; Fang, B.; Kim, M.; Yu, J.-S. *Catalysis Today* **2009,** 146, (1–2), 25-30.
71. Park, S. K.; Kim, K. D.; Kim, H. T. *Colloids and Surfaces A: Physicochemical and Engineering Aspects* **2002,** 197, (1–3), 7-17.
72. Jaramillo, N.; Paucar, C.; García, C. *Journal of Materials Science* **2014,** 49, (9), 3400-3406.
73. Chen, X. H.; Deng, F. M.; Wang, J. X.; Yang, H. S.; Wu, G. T.; Zhang, X. B.; Peng, J. C.; Li, W. Z. *Chemical Physics Letters* **2001,** 336, (3–4), 201-204.
74. Overbeek, J. T. G. *Advances in Colloid and Interface Science* **1982,** 15, (3–4), 251-277.

75. Van Blaaderen, A.; Van Geest, J.; Vrij, A. *Journal of Colloid and Interface Science* **1992,** 154, (2), 481-501.
76. Harris, M. T.; Brunson, R. R.; Byers, C. H. *Journal of Non-Crystalline Solids* **1990,** 121, (1), 397-403.
77. Chen, S.-L.; Dong, P.; Yang, G.-H.; Yang, J.-J. *Industrial & Engineering Chemistry Research* **1996,** 35, (12), 4487-4493.
78. Chung, Y.; Jeon, M.; Kim, C. *Macromolecular Research* **2009,** 17, (1), 37-43.
79. Thommes, M. *Chemie Ingenieur Technik* **2010,** 82, (7), 1059-1073.
80. Tao, H.; Yang, H.; Liu, X.; Ren, J.; Wang, Y.; Lu, G. *Chemical Engineering Journal* **2013,** 225, 686-694.
81. Li, Y.; Xia, W.; Zou, R.; Zhang, J.; Chen, Z.; Xu, Q. *RSC Advances* **2015,** 5, (117), 96580-96586.
82. Zhang, J.; Wang, K.; Guo, S.; Wang, S.; Liang, Z.; Chen, Z.; Fu, J.; Xu, Q. *ACS Applied Materials & Interfaces* **2014,** 6, (3), 2192-2198.
83. Bogatyrev, V. M.; Borisenko, N. V.; Pokrovskii, V. A. *Russian Journal of Applied Chemistry* **2001,** 74, (5), 839-844.
84. Du, Y. K.; Yang, P.; Mou, Z. G.; Hua, N. P.; Jiang, L. *Journal of Applied Polymer Science* **2006,** 99, (1), 23-26.
85. Kooli, F. *Journal of Chemistry* **2015,** 2015, 8.
86. Luo, J.; Jang, H. D.; Huang, J. *ACS Nano* **2013,** 7, (2), 1464-1471.
87. Ferrari, A. C. *Solid State Communications* **2007,** 143, (1–2), 47-57.
88. Tuinstra, F.; Koenig, J. L. *The Journal of Chemical Physics* **1970,** 53, (3), 1126-1130.
89. Ferrari, A. C.; Basko, D. M. *Nature Nanotechnology* **2013,** 8, (4), 235-246.
90. Jorio, A. *ISRN Nanotechnology* **2012,** 2012, 16.
91. Liu, J.; Shao, S.; Wang, H.; Zhao, K.; Xue, L.; Gao, X.; Xie, Z.; Han, Y. *Organic Electronics* **2010,** 11, (5), 775-783.
92. Kiriy, N.; Jähne, E.; Adler, H.-J.; Schneider, M.; Kiriy, A.; Gorodyska, G.; Minko, S.; Jehnichen, D.; Simon, P.; Fokin, A. A.; Stamm, M. *Nano Letters* **2003,** 3, (6), 707-712.
93. Sirringhaus, H.; Brown, P. J.; Friend, R. H.; Nielsen, M. M.; Bechgaard, K.; Langeveld-Voss, B. M. W.; Spiering, A. J. H.; Janssen, R. A. J.; Meijer, E. W.; Herwig, P.; de Leeuw, D. M. *Nature* **1999,** 401, (6754), 685-688.
94. Botiz, I.; Stingelin, N. *Materials* **2014,** 7, (3), 2273.
95. Yang, C.; Hu, J. G.; Heeger, A. J. *Journal of the American Chemical Society* **2006,** 128, (36), 12007-12013.
96. Bernardi, M.; Giulianini, M.; Grossman, J. C. *ACS Nano* **2010,** 4, (11), 6599-6606.
97. Lange, I.; Kniepert, J.; Pingel, P.; Dumsch, I.; Allard, S.; Janietz, S.; Scherf, U.; Neher, D. *The Journal of Physical Chemistry Letters* **2013,** 4, (22), 3865-3871.
98. Günes, S.; Neugebauer, H.; Sariciftci, N. S. *Chemical Reviews* **2007,** 107, (4), 1324-1338.
99. Brabec, C. J.; Cravino, A.; Meissner, D.; Sariciftci, N. S.; Fromherz, T.; Rispens, M. T.; Sanchez, L.; Hummelen, J. C. *Advanced Functional Materials* **2001,** 11, (5), 374-380.

CHAPTER 7

Synthesis and Characterization of Gold Nanospheres and Nanorods for Application in Organic Photovoltaic Devices

7.1 Introduction

Nanotechnology has grown over recent years due to the importance and versatile applicability of nanomaterials. The chemical, physical, optical, catalytic and electronic properties of nanomaterials are dependent on their quantum confinement and the dielectric environment. Among these nanomaterials, are the noble metals such as gold and silver that are of considerable interest owing to the tunability of their surface plasmon resonance modes using their aspect ratio (length to width ratio)[1]. The aspect ratio of these nanomaterials can be controlled during synthesis[2-5]. Thus, gold nanoparticles can exhibit a spherical shape as gold nanospheres or a rod-like shape as gold nanorods amongst other geometric forms depending on the competition between nucleation and agglomeration[6, 7]. The gold nanospheres show only a transverse surface plasmon peak while the gold nanorod exhibits an additional mode, namely the longitudinal surface plasmon resonance. The surface plasmon resonance properties of gold nanomaterials make them applicable in optical and electronic industries. Different sizes of gold nanorods portray different properties based on the aspect ratio due to the presence of the longitudinal and transverse surface plasmon peaks corresponding to a free electron oscillation along and perpendicular to the major axis of the rods. This is due to the different surface energies resulting from the various crystallographic facets present in gold nanorods[8-10].

The synthesis of colloidal gold nanospheres using the citrate method was introduced by Turkevich *et al.* in 1951 and modified in the 1970s by Frens *et al.*[11, 12]. The kinetics and growth dynamics of gold nanospheres are dominated by a nucleation and coarsening mechanism which is dependent on physicochemical properties such as time, temperature and pH[13]. In using the modified Turkevich method, it is possible to vary the size and shape of gold nanospheres by changing the citrate to gold precursor molar ratio[14], the pH[15] or the temperature[15, 16]. On the other hand, gold nanorods can be synthesized by several methods; template[17, 18], electrochemical[19, 20],

photochemical[21] and seed mediated processes among others[22-26] . The seed mediated route is simple and offers the advantage of manipulating the aspect ratio of the nanorods depending on the seed solution, temperature, reducing agent and surfactant concentration.

Typically, metals are surrounded by a cloud of free electrons. A surface plasmon resonance occurs when a noble metal particle is exposed to an electromagnetic field (wave) which induces a collective oscillation of the free electrons in response to the dispersion of the electromagnetic wave. The oscillation of free electrons causes a transient charge separation forming a dipole oscillation along the direction of the electric field. The amplitude of the oscillation reaches a maximum at a resonance frequency; referred to as the surface plasmon resonance (SPR) effect. According to Mie's theory, the SPR band width and amplitude depend on the metal type, the particle shape, particle size and the dielectric constant of the surrounding media[27]. The scattering or absorption cross sections of light by noble metal nanoparticles depends on the interparticle spacing, particle size and shape that varies the SPR intensity and wavelength[28-31]. Light absorption is dominant in gold nanoparticles of 20 nm while scattering processes takes place in larger gold nanoparticles (> 40 nm)[32]. Thus, the SPR response is dependent on the particle shape, particle size, dielectric constant, orientation of particle in the electrical field and metal type[33-36]. The SPR property of gold nanomaterials have been used to enhance Raman scattering[37], photoluminescence[38] and charge separation in photochemical cells[39], electrochemical cells[40], drug delivery systems[41, 42] and in plasmon sensitized solar cells[43, 44].

Organic photovoltaic devices (OPVs) portray low optical absorption in the visible range is attributed to the thickness dependent absorption of the photoactive layer and the short exciton diffusion length. In OPVs, there exists a competition between the device thickness and the exciton diffusion length[45-47]. To improve the optical absorption, thicker OPV films have to be fabricated. However, increasing the film thickness leads to a low charge carrier transport due to the low charge carrier mobility and recombination which is favoured by the short exciton diffusion length of organic materials[45-47]. To circumvent this problem, the SPR effect of gold has been exploited in organic photovoltaic devices as a strategy to enhance the light harvesting ability. Thus, gold nanospheres, gold nanorods and composites comprising of gold nanomaterials have been incorporated into the anode, the hole transport layer (HTL) or the active layer of

OPVs[48-54]. Linfang *et al.* used gold nanospheres of diameters 5 nm and 15 nm in PEDOT:PSS of OPVs with a MEH-PPV:PCBM as the active layer to obtain an absolute power conversion efficiency (PCE) values of 2.04 and 2.36%, respectively[55]. Chuang *et al.* incorporated Au-graphene oxide nanocomposites as a hole transport layer in a P3HT:PCBM active layer and obtained a PCE of 3.98%[56]. The LSPR enhanced the photocurrent, the charge carrier generation and the overall energy conversion efficiency. Similarly, gold nanorods have also been incorporated in the active layer as reported by Wadans *et al.* to enhance light absorption and film morphology. The effect of which was an attainment of higher photovoltaic efficiency[57]. The Au plasmonic modes can improve the charge transfer process and exciton dissociation and optical free path of light resulting in an enhanced current density (Jsc), fill factor (FF) and power conversion efficiency (PCE) of the OPV device[58, 59]. These OPV parameters are calculated using equation (7.1);

$$PCE = \frac{JscV_{OC}FF}{P_{in}} \qquad \textbf{(7.1)}$$

where P_{in} is the power input.

In this chapter, the synthesis of gold nanospheres and nanorods with controlled parameters using modified Turkevich and a seed mediated methods are reported[60]. The effect of varying the gold precursor to citrate volume ratio on the gold nanoparticle size was evaluated. Also, the effect of aging of gold nanorods on their morphology and aspect ratio was studied using the seed mediated method. The obtained gold nanoparticles and gold nanorods were incorporated into the hole transport layer, (PEDOT:PSS, 120 ± 5 nm thick) of organic solar cells and their current-voltage characteristics determined. The objective was to improve the solar cell device performance by incorporating Au nanostructures in the hole transport layer matrix through plasmonic effects.

7.2 Experimental Procedure

7.2.1 Starting Materials

Chloroauric acid, ($HAuCl_4.3H_2O$, 99.99%, Aldrich), polyvinylpyrrolidone, (PVPK30, Mw 40,000, Aldrich), hexadecyltrimethylammonium bromide, (CTAB, 95%, Aldrich), sodium borohydride ($NaBH_4$, 99%, Aldrich), silver nitrate ($AgNO_3$, 99%, Aldrich), L-ascorbic acid

($C_6H_6O_6$, 99.99%, Aldrich) and trisodium citrate dihydrate ($Na_3C_6H_5O_7.2H_2O$, 99%, Aldrich) were used as reagents for the synthesis of gold nanoparticles and gold nanorods. The solar cell devices were fabricated using PEDOT:PSS (3-4% in H_2O), chlorobenzene, P3HT (99.99%) and PCBM (99.5%) purchased from Sigma Aldrich. A transparent conducting anode; ITO coated glass (25 mm × 25 mm × 1.1 mm, 8-12 Ω/sq.) was purchased from Sigma Aldrich.

7.2.2 Preparation of gold nanospheres

Gold nanospheres were synthesized using the classical Turkevich-Frens method[11] as illustrated in Fig.7.1. Two different volumes (5 mL and 25 mL) of 0.01 M $HAuCl_4.3H_2O$ were put into two round bottomed flasks and refluxed at 80°C for 30 min. To each of the Au solutions, trisodium citrate dihydrate (0.01 M, 50 mL) was added and the mixture was stirred for 30 min. Polyvinylpyrrolidone (PVP; 0.5 g) was dissolved in 20 mL of distilled water and added dropwise to the two Au solutions and stirred at room temperature for 12 h. Centrifugation at 12,000 rpm for 15 min gave suspensions of gold nanoparticles (d = 14 ± 4 nm) in solution from the 5 mL while gold nanoparticles (d = 32 ± 6 nm) were obtained from the Au precursor volume of 25 mL.

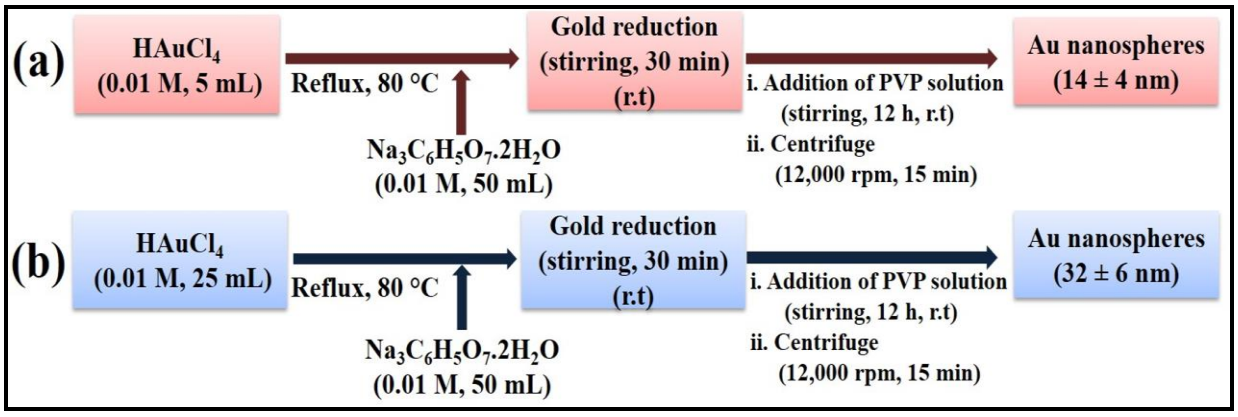

Figure 7.1. The synthesis of gold nanospheres; (a) 14 ± 4 nm and (b) 32 ± 6 nm, respectively.

7.2.3 Preparation of gold nanorods

The seed mediated method was used with CTAB and $AgNO_3$ as structure directing agents[61].

7.2.3.1 Preparation of seed solution

A CTAB solution (0.2 M; 10 mL) was mixed with 2.0 mL of 0.01M chloroauric acid and stirred for 10 min (Fig. 7.2a). An ice cold $NaBH_4$ solution (0.02 M; 2 mL,) was added resulting in a yellowish brown solution. The seed solution was stirred for 2 min and divided into two portions; one was used immediately (non-aged) while the other was used after 3 h (aged).

7.2.3.2 Preparation of the growth solution

A CTAB solution (0.02 M; 10 mL) was added to 1 mL 0.008 M $AgNO_3$ and stirred for 10 min at room temperature (Fig. 7.2b). A chloroauric acid (5 mL, 0.01M) was added and the solution gently mixed with 5 mL of 0.01 M L-ascorbic acid. The solution was stirred for 10 min and used immediately.

A seed solution (5 mL) was added to a growth solution (5 mL) and stirred for 1 h for the aged and just prepared solutions as illustrated in Fig. 7.2. The solutions were then centrifuged at 12,000 rpm for 20 min and labeled as non-aged and aged gold nanorods respectively.

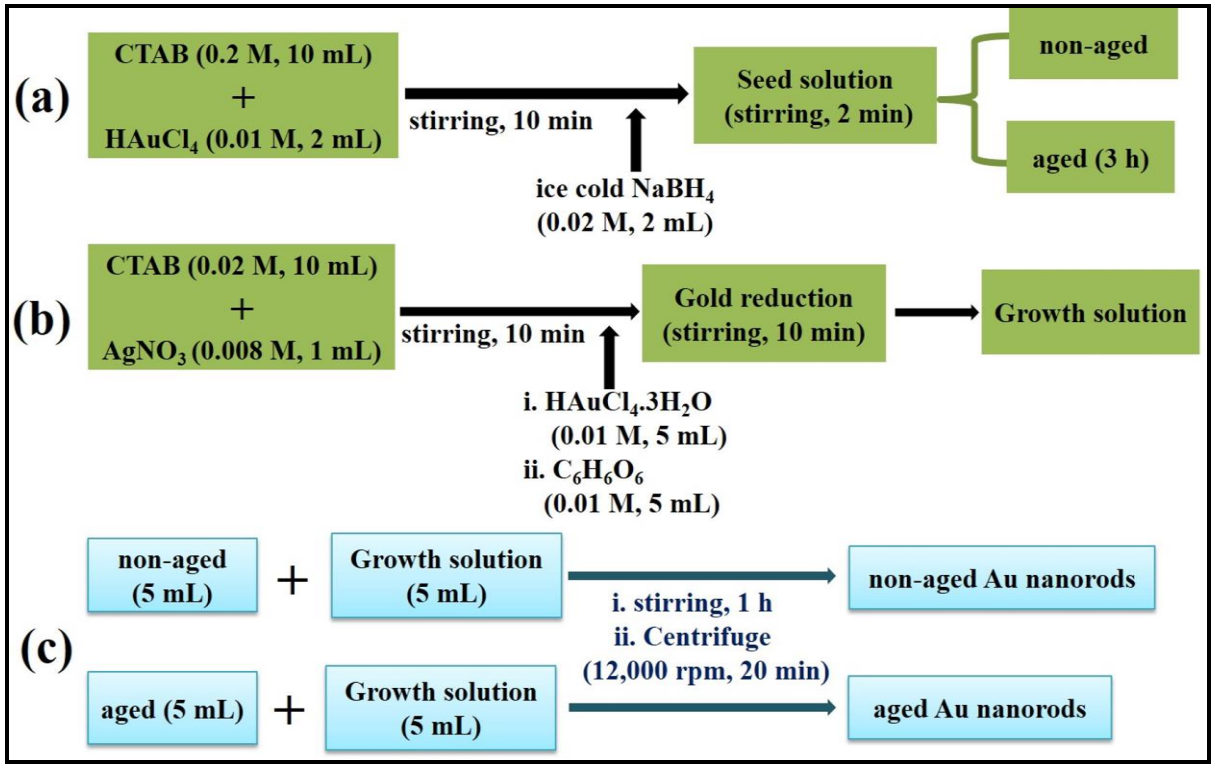

Figure 7.2. The synthesis of gold nanorods; (a) seed solution and (b) growth solution and (c) non-aged and aged gold nanorods, respectively.

7.2.4 Fabrication of an organic solar cell with a modified PEDOT:PSS hole transport layer

The devices architectures fabricated with ITO-coated substrates are shown in Fig. 7.3. The ITO coated glasses were cleaned and dried as described previously in Section 6.2.7. A hole transport layer, PEDOT:PSS was then spin coated onto the ITO coated substrate at 2000 rpm for 1 min. This sample will be subsequently be referred to as pristine PEDOT:PSS. Three sets of modified PEDOT:PSS solutions were prepared by mixing PEDOT:PSS with gold nanoparticle solutions (14 nm and 32 nm) and an aged gold nanorod solution in a PEDOT:PSS:Au volume ratio of 5:1 respectively. The modified PEDOT:PSS solutions were then spin coated onto the ITO coated substrates at 2000 rpm for 1 min. The resulting films (pristine and modified) were thermally treated on a hot plate at 70ºC for 15 min. Two sets of P3HT and PCBM samples (10 mg each) were separately dissolved in 0.5 mL of chlorobenzene and stirred in air for 3 h at room temperature. The active layer was prepared by mixing the separate solutions of P3HT and PCBM to form a polymer blend solution and stirred for 2 h. The active layer (190 ± 10 nm) was then spin coated at 2000 rpm for 1 min on top of the pristine and modified PEDOT:PSS thin films and the cathode was deposited by thermal evaporation of aluminium under 8.0×10^{-6} mbar.

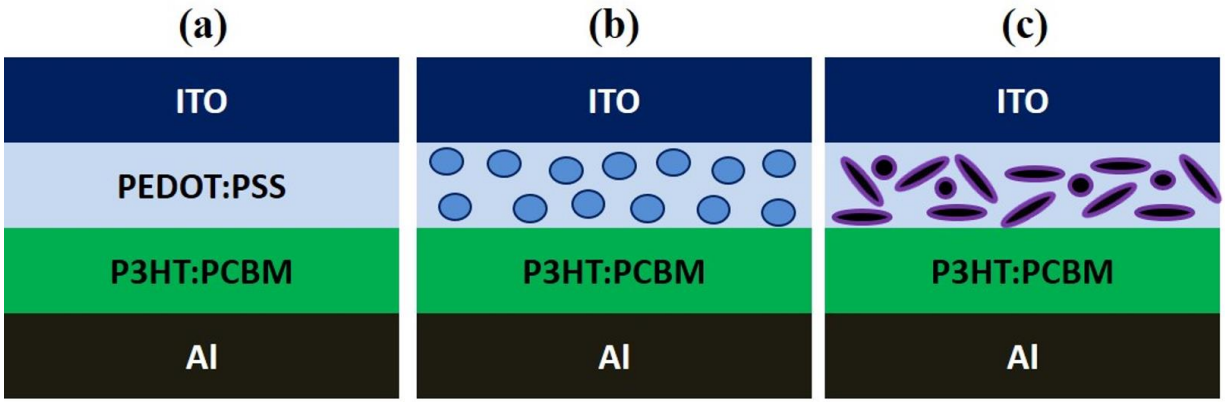

Figure 7.3. The architecture of the fabricated devices; (a) with pristine PEDOT:PSS, (b) with Au nanospheres incorporated in PEDOT:PSS and (c) with Au nanorods incorporated in PEDOT:PSS, respectively.

7.2.5 Characterization of gold nanospheres and nanorods containing films

The morphological features, concentration and absorbance of the synthesized gold nanoparticles and gold nanorods was determined by TEM, ICP-OES and UV-vis spectrophotometer, respectively. The surface roughness and topographic images of the pristine and modified PEDOT:PSS films were studied using a Veeco Di3100 AFM in tapping mode installed with a Si_3N_4 tip. Surface enhanced Raman spectroscopy measurements were done using a Jobin Yvon T64000 Raman spectrometer equipped with an Ar ion laser (514.5 nm) and a laser power of 5 mW. Current-voltage characteristics were done using a HP4141B DC source model under 1.5 Air mass (100 mW/cm^2 illumination). All the measurements were carried out at room temperature under standard conditions.

7.3 Results and discussion

7.3.1 Characterization of gold nanospheres

7.3.1.1 Morphology

Fig. 7.4 shows the TEM images of gold nanoparticles with particle sizes of 14 ± 4 nm and 32 ± 6 nm respectively. This increase in particle size is due to an increase in the gold precursor to citrate volume ratio. Gold nanoparticle size control occurs via a nucleation and growth mechanism whose parameters can be manipulated by varying the time, the precursor and reducing agent concentration and volume ratios among others[62]. The nucleation rate of gold increases with the concentration of sodium citrate[63]. Thus, a higher citrate to gold volume ratio of (10:1) resulted in smaller Au nanospheres due to a faster nucleation rate. Also, the increase in the number of moles of citrate relative to those of gold precursor resulted in the monomer nuclei decreasing substantially resulting in the formation of smaller sized Au nanospheres (Fig. 7.4a and 7.4b). In contrast, a lower citrate to gold volume ratio (2:1) resulted in larger Au nanospheres due to a slower nucleation rate. This can be attributed to the less number of moles of citrate relative to gold precursor that favored Au growth to form larger nanospheres ((Fig. 7.4c and 7.4d). The nucleation and growth in both cases were different resulting in varying particle sizes of gold nanospheres with citrate to gold volume ratios[13]. This is corroborated by the increase in the concentration of obtained gold nanospheres with particle size as determined by the ICP-OES. The gold concentration in the 14 ± 4 nm and 32 ± 6 nm gold nanospheres was 1.6×10^{-4} M and 3.4×10^{-4} M, respectively.

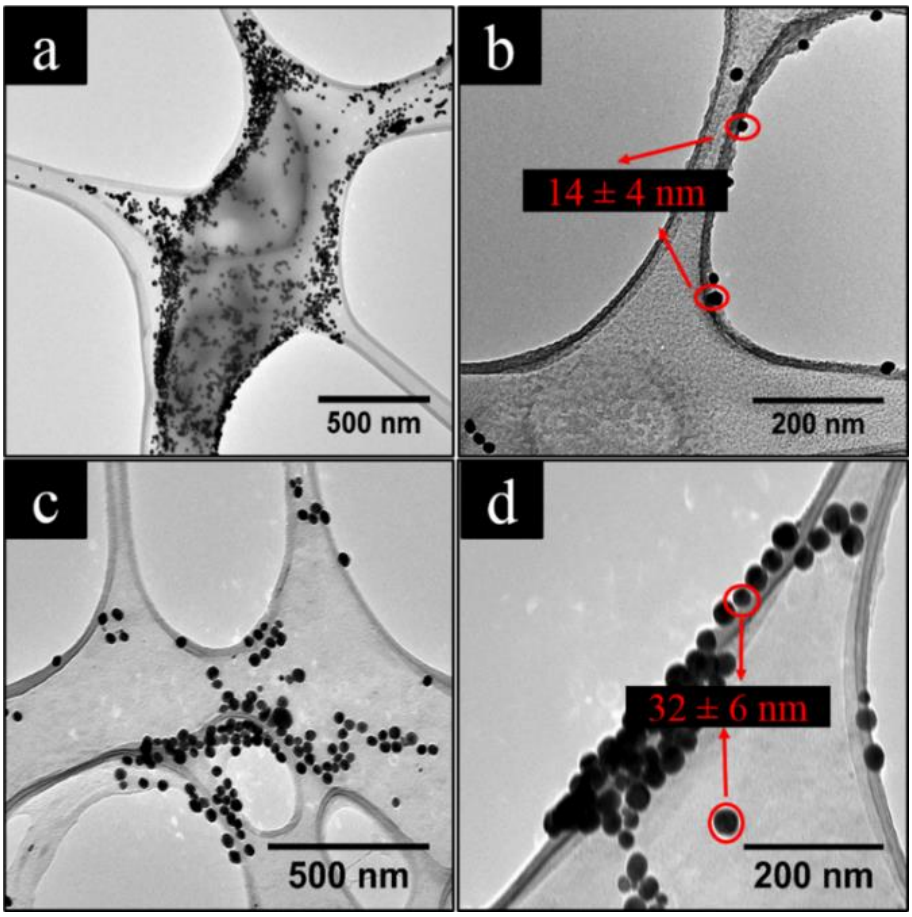

Figure 7.4. TEM images of gold nanoparticles; (a and b) 14 ± 4 nm and (c and d) 32 ± 6 nm particle sizes, respectively.

7.3.1.2 UV-visible absorption spectroscopy analysis

Metallic nanoparticles of dimensions much smaller than the probing light source experience a broad absorption in the visible spectrum. The optical absorption spectra (Fig. 7.5) of the obtained gold nanospheres was within the visible region. This is determined by the boundary conditions of the coherent oscillations of the conduction electrons and the interband electronic transitions between the d and sp orbitals[64]. The short wavelength resonance (transverse SPR mode) is caused by the transverse oscillation of the free electrons. The absorption wavelength of larger sized gold nanospheres (32 ± 6 nm) was at 535 nm while that of the 14 ± 4 nm sized gold nanospheres was at 529 nm respectively. This red shift is attributed to dipole resonance and

correlated with the increase in the particle size[35]. Similar SPR peak wavelengths between 525 nm to 536 nm were reported by Leng *et al.* for gold nanospheres of less than 40 nm particle sizes[65]. As reported in literature, the LSPR band is dependent on the particle size and shape of the gold nanospheres[66-68]. The large variation in full width half maxima (FWHM) scales with the differences in the size dispersion. The dispersion of the 14 nm and 32 nm was approximately 29% and 19%, respectively, as shown in equation 7.2 below. The % dispersion corroborates with the large FWHM of the absorbance curves in Fig. 7.5.

$$\partial_{size} = {}^{4}\!/_{14} \times 100 \approx 29\%$$
$$\partial_{size} = {}^{6}\!/_{32} \times 100 \approx 19\% \qquad (7.2)$$

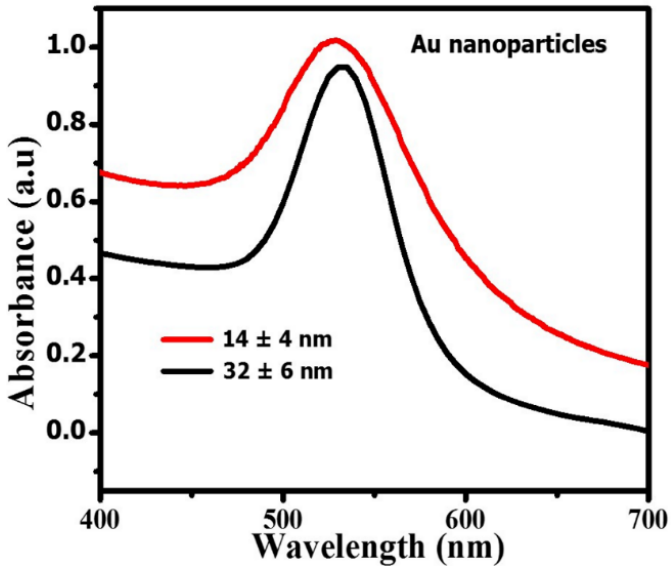

Figure 7.5. The UV-visible absorbance spectra of the gold nanoparticles in solution due to dipole resonance.

7.3.1.3 AFM topographic analysis

The AFM images of the pristine PEDOT:PSS and Au nanoparticles in PEDOT:PSS show an increase in surface roughness upon incorporation of gold nanospheres into the hole transport layer, PEDOT:PSS (Fig. 7.6). The calculated root mean square (rms) surface roughness of the pristine PEDOT:PSS was 25.4 ± 0.2 nm while incorporation of gold nanospheres into the PEDOT:PSS matrix, led to calculated rms values of 35.6 ± 0.3 nm and 54.6 ± 0.3 nm for 14 ± 4

nm and 32 ± 6 nm gold sizes respectively. The increase in surface roughness is attributed to the dispersion of Au nanospheres in the hole transport layer. The higher the surface roughness, the closer the interfacial interactions between the active layer, anode and the hole transport layer. This can create hole transport pathways that enhance power conversion efficiency upon light illumination.

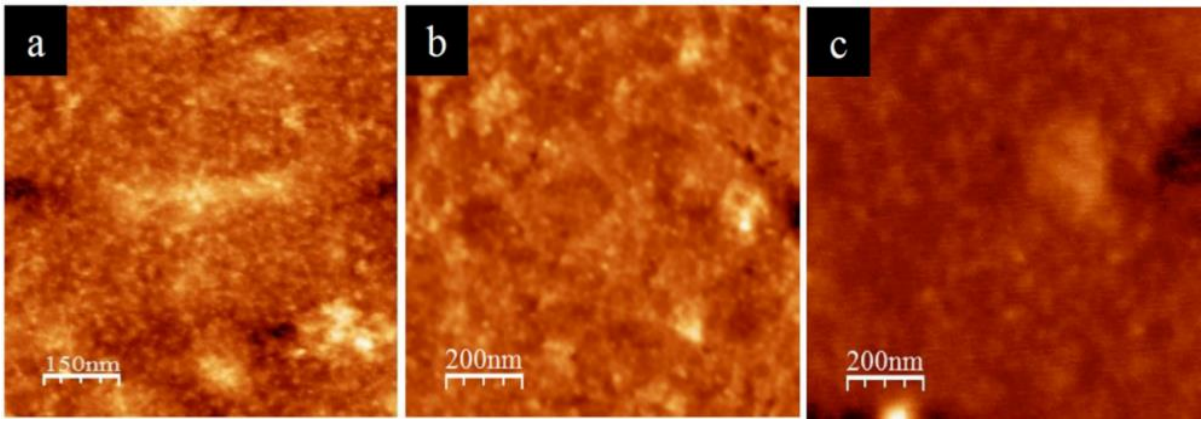

Figure 7.6. AFM images of pristine and modified PEDOT:PSS films; (a) pristine PEDOT:PSS, (b) with Au nanoparticles (14 ± 4 nm) and (c) with Au nanoparticles (32 ± 6 nm), respectively.

7.3.2 Gold nanorods characterization

7.3.2.1 Morphology

Figs. 7.7a-d show that the gold nanorod containing solution comprised of gold nanospheres (30%) and asymmetric gold nanostructures (70%) with an aspect ratio ranging from 1.7 to 3.0. The gold nanorod aspect ratio increased with aging time (Fig. 7.7a, b versus 7.7c, d). The concentration of the obtained gold nanorods was measured and showed that the value did not change with aging (1.4×10^{-5} M) as determined by the ICP-OES. Figs. 7.7a-b show varying sizes of gold nanospheres and gold nanorods and also a few very small gold nanoparticles (< 5 nm). This broad distribution of gold sizes and shapes implies incomplete gold (III) ion reduction[26, 69]. Thus, a continuous nucleation and growth process occurred during the aging process. The presence of gold nanospheres and gold nanorods in solution suggests a bilayer assembly of CTAB around the gold nanorods[70]. In seed mediated synthesis of gold nanorods, CTAB acts as a structure directing agent. In solution, CTAB forms micelles where the gold seed attach and thus directs the rod-like morphology. When CTAB concentration is high, the excess CTAB assembles

between the already formed gold nanorods creating a bilayer assembly in a stable gold nanorod solution. Fig. 7.7c and 7.7d show the aged gold nanorods with an increased aspect ratio. The increase in the aspect ratio and the characteristic disappearance of the tiny gold nanoparticles in the aged gold nanorod solution is likely to have resulted from further particle growth by a coarsening mechanism leading to the increased gold particle dimension[71].

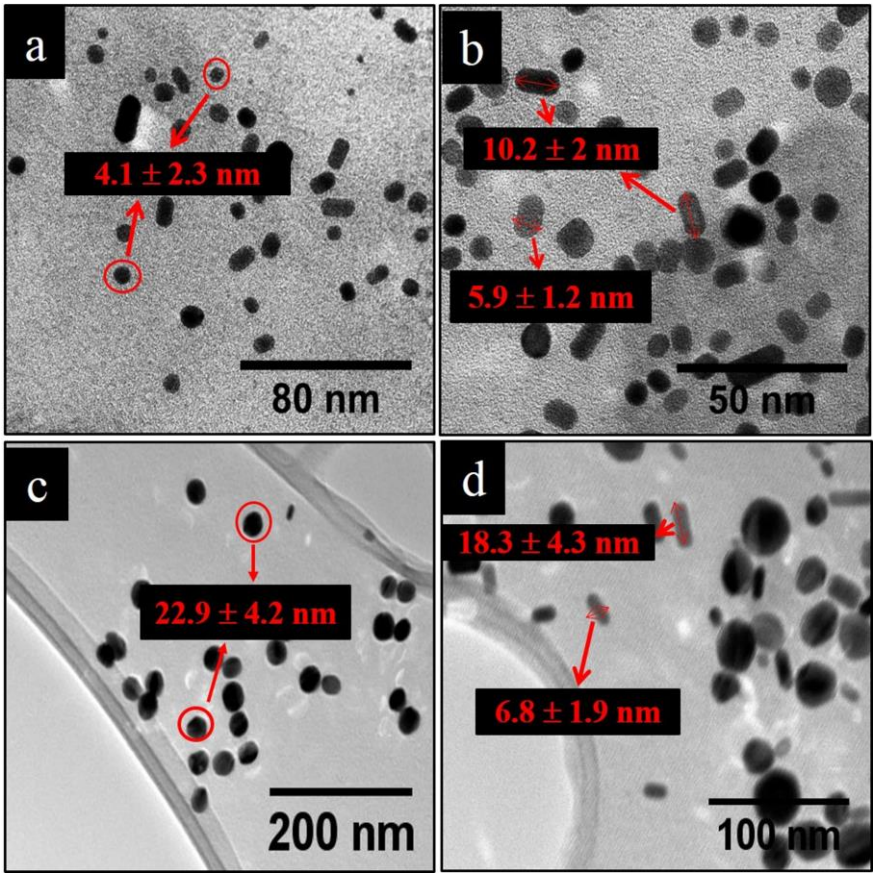

Figure 7.7. TEM images of gold nanorods; (a and b) without aging and (c and d) with aging, respectively.

7.3.2.2 UV-visible absorption analysis

The solution containing gold nanorod is a mixture of polydispersed gold nanospheres and gold nanorods that absorbed in the visible and infrared region, respectively (Fig. 7.8). Two intense absorption peaks were observed at 515 nm and 525 nm representing the transverse surface plasmon resonance modes of the non-aged and the aged gold nanorods. The redshift at a short wavelength is attributed to an increase in the size of the gold nanospheres with aging time as

shown from TEM images. Long wavelength bands were observed at 835 nm, 875 nm and 970 nm due to longitudinal SPR modes of the non-aged and the aged gold nanorods. The three band position indicated the presence of gold nanorods with varying aspect ratios in both non-aged and aged nanorod solutions. The localized surface plasmon resonance (LSPR) peak intensity was higher for the aged gold nanorod than for the non-aged gold nanorod solution. This can be attributed to the increase in the aspect ratio with aging time as corroborated by TEM. Theoretical calculations using El. Sayed *et.al.* model[72] of the maximum absorption based on the aspect ratio and medium dielectric function gave LSPR peak positions at 568 nm and 970 nm for the non-aged and aged sample respectively. However, the theoretical values differed with the experimental values due to the limitations of the theoretical calculations; the minimum nanorod width reported in literature is 20 nm while that in our study was 7 nm[73]. However, the peak at 525 nm is broad indicating the formation of nanospheres of different sizes which agrees with the AFM and TEM images. This implies that during the aging process, particle growth occurred by the coarsening of small spheres or rods to form larger particles. Consequently, seed aging affected the nucleation kinetics and particle growth mechanism through the Ostwald ripening. The formation of gold aggregates resulted in band shifts to higher wavelength due to self-assembly[74]. The aged gold nanorods showed a higher SPR effect as portrayed by the increased peak intensity. In the UV-visible plasmon spectra, an increase in intensity implies an increase in the surface plasmon resonance effect. Thus, aged gold nanorods were used for the study of their optoelectronic properties in organic solar cells.

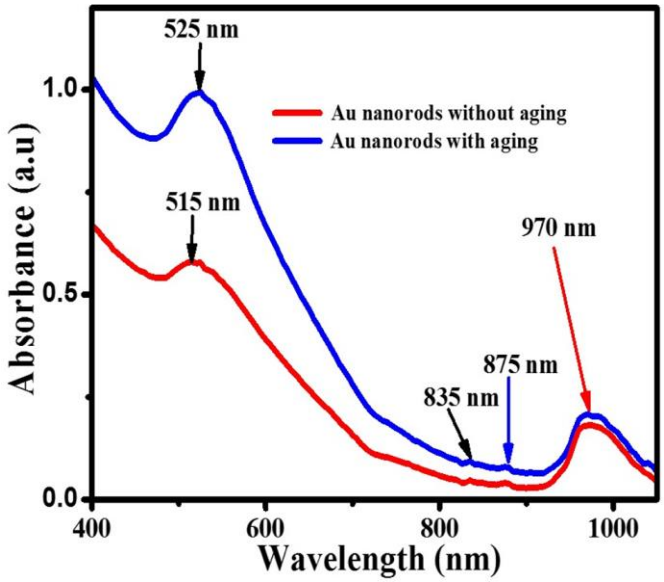

Figure 7.8. UV-visible absorption spectra of non-aged and aged gold nanorods.

7.3.2.3 AFM topographic analysis

The AFM images of the Au nanorod in PEDOT:PSS thin film show the presence of various sizes and shapes of the gold nanomaterials non-uniformly dispersed in the PEDOT:PSS matrix (Fig. 7.9). The calculated rms surface roughness was 86.2 nm and 73.7 nm for the PEDOT:PSS modified with Au nanorods with and without aging respectively. The surface roughness increased with increasing particle sizes from non-aged to aged gold nanorods. The large surface roughness of PEDOT:PSS with aged gold nanorods resulted from the presence of the large sizes of polydispersed nanospheres and nanorods as observed in the TEM images.

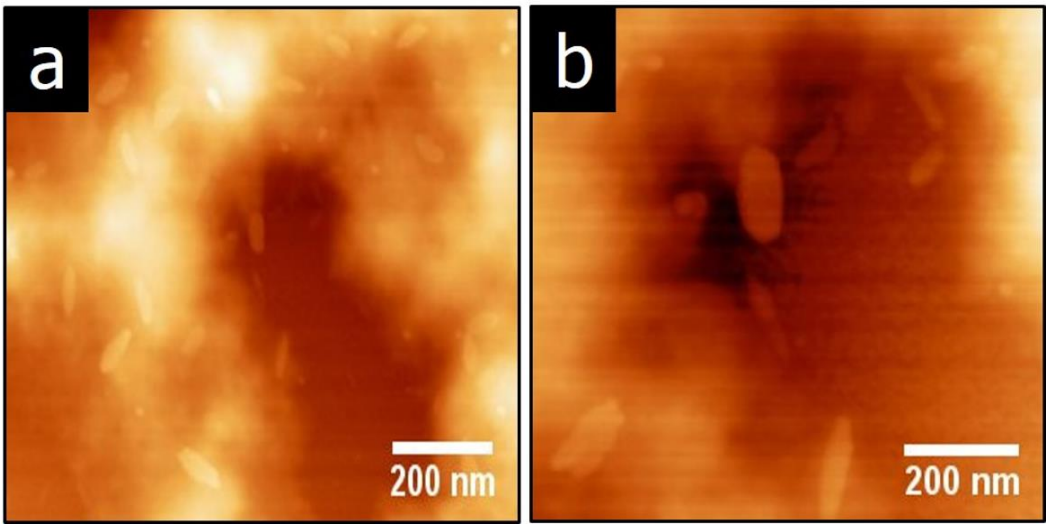

Figure 7.9. Atomic force microscopy (AFM) images of (a) PEDOT:PSS with non-aged Au nanorods and (b) PEDOT: PSS with aged Au nanorods, respectively.

7.3.3 Surface enhanced Raman spectroscopy (SERS) analysis

The surface enhanced Raman spectra were observed after modification of the PEDOT:PSS with gold nanospheres and nanorods. A characteristic change in intensity of the PEDOT:PSS peaks indicated the presence of a surface enhanced Raman spectroscopy effect (Fig. 7.10a and 7.10b). The SERS effect by noble metals is particle size dependent, with an increase in SERS intensity with increase in particle size[75-77]. However, an optimal particle size is achieved where an increase in the electromagnetic field leads to scattering thus reducing the overall SERS effect. Bands were observed at 1452, 1496 and 1570 cm^{-1} due to symmetric and asymmetric C-O stretch vibrations. A ring deformation mode was observed at 1259 cm^{-1} with C-O-C stretching bands observed at 989 and 1125 cm^{-1}. Bands at 438 cm^{-1} (SO_2 bending), 703 cm^{-1} (symmetric C-S-C stretch), 575 cm^{-1} and 852 cm^{-1} (oxyethylene ring deformation) were also observed. As expected, PEDOT:PSS modified with Au nanoparticles and nanorods also showed similar bands but with increased intensity[37]. To note: it was difficult to separate the bands exhibited by the Au nanospheres or Au nanorods in PEDOT:PSS as similar bands were observed in both cases. However, the gold nanorods exhibited an increase in SP bands intensity which corroborates with the additional longitudinal excitation modes observed in UV-vis data.

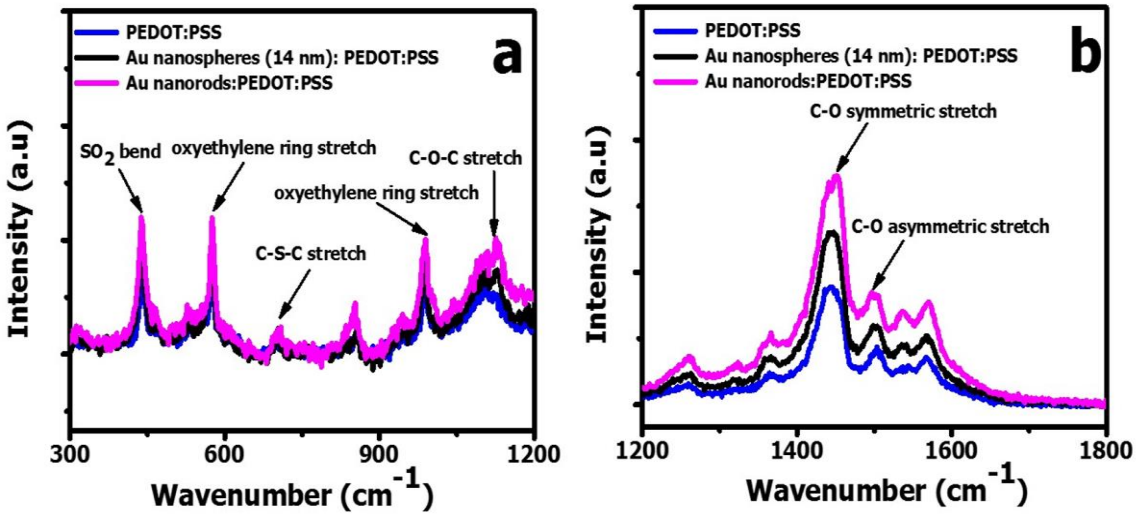

Figure 7.10. Surface enhanced Raman spectra of the pristine and modified PEDOT:PSS.

7.3.4 Current-voltage characteristics of the organic photovoltaic cell devices after incorporation gold nanospheres and nanorods into PEDOT: PSS

The current-voltage characteristics showed that relative to the gold nanorods, an increase in current density was obtained when monodispersed 14 ± 4 nm sized gold nanospheres were incorporated into the PEDOT:PSS (Fig. 7.11a). This could be attributed to the good dispersion of gold nanoparticles in the PEDOT:PSS solution as corroborated by AFM images. Also, the surface roughness of the device was less, (35.6 nm) when smaller sized Au nanospheres were incorporated into PEDOT:PSS matrix. The increase in current density and shunt resistance resulted in a 51% enhancement in the cell efficiency from 0.66% in the reference device to 1.00% in the device incorporated Au nanospheres (Table 7.1). Also, the open circuit voltage decreased in the device with Au nanoparticles of 14 nm showing a change in the interfacial energy levels of the device. In our study, the measurements were carried out in the ambient atmosphere and thus, lower efficiencies were reported relative to the measurements done under N_2 as reported in literature. For instance, Woo *et al.* incorporated gold nanoparticles into the PEDOT:PSS HTL layer and reported a PCE of 3.2% after annealing the films at 140°C for 20 min in a N_2 glovebox[78]. Similarly, Chen *et al.* reported a PCE of 3.89% on incorporating gold nanoparticles in PEDOT:PSS when devices were fabricated in a N_2 glovebox and measurements done after solvent annealing of the films[79].

A current density of 6.82 mA/cm^2 and a lower fill factor (20.08%) was obtained in the device incorporated with larger size gold nanoparticles (32 nm) (Table 7.1). This increase in fill factor could result from the increased interfacial surface area between the buffer layer and the active layer resulting in increased leakage currents. The current-voltage curves under illumination of the devices that incorporated the smaller sized gold nanospheres (14 nm, in blue) does not have an S-curve shape between 0.4 V and 0.6 V as observed for the larger Au nanospheres (32 nm, in red). This is confirmed by the shift in the curve positions relative to the x-axis as seen in the dark current semi-log plot of the current-voltage characteristics (Fig. 7.11b). In contrast, incorporation of gold nanorods into the PEDOT: PSS hole transport layer resulted in a decrease in current density and a consequent decrease in efficiency. This can be attributed to the higher values of series resistance (Table 7.1). Idealy it is required that the shunt resistance be several orders of magnitude larger than the series resistance for better FF and device perfomance.

The synthesis and growth of gold nanorods by a seed mediated method involves the use of CTAB, which acted as a nucleation site for the growth of nanorods from the gold seeds[80]. The presence of small amounts of CTAB on the gold nanorods surface during mixing with PEDOT:PSS may result in an inhomogeneous mixing of gold nanorods in the PEDOT:PSS matrix and the formation of a CTAB layer around Au nanorods that minimized charge transport. In addition, the surface roughness of the gold nanorods in PEDOT:PSS was high (86.2 nm) and could provide a pathway for electron-hole recombination resulting in increased leakage currents and hence a reduced device performance. In addition, due to the Au nanoparticles can be close to the P3HT:PCBM active layer matrix creating interfacial resistance and a barrier height at the metal-semiconductor interface. Consequently, a reduction in the J_{SC} and FF occurs due to leakage tunneling of charge carriers along /through the barrier leading to the formation of a S-shaped curved[81]. This is further confirmed by the non-linearity in the semilogarithmic plot of the dark current within an exponential regime (Fig. 7.11b magenta and red curves).

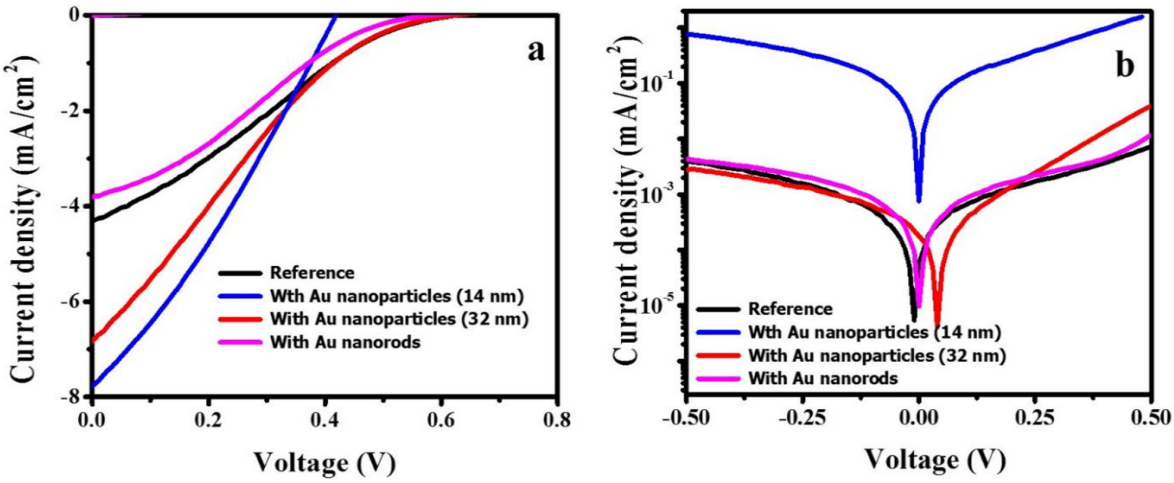

Figure 7.11. Current-Voltage characteristics of devices fabricated using gold nanoparticles and gold nanorods; (a) under illumination and (b) Semi-log current-voltage curve in the dark.

Table 7.1. Current-voltage characteristics of the devices modified with Au nanomaterials

Device Architecture	Jsc (mA/cm^2)	Voc (V)	FF (%)	R_S (ohms)	R_{SH} (ohms)	Efficiency (%)
ITO/PEDOT:PSS/P3HT:PCBM/Al	4.31	0.62	24.70	4.0×10^{-2}	9.0×10^{-2}	0.66
ITO/PEDOT:PSS:Au (14 nm)/P3HT:PCBM/Al	7.80	0.42	30.02	6.0×10^{-2}	1.8×10^{-1}	1.00
ITO/PEDOT:PSS:Au (32 nm)/P3HT:PCBM/Al	6.82	0.61	20.38	1.32×10^{-3}	5.0×10^{-4}	0.85
ITO/PEDOT:PSS:Au nanorods/P3HT:PCBM/Al	3.50	0.59	22.28	1.25×10^{4}	2.8×10^{1}	0.46

To obtain a good performance in a solar cell device, effective current generation, transport and current collection are paramount factors. A low series resistance, a high shunt resistance and low leakage currents are of considerable importance. However, factors such an increased surface roughness and the interfacial surface area can enhance or degrade the cell performance. An increase in surface roughness results in an increase in interfacial area between the buffer layer and active layer. This can create a hole transport pathway thus enhancing the overall device efficiency. On the other hand, a further increase in surface roughness may result in leakage currents, electron-hole recombination and greater series resistances which are detrimental to the

cell efficiency[82]. Fig. 7.12 shows a mechanism to elaborate the three factors that affect the conductivity mechanism of the hole transport layer incorporated with gold nanoparticles and gold nanorods. This scheme can rationalize our data.

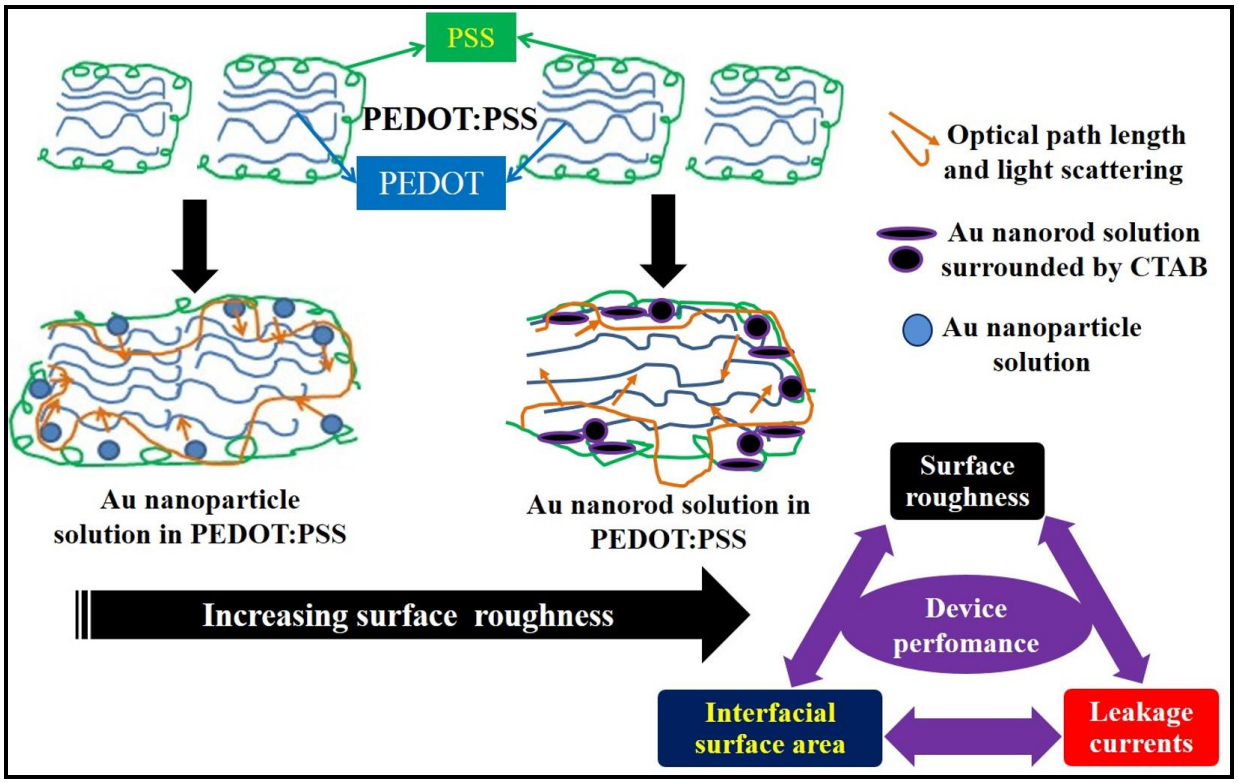

Figure 7.12. Plausible conductivity mechanism on incorporating gold nanomaterials in PEDOT:PSS.

The hole transport pathways increase with an increase in gold nanoparticle size and change in shape (for the case of Au nanorods). Incorporation of gold nanomaterials leads to increased surface roughness which increases the hole transport pathways in PEDOT:PSS and hence increased the current density and fill factors[53, 83]. This increase in conductive networks in PEDOT:PSS is due to a decreased resistance barrier for interchain hole transfer pathway. The interchain interactions lead to structural conformation changes that enhances the conductivity of PEDOT:PSS[84]. Interchain interactions of solvents or additives with PEDOT:PSS chains as reported in literature either increase or decrease the device conductivity[85, 86]. However, the

presence of an insulating material like CTAB or a larger Au particle size results in an increased leakage current that lowers the fill factor leading to a decrease in device efficiency. This study shows that gold enhances the electrical properties of organic photovoltaic devices.

7.4 Conclusions

Gold nanoparticles and gold nanorods were successfully obtained using a modified Turkevich method and a seed mediated method respectively. An increase in the volume ratio of gold precursor to citrate ratio increased the gold nanoparticle size. Aging of gold nanorods resulted in particle growth via a coarsening route which led to an increase in the nanorod aspect ratio. Improved short circuit current and cell efficiency were noted on incorporating gold nanospheres (14 nm) into the hole transport layer of the organic solar cell. However, the presence of larger size gold nanospheres (32 nm), gold nanorods and CTAB in PEDOT:PSS increased the surface roughness of PEDOT:PSS resulting in low fill factors. Size dependent optical absorption and a SERS effect were observed after incorporation of gold nanomaterials into the hole transport layer matrix.

References

1. Paolo, B.; Jer-Shing, H.; Bert, H. *Reports on Progress in Physics* **2012,** 75, (2), 024402.
2. Pérez-Juste, J.; Pastoriza-Santos, I.; Liz-Marzán, L. M.; Mulvaney, P. *Coordination Chemistry Reviews* **2005,** 249, (17–18), 1870-1901.
3. Chan, Y.-T.; Li, S.; Moorefield, C. N.; Wang, P.; Shreiner, C. D.; Newkome, G. R. *Chemistry – A European Journal* **2010,** 16, (14), 4164-4168.
4. Dujardin, E.; Hsin, L.-B.; Wang, C. R. C.; Mann, S. *Chemical Communications* **2001**, (14), 1264-1265.
5. Ye, X.; Jin, L.; Caglayan, H.; Chen, J.; Xing, G.; Zheng, C.; Doan-Nguyen, V.; Kang, Y.; Engheta, N.; Kagan, C. R.; Murray, C. B. *ACS Nano* **2012,** 6, (3), 2804-2817.
6. Thanh, N. T.; Maclean, N.; Mahiddine, S. *Chemical Reviews* **2014,** 114, (15), 7610-7630.
7. Abedini, A.; Daud, A. R.; Abdul Hamid, M. A.; Kamil Othman, N.; Saion, E. *Nanoscale Research Letters* **2013,** 8, (1), 474-474.
8. Wang, Z. L.; Mohamed, M. B.; Link, S.; El-Sayed, M. A. *Surface Science* **1999,** 440, (1–2), L809-L814.
9. Wang, Z. L.; Gao, R. P.; Nikoobakht, B.; El-Sayed, M. A. *The Journal of Physical Chemistry B* **2000,** 104, (23), 5417-5420.
10. Zhang, Q.; Han, L.; Jing, H.; Blom, D. A.; Lin, Y.; Xin, H. L.; Wang, H. *ACS Nano* **2016**.
11. Turkevich, J.; Stevenson, P. C.; Hillier, J. *Discussions of the Faraday Society* **1951,** 11, 55-75.
12. Frens, G. *Kolloid-Zeitschrift und Zeitschrift für Polymere* 250, (7), 736-741.
13. Thanh, N. T. K.; Maclean, N.; Mahiddine, S. *Chemical Reviews* **2014,** 114, (15), 7610-7630.
14. Zabetakis, K.; Ghann, W. E.; Kumar, S.; Daniel, M.-C. *Gold Bulletin* **2012,** 45, (4), 203-211.
15. Li, C.; Li, D.; Wan, G.; Xu, J.; Hou, W. *Nanoscale Research Letters* **2011,** 6, (1), 1-10.
16. Bastús, N. G.; Comenge, J.; Puntes, V. *Langmuir* **2011,** 27, (17), 11098-11105.
17. Guo, X.; Ye, W.; Zhu, R.; Wang, W.; Xie, F.; Sun, H.; Zhao, Q.; Ding, Y.; Yang, J. *Nanoscale* **2014,** 6, (20), 11732-11737.
18. Gao, C.; Zhang, Q.; Lu, Z.; Yin, Y. *Journal of the American Chemical Society* **2011,** 133, (49), 19706-19709.
19. Yu; Chang, S.-S.; Lee, C.-L.; Wang, C. R. C. *The Journal of Physical Chemistry B* **1997,** 101, (34), 6661-6664.
20. Kim, J.-Y.; Ah, C. S.; Jang, D.-J. *Journal of Nanomaterials* **2011,** 2011, 7.
21. Kim, F.; Song, J. H.; Yang, P. *Journal of the American Chemical Society* **2002,** 124, (48), 14316-14317.
22. Ward, C. J.; Tronndorf, R.; Eustes, A. S.; Auad, M. L.; Davis, E. W. *Journal of Nanomaterials* **2014,** 2014, 7.
23. Johnson, C. J.; Dujardin, E.; Davis, S. A.; Murphy, C. J.; Mann, S. *Journal of Materials Chemistry* **2002,** 12, (6), 1765-1770.
24. Gole, A.; Murphy, C. J. *Chemistry of Materials* **2004,** 16, (19), 3633-3640.
25. Koeppl, S.; Solenthaler, C.; Caseri, W.; Spolenak, R. *Journal of Nanomaterials* **2011,** 2011, 13.
26. Gou, L.; Murphy, C. J. *Chemistry of Materials* **2005,** 17, (14), 3668-3672.
27. Mie, G. *Annalen der Physik* **1908,** 25, (3), 377-445.
28. Papavassiliou, G. C. *Progress in Solid State Chemistry* **1979,** 12, (3–4), 185-271.
29. Huang, X.; El-Sayed, M. A. *Journal of Advanced Research* **2010,** 1, (1), 13-28.

30. Rayleigh, J. W. S. B., *On The Scattering of Light by Small Particles*. 1871.
31. Kreibig, U.; Fragstein, C. v. *Zeitschrift für Physik* **1969,** 224, (4), 307-323.
32. Jain, P. K.; Lee, K. S.; El-Sayed, I. H.; El-Sayed, M. A. *The Journal of Physical Chemistry B* **2006,** 110, (14), 7238-7248.
33. Liz-Marzán, L. M. *Materials Today* **2004,** 7, (2), 26-31.
34. Creighton, J. A.; Eadon, D. G. *Journal of the Chemical Society, Faraday Transactions* **1991,** 87, (24), 3881-3891.
35. Link, S.; El-Sayed, M. A. *The Journal of Physical Chemistry B* **1999,** 103, (21), 4212-4217.
36. Turkevich, J.; Garton, G.; Stevenson, P. C. *Journal of Colloid Science* **1954,** 9, 26-35.
37. Stavytska-Barba, M.; Kelley, A. M. *The Journal of Physical Chemistry C* **2010,** 114, (14), 6822-6830.
38. Niu, B. J.; Wu, L. L.; Tang, W.; Zhang, X. T.; Meng, Q. G. *CrystEngComm* **2011,** 13, (11), 3678-3681.
39. Brennan, L. J.; Purcell-Milton, F.; Salmeron, A. S.; Zhang, H.; Govorov, A. O.; Fedorov, A. V.; Gun'ko, Y. K. *Nanoscale Research Letters* **2015,** 10, 38.
40. Gordon, J. G.; Ernst, S. *Surface Science* **1980,** 101, (1), 499-506.
41. Patching, S. G. *Biochimica et Biophysica Acta (BBA) - Biomembranes* **2014,** 1838, (1, Part A), 43-55.
42. Homola, J.; Yee, S. S.; Gauglitz, G. *Sensors and Actuators B: Chemical* **1999,** 54, (1–2), 3-15.
43. Su, Y.-H.; Ke, Y.-F.; Cai, S.-L.; Yao, Q.-Y. *Light Science Applications* **2012,** 1, e14.
44. Costa de Oliveira, M.; Silveira Fraga, A.; #xe9; Luis; Thesing, A.; Lopes de Andrade, R.; Ferreira Leite Santos, J.; Jos; #xe9; Leite Santos, M. *Journal of Nanomaterials* **2015,** 2015, 9.
45. Blom, P.; De Jong, M.; Van Munster, M. *Physical Review B* **1997,** 55, (2), R656.
46. Li, G.; Shrotriya, V.; Yao, Y.; Yang, Y. *Journal of Applied Physics* **2005,** 98, (4), 043704.
47. Lunt, R. R.; Giebink, N. C.; Belak, A. A.; Benziger, J. B.; Forrest, S. R. *Journal of Applied Physics* **2009,** 105, (5), 053711.
48. Shahin, S.; Gangopadhyay, P.; Norwood, R. A. *Applied Physics Letters* **2012,** 101, (5), 053109.
49. Spyropoulos, G. D.; Stylianakis, M. M.; Stratakis, E.; Kymakis, E. *Applied Physics Letters* **2012,** 100, (21), 213904.
50. Wu, X.; Centeno, A.; Zhang, X.; Darvill, D.; Ryan, M. P.; Riley, D. J.; Alford, N. M.; Xie, F. *Solar Energy Materials and Solar Cells* **2015,** 138, (0), 80-85.
51. Kozanoglu, D.; Apaydin, D. H.; Cirpan, A.; Esenturk, E. N. *Organic Electronics* **2013,** 14, (7), 1720-1727.
52. Meen, T.-H.; Tsai, J.-K.; Chao, S.-M.; Lin, Y.-C.; Wu, T.-C.; Chang, T.-Y.; Ji, L.-W.; Water, W.; Chen, W.-R.; Tang, I. T.; Huang, C.-J. *Nanoscale Research Letters* **2013,** 8, (1), 450-450.
53. Aniket, R.; Richa, B.; Renu, P.; Rajiv, K. S. *Materials Research Express* **2014,** 1, (4), 045506.
54. Mahmoud, A. Y.; Izquierdo, R.; Truong, V.-V. *Journal of Nanomaterials* **2014,** 2014, 7.
55. Qiao, L.; Wang, D.; Zuo, L.; Ye, Y.; Qian, J.; Chen, H.; He, S. *Applied Energy* **2011,** 88, (3), 848-852.
56. Chuang, M.-K.; Lin, S.-W.; Chen, F.-C.; Chu, C.-W.; Hsu, C.-S. *Nanoscale* **2014,** 6, (3), 1573-1579.

57. Wadams, R. C.; Yen, C.-w.; Butcher Jr, D. P.; Koerner, H.; Durstock, M. F.; Fabris, L.; Tabor, C. E. *Organic Electronics* **2014,** 15, (7), 1448-1457.
58. Stratakis, E.; Kymakis, E. *Materials Today* **2013,** 16, (4), 133-146.
59. Wu, J.-L.; Chen, F.-C.; Hsiao, Y.-S.; Chien, F.-C.; Chen, P.; Kuo, C.-H.; Huang, M. H.; Hsu, C.-S. *ACS Nano* **2011,** 5, (2), 959-967.
60. Nikoobakht, B.; El-Sayed, M. A. *Chemistry of Materials* **2003,** 15, (10), 1957-1962.
61. Gao, J.; Bender, C. M.; Murphy, C. J. *Langmuir* **2003,** 19, (21), 9065-9070.
62. Young, J. K.; Lewinski, N. A.; Langsner, R. J.; Kennedy, L. C.; Satyanarayan, A.; Nammalvar, V.; Lin, A. Y.; Drezek, R. A. *Nanoscale Research Letters* **2011,** 6, (1), 1-11.
63. Ji, X.; Song, X.; Li, J.; Bai, Y.; Yang, W.; Peng, X. *Journal of the American Chemical Society* **2007,** 129, (45), 13939-13948.
64. Mohamed, M. B.; Volkov, V.; Link, S.; El-Sayed, M. A. *Chemical Physics Letters* **2000,** 317, (6), 517-523.
65. Leng, W.; Pati, P.; Vikesland, P. J. *Environmental Science: Nano* **2015,** 2, (5), 440-453.
66. Daniel, M.-C.; Astruc, D. *Chemical Reviews* **2004,** 104, (1), 293-346.
67. Liz-Marzán, L. M. *Langmuir* **2006,** 22, (1), 32-41.
68. Murphy, C. J.; Sau, T. K.; Gole, A. M.; Orendorff, C. J.; Gao, J.; Gou, L.; Hunyadi, S. E.; Li, T. *The Journal of Physical Chemistry B* **2005,** 109, (29), 13857-13870.
69. Bode, A. M.; Cunningham, L.; Rose, R. C. *Clinical Chemistry* **1990,** 36, (10), 1807-9.
70. Nikoobakht, B.; El-Sayed, M. A. *Langmuir* **2001,** 17, (20), 6368-6374.
71. Shields, S. P.; Richards, V. N.; Buhro, W. E. *Chemistry of Materials* **2010,** 22, (10), 3212-3225.
72. Link, S.; Mohamed, M.; El-Sayed, M. *The Journal of Physical Chemistry B* **1999,** 103, (16), 3073-3077.
73. Ungureanu, C.; Rayavarapu, R. G.; Manohar, S.; van Leeuwen, T. G. *Journal of Applied Physics* **2009,** 105, (10), 102032.
74. Wang, S.; Qian, K.; Bi, X.; Huang, W. *The Journal of Physical Chemistry C* **2009,** 113, (16), 6505-6510.
75. Hong, S.; Li, X. *Journal of Nanomaterials* **2013,** 2013, 9.
76. Seney, C. S.; Gutzman, B. M.; Goddard, R. H. *The Journal of Physical Chemistry C* **2009,** 113, (1), 74-80.
77. Boca, S. C.; Farcau, C.; Astilean, S. *Nuclear Instruments and Methods in Physics Research Section B: Beam Interactions with Materials and Atoms* **2009,** 267, (2), 406-410.
78. Woo, S.; Jeong, J. H.; Lyu, H. K.; Han, Y. S.; Kim, Y. *Nanoscale Research Letters* **2012,** 7, (1), 641-641.
79. Chen, F.-C.; Wu, J.-L.; Lee, C.-L.; Hong, Y.; Kuo, C.-H.; Huang, M. H. *Applied Physics Letters* **2009,** 95, (1), 013305.
80. Leonov, A. P.; Zheng, J.; Clogston, J. D.; Stern, S. T.; Patri, A. K.; Wei, A. *ACS Nano* **2008,** 2, (12), 2481-2488.
81. Finck, B. Y.; Schwartz, B. J. *Applied Physics Letters* **2013,** 103, (5), 053306.
82. Proctor, C. M.; Nguyen, T.-Q. *Applied Physics Letters* **2015,** 106, (8), 083301.
83. Woo, S.; Jeong, J. H.; Lyu, H. K.; Han, Y. S.; Kim, Y. *Nanoscale Research Letters* **2012,** 7, (1), 1-6.
84. Ouyang, J.; Chu, C. W.; Chen, F. C.; Xu, Q.; Yang, Y. *Advanced Functional Materials* **2005,** 15, (2), 203-208.
85. Hu, Z.; Zhang, J.; Zhu, Y. *Renewable Energy* **2014,** 62, 100-105.

86. Alemu, D.; Wei, H.-Y.; Ho, K.-C.; Chu, C.-W. *Energy & Environmental Science* **2012,** 5, (11), 9662-9671.

CHAPTER 8

Improvement of an Organic Photovoltaic Device Performance by P3HT:PCBM Solution Heat Treatment

8.1 Introduction

Organic solar cells are devices that convert solar energy into electrical energy using semiconducting polymers. Semiconducting polymers, in particular, poly-alkylthiophenes and fullerenes, have been used extensively as electron donors and acceptors, respectively in organic photovoltaic devices[1-3]. The unique advantages of organic photovoltaic devices such as low cost, flexibility, solution process ability and low temperature synthesis have led to these devices being considered as potential alternatives in commercial electronic applications[4]. However, their low photoconversion efficiency and limited device stability hinders their commercialization. These devices are based on a bulk heterojunction (BHJ) approach that maximizes the donor-acceptor interfacial area. In a BHJ, the active layer comprises of an interpenetrating network of p-type donor and n-type acceptor molecules represented by P3HT and PCBM[5]. The most extensively used device configuration for a BHJ organic solar cell consists of an active layer sandwiched between a low work function Al cathode and a hole conducting PEDOT:PSS layer on top of an indium tin oxide substrate[3, 6] (Fig. 8.1). Based on the a modified P3HT:PCBM triple junction system, a PCE greater than 11% has been achieved[7].

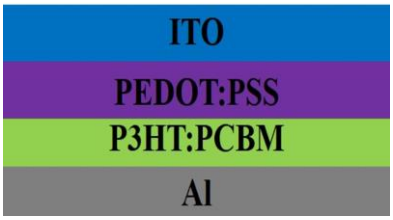

Figure 8.1. A typical BHJ organic solar cell.

Extensive research efforts have been devoted to improving the power conversion efficiency (PCE) of organic photovoltaic devices. These strategies can be characterized by two pronged approaches;

F. Otieno, B.K. Mutuma*, K. Ranganathan, M. Airo, R. Erasmus, N. J. Coville, D. Wamwangi " Enhanced Organic Photovoltaic Device Performance by Solution Heat Treatment", Thin solid films, 2016 (under review).*

- Firstly, through material modification, this process entails the incorporation of new additional blend component that enhances the optical absorption to utilize a greater proportion of the solar emission spectrum by using a lower band gap material. This material based strategy attempts to modify exciton generation and charge transport of the device[8].
- Secondly, through a process based modification to alter the morphology of the polymer blend. The variation of the kinetics of diffusion of the polymer and fullerene significantly improve the exciton generation and diffusion to the interface. Furthermore, it is expected that an increased donor-acceptor interface area enhances charge separation and transport. The exciton diffusion length in polymers is short (10~20 nm) hence short pathways are needed for an efficient charge transport[3].

Thermal annealing of the P3HT:PCBM blend film has been proposed to increase the optical, electronic[9, 10] and nanomechanical properties[11] of organic polymer solar cells. Most research has focused on post-thermal annealing of P3HT:PCBM films[12, 13] and solvent vapor annealing[9, 14-17] as a way to enhance the performance of P3HT:PCBM based solar cells through nanoscale morphology modification. Other methods such as varying the solvents used for films preparation[18] have been employed in the quest to obtain good polymer miscibility. Heat treatment of P3HT:PCBM influences the ordering of the P3HT by varying its hole mobility properties[19] thus, leading to an increased cell efficiency[20-22]. Usually, the charge transport and separation in organic solar cells is highly dependent on the interphase segregation and diffusion of the electron acceptor (PCBM) and the electron donor (P3HT). Good segregation of P3HT and PCBM is influenced by P3HT crystallization and the diffusion of PCBM during thermal annealing of P3HT:PCBM films[23]. In particular, the ordering of P3HT in the fullerene matrix is a critical factor that affects the efficiency of an organic photovoltaic device during solution processing of the active layer. In this study, the kinetics and energetics of solution heating of P3HT on the nanoscale morphology and properties of a solar cell device are investigated. Furthermore, these diffusion mechanisms are compared to the effect of heating of a P3HT:PCBM blend solution.

F. Otieno, B.K. Mutuma*, K. Ranganathan, M. Airo, R. Erasmus, N. J. Coville, D. Wamwangi " Enhanced Organic Photovoltaic Device Performance by Solution Heat Treatment", Thin solid films, 2016 (under review).*

8.2 Experimental

The devices were fabricated on top of ITO-coated substrates. The ITO coated glass was cleaned in an ultrasonic bath containing distilled water-acetone-ethanol solutions and the residual solvent was removed by a stream of nitrogen gas. A hole transporting layer, PEDOT:PSS was then spin coated onto the ITO coated glass substrate at 2000 rpm for 60 seconds. The resulting film was dried on a hot plate at 100 ºC for 15 min to remove any residual water. To prepare the active layer solutions, two sets of P3HT and PCBM samples (10 mg each) were separately dissolved in 0.5 mL of chlorobenzene (C_6H_5Cl) and stirred in ambient conditions for 3 h at 40 ºC (Fig. 8.2a, b). One set of P3HT and PCBM solution was mixed and stirred for 2 h before heating the blend solutions at 70 ºC for 1 min (Fig. 8.2c). The heated solutions were kept at room temperature for 5 min before spin coating. The pristine P3HT:PCBM blend solution (i.e. without any heat treatment) is referred as pr-P3HT:PCBM and the heat treated P3HT:PCBM blend is referred as ht-P3HT:PCBM respectively. Similarly, the pristine P3HT and heat treated P3HT solutions are referred to as pr-P3HT and ht-P3HT respectively. In another set of experiment, a P3HT solution was first heated for 1 min at 70 ºC before mixing it with PCBM and the blend was then stirred for 2 h; this sample is referred to as P3HT:PCBM using ht-P3HT.

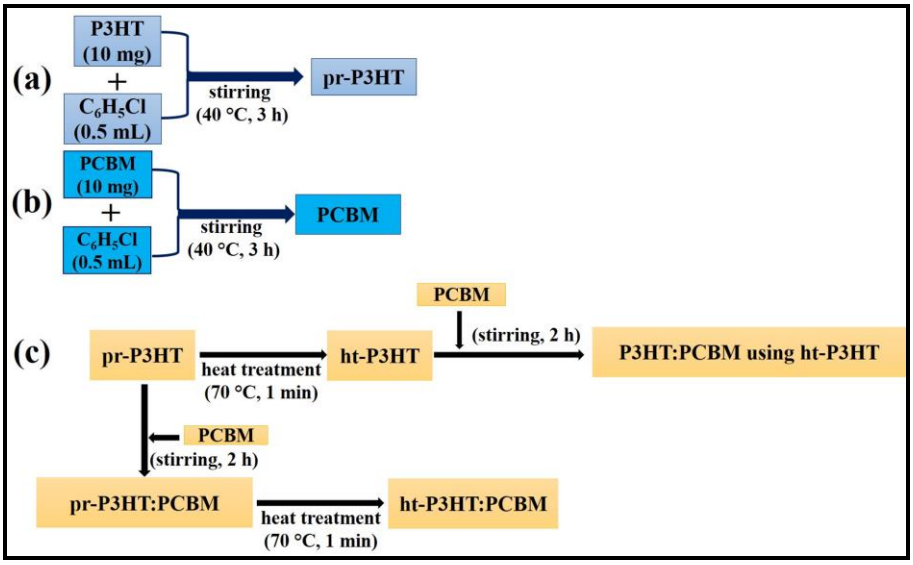

Figure 8.2. A schematic diagram showing the preparation of (a) pr-P3HT, (b) PCBM and (c) P3HT:PCBM solutions, respectively.

F. Otieno, B.K. Mutuma*, K. Ranganathan, M. Airo, R. Erasmus, N. J. Coville, D. Wamwangi " Enhanced Organic Photovoltaic Device Performance by Solution Heat Treatment", Thin solid films, 2016 (under review).*

The active layer was then spin coated at 2000 rpm on top of a dried PEDOT:PSS thin film. The cathode was metalized by thermal evaporation of aluminum. Optical absorption measurements of the film blends were made using a Cary 500 UV–visible spectrometer. The morphology of the films were studied using atomic force microscopy (Veeco Di3100 AFM) in tapping mode. The morphology was further ascertained by transmission electron microscopy (TEM) using a FEI Technai G2 spirit electron microscope at 120 keV equipped with an energy-dispersive X-ray spectroscopy detector (EDX). A Jobin Yvon T64000 Raman spectrometer equipped with an Ar ion laser (514.5 nm) and a laser power of 5 mW was used to examine the vibrational bands of the polymer blend. Photoluminescence (PL) measurements were carried out using a Varian PL spectrophotometer at a wavelength of 458 nm. The pristine and heat treated solutions of P3HT and P3HT:PCBM were spin coated on a glass substrate and PL measurements carried out on the films. The current density–voltage (J–V) characteristics were obtained using a HP 4141B source measure unit under 100 mW/cm^2 illumination (AM 1.5G) generated with a Newport xenon-lamp solar simulator. All the measurements were carried out at room temperature under standard conditions. The results obtained from the devices (more than 60 devices) fabricated and characterized showed a high degree of repeatability. The performance of the devices was also compared to a standard reference device made of P3HT:PCBM blend stirred for 5 h using a low heat treatment (about 40 ºC).

8.3 Results and discussion

8.3.1 Morphology

The AFM images of pr-P3HT and ht-P3HT solutions spin coated on top of PEDOT:PSS are shown in Fig. 8.3. The pr-P3HT (Fig. 8.3a) formed an inhomogeneous film with a surface root square (rms) roughness of 74.0 nm. The ht-P3HT solution changed color from brown to orange on heating and the homogeneous film obtained had a rms of 63.0 nm in the scanned surface area of 0.07 μm^2 (Fig. 8.3b). This decrease in rms is attributed to the increased solubility of P3HT in chlorobenzene solvent upon heat treatment. The EDX spectra show no oxidation in pr-P3HT but some slight oxidation (presence of oxygen) in ht-P3HT (Fig. 8.4).

F. Otieno, B.K. Mutuma*, K. Ranganathan, M. Airo, R. Erasmus, N. J. Coville, D. Wamwangi " Enhanced Organic Photovoltaic Device Performance by Solution Heat Treatment", Thin solid films, 2016 (under review).*

The inhomogeneous and uniform morphology of the pr-P3HT and ht-P3HT films was ascertained from the TEM images, respectively (inset Fig. 8.4).

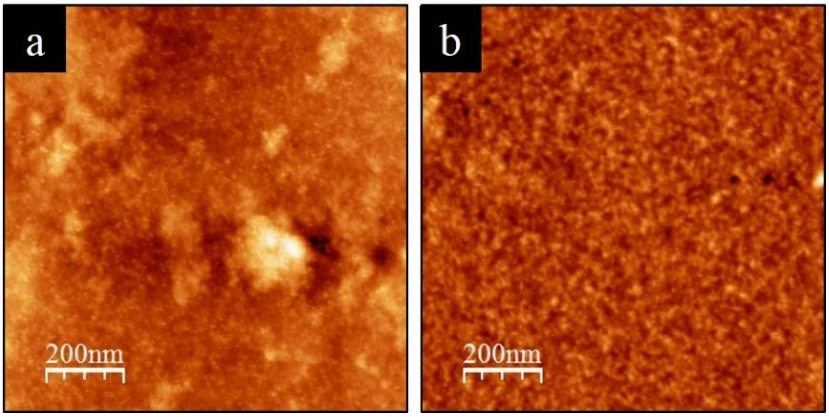

Figure 8.3. Morphology of spin coated P3HT films (a) pr-P3HT and (b) ht-P3HT, respectively.

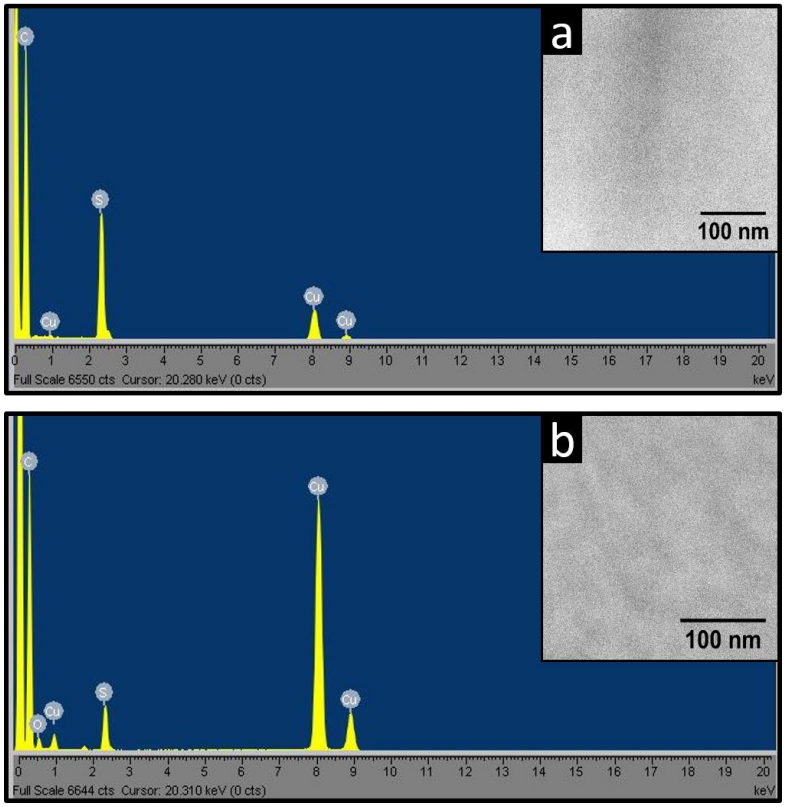

Figure 8.4. Energy-dispersive X-ray (EDX) spectra of: (a) pr-P3HT and (b) ht-P3HT with insets (TEM images), respectively.

F. Otieno, B.K. Mutuma*, K. Ranganathan, M. Airo, R. Erasmus, N. J. Coville, D. Wamwangi " Enhanced Organic Photovoltaic Device Performance by Solution Heat Treatment", Thin solid films, 2016 (under review).*

Fig. 8.5a compares the AFM images of a pr-P3HT:PCBM and a ht-P3HT:PCBM blend spin coated on top of PEDOT:PSS. An inhomogeneous film was observed in pr-P3HT:PCBM and upon heat treatment PCBM diffused into P3HT and it became evenly dispersed in the P3HT matrix (Fig. 8.5b and 8.5c). The measured surface rms roughness of the obtained films was 35 nm, 60 nm and 64 nm for the pr-P3HT:PCBM, ht-P3HT:PCBM and P3HT:PCBM using ht-P3HT respectively. Heat treatment caused the PCBM molecules to diffuse readily inside the P3HT thus, causing the roughness of the P3HT:PCBM film to increase substantially[24]. To note: heating of the blend solution resulted in a color change, from orange to purple. The change in color during the heat treatment corresponds to the diffusion of PCBM into P3HT matrix with no PCBM aggregation at the low temperature used (< 140 ºC)[25, 26]. Also, during the heat treatment, P3HT is ordered in the blend solution and thus results in its reorientation in the P3HT:PCBM blend[27]. Fig. 8.5c shows that a non-homogenous film was formed in the P3HT:PCBM using ht-P3HT. The evidence of inhomogeneity is an indication of the non-uniform dispersion of the PCBM into the crystalline P3HT matrix. However, a greater dispersion was attained when PCBM diffused in the disordered P3HT in the ht-P3HT:PCBM blend.

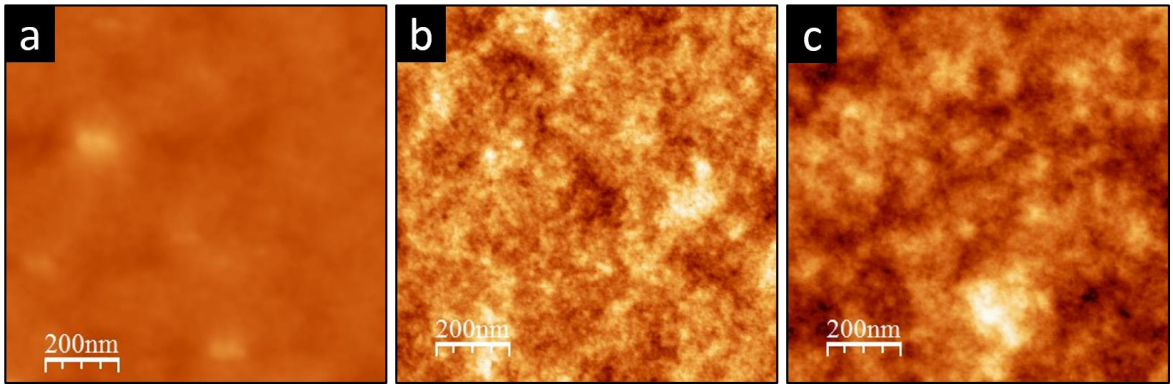

Figure 8.5. Morphology of spin coated P3HT:PCBM films (a) pr-P3HT:PCBM (b) ht-P3HT:PCBM and (c) P3HT:PCBM using ht-P3HT, respectively.

8.3.2 Optical characteristics

Fig. 8.6 shows the effect of heat treatment on the absorption spectra of the two types of P3HT films and the P3HT:PCBM blends spin coated onto the ITO coated glass substrates

F. Otieno, B.K. Mutuma*, K. Ranganathan, M. Airo, R. Erasmus, N. J. Coville, D. Wamwangi " Enhanced Organic Photovoltaic Device Performance by Solution Heat Treatment", Thin solid films, 2016 (under review).*

with their respective UV-vis absorption band positions shown in Table 8.1. The main absorption peak for P3HT was observed at 525 nm (Fig. 8.6a; shown by x) due to π - π^* transition[28], with two vibronic shoulder absorption peaks at 555 nm and 605 nm (#) in both ht-P3HT and pr-P3HT respectively. The peak at 550 nm corresponds to the P3HT extended conjugation[29] while that above 600 nm is attributed to interchain P3HT stacking[19]. An increased intensity of the P3HT peak at 525 nm of 1.48 ($I_{ht\text{-}P3HT}/I_{pr\text{-}P3HT}$) upon heat treatment can be due to an increase in P3HT crystallinity[30]. The increase in optical absorption at $\lambda < 650$ nm could lead to improved exciton dissociation and charge carrier transport. It is noted that annealing does not seem to have any effect on the PCBM as these absorption features (< 400 nm) do not change significantly (Fig. 8.6b indicated by Δ). This indicates that the nanoscale morphological transformation could be due to the structural ordering of P3HT.

Fig. 8.6b shows the absorption spectra of the P3HT:PCBM blend films. In all the blend films, an absorption peak was observed at 334 nm characteristic of PCBM[31]. Three absorption peaks attributed to P3HT were observed between 500 nm and 650 nm (Table 8.1). For the pr-P3HT:PCBM blend, the film shows a strong, broad absorption at 511 nm with shoulders at 557 nm and 602 nm (#). In P3HT:PCBM using ht-P3HT, the absorption peak at 511 nm is blue shifted to 507 nm and the two shoulder peaks were observed at 551 nm and 602 nm respectively. In the ht-P3HT:PCBM blend, the absorption peak red shifted to 513 nm and had a higher intensity; with the shoulder peaks observed at 554 nm and 606 nm respectively. This enhanced absorption corresponds to a vibronic effect that leads to an increased ordering of the interchain interaction in the P3HT and the rearrangement of PCBM into the P3HT matrix[32]. These results arose from the presence of delocalized conjugated electrons that lowered the band gap between π and π^* orbitals, and increased the optical π - π^* transition which led to a redshift observed in the peak absorption wavelength[33, 34].

F. Otieno, B.K. Mutuma*, K. Ranganathan, M. Airo, R. Erasmus, N. J. Coville, D. Wamwangi " Enhanced Organic Photovoltaic Device Performance by Solution Heat Treatment", Thin solid films, 2016 (under review).*

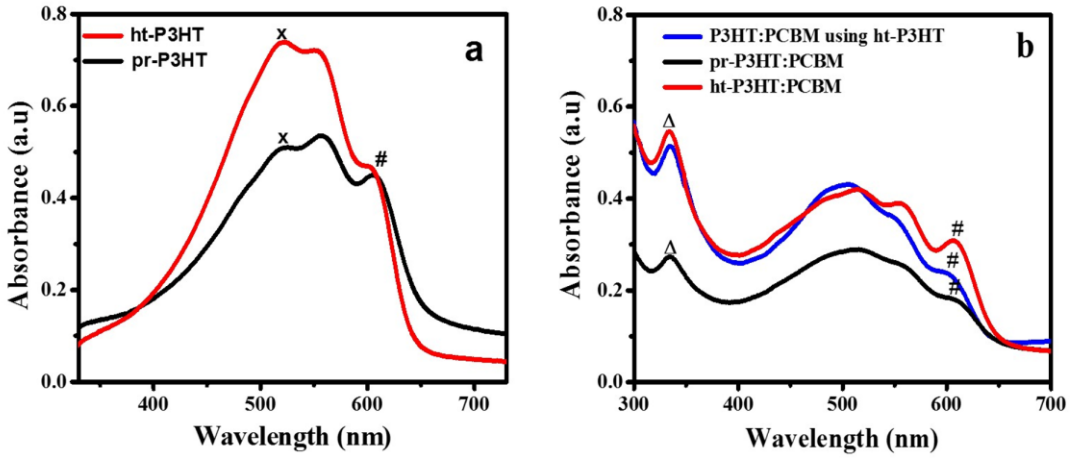

Figure 8.6. UV-visible absorption spectra of (a) P3HT films and (b) P3HT: PCBM films before and after heat treatment. The (Δ) marks the PCBM absorption peak and (#) marks the P3HT absorption peak at 600 nm.

Table 8.1. UV-visible absorption bands in P3HT:PCBM films

Description	Band position (cm^{-1})	Band position (cm^{-1})	Band position (cm^{-1})	Band position (cm^{-1})
pr-P3HT:PCBM	334	511	557	602
P3HT:PCBM using ht-P3HT	334	507	551	602
ht-P3HT:PCBM	334	513	554	606

8.3.3 Fourier transform infrared spectroscopy (FTIR)

The molecular structure and charge transfer of P3HT:PCBM solutions were studied by FTIR spectroscopy. Fig. 8.7 shows the FTIR spectra of the P3HT:PCBM blend solutions. In pr-P3HT:PCBM, bands were observed at 2886, 2975, 3070 cm^{-1} due to CH_2 out of phase, CH_2 in phase and CH_3 asymmetric stretching modes respectively. A symmetric ring stretching mode was observed at 1147 cm^{-1} with C-O-S stretching bands observed at 724 cm^{-1}. Bands at 1440-1480 cm^{-1} (symmetric ring stretching), 1583 cm^{-1} (asymmetric ring vibration), 1377 cm^{-1} (methyl deformation) and 1082 cm^{-1} (C-H bending) were also observed. As expected the ht-P3HT:PCBM blend also showed similar bands with very slight changes[35].

F. Otieno, B.K. Mutuma*, K. Ranganathan, M. Airo, R. Erasmus, N. J. Coville, D. Wamwangi " Enhanced Organic Photovoltaic Device Performance by Solution Heat Treatment", Thin solid films, 2016 (under review).*

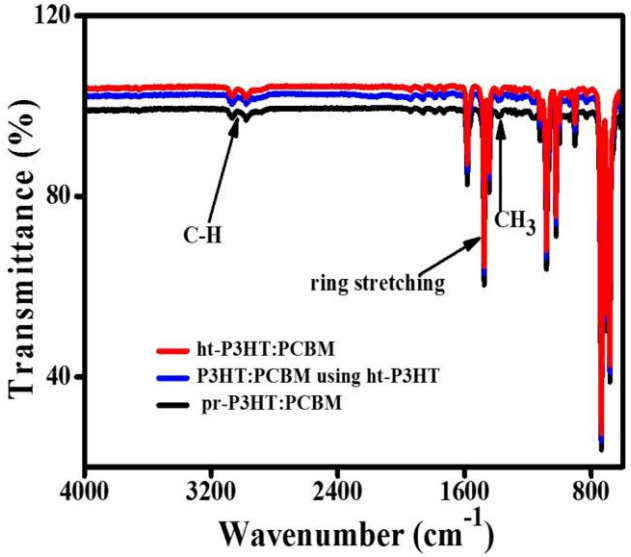

Figure 8.7. FTIR spectra of pristine and heat treated P3HT:PCBM blends in solution.

8.3.4 Raman spectroscopy

The Raman spectra of the 5 samples are shown in Fig. 8.8. Differences in peak intensities for both the pristine and heat treated films of the P3HT and P3HT:PCBM blends was observed. In all the films, bands at 1447.5 cm^{-1} (C=C antisymmetric stretch), at 1378 cm^{-1} (C-C stretch), 1190 cm^{-1} (inter-ring stretch), 1107 cm^{-1} (C-H bending) and 728 cm^{-1} the (C-S-C bands) were observed. Fig. 8.8a shows the Raman spectra of pr-P3HT and ht-P3HT films with an increased Raman intensity at 1447.5 cm^{-1} (C=C asymmetric stretch) after heat treatment. Fig. 8.8b shows the Raman spectra of the P3HT:PCBM films where an increase in the intensity of the same peak (C=C), was observed in P3HT:PCBM using ht-P3HT and in ht-P3HT:PCBM relative to the pr-P3HT:PCBM films respectively. This could be attributed to an increase in P3HT ordering after heat treatment[30, 32]. The P3HT:PCBM using ht-P3HT had a lower peak intensity than the ht-P3HT:PCBM film. This could be attributed to a decreased dispersion of PCBM into the already ordered P3HT matrix. In contrast, in ht-P3HT:PCBM a simultaneous diffusion of PCBM into the P3HT matrix and an increased P3HT ordering contributed to the change in peak intensity[36]. Also, a change in full width half maxima (FWHM) in the ht-P3HT:PCBM films was observed representing a change in the polymer ordering during the solution heat treatment. The ht-P3HT:PCBM film showed a narrower

F. Otieno, B.K. Mutuma*, K. Ranganathan, M. Airo, R. Erasmus, N. J. Coville, D. Wamwangi " Enhanced Organic Photovoltaic Device Performance by Solution Heat Treatment", Thin solid films, 2016 (under review).*

FWHM (29.63 ± 0.03 cm^{-1}) than the pr-P3HT:PCBM (32.48 ± 0.04 cm^{-1}) at 1447.5 cm^{-1} due to the presence of the ordered P3HT segments[37].

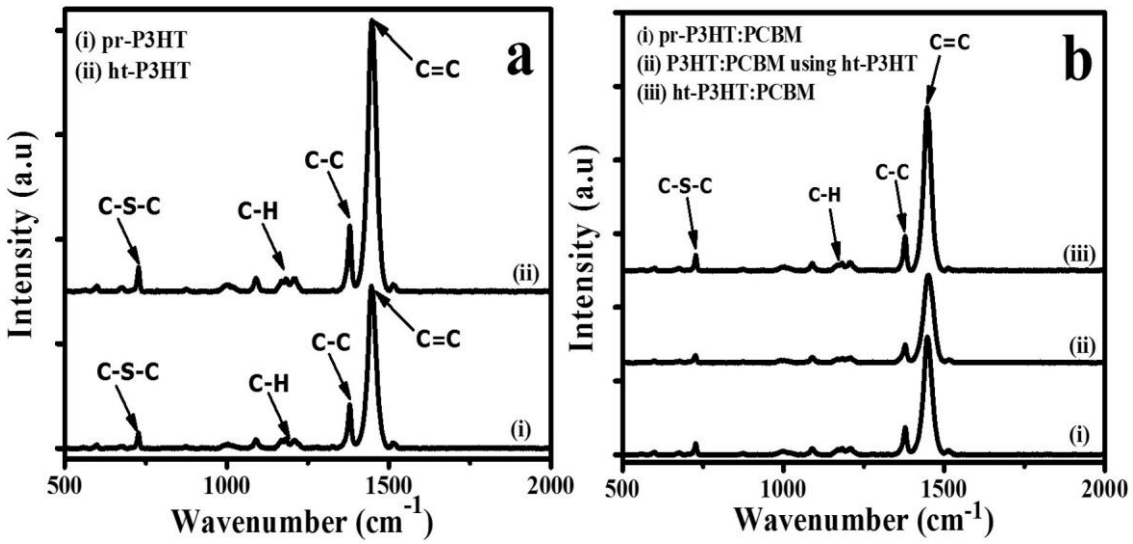

Figure 8.8. Raman spectra of (a) P3HT films and (b) P3HT: PCBM films before and after heat treatment.

8.3.5 Photoluminescence analysis

8.3.5.1 Photoluminescence analysis of the P3HT and P3HT:PCBM solutions

Conjugated thiophene photoluminescence (PL) spectra are known to arise from radiative recombination of polariton-exciton pairs into Frank-Condon (FC) states and the polaron excitation binding energy[38, 39]. Bulk heterojunction photoluminescence quenching is a powerful indication of the degree of exciton dissociation. Figs. 8.9a and 8.9b show the photoluminescence spectra of solutions of the prepared P3HT and P3HT:PCBM blends. Fig 8.9a shows the PL spectra of the pr-P3HT solution with the main peak observed at 637 nm. Heat treatment of the P3HT solution resulted in a decreased PL emission intensity in both ht-P3HT solution and film and a prominent vibronic structure in (Table 8.2). This can be attributed to an improved P3HT ordering upon heat treatment[32] and thus, an increase in the delocalized photoexcitation[40] that led to a reduced PL intensity[41]. Photoluminescence quenching was observed in the heat treated P3HT:PCBM solutions (Fig. 8.9b). However, in the solution of P3HT:PCBM using ht-P3HT, a blue shifted emission peak at 583 nm relative

F. Otieno, B.K. Mutuma*, K. Ranganathan, M. Airo, R. Erasmus, N. J. Coville, D. Wamwangi " Enhanced Organic Photovoltaic Device Performance by Solution Heat Treatment", Thin solid films, 2016 (under review).*

to the pr-P3HT:PCBM and ht-P3HT:PCBM solutions was observed (Fig. 8.9a). This shows that a limited charge transfer occurred from ht-P3HT to PCBM.

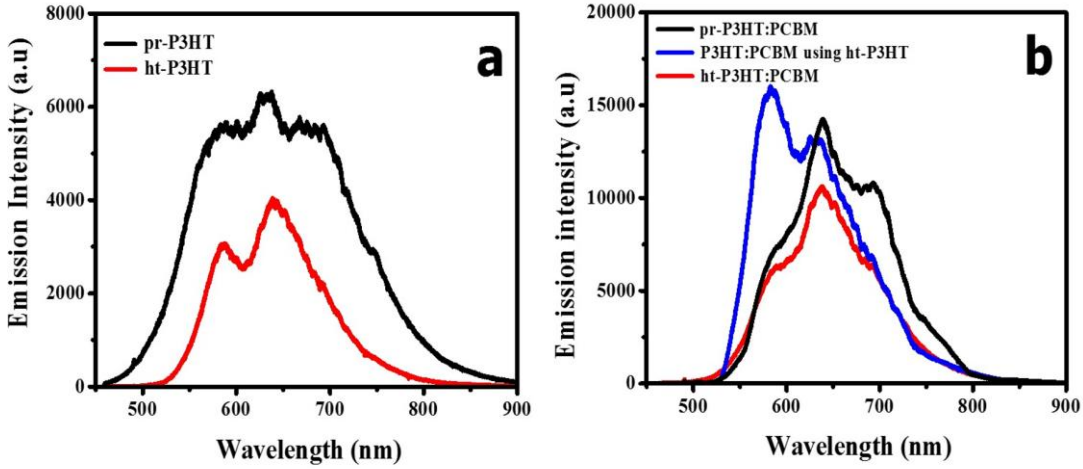

Figure 8.9. Photoluminescence spectra of as prepared and heat treated (a) P3HT and (b) P3HT:PCBM blends in solution.

Table 8.2. PL spectra properties of P3HT and P3HT:PCBM solutions and films

Description	Solutions		Films	
	Max (cm^{-1})	Max (cm^{-1})	Max (cm^{-1})	Max (cm^{-1})
pr-P3HT	637	-	647	694
ht-P3HT	586	639	652	695
pr-P3HT:PCBM	638	692	643	693
P3HT:PCBM using ht-P3HT	583	625	638	700
ht-P3HT:PCBM	593	638	638	708

F. Otieno, B.K. Mutuma*, K. Ranganathan, M. Airo, R. Erasmus, N. J. Coville, D. Wamwangi " Enhanced Organic Photovoltaic Device Performance by Solution Heat Treatment", Thin solid films, 2016 (under review).*

8.3.5.2 Photoluminescence analysis of the P3HT and P3HT:PCBM films

To determine if the PL spectra of the P3HT and P3HT:PCBM solutions varied after film formation; the PL spectra of the as prepared and heat treated P3HT and P3HT:PCBM films was recorded in Fig. 8.10. In the pr-P3HT film, the 637 peak redshifted to 647 nm and this corresponds to band to band emission of the P3HT since its band gap is approximately 1.9 eV[42]. The red shifted peak observed at 694 nm could be attributed to Franck –Condon states leading to a possible polaron exciton binding energy of ~0.13 eV. The PL emission at λ>700 nm could correspond to the transitions between the Frank-Condon states and mid bandgap states associated with the disorder in P3HT. Similarly, the peaks observed in ht-P3HT solution at 586 nm and 639 nm redshifted to 652 nm and 695 nm respectively in the ht-P3HT film (Fig. 8.10a). This change can be attributed to P3HT interchain excited states and symmetry in solid state films resulting in an increase in conjugation length and planarity[43, 44].

Analogous to the solutions, a decrease in PL intensities was observed in the films of P3HT:PCBM after heat treatment (Fig. 8.10b). This can be attributed to a charge transfer and good exciton dissociation in agreement with the literature[45, 46]. The PL of P3HT in P3HT:PCBM is almost completely quenched indicating a close contact between P3HT and PCBM and a sufficient exciton dissociation[47]. This agrees with the Raman spectral data that portrays limited diffusion of PCBM into the highly crystalline P3HT matrix resulting in limited charge transfer and hence a lower PL intensity. The broadening in the thin films is due to the presence of mid band gap states ascribed to disorder.

F. Otieno, B.K. Mutuma*, K. Ranganathan, M. Airo, R. Erasmus, N. J. Coville, D. Wamwangi " Enhanced Organic Photovoltaic Device Performance by Solution Heat Treatment", Thin solid films, 2016 (under review).*

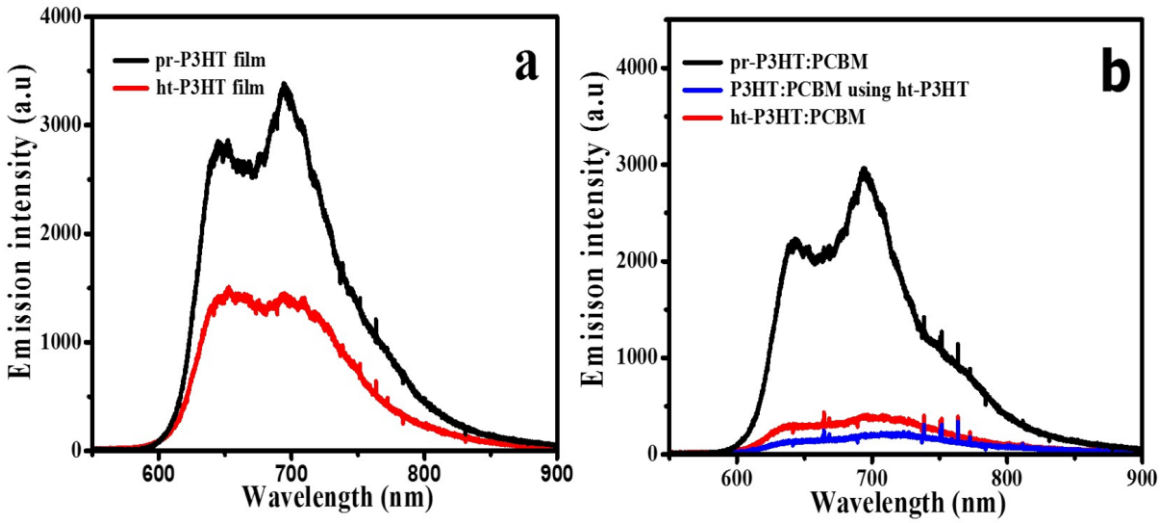

Figure 8.10. Photoluminescence spectra of as prepared and heat treated (a) P3HT and (b) P3HT:PCBM films, respectively.

8.3.6 Current-voltage (J-V) characteristics of the fabricated devices

Fig. 8.11 shows the J-V characteristics of devices fabricated using the pr-P3HT:PCBM, the P3HT:PCBM using ht-P3HT as well the ht-P3HT:PCBM blend films. As can be seen, the heat treatment of the P3HT resulted in an improved device performance (Table 8.3). A device fabricated with ht-P3HT:PCBM had a short circuit current (Jsc) of 13.16 ± 0.15 mA/cm^2, more than threefold higher than a device fabricated with pr-P3HT:PCBM that had a Jsc of 3.59 ± 0.12 mA/cm^2 (Fig. 8.11a). Similarly, a twofold increase in the Jsc of the device fabricated with P3HT:PCBM using ht-P3HT (8.99 ± 0.05 mA/cm^2) was observed. From similar studies on related systems, these large increases in Jsc after heat treatment can be attributed to an increased P3HT ordering and PCBM improved diffusion in the blend[48, 49]. The ordering occurred when small molecules of the PCBM diffused into the P3HT matrix allowing the latter to re-organize itself[50]. Such ordering provides an easy transport pathway for the charge carriers as the donor acceptor interface area is enhanced. Moreover, from an analysis of the vibronic peaks in the absorption spectrum, there is enhanced light absorption giving an increased current. The V_{oc} of the device fabricated with the heat treated P3HT:PCBM blends was slightly higher (0.61) than that of the pr-P3HT:PCBM blend (0.59). In Fig. 8.11a it is seen that there is an S-shaped curve in the vicinity of the Voc, this indicates the formation of space charge effects due to the segregation of the PCBM (acceptor) to the

F. Otieno, B.K. Mutuma*, K. Ranganathan, M. Airo, R. Erasmus, N. J. Coville, D. Wamwangi " Enhanced Organic Photovoltaic Device Performance by Solution Heat Treatment", Thin solid films, 2016 (under review).*

hole transport layer (PEDOT:PSS) which can cause undesired charge carrier recombination at the PCBM/PEDOT interface, and a reduction of Voc[16]. The undesired charge carrier recombination is further corroborated by a high leakage current for the pristine blend as shown in Fig. 8.11b; the leakage current reduces upon heat treatment.

Series resistances of $233.3\,\Omega\,cm^2$ and $19.7\ \Omega\,cm^2$ were obtained in the devices with pr-P3HT:PCBM and ht-P3HT:PCBM respectively (Table 8.3). This large decrease in series resistance after heating can be attributed to an increased contact area between the polymer film and the aluminium electrode resulting in more efficient charge collection[51]. This is in agreement with the AFM morphology study where an increase in rms was observed after heat treatment. Such roughness may also enhance internal reflection thus increasing the effective path length in the layer resulting in an increased absorption and more efficient charge collection[33]. The shunt resistance (R_{sh}) is sensitive to the donor acceptor interface area and hence should correlate to changes in nanoscale morphology of the blend, as seen from the data given in Table 8.3 that shows that the efficiency of the device improved with increased $R_{sh.}$ The results indicate that the device performance showed marked improvement upon heat treatment with an overall 4 times PCE increase. The current-voltage measurements of our films were done in air and the obtained PCE was enhanced to 3.5%. Indeed, the obtained PCE value was higher than that of the standard reference cell

F. Otieno, B.K. Mutuma*, K. Ranganathan, M. Airo, R. Erasmus, N. J. Coville, D. Wamwangi " Enhanced Organic Photovoltaic Device Performance by Solution Heat Treatment", Thin solid films, 2016 (under review).*

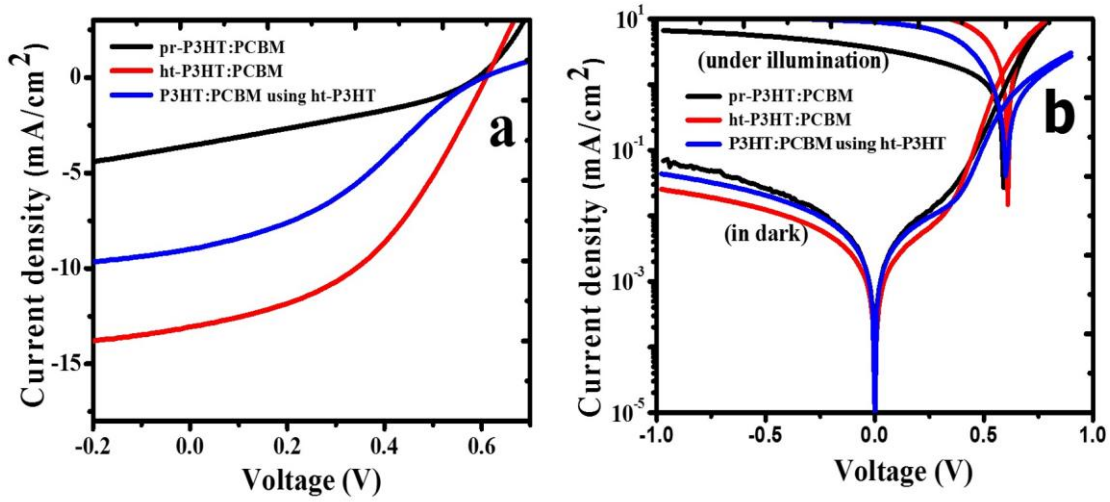

Figure 8.11. *J–V* characteristics (a) under illumination of devices formed from pristine and heat treated P3HT:PCBM blends (b) Semi-log J-V characteristics in the dark and under illumination.

Table 8.3. A summary of the performance of the OPVs devices from pristine and heat treated P3HT:PCBM blends

Device	Jsc (mA/cm^2)	Voc (V)	R_s (Ω cm^2)	R_{sh} (kΩ cm^2)	FF (%)	PCE (%)
pr-P3HT:PCBM	3.59 ± 0.12	059 ± 0.02	233.2 ± 0.23	53.9 ± 3	32.4 ± 1.2	0.69 ± 0.10
P3HT:PCBM using ht-P3HT	8.99 ± 0.05	0.61 ± 0.01	86.3 ± 0.46	200.0 ± 2	34.8 ± 0.8	1.91 ± 0.04
ht-P3HT:PCBM	13.16 ± 0.15	0.61 ± 0.02	19.7 ± 0.68	233.3 ± 2	42.9 ± 1.1	3.46 ± 0.08

A summary of the literature of the different annealing conditions used during photovoltaic device fabrication and the obtained current-voltage properties of the devices is given in Table 8.4. The post thermal annealing and solvent vapor annealing reported in the table was carried out on films and not on solutions. Ma *et al.*[13] did post thermal annealing of P3HT:PCBM films at 150°C for 10 min in a N_2 atmosphere and obtained a PCE of 5%, higher than the PCE obtained in our study. To note, most of the post thermal annealing techniques reported in literature were carried out at high temperatures and for longer times and under inert conditions (N_2 or Ar). In our approach, we used solution heat treatment and carried out our measurements in air. From Table 8.4, it can be seen that post thermal heat treatment at

F. Otieno, B.K. Mutuma*, K. Ranganathan, M. Airo, R. Erasmus, N. J. Coville, D. Wamwangi " Enhanced Organic Photovoltaic Device Performance by Solution Heat Treatment", Thin solid films, 2016 (under review).*

temperatures above 130ºC gave a Jsc > 8 mA/cm^2, a FF > 52% and a PCE > 3%[52] When no heat treatment was carried out on the P3HT:PCBM, a PCE of < 1% was obtained[17]. A solvent vapor annealing technique has also been reported by Sun *et al.* who used different solvents and obtained the best performance with chlorobenzene and cyclohexanone vapors. However, both chlorobenzene and dichlorobenzene vapor annealing gave a relatively low PCE (2-3%)[9]. Park *et. al*. used acetone vapor annealing and obtained a PCE of 3.29%. In solvent vapor annealing, the solubility of the P3HT and PCBM polymer is a determining factor[16]. In essence, both post thermal annealing and solvent vapor annealing improve the short circuit current, the fill factor and consequently the PCE of the organic solar cells. Comparing our results to those reported in literature, we see that the PCE obtained was slightly higher than those reported by earlier researchers.

Table 8.4. A summary of thermal annealing effect on the current-voltage properties of organic photovoltaic devices

Author	Annealing method	Conditions	Jsc (mA/cm^2)	FF (%)	PCE (%)	Ref
Ma *et. al*	no heat treatment	N_2	4.00	30.0	1.00	[13]
	film post thermal annealing	150 °C for 10 min, N_2	10.0	68.0	5.00	
Kim *et. al*	film post thermal annealing	140 °C for 15 min, N_2	9.40	53.0	3.00	[12]
Tsoi *et. al*	no heat treatment	N_2	4.79	33.0	1.07	[37]
	film post thermal annealing	140 °C for 30 min, N_2	8.72	64.0	3.39	
Chirvase *et. al*	film post thermal annealing	130 °C for 20 sec, N_2	6.35	63.2	2.39	[50]
Kadem *et. al*	Post heat treatment	100 °C for 10 min, N_2	12.56	62.2	5.0	[52]
		180 °C for 10 min, N_2	9.74	57.8	3.6	
Padinger *et. al*	film post thermal annealing	75 °C for 4min, Ar	7.50	57.0	2.50	[20]
	no heat treatment	N_2	3.74	35.0	0.94	
Park *et. al*	Solvent vapor annealing	Chlorobenzene, N_2	8.35	54.0	2.88	[16]
		Acetone, N_2	10.54	54.0	3.29	
Li *et. al*	no heat treatment	N_2	1.33	37.4	0.35	[17]
	Solvent vapor annealing	dichlorobenzene	8.29	62.8	2.94	
Sun *et. al*	no heat treatment	N_2	6.14	41.0	1.43	[9]
	Solvent vapor annealing	Chlorobenzene	6.87	56.0	2.25	
		Cyclohexanone	7.80	59.0	2.64	

F. Otieno, B.K. Mutuma*, K. Ranganathan, M. Airo, R. Erasmus, N. J. Coville, D. Wamwangi " Enhanced Organic Photovoltaic Device Performance by Solution Heat Treatment", Thin solid films, 2016 (under review).*

Fig. 8.12 shows a possible reaction scheme that show the effect of heat treatment of P3HT separately and in the P3HT:PCBM blend. Fig. 8.12a shows pristine P3HT:PCBM with entangled chains of P3HT mixed with PCBM. The presence of entangled chains and a disordered coil like structure is attributed to the pristine nature of the P3HT polymer in solution[53]. The presence of PCBM during heat treatment gives a more ordered P3HT as well as a uniform distribution of PCBM within the P3HT matrix giving a homogeneous P3HT:PCBM blend (Fig. 8.12b). The presence of disordered P3HT domains controls the domains of PCBM leading to easy miscibility of PCBM in P3HT[54, 55]. Consequently, the dimensions of the disordered P3HT domains govern the morphology and phase separated nanostructure of the P3HT:PCBM[54]. This prevents the formation of donor and acceptor rich domains which could act as recombination sites. In contrast, a slightly disordered P3HT in a P3HT:PCBM using ht-P3HT was observed. The preheat treatment of P3HT separately reduces the degree of chain entanglement resulting to an ordered P3HT (Fig. 8.12c). However, the ordered P3HT inhibits diffusion of PCBM into the P3HT matrix. This is in agreement with literature where an increased P3HT ordering in P3HT:PCBM films upon heat treatment has been reported[32, 56].

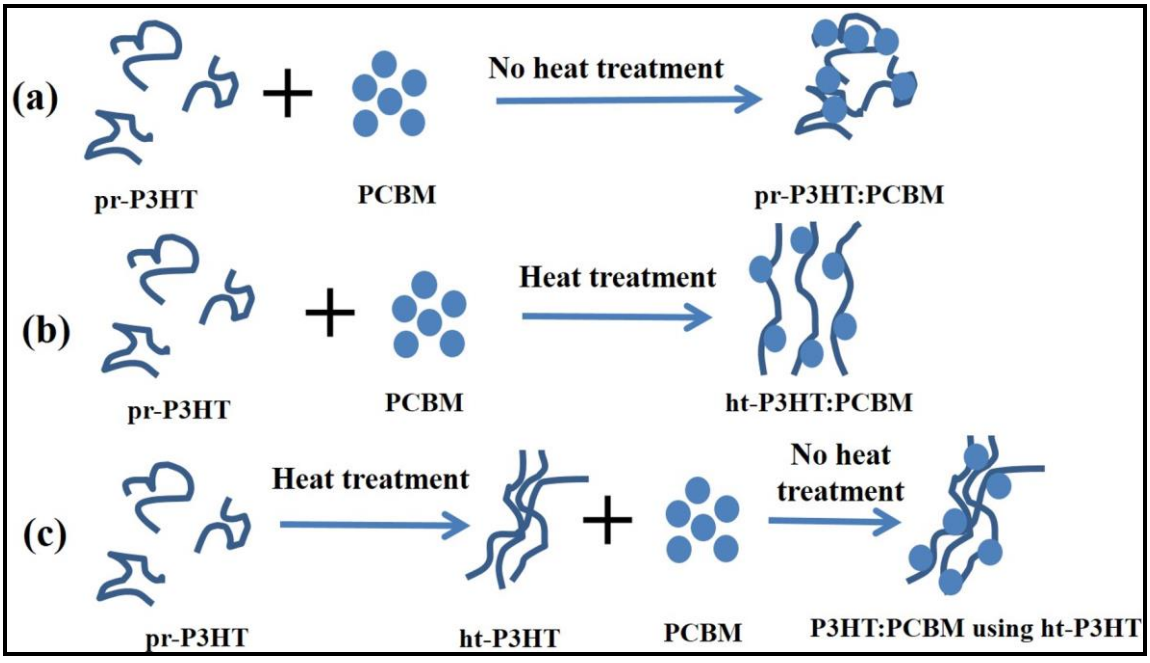

Figure 8.12. A schematic diagram showing the role of heat treatment of P3HT in PCBM.

F. Otieno, B.K. Mutuma*, K. Ranganathan, M. Airo, R. Erasmus, N. J. Coville, D. Wamwangi " Enhanced Organic Photovoltaic Device Performance by Solution Heat Treatment", Thin solid films, 2016 (under review).*

8.4 Conclusions

From this study, it was observed that solution heat treatment of a P3HT:PCBM blend enhanced the PCE of organic photovoltaic devices by four times relative to a pristine P3HT:PCBM blend. Pristine P3HT has a rougher morphology than a heat treated P3HT as evidenced in the AFM morphology study. Heating P3HT before mixing the blend increased its structural order. However, the high P3HT polymer ordering hindered the PCBM penetration into the matrix leading to disconnection of P3HT and PCBM domains in the blend matrix. The matrix segregation resulted in a decreased P3HT ordering in the P3HT:PCBM blend thus producing a lower PCE. In contrast, heating a P3HT:PCBM blend gave a highly ordered P3HT and a higher PCE. During solution heating, PCBM diffused into the polymer matrix to form a percolated network with enhanced electron transport properties. This study clearly shows that solution heat treatment of P3HT:PCBM leads to a structural ordering of the P3HT polymer that modifies the optical, morphological, PL and Raman spectra characteristics of the blend. The high P3HT polymer ordering, red shifted optical absorption, narrow FWHM of Raman peaks and decreased PL intensity upon solution heat treatment contributed to the increased short circuit current and power conversion efficiency of 13.16 mA/cm^2 and 3.46% respectively. A simultaneous ordering of P3HT alongside PCBM diffusion was found to be the main contributor to a good performing device. However, to enhance the hole mobility of P3HT, heat treatment at temperatures lower than 110 °C are preferable[21]. In our study, we have attempted to use a lower temperature (70 °C) and a shorter heating time (1 min) during the solvent heat treatment process. Since heat transfer within a solution is much faster than in a solid film a shorter time could be used.

F. Otieno, B.K. Mutuma*, K. Ranganathan, M. Airo, R. Erasmus, N. J. Coville, D. Wamwangi " Enhanced Organic Photovoltaic Device Performance by Solution Heat Treatment", Thin solid films, 2016 (under review).*

References

1. Yu, G.; Gao, J.; Hummelen, J. C.; Wudl, F.; Heeger, A. J. *Science-AAAS-Weekly Paper Edition* **1995,** 270, (5243), 1789-1790.
2. Friend, R. H. *Physica Scripta* **1996,** 1996, (T66), 9.
3. Günes, S.; Neugebauer, H.; Sariciftci, N. S. *Chemical Reviews* **2007,** 107, (4), 1324-1338.
4. Li, G.; Shrotriya, V.; Huang, J.; Yao, Y.; Moriarty, T.; Emery, K.; Yang, Y. *Nature Materials* **2005,** 4, (11), 864-868.
5. Facchetti, A. *Chemistry of Materials* **2011,** 23, (3), 733-758.
6. Brabec, C. J.; Sariciftci, N. S.; Hummelen, J. C. *Advanced Functional Materials* **2001,** 11, (1), 15-26.
7. Chen, C.-C.; Chang, W.-H.; Yoshimura, K.; Ohya, K.; You, J.; Gao, J.; Hong, Z.; Yang, Y. *Advanced Materials* **2014,** 26, (32), 5670-5677.
8. Yu, G.; Gao, J.; Hummelen, J. C.; Wudl, F.; Heeger, A. J. *Science* **1995,** 270, (5243), 1789-1791.
9. Sun, Y.; Han, Y.; Liu, J. *Chinese Science Bulletin* **2013,** 58, (22), 2767-2774.
10. Abramavicius, V.; Amarasinghe Vithanage, D.; Devizis, A.; Infahsaeng, Y.; Bruno, A.; Foster, S.; Keivanidis, P. E.; Abramavicius, D.; Nelson, J.; Yartsev, A.; Sundstrom, V.; Gulbinas, V. *Physical Chemistry Chemical Physics* **2014,** 16, (6), 2686-2692.
11. Karagiannidis, P. G.; Kassavetis, S.; Pitsalidis, C.; Logothetidis, S. *Thin Solid Films* **2011,** 519, (12), 4105-4109.
12. Kim, Y.; Choulis, S. A.; Nelson, J.; Bradley, D. D. C.; Cook, S.; Durrant, J. R. *Applied Physics Letters* **2005,** 86, (6), 063502.
13. Ma, W.; Yang, C.; Heeger, A. J. *Advanced Materials* **2007,** 19, (10), 1387-1390.
14. Verploegen, E.; Miller, C. E.; Schmidt, K.; Bao, Z.; Toney, M. F. *Chemistry of Materials* **2012,** 24, (20), 3923-3931.
15. Miller, S.; Fanchini, G.; Lin, Y.-Y.; Li, C.; Chen, C.-W.; Su, W.-F.; Chhowalla, M. *Journal of Materials Chemistry* **2008,** 18, (3), 306-312.
16. Park, J. H.; Kim, J. S.; Lee, J. H.; Lee, W. H.; Cho, K. *The Journal of Physical Chemistry C* **2009,** 113, (40), 17579-17584.
17. Li, G.; Yao, Y.; Yang, H.; Shrotriya, V.; Yang, G.; Yang, Y. *Advanced Functional Materials* **2007,** 17, (10), 1636-1644.
18. Chan, S.-H.; Hsiao, Y.-S.; Hung, L.-I.; Hwang, G.-W.; Chen, H.-L.; Ting, C.; Chen, C.-P. *Macromolecules* **2010,** 43, (7), 3399-3405.
19. Sirringhaus, H.; Brown, P. J.; Friend, R. H.; Nielsen, M. M.; Bechgaard, K.; Langeveld-Voss, B. M. W.; Spiering, A. J. H.; Janssen, R. A. J.; Meijer, E. W.; Herwig, P.; de Leeuw, D. M. *Nature* **1999,** 401, (6754), 685-688.
20. Padinger, F.; Rittberger, R. S.; Sariciftci, N. S. *Advanced Functional Materials* **2003,** 13, (1), 85-88.
21. Mihailetchi, V. D.; Xie, H. X.; de Boer, B.; Koster, L. J. A.; Blom, P. W. M. *Advanced Functional Materials* **2006,** 16, (5), 699-708.
22. Yao, E.-P.; Ho, C.-S.; Yu, C.; Huang, E.-L.; Lai, Y.-N.; Hsu, W.-C. *International Journal of Photoenergy* **2014,** 2014, 7.
23. Wu, W.-R.; Jeng, U. S.; Su, C.-J.; Wei, K.-H.; Su, M.-S.; Chiu, M.-Y.; Chen, C.-Y.; Su, W.-B.; Su, C.-H.; Su, A.-C. *ACS Nano* **2011,** 5, (8), 6233-6243.
24. Malgas, G.; Motaung, D.; Arendse, C. *Journal of Materials Science* **2012,** 47, (10), 4282-4289.

25. Motaung, D. E.; Malgas, G. F.; Arendse, C. J. *Synthetic Metals* **2010,** 160, (9–10), 876-882.
26. Klimov, E.; Li, W.; Yang, X.; Hoffmann, G. G.; Loos, J. *Macromolecules* **2006,** 39, (13), 4493-4496.
27. Campoy-Quiles, M.; Ferenczi, T.; Agostinelli, T.; Etchegoin, P. G.; Kim, Y.; Anthopoulos, T. D.; Stavrinou, P. N.; Bradley, D. D. C.; Nelson, J. *Nature Materials* **2008,** 7, (2), 158-164.
28. Chen, T.-A.; Wu, X.; Rieke, R. D. *Journal of the American Chemical Society* **1995,** 117, (1), 233-244.
29. Kiriy, N.; Jähne, E.; Adler, H.-J.; Schneider, M.; Kiriy, A.; Gorodyska, G.; Minko, S.; Jehnichen, D.; Simon, P.; Fokin, A. A.; Stamm, M. *Nano Letters* **2003,** 3, (6), 707-712.
30. Liu, J.; Shao, S.; Wang, H.; Zhao, K.; Xue, L.; Gao, X.; Xie, Z.; Han, Y. *Organic Electronics* **2010,** 11, (5), 775-783.
31. De Bettignies, R.; Leroy, J.; Firon, M.; Sentein, C. *Synthetic Metals* **2006,** 156, (7–8), 510-513.
32. Erb, T.; Zhokhavets, U.; Gobsch, G.; Raleva, S.; Stühn, B.; Schilinsky, P.; Waldauf, C.; Brabec, C. J. *Advanced Functional Materials* **2005,** 15, (7), 1193-1196.
33. Li, G.; Shrotriya, V.; Yao, Y.; Yang, Y. *Journal of Applied Physics* **2005,** 98, (4), 043704.
34. Yang, X.; Loos, J.; Veenstra, S. C.; Verhees, W. J. H.; Wienk, M. M.; Kroon, J. M.; Michels, M. A. J.; Janssen, R. A. J. *Nano Letters* **2005,** 5, (4), 579-583.
35. Shrotriya, V.; Ouyang, J.; Tseng, R. J.; Li, G.; Yang, Y. *Chemical Physics Letters* **2005,** 411, (1–3), 138-143.
36. Francis, L. A.; Iniewski, K., *Novel Advances in Microsystems Technologies and Their Applications*. CRC Press: 2013.
37. Tsoi, W. C.; James, D. T.; Kim, J. S.; Nicholson, P. G.; Murphy, C. E.; Bradley, D. D. C.; Nelson, J.; Kim, J.-S. *Journal of the American Chemical Society* **2011,** 133, (25), 9834-9843.
38. Xu, B.; Holdcroft, S. *Macromolecules* **1993,** 26, (17), 4457-4460.
39. Kim, Y. H.; Spiegel, D.; Hotta, S.; Heeger, A. J. *Physical Review B* **1988,** 38, (8), 5490-5495.
40. Skotheim, T. A.; Reynolds, J., *Conjugated Polymers: Theory, Synthesis, Properties, and Characterization*. CRC press: 2006.
41. Van Bavel, S. S.; Bärenklau, M.; de With, G.; Hoppe, H.; Loos, J. *Advanced Functional Materials* **2010,** 20, (9), 1458-1463.
42. Brabec, C.; Scherf, U.; Dyakonov, V., *Organic Photovoltaics: Materials, Device Physics, and Manufacturing Technologies*. John Wiley & Sons: 2011.
43. Cook, S.; Furube, A.; Katoh, R. *Energy & Environmental Science* **2008,** 1, (2), 294-299.
44. Xu, B.; Holdcroft, S. *Macromolecules* **1993,** 26, (17), 4457-4460.
45. Miller, S.; Fanchini, G.; Lin, Y. Y.; Li, C.; Chen, C. W.; Su, W. F.; Chhowalla, M. *Journal of Materials Chemistry* **2008,** 18, (3), 306--312.
46. Huang, P.-T.; Huang, P.-F.; Horng, Y.-J.; Yang, C.-P. *Journal of the Chinese Chemical Society* **2013,** 60, (5), 467-472.
47. Zhang, C.; Hu, Y.; Tang, A.; Deng, Z.; Teng, F. *Journal of Applied Polymer Science* **2015,** 132, (14), n/a-n/a.

48. Hu, S.; Dyck, O.; Chen, H.; Hsiao, Y.-c.; Hu, B.; Duscher, G.; Dadmun, M.; Khomami, B. *RSC Advances* **2014,** 4, (53), 27931-27938.
49. Li, G.; Shrotriya, V.; Yao, Y.; Huang, J.; Yang, Y. *Journal of Materials Chemistry* **2007,** 17, (30), 3126-3140.
50. Chirvase, D.; Parisi, J.; Hummelen, J. C.; Dyakonov, V. *Nanotechnology* **2004,** 15, (9), 1317.
51. Yu, H.-Z.; Peng, J.-B. *Chinese Physics Letters* **2008,** 25, (4), 1411.
52. Kadem, B.; Hassan, A.; Cranton, W. *Journal of Materials Science: Materials in Electronics* **2016,** 27, (7), 7038-7048.
53. Zhao, K.; Xue, L.; Liu, J.; Gao, X.; Wu, S.; Han, Y.; Geng, Y. *Langmuir* **2010,** 26, (1), 471-477.
54. Treat, N. D.; Mates, T. E.; Hawker, C. J.; Kramer, E. J.; Chabinyc, M. L. *Macromolecules* **2013,** 46, (3), 1002-1007.
55. Treat, N. D.; Brady, M. A.; Smith, G.; Toney, M. F.; Kramer, E. J.; Hawker, C. J.; Chabinyc, M. L. *Advanced Energy Materials* **2011,** 1, (1), 82-89.
56. Kim, K.; Liu, J.; Namboothiry, M. A. G.; Carroll, D. L. *Applied Physics Letters* **2007,** 90, (16), 163511.

CHAPTER 9

Sensing Ammonia Vapours in a Humid Environment using Hollow Carbon Spheres and Hollow Carbon Sphere-Polyvinylpyrrolidone Composites

9.1 Introduction

Carbon based nanomaterials have been of great interest to scientists since the discovery of fullerenes[1] and carbon nanotubes[2] due to their unique structural and electronic properties. Other forms of carbon based nanomaterials include graphene, graphene oxide and carbon spheres. Carbon spheres can be categorized based on their nanometric texture[3], the level of graphitization[4] or on their structural features such as whether they are hollow or solid[5]. Extensive research has been carried out on the synthesis and application of solid carbon spheres unlike their hollow carbon spheres (HCSs) counterparts[6, 7]. HCSs are commonly synthesized by techniques such as the hydrothermal[8], pyrolysis[9] or templating[10,11], procedures among others. The templating method offers the advantages of manipulating the pore structure, the shell thickness and the internal diameter of the HCSs[12] in addition to their ease of processing by the sol-gel or the Stober method[13-15]. Thus, HCSs with their size-dependent properties are attractive nanomaterials with versatile applications in catalysis[16], fuel cells[17], supercapacitors[18] and lithium ion batteries[19].

Recently, solid carbon spheres-polymer composites were also applied to electronic devices such as hydrostatic pressure sensors[20, 21], relative humidity sensors[22] and write once read many times memory devices[23, 24]. The application of carbon nanospheres in sensor devices is simple, inexpensive and provides materials with high sensitivity and short response and recovery times. Despite their hydrophobic behaviour they can be dispersed in water with the assistance of a surfactant such as hexadecyltrimethylammonium bromide (CTAB), at a temperature below the Kraft temperature[22, 25, 26, 27]. In addition, a polar group on a polymer such as polyvinyl alcohol or polyvinylpyrrolidone can aid the dispersion of the carbon materials[27]. The presence of the polyvinylpyrrolidone polymer as an insulating matrix within a conductive material such as graphene has been reported to create percolation pathways that aid electrical conductivity[28]. Carbon based nanomaterials being cheap, easily processable

and exhibiting high surface to volume ratio and tunable electrical properties are advantageously applicable for use as resistive or capacitive chemical sensors[29-31].

The real time monitoring of toxic compounds such as ammonia, nitrogen dioxide and volatile organic compounds is essential to human health and environmental safety. In particular, high ammonia concentrations in the environment are hazardous to human health and vegetation[32, 33]. This high ammonia concentration may result from the use of nitrogen containing fertilizers in agricultural crops that increase soil acidification and the reaction of ammonium compounds to form fine particles[34, 35]. Thus, ammonia sensors find a broad range of application in the automotive, biomedical and agricultural industries[36, 37]. However, research on ammonia detection and sensing is mostly carried out in a gas testing chamber, limiting their applicability in a day to day application. At ambient conditions, the environmental factors such as temperature and humidity affect the performance of chemical sensors. For instance, Al_2O_3 sensors are readily susceptible to contamination by water vapour requiring regular maintenance[38]. Also, the presence of water vapour on p-type semiconducting materials has been reported to cause a reduction in conductance and a delay in the sensor recovery time[39-42].

In essence, the monitoring of humidity levels is of great importance to the application of sensors in the automotive and food packaging industry[43, 44]. It results from the role of humidity in determining the surface reactions of the sensing materials that rely heavily on the environment. Thus, the study of ammonia response in different sensing materials at ambient conditions is relevant for their applicability in varying environments[8, 29]. In recent years, several researchers have investigated the effects of surface functionalities on the ammonia adsorption on activated carbons[45], single walled carbon nanotubes[46, 47], multiwalled carbon nanotubes[48, 49] and graphene oxide[50] using theoretical and experimental techniques. The surface functionalities such as oxygen containing groups are highly dependent on the humidity, which then modify the adsorption and desorption of ammonia. For instance, Sangaletti and his co-workers reported on the highly sensitive ammonia gas sensors based on single walled carbon nanotubes (SWCNT) at ambient conditions[51]. Their SWCNT-based sensors showed an increase in resistance with the relative humidity by using human breath as a water source for humidity tests. Nayaranaswamy and Raimundo reported on the simultaneous determination of ammonia (5 - 27 ppm) and relative humidity (RH) in the range

30-70% using a Nafion-crystal violet composite in air through reflectance measurements using an optical fibre sensor[52].

In this study, we examine the response of hollow carbon spheres (as synthesized, annealed and in a composite) to ammonia vapours at various RH values. The study critically investigates the role of RH on the ammonia sensing properties of carbons (HCSs) which is vital to their applicability in real life situations. The effect of annealing hollow carbon spheres was investigated by comparing the relative humidity response of pristine and annealed HCSs. Surfactant assisted dispersion of pristine HCSs, annealed HCSs and a hollow carbon spheres-polyvinylpyrrolidone (HCSs-PVP) composite was used to prepare the sensor active layer by casting. A controlled RH environment was created using saturated saline solutions. We have also investigated the simultaneous response to ammonia and relative humidity of HCSs and the HCSs-PVP composite using a tristimulus analysis as a pattern recognition technique in a way that makes it possible to map different clusters of ammonia responses and relative humidity levels.

9.2 Experimental

9.2.1 Materials

The starting materials for SiO_2 spheres and HCSs synthesis are as reported in Chapter 4. Hexadecyltrimethylammonium bromide (CTAB; 98%, Aldrich) and polyvinylpyrrolidone, PVPK30 (Mw 40,000, Aldrich) were used for the preparation of the surfactant solutions and the HCSs:PVP composite respectively. The saturated saline salts were prepared from potassium hydroxide (KOH, 99.99%), magnesium chloride hexahydrate ($MgCl_2.6H_2O$, 99%), sodium bromide (NaBr, 99%), sodium chloride (NaCl, 99%) and potassium sulphate (K_2SO_4, 99%) supplied by NEON chemicals.

9.2.2 Synthesis of the SiO_2 spheres and the HCSs

The synthesis of the pristine SiO_2 spheres was carried out using the procedure reported in Chapter 4 (Section 4.2.3). Carbonization of the SiO_2 spheres was carried out by a bubbling method using toluene as the carbon source and argon as the carrier gas in a chemical vapor deposition reactor for 1 h[53]. The carbonized silica was then etched with 10% HF for 24 h at room temperature and dried to give the pristine hollow carbon spheres (HCSs). A portion (5 mg) of the HCSs was annealed in air at 300°C for 4 h to give the annealed HCSs.

9.2.3 Characterization of the SiO_2 spheres and the HCSs

The morphology and thermal properties of the SiO_2 spheres and HCSs were determined using TEM and TGA. The graphitic nature and surface area of the HCSs were ascertained using Raman and BET as described previously in Chapter 4.

9.2.4 Preparation of HCS solutions using a surfactant dispersion method

Two solutions of the pristine HCSs were prepared by dissolving 2 mg separately in 1 mL of deionized H_2O. Similarly, a 2 mg sample of annealed HCSs was dissolved in 1 mL of deionized H_2O. In order to promote a good dispersion of all the carbon nanostructures in water, a surfactant assisted method was used as previously reported[31]. To each solution, was added 5 mg of CTAB and the subsequent solutions sonicated at 60°C for 30 min. The dispersions were then sonicated at 0°C for a further 30 min. The samples were then left for 2 days at 0°C (below the CTAB Kraft temperature, 25°C)[25]. The amount of surfactant and the time that the samples were kept at the low temperature was optimized for each nanostructure. The supernatant part of the pristine and annealed HCSs solution (500 µL) was extracted and will be referred to as pristine HCSs and annealed HCSs respectively. A PVP solution was prepared by dissolving a 25 mg of PVP (M_W = 30 kDa) in 0.2 mL of deionized H_2O, and sonicating the mixture for 30 min at 50°C. The HCSs:PVP composite dispersion was prepared by mixing a pristine HCSs supernatant dispersion (250 µL) with a PVP solution (50 µL) followed by sonication for 30 minutes at room temperature.

9.2.5 Device fabrication

The interdigitated electrodes composed of 18 pairs of 7.9 mm long ENIG (Electroless Nickel Immersion Gold), with a width of 0.1 mm and a gap of 0.1 mm between electrode strips on FR4 epoxy resin/fiber glass board were sequentially cleaned in acetone, deionized water and isopropyl alcohol by ultrasonication for 20 min in each step. The substrates were dried in the oven at 100°C for 30 min. Then 20 µL of each solution was drop casted separately on the active area of the interdigitated electrode and the sensor device dried at 120°C for 1 h. The thickness of the films was measured using a Bruker Dektak XT profilometer and the morphology was ascertained by optical microscopy (Wild M20).

The conductance measurements were carried out using a Agilent 4284A LCR meter at input signal with amplitude of 500 mV and a frequency of 1 kHz. Ammonia solutions of varying volumes (1 µL to 4 µL) were dropped into a sealed 2.4 L glass chamber using a micropipette and measurements taken after 10 min. The chamber contained a ventilator to homogenize the

volatile concentration. The change in conductance was monitored at room temperature and pressure by switching the sensor response between the inside of the chamber (ammonia vapour) and outside of the chamber (ambient air) using a rotating cap system, previously described elsewhere (Fig. S9.1)[54]. The sensor saturation and recovery times for 1 µL of ammonia were approximately 2700-3100 s and 200 s respectively; thus a 400 s response time and 250 s recovery time were chosen for the study. The relative humidity measurements were carried out using saturated saline solutions of KOH, $MgCl_2$, NaBr, NaCl or K_2SO_4 as described by Greenspan *et. al* [55] to obtain 10%, 33%, 59%, 75% or 97% RH, respectively. To confirm the relative humidity during the measurement, a hygrometer (Minipa MT-241) was kept inside the chamber. The measurements were carried out at 20°C or 40°C.

9.3 Results and discussion

9.3.1 Characterization of the SiO_2 spheres and the HCSs

The TEM micrographs of the SiO_2 show that the spheres exhibited a spherical morphology with an average diameter size of 212 ± 17 nm (Fig. 9.1a). In the TG-DTA curves of the SiO_2 spheres, a first derivative peak was observed between 40°C and 200°C, which can be attributed to the loss of adsorbed water and ethanol molecules (Fig. 9.1b). From 250°C to 380°C, a considerable weight loss was observed due to the removal of organic residues and further polymerization of the silica network (removal of OH from Si-OH)[56]. After 1 h carbonization and silica removal, complete hollow carbon spheres with a mean diameter of 211 ± 18 nm were obtained (Fig. 9.2a). The shell diameter in the pristine HCSs was approximately 18 ± 4 nm due to the short carbonization time of 1 h.

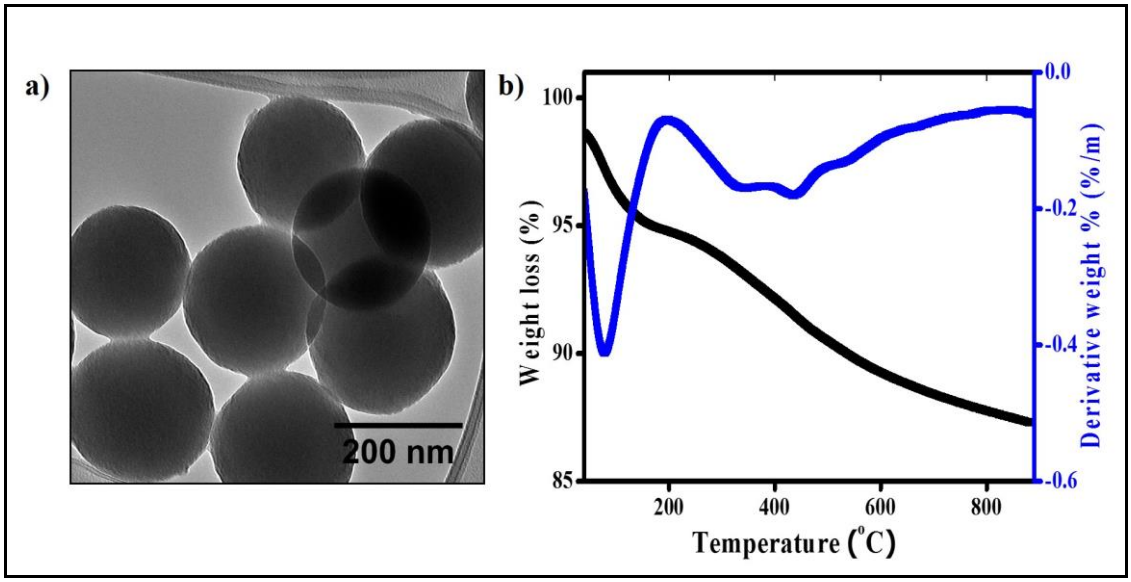

Figure 9.1. The pristine SiO_2 spheres. (a) TEM image and; (b) Thermal gravimetric and derivative weight curves, respectively.

The TG-DTA curve of the HCSs shows a small derivative peak between 280 and 400°C that can be attributed to organic residues that were not completely removed during the SiO_2 etching process[57]. The onset decomposition of the pristine HCSs in air was observed at 505°C; characteristic of amorphous carbon materials (Fig. 9.2b). To understand the surface properties of the HCSs, their surface area properties were investigated using the BET method and the pore size distributions determined using the BJH method. Fig. 9.2c shows that the HCSs exhibited a type (III) isotherm with a H3 hysteresis loop at a relative pressure of P/Po = 0.7 – 1.0 indicating an assemblage of slit shaped pores or platelike particles[58] and a BET surface area of 88 m^2/g. The Raman spectra of the pristine HCSs show strong D band peaks at 1346 cm^{-1} due to the breathing mode of sp^3 carbon atoms and defects in the carbon structure[59, 60] (Fig. 9.2d). In addition, a G peak was observed at 1581 cm^{-1}; a characteristic of bond stretching of sp^2 atoms[61]. The I_D/I_G ratio of the pristine HCSs was 0.92 indicating the presence of defects and a low degree of graphitization (I_D/I_G ratio greater than 0.6).

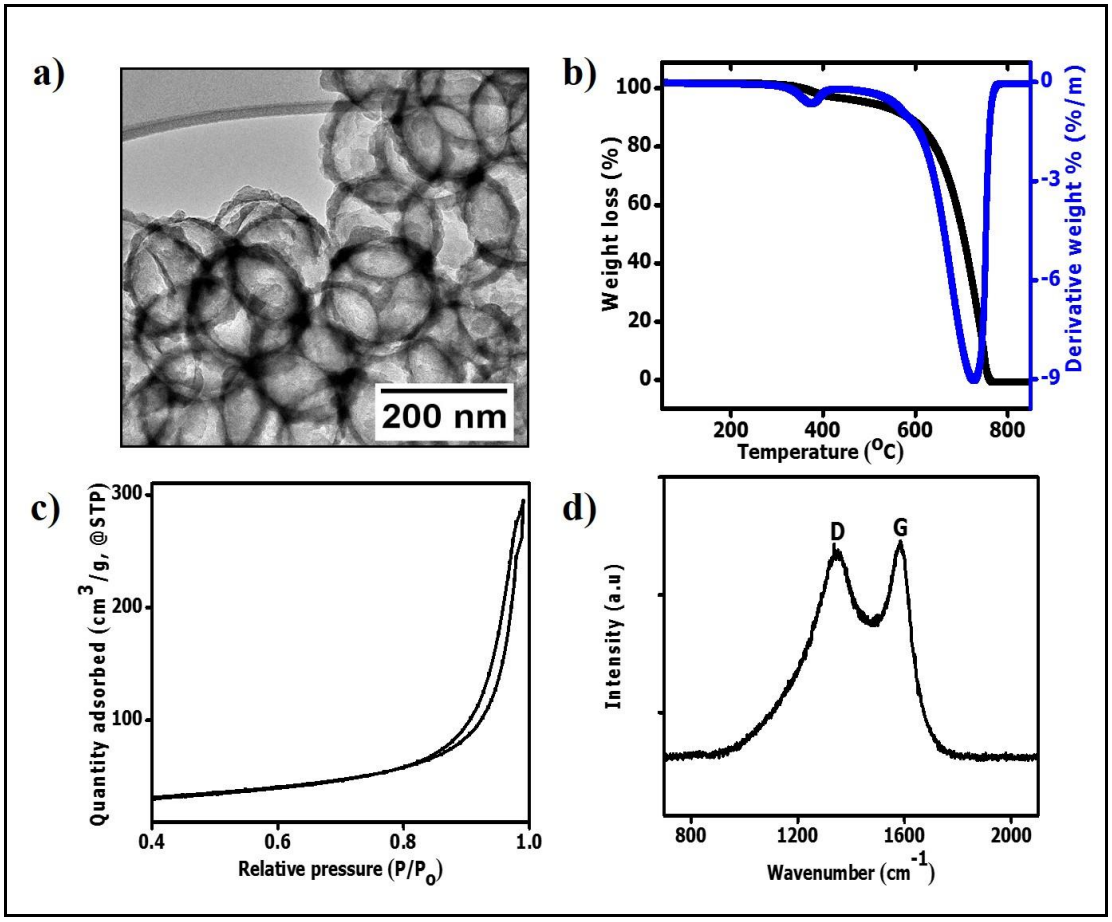

Figure 9.2. The characteristics of the pristine HCSs. (a) TEM image; (b) TG-DTA curves; (c) N_2 adsorption and desorption isotherms and; (d) Raman spectrum.

9.3.2 Characterization of the ammonia sensors

The morphology of the pristine and annealed HCSs dispersed in CTAB was investigated using optical microscopy. The images show that the spheres were homogeneously dispersed by the CTAB with the HCSs forming percolation pathways as shown by the optical micrographs of pristine and annealed HCSs in Supplementary Fig. S9.2. The average film thickness obtained from the CTAB dispersed carbon solutions was 378 nm, 457 nm and 325 nm for the pristine HCSs, HCSs:PVP composite and the annealed HCSs respectively. To determine the best working frequency, the sensors were exposed to 74 ppm of ammonia vapour and conductivity measurements were carried out by varying the frequency (Fig. 9.3). At low frequency, the HCSs:PVP composite and the annealed HCSs exhibited a high noise to signal ratio. At 1 kHz, the signal to noise ratio was low and the sensor response was still relatively higher than at higher frequencies, as shown in Fig. 9.3. Thus, 1 kHz was chosen as the best frequency for the measurements and used in all further experiments.

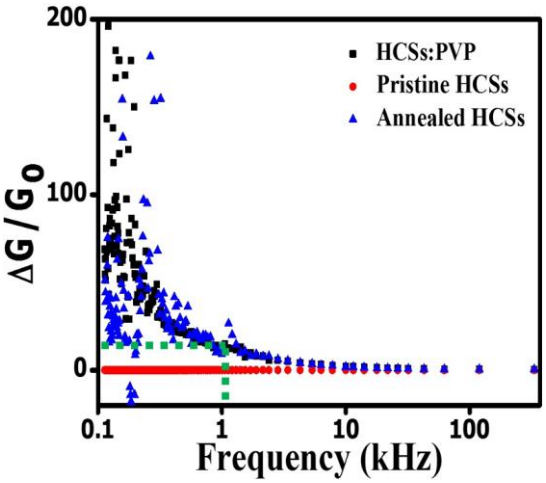

Figure 9.3. Response of pristine HCSs, HCSs:PVP composite and annealed HCSs based sensors as a function of frequency. Ammonia concentration: 74 ppm; RH: 50%, T: 20^{o}C.

9.3.3 Sensor response and recovery time

The three different sensors were exposed to ammonium hydroxide vapours and their response and sensitivity determined. The concentration of the ammonia vapour was determined from the volume of ammonium hydroxide added using the equation below, as reported elsewhere[62];

$$C\ (ppm) = \frac{2.46(Vd)}{V_s M_w} \times 10^7 \qquad \textbf{(9.1)}$$

where V represents volume added in µL, d is the density of ammonia in g/mL, V_s is the volume of the chamber in mL (in this case 2400 mL) and M_w is the molecular weight of the ammonia solution in g/mole. Different NH_4OH volumes were added (1 µL to 4 µL with steps of 1 µL) corresponding to 74 ppm, 147 ppm, 221 ppm and 295 ppm ammonia vapour concentration respectively. The response time was determined as the time taken for the sensors to achieve 90% of the saturation value. The recovery time refers to the time taken to recover 90% of the sensor response at the same temperature. Figs. 9.4 a, c and e show that long saturation times (> 3000 s) and response times (> 2000 s) are shown by the pristine HCSs, HCSs:PVP and annealed HCSs based sensors after exposure to 74 ppm of ammonia at room temperature. However, at 40°C, the response and recovery times in all the sensors were significantly reduced as shown in Figs. 9.4b, d and f.

At 40°C the recovery time in the pristine HCSs and HCSs:PVP sensors was less than 300 s while that of the annealed HCSs was 504 s, indicating a stronger ammonia vapour interaction

with the annealed carbon surface. The increase in temperature significantly increased the ammonia adsorption and desorption rates on the carbon surface[63]. The pristine HCSs gave a shorter response and recovery time with a higher signal to noise ratio than the HCSs:PVP composite (Table 9.1). This results from the formation of carbon-polymer composite in the presence of PVP yielding a lower signal to noise ratio. However, longer response and recovery times were exhibited in the HCSs:PVP composite at room temperature (20°C) and 40°C. This can be attributed to the PVP polymer functional groups restricting the fast response and recovery, probably hindering ammonia transport in the sensor active layer. The ammonia adsorption rate in the annealed HCS surface was slower than in the pristine HCS resulting in longer response times at room temperature and 40°C.

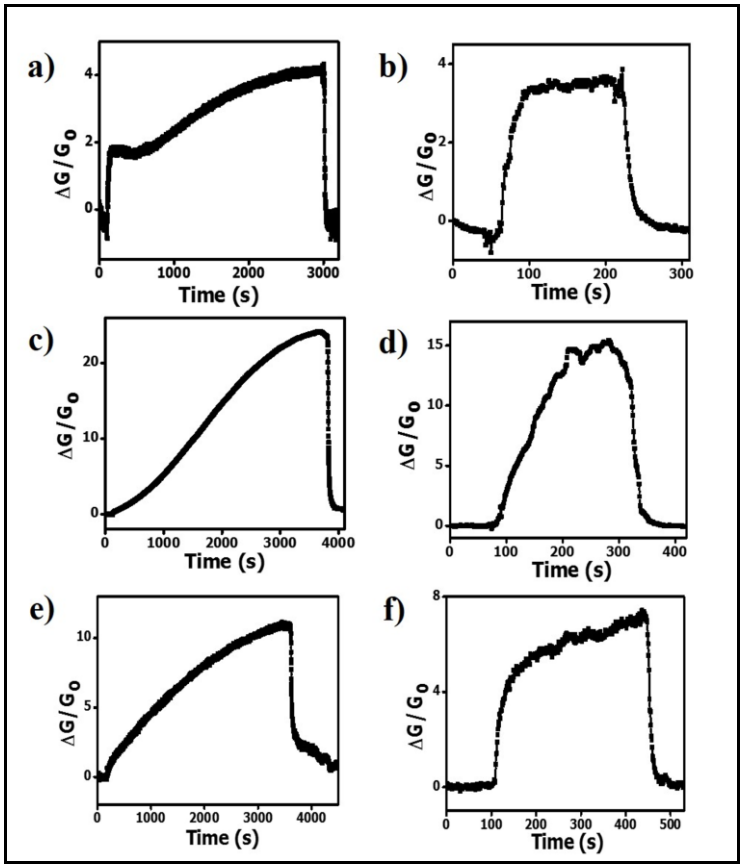

Figure 9.4. Transient response curves of; (a and b) pristine HCSs, (c and d) HCSs:PVP and (e and f) annealed HCSs at room temperature and at 40°C, respectively. Ammonia concentration: 74 ppm; RH: 50%.

Table 9.1. Effect of temperature on the sensor response (t_{resp}) and recovery (t_{recov}) time. Ammonia concentration: 74 ppm; RH: 50%.

Material	t_{resp} at 20°C (s)	t_{recov} at 20°C (s)	t_{resp} at 40°C (s)	t_{recov} at 40°C (s)
Pristine HCSs	2542	104	49	50
HCSs:PVP	3146	259	125	82
Annealed HCSs	3078	504	149	32

9.3.4 Ammonia sensitivity

The ammonia sensing mechanism of HCSs (a porous carbon) is a physisorption process that involves pore filling mechanism[64]. The electrical measurements of the carbon based materials for ammonia sensing at room temperature (Fig. 9.5) showed a fast recovery and an increase in response with the ammonia concentration. At low ammonia concentration (less than 222 ppm), a nearly linear behaviour was portrayed by the pristine HCSs and HCSs-PVP composite (Figs. 9.5a-d). However, the annealed HCSs exhibited a non-linear behaviour with a non-linear increase in response at higher ammonia concentration (Fig. 9.5e and f). The sensitivity of the sensors was measured using equation 9.2;

$$S = \frac{\partial R}{\partial C} \quad \textbf{(9.2)}$$

where the response R corresponds to the relative variation of the conductance, $R = {}^{\Delta G}/_{G_0}$, was 0.0094/ppm, 0.0252/ppm and 0.0089/ppm for the pristine HCSs, HCSs:PVP and annealed HCSs, respectively. This sensitivity is much higher than that reported in literature for other carbon based ammonia sensors. For instance, Ghosh *et al.* obtained a 5 % response of reduced graphene oxide for 400 ppm of ammonia at room temperature[65].

When the temperature was increased to 40°C, the pristine HCSs sensitivity to ammonia gradually decreased to 0.0008/ppm (Fig. 9.6). However, the ammonia sensitivity of the HCSs:PVP composite increased to 0.04/ppm. In the case of HCS:PVP, the presence of PVP enhances the homogeneous dispersion of the carbons in the electrode matrix. Consequently, the surface interaction of the water molecules with the good dispersed carbon-polymer composite resulted in an increased sensitivity. The annealed HCSs gave a slight increase in

ammonia sensitivity at 40°C. The HCSs and HCSs:PVP composite exhibited a higher selectivity to ammonia compared to ethanol and acetone vapours. In particular, the HCSs:PVP and annealed HCSs gave a sensitivity of 0.0007/ppm and 0.0003/ppm towards ethanol vapours and 0.00004/ppm and 0.026/ppm towards acetone vapours respectively (Fig. S9.3).

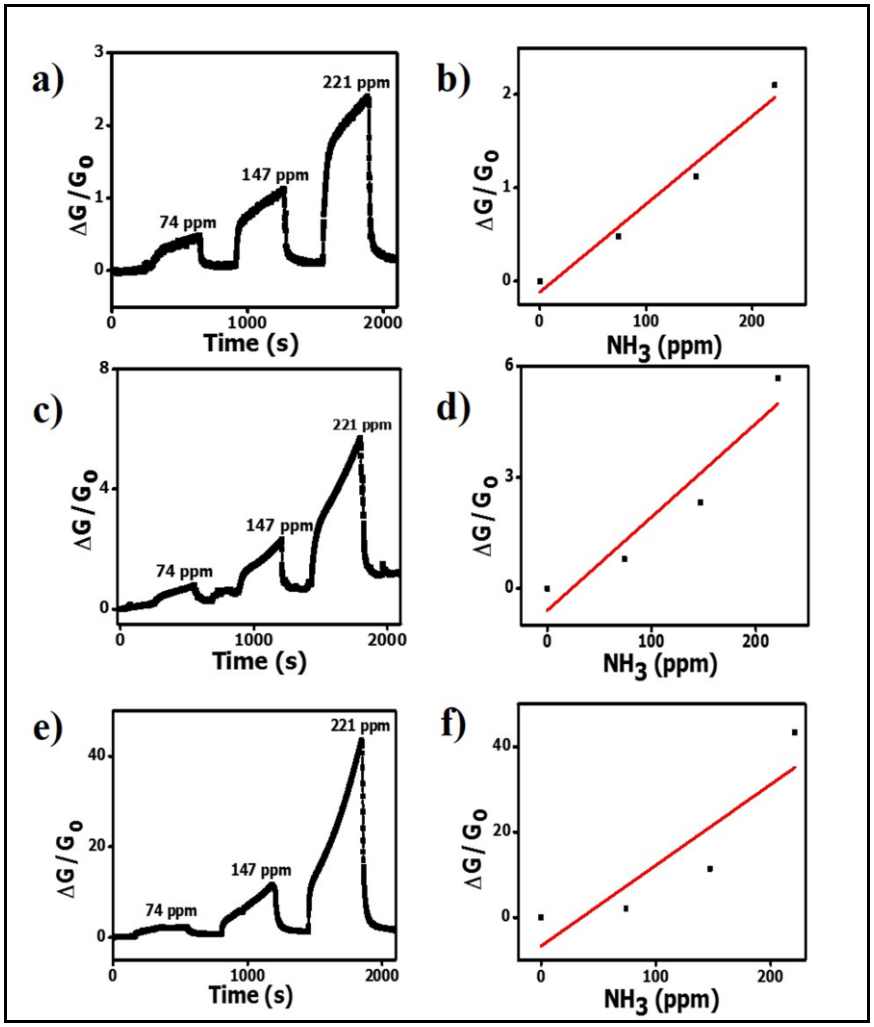

Figure 9.5. Response and sensitivity, respectively, of (a and b) pristine HCSs; (c and d) HCSs:PVP and (e and f) annealed HCSs based ammonia sensors at room temperature. RH: 50 %.

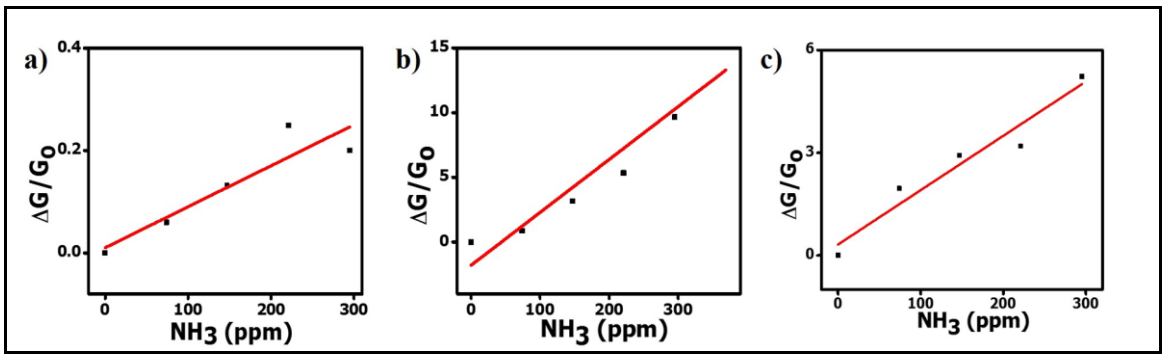

Figure 9.6. Sensitivity of the carbon materials to varying ammonia concentrations at 40° C. (a) pristine HCSs; (b) HCSs:PVP and; (c) annealed HCSs. Ammonia concentration: 74 ppm; RH: 50%.

9.3.5 Relative humidity response

To explore the effect of the relative humidity on the ammonia response for the carbon materials, the sensors were exposed to different relative humidity environments (closed environments at equilibrium with saline solutions) and their response determined in simultaneous presence of the RH. The HCSs comprise of surface pores and interparticle voids between adjacent spheres. Upon exposure to water vapour (RH) the water vapor infiltrates the interparticle voids and the surface pores creating an electrical charge through the pore filling mechanism. The electrical charge gets transferred from carbon to carbon enhancing the conductivity. In addition, the water layers get physically adsorbed onto the surface allowing for proton conductivity that further increases the conductivity.

The relative humidity response for the pristine HCSs, HCSs:PVP and the annealed HCSs was determined by initially exposing the sensors to varying relative humidity in the absence of ammonia vapors. Fig. 9.7a shows that the conductivity of the pristine HCSs increased with % RH and was approximately 40 and 300 times higher than that of the HCSs:PVP composite and annealed HCSs respectively. This can be attributed to the presence of surface hydroxyls and amorphous domains that are characterized by a large number of defects confirmed by TGA and Raman data (Fig. 9.2b and d). The amorphous sp^3 domains within the carbon matrix are more hydrophilic and thus adsorb more water molecules[66]. The conductivity of the pristine HCSs increased with % RH with the highest RH response observed at 97% RH (Table 9.2). This is ascribed to the increase in water vapor molecules physisorbed on the surface with humidity.

In contrast, the HCSs:PVP sensors exhibited the lowest conductivity at 10% RH and the highest conductivity at 59% RH (Fig. 9.7b). This effect could be due to the plasticization of PVP polymer that is known to start at 55% humidity. The reduction in conductivity at 97% RH in HCSs:PVP is related to an increased resistance resulting from PVP swelling and plasticization[67]. In addition, the swelling of the polymers covered the pores restricting physisorption of water vapor molecules. Thus a tremendous decrease in response was observed above 60% RH (Table 9.2). The annealed HCSs sensors showed an increase in conductivity with increased RH. However, the conductivity values were 250 times lower than that of the pristine HCSs (Fig. 9.7c). The decrease in conductivity can be attributed to significant reduction of the number of defects (amorphous domains) by the annealing process resulting in more graphitic domains that restricts water adsorption. This is ascertained by the disappearance of the shoulder between 280 ºC and 400 ºC in the TG-DTG curve (Fig. S9.4). The Raman spectra shows that the annealed HCSs exhibited a D band position at 1349 cm^{-1} and a G band at 1581 cm^{-1} with an I_D/I_G ratio of 0.71. This clearly shows that annealing resulted in a decrease in the number of defects of the HCSs. Consequently, increasing the hydrophobic character of the HCSs which lead to less RH response.

At 97% RH, the annealed HCSs gave a RH response of 460 whereas the pristine HCSs exhibited a very high RH response of 199119 (Table 9.2). This indicates that higher structural defects and number of surface hydroxyls in the pristine HCSs highly favoured RH response compared to the annealed HCSs that had fewer defects. Our reported response is higher than that reported in literature. In particular, Mauricio and co-workers reported a 37800% humidity sensitivity of graphene oxide at 15% - 97% RH and 1 kHz[68]. They studied the change in capacitance using saturated saline solutions and attributed the increased humidity response to the presence of functional groups on the graphene oxide surface. Similarly, Watts and co-workers reported an increase in response of acid functionalized multiwalled carbon nanotubes (MWCNT-COOH) in a humid atmosphere created by the introduction of 0.1 mL of deionized water during the measurements[48].

In all of HCSs sensors, our reported response is higher than most of those reported in literature for carbon based relative humidity sensors. For instance, Zhang *et al* reported a response of 8.69–37.43% by exposing a self-assembled reduced graphene oxide-poly(diallylimethylammonium chloride) (PDDA) nanocomposite to saturated saline salts of 11-97% RH[69]. Higher humidity responses were reported by Cunha et al[22] for carbon sphere-

poly(vinyl alcohol) based sensors, but their sensors showed a non-linear response and sensitivity was defined using a logarithmic scale so that a direct sensitivity comparison is not possible.

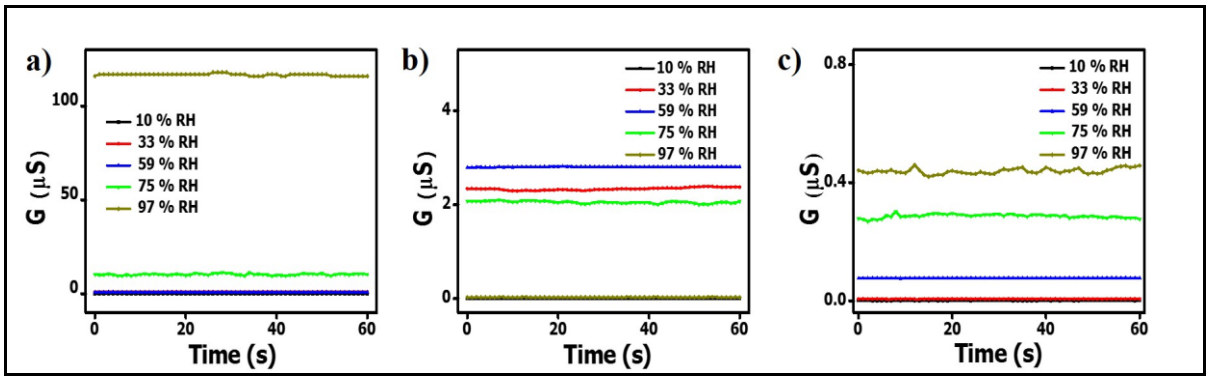

Figure 9.7. The conductivity of (a) pristine HCSs; (b) HCSs:PVP and; (c) annealed HCSs based sensors at different relative humidity.

Table 9.2. The relative humidity response of the pristine HCSs, HCSs:PVP and annealed HCSs. The subscript of *G* corresponds to the RH value.

Response	$(G_{33}-G_{10})/G_{10}$	$(G_{59}-G_{10})/G_{10}$	$(G_{75}-G_{10})/G_{10}$	$(G_{97}-G_{10})/G_{10}$
Pristine HCSs	1758	1396	17665	199119
HCSs:PVP	1981	2376	1741	24
Annealed HCSs	6	80	300	460

9.3.6 Ammonia sensitivity at varying RH

Fig. 9.8 shows the ammonia conductivity and sensitivity values of the pristine HCSs, HCSs:PVP and annealed HCSs at 10% RH. The conductivity increased with the ammonia concentration in both the HCSs and the HCSs:PVP composites. The conductivity values in the pristine and annealed HCSs was one order of magnitude lower than that of the HCSs:PVP composites (Fig. 9.8a,c and e). The ammonia sensitivity was 0.015/ ppm, 0.0707/ppm and 0.0069/ppm in the pristine HCSs, HCSs:PVP and the annealed HCSs (Fig. 9.8b, d and f). The ammonia sensitivity curves of the three carbon based sensors at 33%, 59%, 75% and 97% RH are shown in Figs. S9.5, S9.6 and S9.7. A summary of the ammonia sensitivity in Table 9.3

shows that the pristine HCSs and HCSs:PVP exhibited the highest sensitivity at 10% RH while that of the annealed HCSs was at 33% RH. However, the overall ammonia sensitivity of the annealed HCSs was higher than that of the pristine HCSs. This can be attributed to a decrease in the number of surface functional groups and structural defects.

The ammonia sensitivity of the pristine HCSs at 97% RH was nearly zero. This behaviour could result from supersaturation of hydroxyl groups and water vapor molecules on the HCSs surface that inhibits ammonia adsorption. In contrast, the ammonia sensitivity of the HCSs:PVP composites at 97% RH was high due to a uniform dispersion of carbon-polymer composite on the surface. However, the polymer (PVP) played a role in decreasing the overall conductivity at higher RH due to PVP swelling. A similar behaviour has been reported in polymeric materials such as Nafion, in which the presence of water vapour molecules slows down the reaction rate related to ammonia sensitivity[70]. Interestingly, the ammonia sensitivity of annealed HCSs was lowest at 10% and 97% RH. This can be attributed to the removal of surface and structural defects thus reducing the dependency of ammonia response on the relative humidity upon HCSs annealing.

Indeed, the presence of functional groups and defects affects ammonia adsorption on the HCSs. As seen from Table 9.3 the overall ammonia sensitivity was highest in the annealed HCSs in almost all the conditions. This further highlights the role of the degree of graphitization of HCSs in improving the conductivity response in the presence of ammonia vapours.

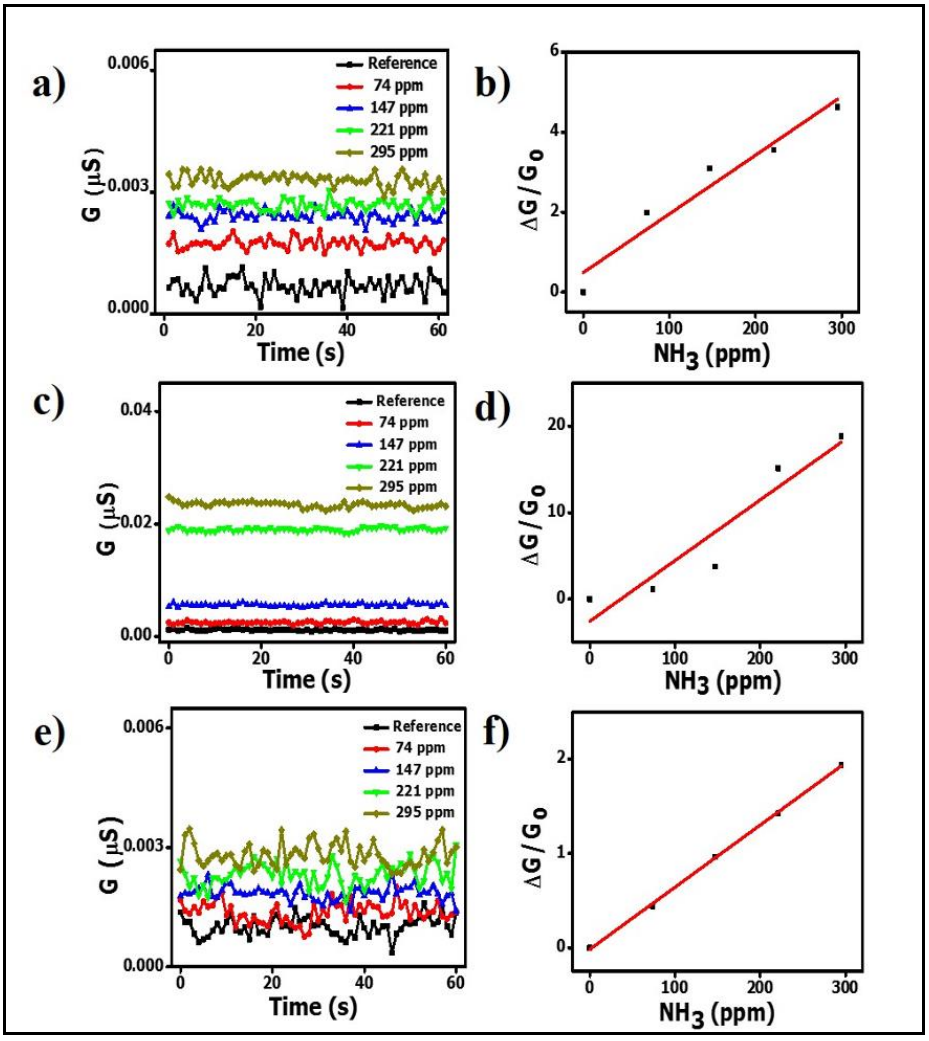

Figure 9.8. Conductance and sensitivity of the HCSs (a and b); HCSs:PVP (c and d) and; annealed HCSs (e and f) based sensors at 10% RH and different ammonia concentrations.

Table 9.3. A summary of the % sensitivity per ppm of ammonia of the carbon based sensors

Sensor	20 °C	40°C	Relative Humidity (%)				
			10	33	59	75	97
Pristine HCSs	1.00	0.08	1.50	0.40	0.40	0.60	-0.03
HCSs:PVP	2.50	4.00	7.10	0.10	0.005	1.50	0.70
Annealed HCSs	0.89	1.60	0.70	7.00	1.80	2.70	0.80

9.3.7 Application of tristimulus methodology

To apply our new ammonia sensors to real situations, we applied a simple pattern recognition technique method based on a previously reported generalized tristimulus analysis (that accepts positive or negative sensitivities without loss in information)[71]. Briefly, this approach takes the responses of three different sensors of an array that is assumed to have a linear response with respect to the concentration of the analyte, as three components of the tristimulus vector $\vec{r} = \alpha[\mathrm{A}]\hat{x} + \beta[\mathrm{A}]\hat{y} + \gamma[\mathrm{A}]\hat{z}$. The responses I_i of the three sensors can be written as $I_1 = \alpha[\mathrm{A}]$, $I_2 = \beta[\mathrm{A}]$ and $I_3 = \gamma[\mathrm{A}]$, where α, β and γ are the respective sensitivities and [A] denotes the concentration of ammonia. These I_i values are then used to calculate

$$i_1 = \frac{I_1}{\sqrt{I_1^2 + I_2^2 + I_3^2}} = \frac{\alpha}{\sqrt{\alpha^2 + \beta^2 + \gamma^2}},$$

$$i_2 = \frac{I_2}{\sqrt{I_1^2 + I_2^2 + I_3^2}} = \frac{\beta}{\sqrt{\alpha^2 + \beta^2 + \gamma^2}} \text{ and}$$

$$i_3 = \frac{I_3}{\sqrt{I_1^2 + I_2^2 + I_3^2}} = \frac{\gamma}{\sqrt{\alpha^2 + \beta^2 + \gamma^2}}. \quad \textbf{(9.3)}$$

In the generalized tristimulus we analyze the angular coordinates θ and ϕ of the point where the tristimulus vector crosses a unitary radius spherical shell given by $\sqrt{i_1^2 + i_2^2 + i_3^2} = 1$, as shown in Fig. 9.9.

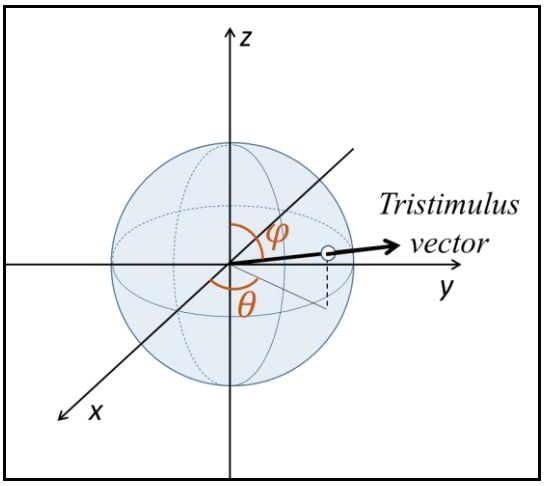

Figure 9.9. Geometrical representation of the tristimulus vector crossing a unitary radius spherical shell and the angles ϕ and θ.

The angular coordinates ϕ and θ of the point where the vector crosses the unitary radius spherical shell can be written as follows:

$$\varphi = \cos^{-1}\frac{I_3}{\sqrt{I_1^2+I_2^2+I_3^2}} \text{ and } \theta = \tan^{-1}\frac{I_2}{I_1} \quad \textbf{(9.4)}$$

In this equation, the angle θ is plotted using the function *atan2*, which analyzes the input arguments (I_1 and I_2) signals returning the correct quadrant of the angle, in a range of $-\pi \leq \theta < \pi$. These angles ϕ and θ constitute a signature of the analyte, confining, the coordinates to the intervals $0 \leq \phi < \pi$ and $-\pi \leq \theta < \pi$. Note that if the concentration of ammonia is increased or decreased the coordinates of the point and angles of the vector will not change (assuming constancy of α, β and γ); only its magnitude will change (Fig. 9.10). As the humidity changes, the number of water molecules that will interact with the active layer will change the response (and consequently the sensitivity), dislocating the tristimulus vector to other regions of the graph. Each region will give a cluster of points that correspond to one different humidity level. Fig. 9.10 shows the presence of four different cluster regions of 10%, 33%, 59%-75% and 97% RH.

The fact that for each humidity cluster, the points corresponding to different ammonia concentrations do not overlap indicates that the sensors response to relative ammonia and humidity are not independent of each other, *i. e.*, the variation of the ammonia concentration produces variations in the sensitivity to water (relative humidity), evidenced by the spread of the points of each cluster. In a case of ideally independent sensitivities, this spread should be very small and only due to electronic noise. An undesired characteristic of this set of sensors is that it is not able to allow distinction of RH values of 59% and 75%. In a practical problem, the sensor set response should give the humidity information and a second analysis using a 3-D map can be used to give the correct ammonia concentration at ambient, as shown in Fig. 9.11. This second analysis complements the tristimulus one and makes possible a real time monitoring of ammonia at different RH levels. If the humidity cannot be determined from the tristimulus analysis, for example in the 59 and 75% RH case, the two values have to be taken in the analysis of the 3D maps of the three sensors. Here only the value that is repeatedly obtained in the three maps as the correct ammonia concentration is taken and the others are disregarded. The value of humidity that leads to repeated ammonia concentration information is the correct humidity value.

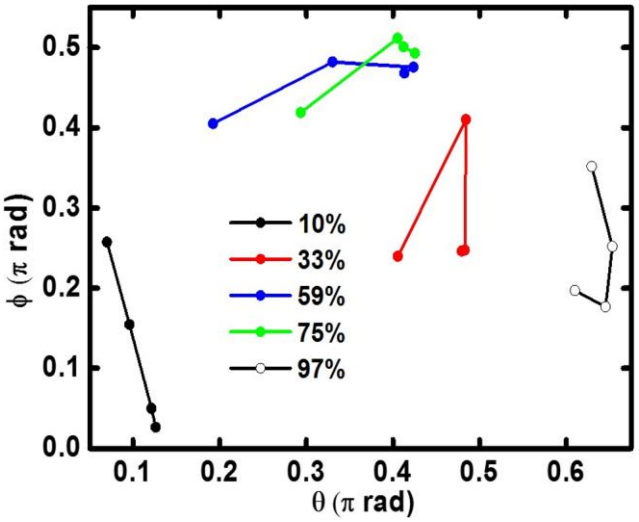

Figure 9.10. Angular coordinates ϕ and θ of the tristimulus vector of the sensor's array based on pristine HCSs, HCSs:PVP composite and the annealed HCSs for ammonia response at different RH.

This procedure described above allows for the concomitant determination of ammonia concentration and relative humidity using a set of three sensors. However the method is not a simple and direct way to obtain the data. Further investigation is still necessary to find a set of sensors in which the clusters of points that correspond to different humidity do not overlap. This would generate a more precise estimative of the humidity. The ideal set of sensors would allow ammonia and RH determination only with the tristimulus analysis, if necessary using the 3D maps as a confirmation of the approach.

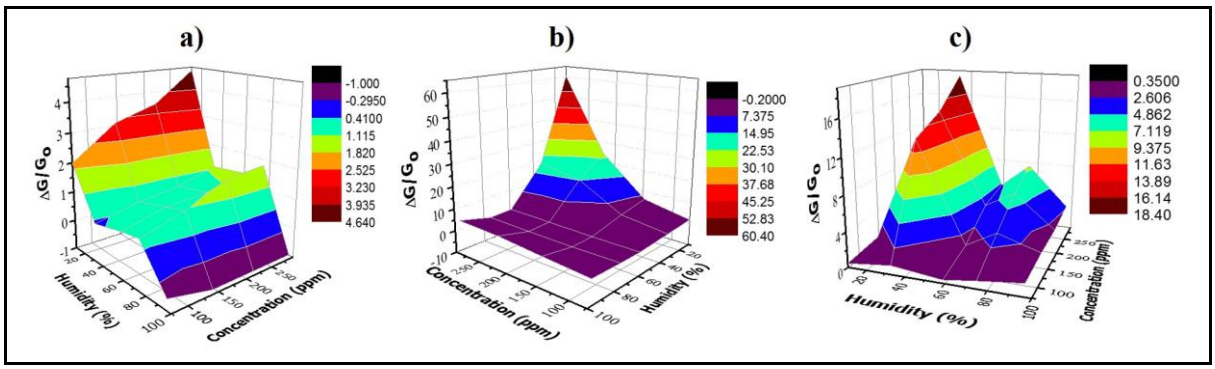

Figure 9.11. Surface plot showing the response for ammonia and different RH for (a) pristine HCSs, (b) HCSs:PVP and (c) the annealed HCSs, respectively.

9.4 Conclusions

This study has investigated the response of hollow carbon spheres to ammonia and relative humidity. The conductivity of the carbon spheres was highly dependent on the relative humidity with HCSs and HCSs:PVP exhibiting the best ammonia response at 10% RH and the annealed HCSs materials at 33% RH. The presence of surface functional groups and defect sites plays a critical role in varying the humidity response of the hollow carbon spheres. The polymer plays a crucial role in enhancing the homogeneous dispersion of the carbon spheres and the formation of a smooth morphology. We report for the first time the humidity dependent ammonia response for HCSs, a HCSs:PVP composite and annealed HCSs based nanomaterials. The data generates insight into the dual behaviour of carbon nanostructures as a function of surface reaction and thus can be applied in catalytic adsorption and desorption studies. We have shown that using a simple pattern recognition technique based on generalized tristimulus analysis it is possible to simultaneously identify the RH of the ambient and the ammonia concentration.

References

1. Iijima, S. *Nature* **1991,** 354, (6348), 56-58.
2. Kroto, H. W.; Heath, J. R.; O'Brien, S. C.; Curl, R. F.; Smalley, R. E. *Nature* **1985,** 318, (6042), 162-163.
3. Inagaki, M. *Carbon* **1997,** 35, (5), 711-713.
4. Serp, P.; Feurer, R.; Kalck, P.; Kihn, Y.; Faria, J. L.; Figueiredo, J. L. *Carbon* **2001,** 39, (4), 621-626.
5. Coville, N. J.; Mhlanga, S. D.; Nxumalo, E. N.; Shaikjee, A. *South African Journal of Science* **2011,** 107, 01-15.
6. Jin, Y. Z.; Gao, C.; Hsu, W. K.; Zhu, Y.; Huczko, A.; Bystrzejewski, M.; Roe, M.; Lee, C. Y.; Acquah, S.; Kroto, H.; Walton, D. R. M. *Carbon* **2005,** 43, (9), 1944-1953.
7. Deshmukh, A. A.; Mhlanga, S. D.; Coville, N. J. *Materials Science and Engineering: R: Reports* **2010,** 70, (1–2), 1-28.
8. He, L.; Jia, Y.; Meng, F.; Li, M.; Liu, J. *Materials Science and Engineering: B* **2009,** 163, (2), 76-81.
9. Jang, B.; Yang, K.; Quan, B.; Piao, Y. *Materials Letters* **2013,** 104, 68-71.
10. Joo, J. B.; Kim, P.; Kim, W.; Kim, J.; Kim, N. D.; Yi, J. *Current Applied Physics* **2008,** 8, (6), 814-817.
11. Cai, P.-j.; Feng, L. *Materials Chemistry and Physics* **2008,** 108, (1), 1-3.
12. Sasidharan, M.; Liu, D.; Gunawardhana, N.; Yoshio, M.; Nakashima, K. *Journal of Materials Chemistry* **2011,** 21, (36), 13881-13888.
13. Scherer, G. W.; Brinker, C. J. *Academic: New York* **1990**.
14. Lu, A. H.; Schüth, F. *Advanced Materials* **2006,** 18, (14), 1793-1805.
15. Chen, Q.-L.; Ji, W.-Q.; Chen, S. *Scientific Reports* **2016,** 6, 19382.
16. Phaahlamohlaka, T. N.; Kumi, D. O.; Dlamini, M. W.; Jewell, L. L.; Coville, N. J. *Catalysis Today* **2016**.
17. Wen, Z.; Wang, Q.; Zhang, Q.; Li, J. *Electrochemistry Communications* **2007,** 9, (8), 1867-1872.
18. Han, J.; Xu, G.; Ding, B.; Pan, J.; Dou, H.; MacFarlane, D. R. *Journal of Materials Chemistry A* **2014,** 2, (15), 5352-5357.
19. Tang, K.; Fu, L.; White, R. J.; Yu, L.; Titirici, M. M.; Antonietti, M.; Maier, J. *Advanced Energy Materials* **2012,** 2, (7), 873-877.
20. Machado, W. S.; Athayde, P. L.; Mamo, M. A.; van Otterlo, W. A. L.; Coville, N. J.; Hümmelgen, I. A. *Organic Electronics* **2010,** 11, (11), 1736-1739.
21. Mamo, M. A.; Machado, W. S.; Coville, N. J.; Hümmelgen, I. A. *Journal of Materials Science: Materials in Electronics* **2012,** 23, (7), 1332-1337.
22. Cunha, B. B.; Greenshields, M. W.; Mamo, M. A.; Coville, N. J.; Hümmelgen, I. A. *Journal of Materials Science: Materials in Electronics* **2015,** 26, (6), 4198-4201.
23. Mamo, M. A.; Machado, W. S.; van Otterlo, W. A.; Coville, N. J.; Hümmelgen, I. A. *Organic Electronics* **2010,** 11, (11), 1858-1863.
24. Hümmelgen, I. A.; Coville, N. J.; Cruz-Cruz, I.; Rodrigues, R. *Journal of Materials Chemistry C* **2014,** 2, (37), 7708-7714.
25. Dölle, S.; Lechner, B.-D.; Park, J. H.; Schymura, S.; Lagerwall, J. P. F.; Scalia, G. *Angewandte Chemie International Edition* **2012,** 51, (13), 3254-3257.
26. Rafael, R.; Messai, A. M.; Neil, J. C.; Ivo, A. H. *Materials Research Express* **2014,** 1, (1), 015605.
27. Torres-Canas, F. J.; Blanc, C.; Zamora-Ledezma, C.; Silva, P.; Anglaret, E. *The Journal of Physical Chemistry C* **2015,** 119, (1), 703-709.
28. Santra, S.; Hu, G.; Howe, R.; De Luca, A.; Ali, S.; Udrea, F.; Gardner, J.; Ray, S.; Guha, P.; Hasan, T. *Scientific Reports* **2015,** 5.
29. Ghosh, R.; Midya, A.; Santra, S.; Ray, S. K.; Guha, P. K. *ACS Applied Materials & Interfaces* **2013,** 5, (15), 7599-7603.
30. Majzlíková, P.; Sedláček, J.; Prášek, J.; Pekárek, J.; Svatoš, V.; Bannov, A. G.; Jašek, O.; Synek, P.; Eliáš, M.; Zajíčková, L. *Sensors* **2015,** 15, (2), 2644-2661.
31. Cui, S.; Pu, H.; Lu, G.; Wen, Z.; Mattson, E. C.; Hirschmugl, C.; Gajdardziska-Josifovska, M.; Weinert, M.; Chen, J. *ACS Applied Materials & Interfaces* **2012,** 4, (9), 4898-4904.

32. Timmer, B.; Olthuis, W.; Berg, A. v. d. *Sensors and Actuators B: Chemical* **2005,** 107, (2), 666-677.
33. Beusen, A. H. W.; Bouwman, A. F.; Heuberger, P. S. C.; Van Drecht, G.; Van Der Hoek, K. W. *Atmospheric Environment* **2008,** 42, (24), 6067-6077.
34. Krupa, S. V. *Environmental Pollution* **2003,** 124, (2), 179-221.
35. Durbin, T. D.; Wilson, R. D.; Norbeck, J. M.; Miller, J. W.; Huai, T.; Rhee, S. H. *Atmospheric Environment* **2002,** 36, (9), 1475-1482.
36. Sekhar, P. K.; Brosha, E. L.; Mukundan, R.; Li, W.; Nelson, M. A.; Palanisamy, P.; Garzon, F. H. *Sensors and Actuators B: Chemical* **2010,** 144, (1), 112-119.
37. Baruah, S.; Dutta, J. *Environmental Chemistry Letters* **2009,** 7, (3), 191-204.
38. Rittersma, Z. M. *Sensors and Actuators A: Physical* **2002,** 96, (2–3), 196-210.
39. Cao, C. L.; Hu, C. G.; Fang, L.; Wang, S. X.; Tian, Y. S.; Pan, C. Y. *Journal of Nanomaterials* **2011,** 2011, 5.
40. Yu, H.; Cao, T.; Zhou, L.; Gu, E.; Yu, D.; Jiang, D. *Sensors and Actuators B: Chemical* **2006,** 119, (2), 512-515.
41. Fei, T.; Jiang, K.; Jiang, F.; Mu, R.; Zhang, T. *Journal of Applied Polymer Science* **2014,** 131, (1), n/a-n/a.
42. Pati, R.; Zhang, Y.; Nayak, S. K.; Ajayan, P. M. *Applied Physics Letters* **2002,** 81, 2638.
43. Patissier, B. *Sensors and Actuators B: Chemical* **1999,** 59, (2–3), 231-234.
44. Duncan, T. V. *Journal of Colloid and Interface Science* **2011,** 363, (1), 1-24.
45. Travlou, N. A.; Seredych, M.; Rodriguez-Castellon, E.; Bandosz, T. J. *Journal of Materials Chemistry A* **2015,** 3, (7), 3821-3831.
46. Feng, X.; Irle, S.; Witek, H.; Morokuma, K.; Vidic, R.; Borguet, E. *Journal of the American Chemical Society* **2005,** 127, (30), 10533-10538.
47. Robinson, J. A.; Snow, E. S.; Bădescu, Ş. C.; Reinecke, T. L.; Perkins, F. K. *Nano Letters* **2006,** 6, (8), 1747-1751.
48. Watts, P. C.; Mureau, N.; Tang, Z.; Miyajima, Y.; Carey, J. D.; Silva, S. R. P. *Nanotechnology* **2007,** 18, (17), 175701.
49. Su, P.-G.; Tsai, J.-F. *Sensors and Actuators B: Chemical* **2009,** 135, (2), 506-511.
50. Tang, S.; Cao, Z. *The Journal of Physical Chemistry C* **2012,** 116, (15), 8778-8791.
51. Rigoni, F.; Drera, G.; Pagliara, S.; Goldoni, A.; Sangaletti, L. *Carbon* **2014,** 80, 356-363.
52. Raimundo, I. M.; Narayanaswamy, R. *Sensors and Actuators B: Chemical* **2001,** 74, (1), 60-68.
53. Xia, Y. D.; Mokaya, R. *Advanced Materials* **2004,** 16, (11), 886-891.
54. Greenshields, M. W.; Hümmelgen, I. A.; Mamo, M. A.; Shaikjee, A.; Mhlanga, S. D.; Van Otterlo, W. A.; Coville, N. J. *Journal of Nanoscience and Nanotechnology* **2011,** 11, (11), 10211-10218.
55. Greenspan, L. *Journal of Research of the National Bureau of Standards* **1977,** 81, (1), 89-96.
56. Maciel, G. E. *Journal of the American Chemical Society* **1996,** 118, (2), 401-406.
57. Wilgosz, K.; Chen, X.; Kierzek, K.; Machnikowski, J.; Kalenczuk, R. J.; Mijowska, E. *Nanoscale Research Letters* **2012,** 7, (1), 1-5.
58. Thommes, M. *Chemie Ingenieur Technik* **2010,** 82, (7), 1059-1073.
59. Ferrari, A. C. *Solid State Communications* **2007,** 143, (1–2), 47-57.
60. Pimenta, M. A.; Dresselhaus, G.; Dresselhaus, M. S.; Cancado, L. G.; Jorio, A.; Saito, R. *Physical Chemistry Chemical Physics* **2007,** 9, (11), 1276-1290.
61. Tuinstra, F.; Koenig, J. L. *The Journal of Chemical Physics* **1970,** 53, (3), 1126-1130.
62. Peng, L.; Zhai, J.; Wang, D.; Zhang, Y.; Wang, P.; Zhao, Q.; Xie, T. *Sensors and Actuators B: Chemical* **2010,** 148, (1), 66-73.
63. Gautam, M.; Jayatissa, A. H. *Solid-State Electronics* **2012,** 78, 159-165.
64. Singh, K.; Travlou, N. A.; Bashkova, S.; Rodríguez-Castellón, E.; Bandosz, T. J. *Carbon* **2014,** 80, 183-192.
65. Ghosh, R.; Singh, A.; Santra, S.; Ray, S. K.; Chandra, A.; Guha, P. K. *Sensors and Actuators B: Chemical* **2014,** 205, 67-73.

66. Zhou, Y.; Wang, B.; Song, X.; Li, E.; Li, G.; Zhao, S.; Yan, H. *Applied Surface Science* **2006,** 253, (5), 2690-2694.
67. Bhattacharya, S.; Sharma, D. K.; Saurabh, S.; De, S.; Sain, A.; Nandi, A.; Chowdhury, A. *The Journal of Physical Chemistry B* **2013,** 117, (25), 7771-7782.
68. Bi, H.; Yin, K.; Xie, X.; Ji, J.; Wan, S.; Sun, L.; Terrones, M.; Dresselhaus, M. S. *Scientific Reports* **2013,** 3, 2714.
69. Zhang, D.; Tong, J.; Xia, B. *Sensors and Actuators B: Chemical* **2014,** 197, 66-72.
70. Raimundo Jr, I. M.; Narayanaswamy, R. *Sensors and Actuators B: Chemical* **2001,** 74, (1–3), 60-68.
71. Rodrigues, R.; Hümmelgen, I. A. *Journal of Solid State Electrochemistry* **2016,** 20, (5), 1295-1301.

CHAPTER 10

General Conclusions and Recommendations

10.1 Conclusions

10.1.1 Synthesis of solid carbon spheres and their properties upon annealing

- The effect of varying the carrier gas and flow rate on the carbon spheres grown in a vertically oriented CVD reactor was investigated. High flow rates of the carbon source resulted in the formation of smaller carbon spheres (< 300 nm).

- The carbon source and carrier gas flow rate and the duration time of the carbon source in the furnace played a key role in the particle size distribution

- The properties of the carbon spheres upon annealing were significantly determined by the type of gas present. In the presence of hydrogen gas, the carbon spheres were characterized by fewer defects and higher thermal stability. Consequently their I_D/I_G ratios were lower and their paramagnetic signals were stronger.

10.1.2 Properties of solid carbon spheres after Nitrogen doping

- The XPS results confirmed the etching of carbon atoms by hydrogen with N-doped CSs in the presence of hydrogen exhibiting low C content and higher % of pyridinic-N.

- The N-doped CSs obtained in the presence of argon showed a higher % of graphitic-N and higher C content from the XPS data. In addition, the total N content was lower than in the N-doped CSs obtained using hydrogen as a carrier gas.

10.1.3 Synthesis of hollow carbon nanostructures with varying morphologies

- The particle size and morphology of SiO_2 spheres can be tuned by controlling the reaction parameters using the Stober method.

- The morphology of the carbon nanostructures obtained via a templating route was highly dependent on the template diameter, size dispersity and surface chemistry.

- Complete and mesoporous HCSs.
- Mesoporous broken HCSs
- Open ended HCSs (high BET open surface area of 894 m^2/g)

- The functionalization of silica with PVP does affect the thermal stability and the degree of graphitization of the resulting HCSs after carbonization and silica removal.

- The use of $Au@SiO_2$ spheres as templates resulted in carbon nanomaterials of different morphologies which were influenced by SiO_2 size dispersity, presence of Au, PVP concentration, PVP adsorption time and CVD carbonization time.
    - Complete HCSs,
    - Worm-like, graphene-like and bubble-like HCSs)

- The open ended worm-like carbon nanostructures gave measurable response in OPVs.

10.1.4 Synthesis and application of gold nanomaterials

- The growth of the gold nanoparticles with varying shapes (spheres or rods) can be controlled by varying the molar ratio of the reducing agent to the gold precursor.

- A homogeneous dispersion of Au nanospheres in the hole transport layer enhanced the OPV perfomance.

- Use of Au nanorods in the hole transport layer resulted in increased series resistance that retarded the OPV perfomance.

- The size dispersion of Au in the polymer matrix played a critical role in the OPV device perfomance despite showing improvements in SERS and the optical properties of the films.

10.1.5 Improvement of OPV performance by solution heat treatment

- Solution heat treatment of a P3HT:PCBM blend enhanced the polymer crystallinity, diffusion, light absorption and overall device performance.

- Pre-heat treatment of P3HT separately hindered the polymer diffusion and limited the OPV performance.

10.1.6 Application of HCSs as ammonia and relative humidity sensors

- For the first time, the use of pristine HCSs, HCSs/PVP and annealed HCSs as humidity dependent ammonia sensors was reported.

- The ammonia sensitivity of pristine HCSs are highly dependent on relative humidity and temperature.

- Increasing the degree of graphitization of HCS based ammonia sensors by annealing resulted in a decreased relative humidity dependence.

- The exact ammonia concentration and relative humidity of the HCS based ammonia sensors at a given response can be determined using tristimulus analysis.

10.2 Recommendations

10.2.1 Properties of carbon nanomaterials

- The paramagnetic properties of the solid carbon spheres annealed in hydrogen can be explored for their suitable application in magnetoresistive devices.

10.2.2 Applications of open ended carbon nanostructures

- The study of the contact angle characteristics and other surface properties will be beneficial to the possible use of these materials as dye adsorbents

- Also, the modified Stober route can be used to explore the formation of open network structures from silica-polymer composites by use of other polymers.

- Theoretical calculations to determine the effects of surface and volume terms in the Gibb's free energy on the shape and stability of HCSs can be undertaken.

- Furthermore, the graphene-like carbon nanostructures can be doped with nitrogen and boron for an improved perfomance in OPVs and other electronic devices.

10.2.3 Synthesis and application of gold nanomaterials

- Increasing the gold precursor to citrate molar ratio during the synthesis of gold nanoparticles and gold nanorods could enable synthesis of more stable gold nanomaterials.

- Dilution of the gold nanorod solution could result in higher PCEs. SERS analysis of PCBM and P3HT would be interesting as they technique could show the effect of gold coupling on the absorption and vibration bands of the active layer constituents.

- Fabrication of organic solar cell devices in an inert atmosphere (N_2 or Ar) will reduce oxidation of the polymers that takes place in ambient atmosphere and enhance the cell performance.

- Vertical variation in the nanoscale morphology to improve charge carrier mobility.

10.2.4 Improvement of OPV performance by solution heat treatment

- The use of different solvents such as acetone and cyclohexanone vapour annealing as chlorobenzene from the "green" aspect is not favourable.

- Fabrication of the OPV devices under N_2 or Ar.

10.2.5 Application of HCSs as ammonia and relative humidity sensors

- From our preliminary results it was not possible to clearly distinguish the ammonia response and sensitivity of HCSs based sensors at RH 50, 60 and 70 %. It will be interesting to differentiate the RH dependency response in these three regions.

- Verification of the possible mechanisms of operation using XPS and Raman after ammonia adsorption.

- Ammonia adsorption/desorption activation barrier dependence studies on the morphology of HCSs.

Appendix A: Supplementary Information

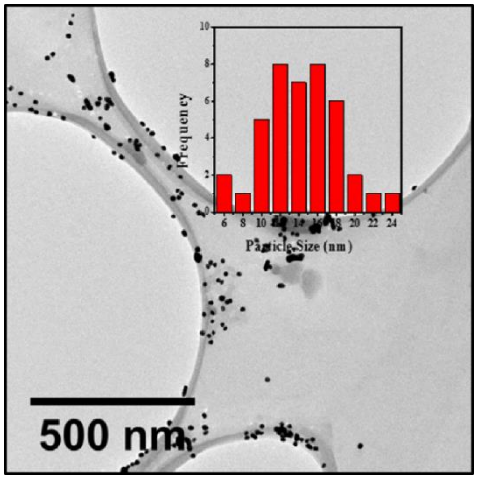

Figure S6.1. TEM image of synthesized gold nanoparticles.

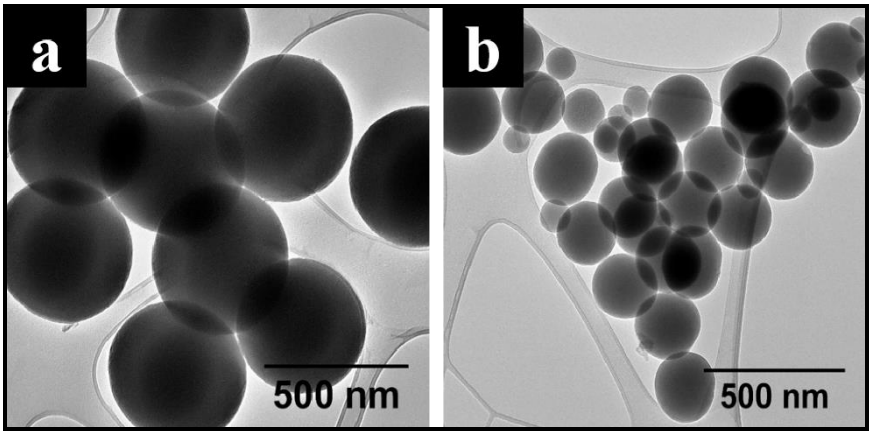

Figure S6.2. TEM images of (a) monodispersed SiO_2 spheres and (b) polydispersed SiO_2 spheres.

B.K. Mutuma, B. Matsoso, K. Ranganathan, D. Wamwangi, N.J. Coville, RSC Advances, 6 (2016) 20399-20408.

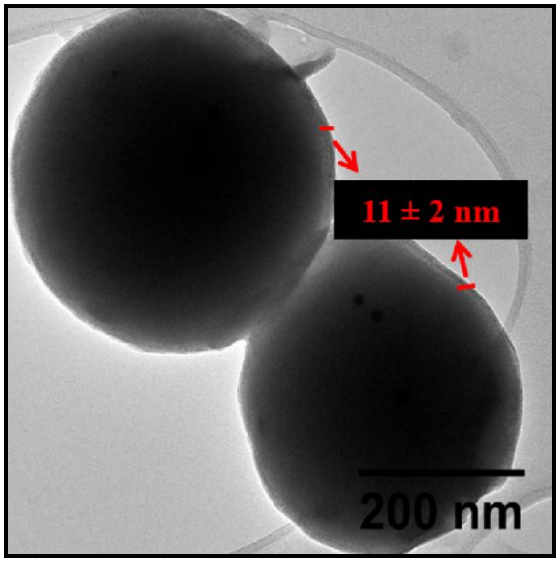

Figure S6.3. TEM image of Au@SiO_2C@C1 after 1 h carbonization time.

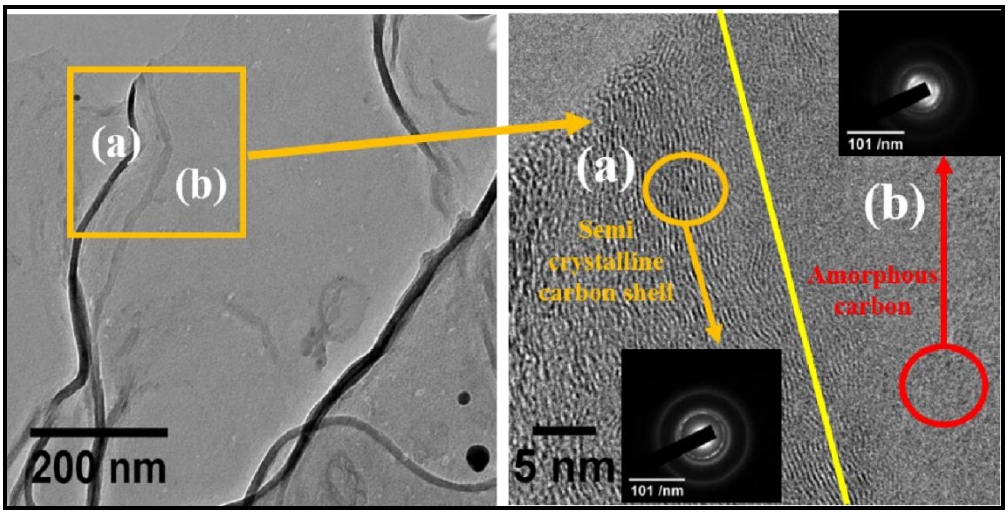

Figure S6.4. HRTEM images of Au@HCSC1; (a) carbon shell which is semicrystalline as shown by the presence of diffuse rings with tiny spots (see SAED pattern) and (b) the amorphous carbon.

B.K. Mutuma, B. Matsoso, K. Ranganathan, D. Wamwangi, N.J. Coville, RSC Advances, 6 (2016) 20399-20408.

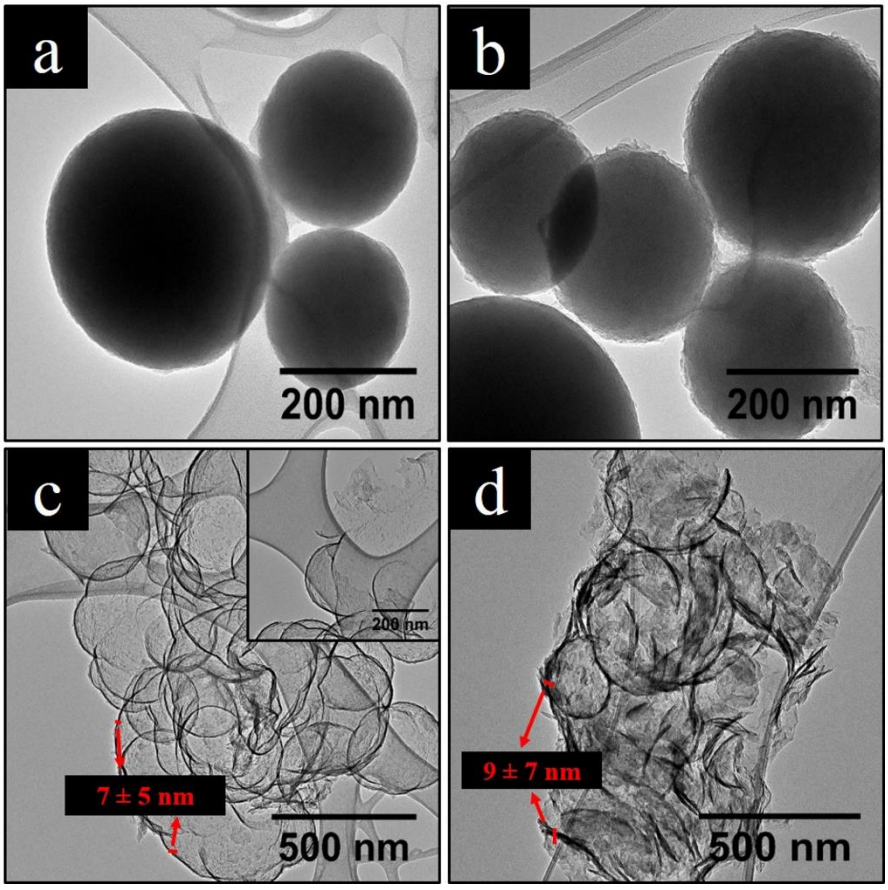

Figure S6.5. TEM images of polydispersed SiO_2 spheres mixed with PVP (a) 1 h and (b) 12 h stirring times and the hollow carbon nanostructures obtained from (c) SiO_2@PVP 1 h and (d) SiO_2@PVP 12 h after 1 h carbonization time and SiO_2 removal, respectively.

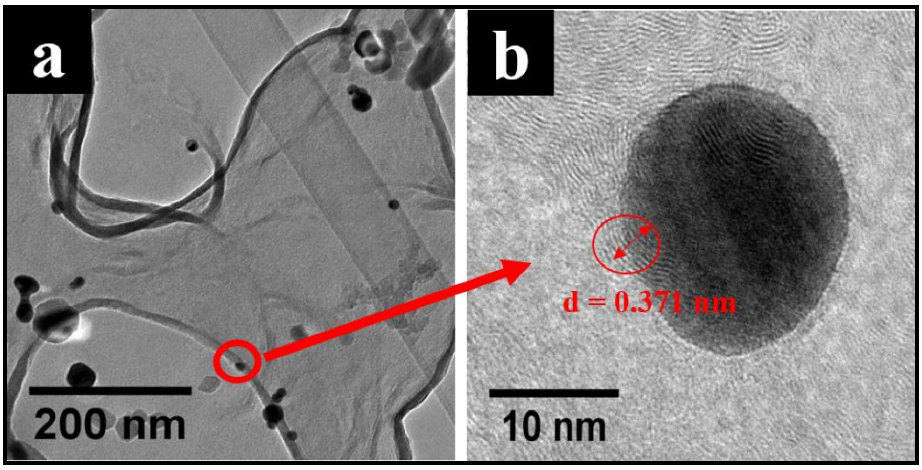

Figure S6.6. HRTEM images of Au embedded in Au@HCSC1.

B.K. Mutuma, B. Matsoso, K. Ranganathan, D. Wamwangi, N.J. Coville, RSC Advances, 6 (2016) 20399-20408.

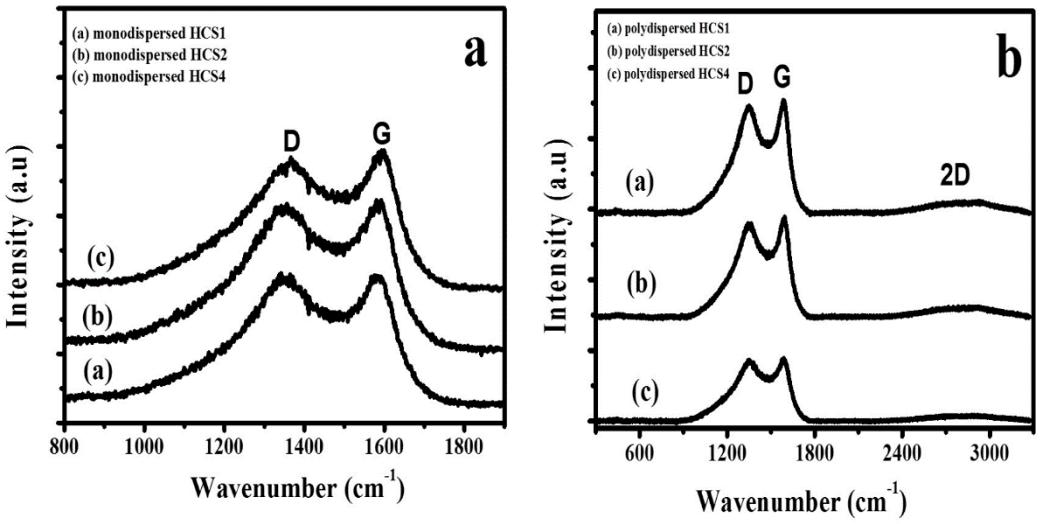

Figure S6.7. Raman spectra of HCSs obtained from **(a)** monodispersed SiO_2 and **(b)** polydispersed SiO_2 spheres after (1 h, 2 h, 4 h) carbonization times and SiO_2 removal, respectively.

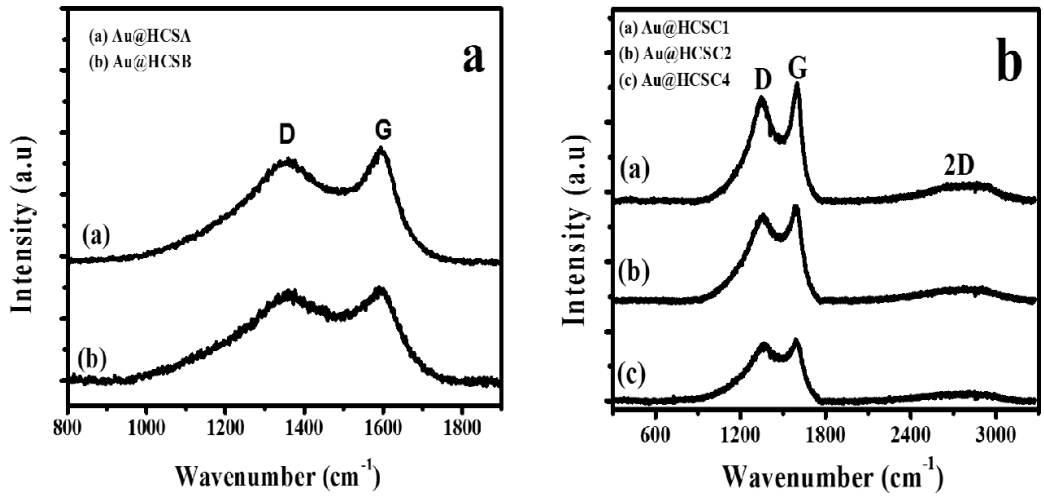

Figure S6.8. Raman spectra of Au@HCSs obtained from (a) monodispersed Au@SiO_2 spheres after 1 h carbonization time and SiO_2 removal and (b) polydispersed Au@SiO_2 spheres after (1 h, 2 h, 4 h) carbonization times and SiO_2 removal, respectively.

B.K. Mutuma, B. Matsoso, K. Ranganathan, D. Wamwangi, N.J. Coville, RSC Advances, 6 (2016) 20399-20408.

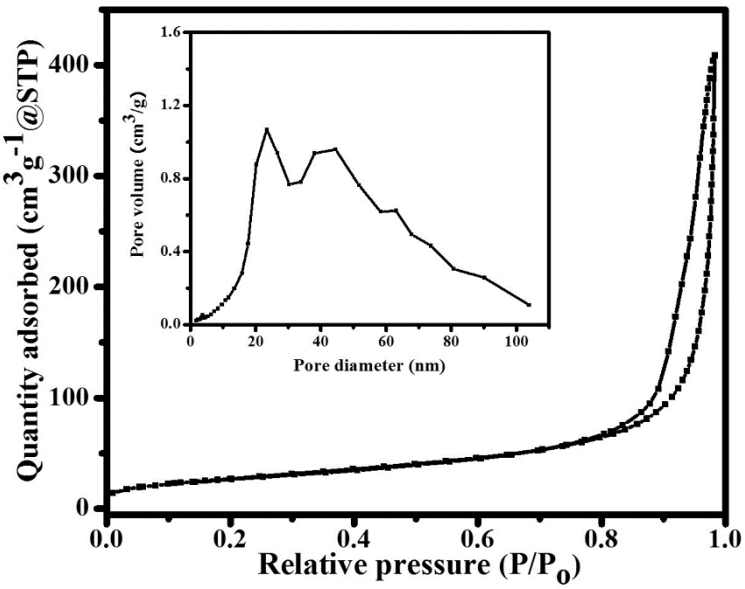

Figure S6.9. Adsorption and desorption curve of the wormlike carbon nanostructure. Inset shows the pore size distribution.

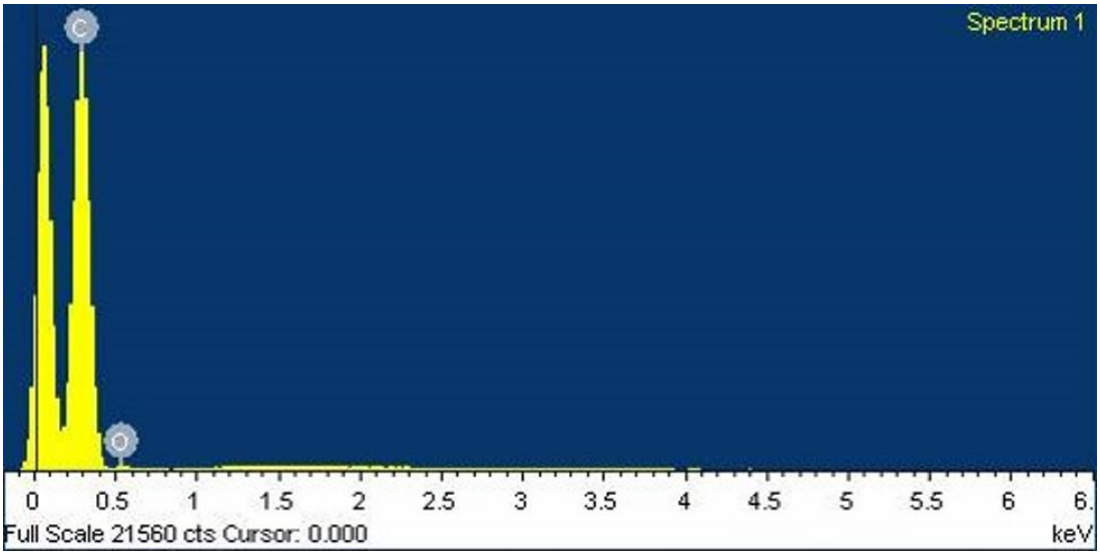

Figure S6.10. EDS spectra of the obtained wormlike hollow carbon nanostructures. The EDS spectrum of the wormlike hollow carbon nanostructure shows a high carbon peak and a negligible oxygen peak that confirms the complete removal of silica during etching.

B.K. Mutuma, B. Matsoso, K. Ranganathan, D. Wamwangi, N.J. Coville, RSC Advances, 6 (2016) 20399-20408.

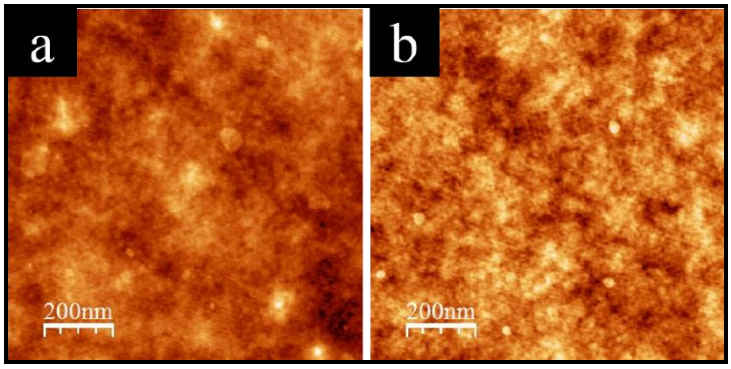

Figure S6.11. AFM topographic images of (a) P3HT:PCBM:wormlike HCSs and (b) P3HT:PCBM:broken HCSs films.

Table S6.1. I_D/I_G ratios of HCSs synthesized at different carbonization time

Description	D band position (cm^{-1})	G band position (cm^{-1})	I_D/I_G ratio
monodispersed HCS1	1356	1592	0.97
monodispersed HCS2	1363	1589	1.00
monodispersed HCS4	1342	1575	1.01
polydispersed HCS1	1349	1583	0.95
polydispersed HCS2	1364	1593	093
polydispersed HCS4	1350	1587	0.97

Table S6.2. I_D/I_G ratios of Au@HCSs synthesized at different carbonization time

Description	D band position (cm^{-1})	G band position (cm^{-1})	I_D/I_G ratio
Au@HCSA	1359	1593	0.90
Au@HCSB	1376	1588	0.97
Au@HCSC1	1370	1590	0.91
Au@HCSC2	1363	1588	0.92
Au@HCSC4	1365	1585	1.03

B.K. Mutuma, B. Matsoso, K. Ranganathan, D. Wamwangi, N.J. Coville, RSC Advances, 6 (2016) 20399-20408.

Appendix B: Supplementary Information

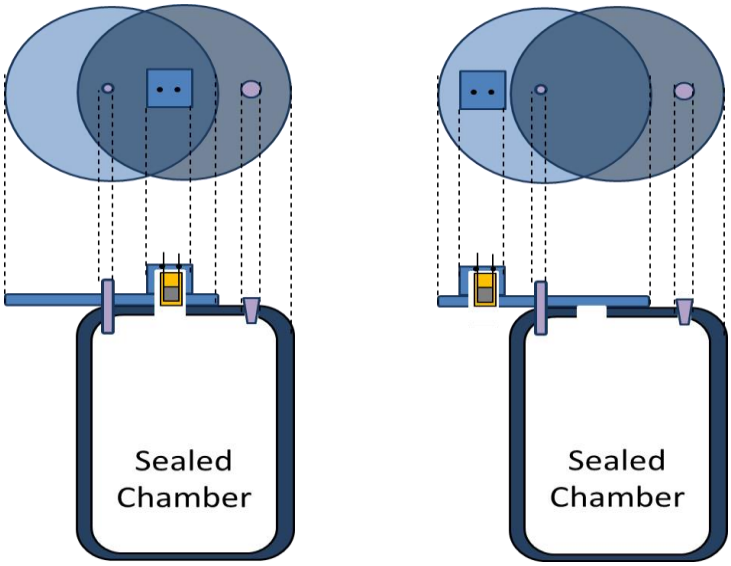

Figure S9.1. A diagram showing the sensor inside and outside of the chamber used for the transient measurements.

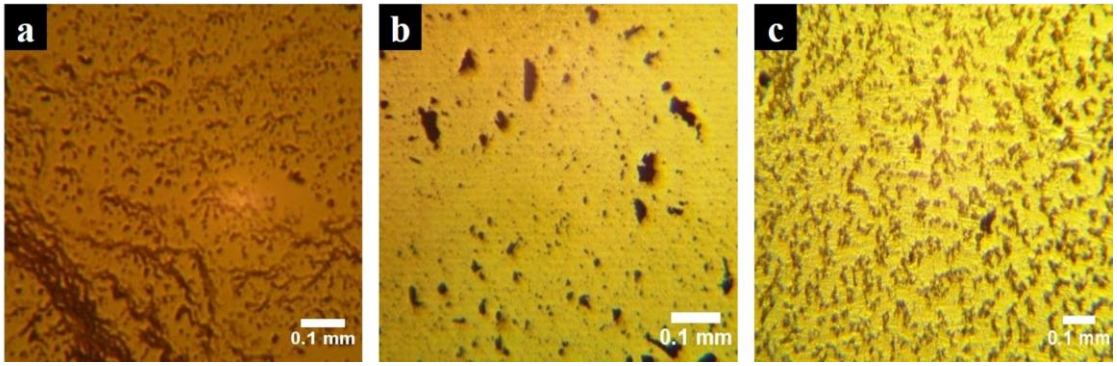

Figure S9.2. Optical images of dispersed spheres in CTAB solution (a) pristine HCSs, (b) HCSs:PVP and (c) annealed HCSs, respectively.

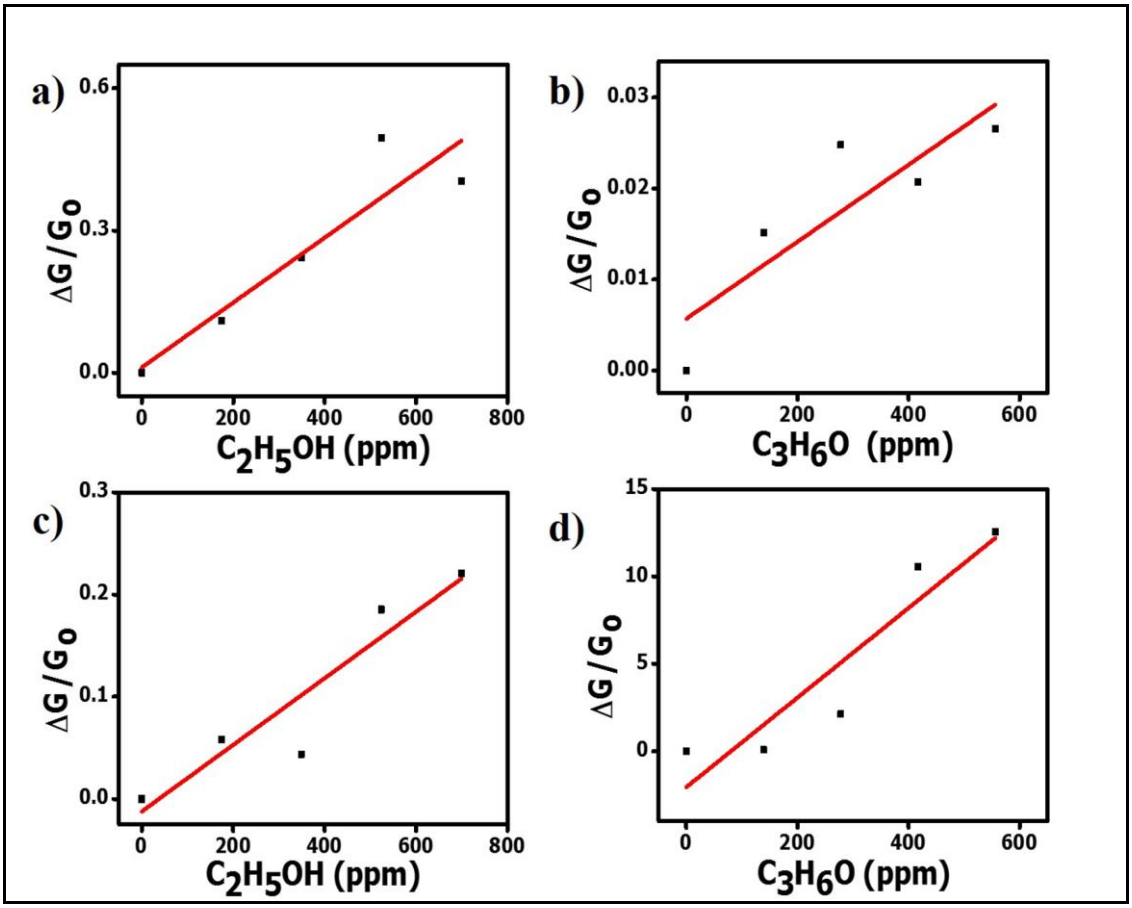

Figure S9.3. The sensitivity curves of the carbon spheres to other vapours: (a and b) obtained from the HCSs:PVP composite and; (c and d) obtained from the annealed HCSs after exposure to ethanol and acetone vapours at 10% RH, respectively. RH: 50%.

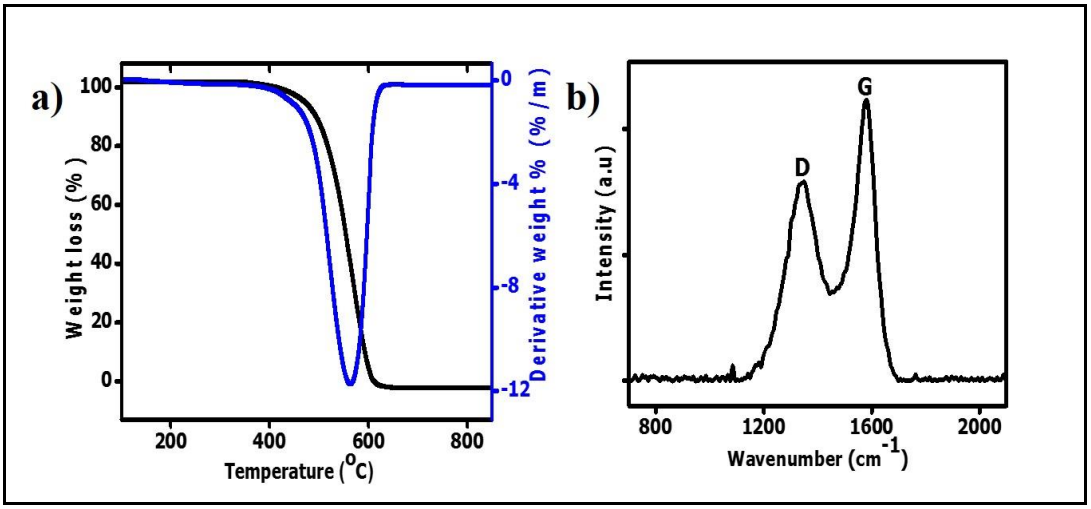

Figure S9.4. The characteristics of the annealed HCSs. (a) TG-DTA curves and (d) Raman spectrum, respectively.

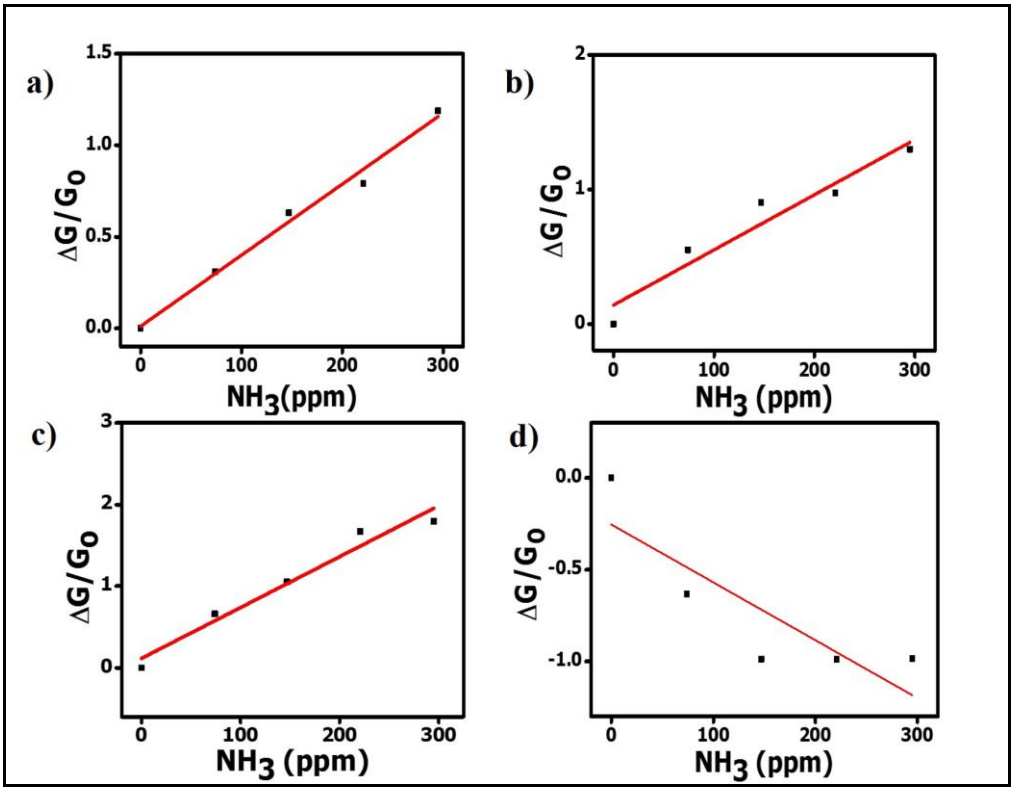

Figure S9.5. The ammonia sensitivity curves in pristine HCSs at different relative humidity. (a) 33% RH; (b) 59% RH; (c) 75% RH and; (d) 97% RH, respectively.

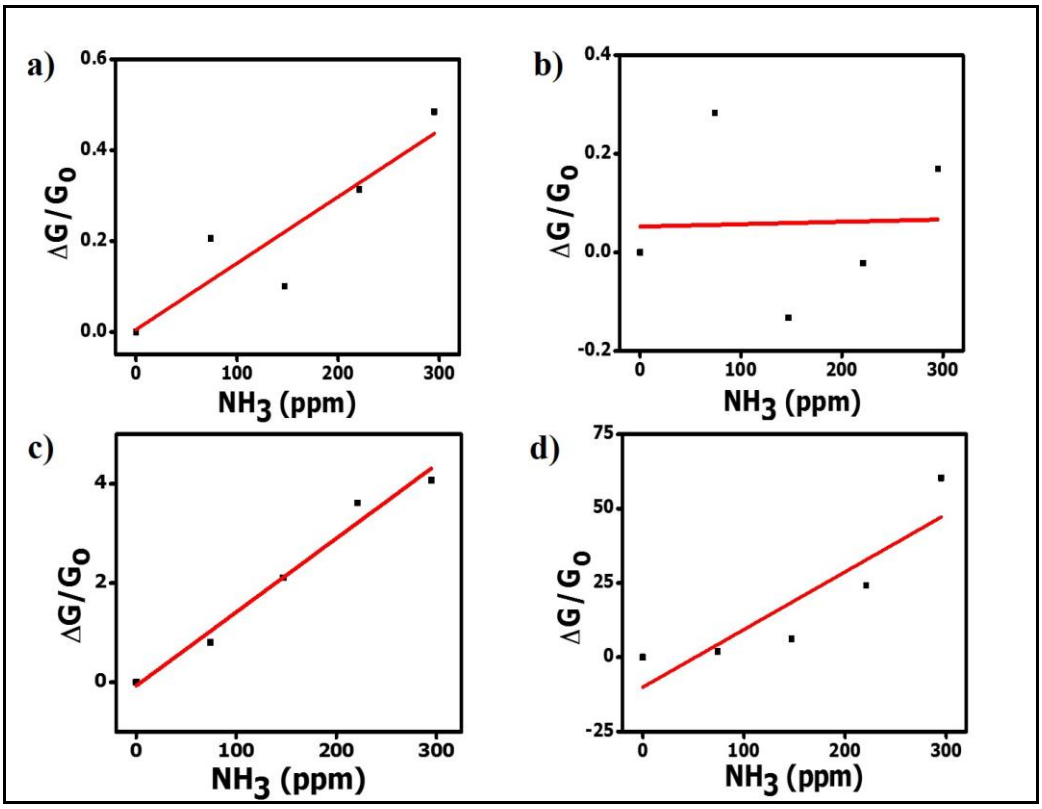

Figure S9.6. The ammonia sensitivity curves in the HCSs:PVP composite at various relative humidity. (a) 33% RH; (b) 59% RH; (c) 75% RH and; (d) 97% RH, respectively.

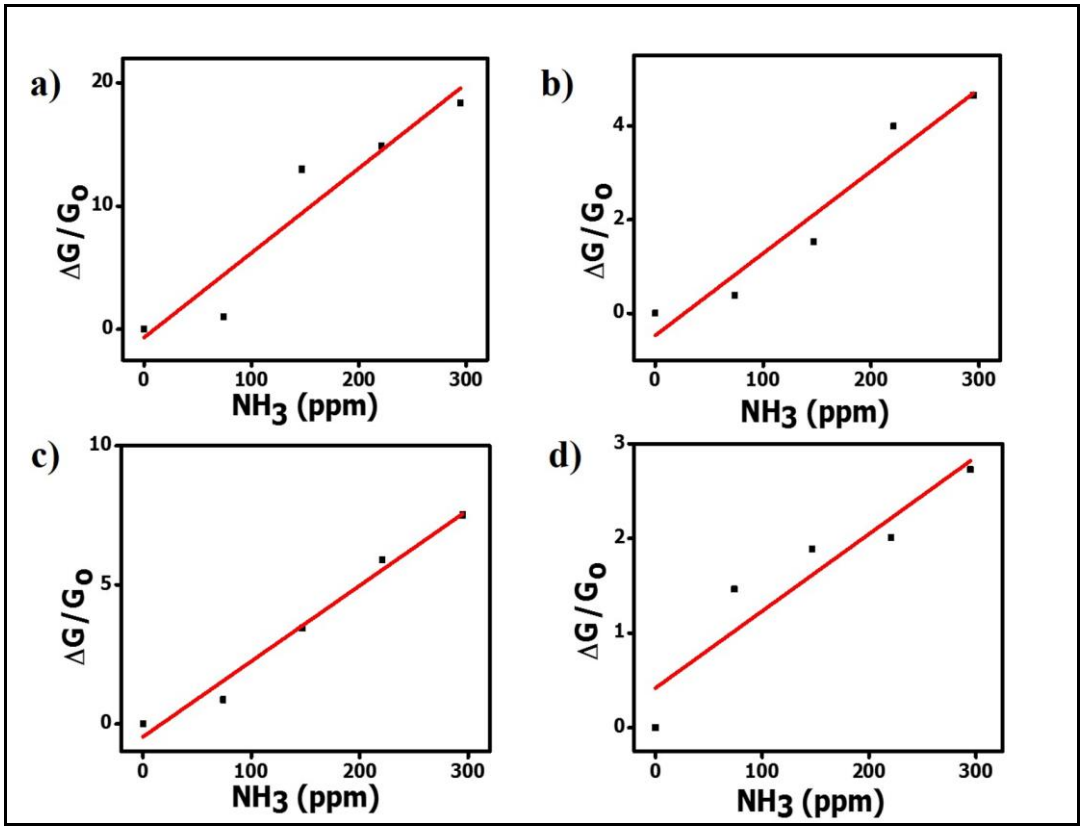

Figure S9.7. The ammonia sensitivity curves in the annealed HCSs at various relative humidity. (a) 33% RH; (b) 59% RH; (c) 75% RH and; (d) 97% RH, respectively.